

Multi-Disciplinary Design Optimization of Subsonic Fixed-Wing Unmanned Aerial Vehicles Projected Through 2025

John Frederick Gundlach, IV

Dissertation submitted to the Faculty of the Virginia Polytechnic Institute
and State University in partial fulfillment of the requirements for the degree
of

Doctorate of Philosophy
in
Aerospace Engineering

J.A. Schetz, Chair
B. Grossman
R. Kapania
E. Cliff
R. Foch

February 9, 2004
Blacksburg, Virginia

Keywords: Multidisciplinary Design Optimization, Aircraft Design, Unmanned Aerial
Vehicle (UAV), Technology Predictions

Copyright 2004, John Gundlach

Multi-Disciplinary Design Optimization of Subsonic Fixed-Wing Unmanned Aerial Vehicles Projected Through 2025

John F. Gundlach

Abstract

Through this research, a robust aircraft design methodology is developed for analysis and optimization of the Air Vehicle (AV) segment of Unmanned Aerial Vehicle (UAV) systems. The analysis functionality of the AV design is integrated with a Genetic Algorithm (GA) to form an integrated Multi-disciplinary Design Optimization (MDO) methodology for optimal AV design synthesis. This research fills the gap in integrated subsonic fixed-wing UAV AV MDO methods. No known single methodology captures all of the phenomena of interest over the wide range of UAV families considered here. Key advancements include: 1) parametric Low Reynolds Number (LRN) airfoil aerodynamics formulation, 2) UAV systems mass properties definition, 3) wing structural weight methods, 4) self-optimizing flight performance model, 5) automated geometry algorithms, and 6) optimizer integration. Multiple methods are provided for many disciplines to enable flexibility in functionality, level of detail, computational expediency, and accuracy.

The AV design methods are calibrated against the High-Altitude Long-Endurance (HALE) Global Hawk, Medium-Altitude Endurance (MAE) Predator, and Tactical Shadow 200 classes, which exhibit significant variations in mission performance requirements and scale from one another. Technology impacts on the design of the three UAV classes are evaluated from a representative system technology year through 2025. Avionics, subsystems, aerodynamics, design, payloads, propulsion, and structures technology trends are assembled or derived from a variety of sources. The technology investigation serves the purposes of validating the effectiveness of the integrated AV design methods and to highlight design implications of technology insertion through future years. Flight performance, payload performance, and other attributes within a vehicle family are fixed such that the changes in the AV designs represent technology differences alone, and not requirements evolution. The optimizer seeks to minimize AV design gross weight for a given mission requirement and technology set.

All three UAV families show significant design gross weight reductions as technology improves. The predicted design gross weight in 2025 for each class is: 1) 12.9% relative to the 1994 Global Hawk, 2) 6.26% relative to the 1994 Predator, and 3) 26.3% relative to the 2000 Shadow 200. The degree of technology improvement and ranking of contributing technologies differs among the vehicle families. The design gross weight is sensitive to technologies that directly affect the non-varying weights for all cases, especially payload and avionics/subsystems technologies. Additionally, the propulsion

technology strongly affects the high performance Global Hawk and Predator families, which have high fuel mass fractions relative to the Tactical Shadow 200 family. The overall technology synergy experienced 10-11 years after the initial technology year is 6.68% for Global Hawk, 7.09% for Predator, and 4.22% for the Shadow 200, which means that the technology trends interact favorably in all cases. The Global Hawk and Shadow 200 families exhibited niche behavior, where some vehicles attained higher aerodynamic performance while others attained lower structural mass fractions. The high aerodynamic performance Global Hawk vehicles had high aspect ratio wings with sweep, while the low structural mass fraction vehicles had straight, relatively low aspect ratios and smaller wing spans. The high aerodynamic performance Shadow 200 vehicles had relatively low wing loadings and large wing spans, while the lower structural mass fraction counterparts sought to minimize physical size.

Acknowledgements

This research would not be possible without the support, advice, guidance, and other contributions from a number of individuals and organizations. My wife and best friend, Katie, provided invaluable encouragement, emotional support, practical advice, time, personal sacrifice, and patience. I will never forget her loving dedication. My advisory committee has shown great flexibility in accommodating an unconventional approach to PhD research. Dr. Schetz, my advisory committee chairman, showed great resourcefulness and creativity in making distance learning arrangements. Dr. Schetz's frequent requests to limit research scope enabled this effort to be completed within a practical timeframe. Guidance and direction provided by the advisory committee has significantly shaped the research. I am grateful to Dr. Fred Lutze, who was a great mentor and guiding influence in my personal and educational development. I will cherish the memory of this great man. Rick Foch shared his extensive experience with me in this effort and during my college internships at NRL. My current employer generously provided tuition funding, which eliminated a financial burden. L.W. championed my quest for knowledge and understood the personal demands associated with pursuing an advanced degree while working full time. I would also like to thank R.L., S.O., M.C., P.A. and R.A. for their steadfast support throughout the duration.

Table of Contents

Abstract.....	ii
Acknowledgements.....	iv
Table of Contents.....	v
List of Figures.....	ix
List of Tables.....	xv
Nomenclature.....	xvii
Chapter 1 Introduction.....	1
1.1 Background.....	1
1.2 Problem Statement.....	6
1.3 Approach.....	6
Chapter 2 Methodology.....	9
2.1 Methodology Overview.....	9
2.2 Methodology Development.....	9
2.3 Applied Methodology Architecture.....	10
2.4 Methods.....	11
2.5 Calibration.....	12
Chapter 3 Optimization.....	13
3.1 Optimization Overview.....	13
3.2 Optimization Code Architecture.....	14
3.3 Design Variables.....	16
3.4 Constraints.....	17
Chapter 4 Technology Modeling.....	21
4.1 Technology Overview.....	21
4.2 Technology Methods.....	23
4.3 Technology Modeling.....	25
4.3.1 Aerodynamics.....	25
4.3.2 Avionics and Subsystems.....	30
4.3.3 Design.....	35
4.3.4 Payloads.....	36
4.3.5 Propulsion.....	39
4.3.6 Structures.....	42
Chapter 5 Geometry.....	46
5.1 Geometry Overview.....	46
5.2 Geometry Definition.....	46
5.2.1 Wings and Tails.....	46
5.2.2 Fuselage.....	46
5.2.3 Propeller.....	48
5.3 Parametric Geometry.....	49
5.3.1 Parametric Fuselage.....	49
5.3.2 Parametric Tails.....	52
5.4 Wing Lift Distribution Paneling.....	53
5.5 Wing Structures Paneling.....	54
5.6 Graphics File Generator.....	57

Chapter 6	Aerodynamics	59
6.1	Aerodynamics Overview	59
6.2	Aerodynamics Code Architecture	60
6.3	Lift Methodology	62
6.3.1	Lift Methodology Overview	62
6.3.2	CG Location Determination	62
6.3.3	Lift Distribution Methods	63
6.3.4	Pitching Moment	68
6.4	Drag Methodology	70
6.4.1	Drag Methodology Overview	70
6.4.2	Profile Drag Overview	71
6.4.3	Interference Drag	89
6.4.4	Fuselage Drag	91
6.4.5	Wave Drag	93
6.4.6	Landing Gear Drag	94
6.4.7	Cooling Drag	95
6.4.8	Miscellaneous Drag	96
Chapter 7	Propulsion	97
7.1	Propulsion Overview	97
7.2	Code Architecture	97
7.3	Propeller Methods	98
7.3.1	Propeller Diameter Sizing	99
7.3.2	Disk Actuator Model	100
7.4	Piston-Prop Engines	102
7.4.1	Piston-Prop Engine Deck	104
7.5	Turbojets and Turbofans	104
7.5.1	Turbojet/Turbofan Engine Decks	105
Chapter 8	Size, Weight, and Power	107
8.1	Size, Weight, and Power Overview	107
8.2	Generic Systems	107
8.2.1	Generic Systems Overview	107
8.2.2	Generic Systems Weights	108
8.2.3	Generic Systems Size	109
8.2.4	Generic Systems Power	110
8.2.5	Generic Systems Thermal Management	110
8.3	Specialized Size, Weight, and Power Methods	111
8.3.1	Subsystems	111
8.3.2	Avionics	116
8.3.3	Structures	118
8.3.4	Propulsion	125
Chapter 9	Flight Performance	128
9.1	Overview	128
9.2	Performance Code Architecture	129
9.3	Performance Methodology	131
9.3.1	Performance Equations	131
9.3.2	Performance Constraints	134

9.3.3	Flight Velocity Optimization	135
9.3.4	Climb Performance	136
9.3.5	Mission Evaluation	139
9.3.6	Mission Completion Criterion	139
Chapter 10	Calibration.....	142
10.1	Calibration Overview	142
10.2	Calibration Methodology	142
10.3	Calibration Cases	143
10.3.1	Global Hawk	143
10.3.2	Predator	155
10.3.3	Shadow 200.....	166
Chapter 11	Reference Year Calibration-Optimization Comparisons	177
11.1	Overview	177
11.2	Reference Case Comparisons	177
11.2.1	Global Hawk 1994 Optimum Design	177
11.2.2	Predator 1994 Optimum Design	185
11.2.3	Shadow 200 2000 Optimum Design	192
Chapter 12	Technology Case Optimization Applications	198
12.1	Overview	198
12.2	Global Hawk Technology Impacts	198
12.2.1	Sizing Overview.....	198
12.2.2	Geometry.....	198
12.2.3	Propulsion	202
12.2.4	Weights	203
12.2.5	Performance	207
12.2.6	Technology Sensitivities	209
12.3	Predator Technology Impacts	211
12.3.1	Sizing Overview.....	211
12.3.2	Geometry.....	211
12.3.3	Propulsion	215
12.3.4	Weights	216
12.3.5	Performance	220
12.3.6	Technology Sensitivities	222
12.4	Shadow 200 Technology Impacts.....	223
12.4.1	Sizing Overview.....	223
12.4.2	Geometry.....	223
12.4.3	Propulsion	226
12.4.4	Weights	227
12.4.5	Performance	230
12.4.6	Technology Sensitivities	232
Chapter 13	Conclusions.....	234
13.1	AV Design Methodology Conclusions	234
13.2	Calibration Cases Conclusions	235
13.3	Technology Cases Conclusions	235
13.4	Recommendations.....	237
Appendix A	Geometry Methods.....	239

Appendix B Blade Element Propeller Methods.....	247
Appendix C Selected Avionics and Subsystem Weights Methods.....	249
Bibliography	256
List of Acronyms	262
Formatting Notes	264
Vita.....	265

List of Figures

Figure 1-1 Model of German V-1 Cruise Missile.....	1
Figure 1-2 AQM-34 Firefly Currently in Operational Service.....	2
Figure 1-3 Models of the Teledyne Ryan Drones (Left to Right: Global Hawk, Compass Cope, AQM-154 Compass Arrow, AQM-147H Firebee, AQM-34 Firefly).....	2
Figure 1-4 Models of Army Battlefield UAVs (Left to Right: Shadow 200, Outrider, Hunter, Aquila)	3
Figure 1-5 Global Hawk	3
Figure 1-6 Predator	4
Figure 1-7 Shadow 200.....	4
Figure 1-8 Scale Comparison of Shadow 200, Predator, and Global Hawk (Left to Right)	7
Figure 2-1 ACMAIN Code Architectre	10
Figure 2-2 EVAL Code Architecture.....	11
Figure 3-1 Genetic Algorithm Code Architecture	14
Figure 4-1 Technology Parameter Ratio Model (Method 1)	23
Figure 4-2 Direct Technology Parameter Lookup Model.....	25
Figure 4-3 Induced Drag Multiplication Factor Technology Trends.....	26
Figure 4-4 Interference Drag Trends	27
Figure 4-5 Wave Drag Technology Factor Trends.....	27
Figure 4-6 Profile Drag Multiplication Factor Trends.....	28
Figure 4-7 Final Profile Drag Multiplication Factor Trends.	29
Figure 4-8 GNC System Technology Phase.....	31
Figure 4-9 GNC System Technology Trends.	31
Figure 4-10 INS Technology Phase.....	32
Figure 4-11 INS Technology Trends	32
Figure 4-12 Subsystems Technology Phase	33
Figure 4-13 Subsystem Weight Technology Trend	34
Figure 4-14 Satellite Communications Dish Antenna Diameter Trends	35
Figure 4-15 Weight Growth Technology.....	36
Figure 4-16 Payload Technology Phase	37
Figure 4-17 SAR Payload Technology Trends.....	37
Figure 4-18 EO/IR Payloads.....	38
Figure 4-19 Large EO/IR Payload Performance Technology Trend	38
Figure 4-20 Small EO/IR Payload Performance Technology Trend.....	39
Figure 4-21 UAV Jet Engine	40
Figure 4-22 Jet Engine Technology Phase.....	40
Figure 4-23 Jet Engine Technology Trends.....	41
Figure 4-24 UAV Internal Combustion Engine.....	41
Figure 4-25 Internal Combustion Engine Technology Phase.....	42
Figure 4-26 Internal Combustion Engine Technology Trends	42
Figure 4-27 Factor of Safety Technology Trends.....	43
Figure 4-28 Structural Technology Phase.....	44
Figure 4-29 Structural Weight Multiplication Factor Technology Trend	45

Figure 5-1 Predator Fuselage Nose Region	47
Figure 5-2 X-45A Geometry.....	48
Figure 5-3 Dragon Eye Fuselage Geometry	48
Figure 5-4 Propeller Integration on Generic Fuselage.....	49
Figure 5-5 Jet Integration on Generic Fuselage.....	50
Figure 5-6 Wing Fairing Geometry	50
Figure 5-7 Radome Impacts on Fuselage Geometry.....	51
Figure 5-8 EO/IR Ball Geometry.....	52
Figure 5-9 Virginia Tech Forestry UAV	53
Figure 5-10 Wing Aerodynamic Paneling for Virginia Tech Forestry UAV	54
Figure 5-11 Vehicle Structural Paneling Example	57
Figure 5-12 Wing Tip Paneling Detail.....	57
Figure 5-13 Example Unconventional Configuration.....	58
Figure 5-14 Tilt-Wing Graphics Option	58
Figure 6-1 AEROC code Architecture.....	61
Figure 6-2 Pitching Moment Subroutine Architecture	62
Figure 6-3 NACA 0009 at Several Reynolds Numbers.....	72
Figure 6-4. Selig Donovan SD7032 at Low Reynolds Numbers.....	72
Figure 6-5 Airfoil 3-D Interpolation Space	73
Figure 6-6 Drag Polar Interpolation Diagram for Two Airfoils	75
Figure 6-7 Angle of Attack Symmetry Diagram	77
Figure 6-8 Curve Fit for 360-Degree Angle of Attack Sweep.....	77
Figure 6-9 Example Drag polar and Lift Curve of an Airfoil Through a Large Angle of Attack Sweep	79
Figure 6-10 Upper and Lower Transition Location vs. Lift Coefficient Comparison Between XFOIL and Empirical Equation Matching for the NACA 2412 Airfoil....	86
Figure 6-11 The Pressure Drag Comparison Between <i>XFOIL</i> and the Empirical Equation Matching for the NACA 2412 Airfoil	86
Figure 6-12 Comparison of Drag Polars Between the Direct Data and Parametric Airfoil Interpolation Methods.....	87
Figure 6-13 Comparison Between <i>XFOIL</i> and Wind Tunnel Data.	87
Figure 6-14 Wing-Fuselage Interference Geometry	90
Figure 6-15 Fuselage Drag Cross Section Penalty	92
Figure 6-16 Fuselage Drag Maximum Diameter Location Penalty.....	92
Figure 7-1 Propulsion Code Architecture.....	98
Figure 7-2 Raymer Propeller Sizing Equation Results.....	99
Figure 7-3 Comparison Between Predicted and Ideal Propeller Efficiencies.....	102
Figure 7-4 Density Ratio Impacts on Brake Specific Fuel Consumption.....	103
Figure 8-1 Macci Wing Factors	121
Figure 9-1 Performance Code Architecture.....	129
Figure 9-2 Flight Envelope Boundaries.....	134
Figure 9-3 Velocity Search Initialization.....	135
Figure 9-4 Standard Mission Profile.....	139
Figure 10-1 Global Hawk	144
Figure 10-2. Global Hawk Engine Thrust Performance	145
Figure 10-3 Global Hawk Engine Specific Fuel Consumption Performance.....	145

Figure 10-4. Global Hawk Avionics Weights Summary	146
Figure 10-5 Global Hawk Subsystems Weights Summary.....	147
Figure 10-6 Global Hawk Structural Weight Summary	149
Figure 10-7 Global Hawk Weights Summary	151
Figure 10-8 Global Hawk Mass Fraction Summary	151
Figure 10-9 Global Hawk Trimmed Incompressible Aerodynamic Performance	152
Figure 10-10 Global Hawk Trimmed Drag Contributors	152
Figure 10-11 Global Hawk Altitude Profile	153
Figure 10-12 Global Hawk Mach Profile	153
Figure 10-13 Global Hawk Mach-Altitude Envelope.....	154
Figure 10-14 Predator	155
Figure 10-15 Predator Installed Thrust Performance.....	156
Figure 10-16 Predator Installed Specific Fuel Consumption Performance	157
Figure 10-17 Predator Avionics Weights Summary	157
Figure 10-18 Predator Subsystems Weights Summary	159
Figure 10-19 Predator Structural Weight Summary	160
Figure 10-20 Predator Weights Summary	162
Figure 10-21 Predator Mass Fraction Summary.....	162
Figure 10-22 Predator Trimmed Aerodynamic Performance	163
Figure 10-23 Predator Trimmed Drag Contributors	163
Figure 10-24 Predator Altitude Profile	164
Figure 10-25 Predator Velocity Profile.....	164
Figure 10-26 Predator Velocity-Altitude Envelope.....	165
Figure 10-27 Shadow 200.....	166
Figure 10-28 Shadow 200 Installed Thrust Performance	167
Figure 10-29 Shadow 200 Installed Specific Fuel Consumption Performance	168
Figure 10-30 Shadow 200 Subsystems Weights Summary	169
Figure 10-31 Shadow 200 Structural Weight Summary.....	170
Figure 10-32 Shadow 200 Weights Summary	172
Figure 10-33 Shadow 200 Mass Fraction Summary.....	172
Figure 10-34 Shadow 200 Trimmed Aerodynamic Performance.....	173
Figure 10-35 Shadow 200 Trimmed Drag Contributors.....	173
Figure 10-36 Shadow 200 Altitude Profile.....	174
Figure 10-37 Shadow 200 Velocity Profile	175
Figure 10-38 Shadow 200 Velocity-Altitude Envelope.....	175
Figure 11-1 1994 Global Hawk Geometry Comparison – Top View.....	179
Figure 11-2 1994 Global Hawk Geometry Comparison – Side View	179
Figure 11-3 1994 Global Hawk Geometry Comparison – Isometric View	180
Figure 11-4 Global Hawk Geometry Comparison.....	180
Figure 11-5 Global Hawk Summary Weights Comparison.....	181
Figure 11-6 Global Hawk Summary Mass Fraction Comparison	181
Figure 11-7 Global Hawk Altitude Profile Comparison.....	182
Figure 11-8 Global Hawk Mach Profile Comparison.....	182
Figure 11-9 Global Hawk Mach-Altitude Envelope Used	183
Figure 11-10 Global Hawk Specific Fuel Consumption Comparison	183
Figure 11-11 Global Hawk Lift to Drag Comparison.....	184

Figure 11-12	1994 Predator Geometry Comparison – Top View.....	186
Figure 11-13	1994 Predator Geometry Comparison – Side View.....	186
Figure 11-14	1994 Predator Geometry Comparison – Isometric View.....	187
Figure 11-15	Predator Geometry Comparison.....	187
Figure 11-16	Predator Weights Summary Comparison.....	188
Figure 11-17	Predator Summary Mass Fraction Comparison	188
Figure 11-18	Predator Altitude Profile Comparison.....	189
Figure 11-19	Predator Velocity Profile Comparison.....	189
Figure 11-20	Predator Velocity-Altitude Envelope Used.....	190
Figure 11-21	Predator Specific Fuel Consumption Comparison.....	190
Figure 11-22	Predator Lift to Drag Comparison.....	191
Figure 11-23	2000 Shadow 200 Geometry Comparison – Top View	193
Figure 11-24	2000 Shadow 200 Geometry Comparison – Side View.....	193
Figure 11-25	2000 Shadow 200 Geometry Comparison – Isometric View.....	193
Figure 11-26	Shadow 200 Geometry Comparison	194
Figure 11-27	Shadow 200 Summary Weights Comparison	194
Figure 11-28	Shadow 200 Summary Mass Fraction Comparison.....	195
Figure 11-29	Shadow 200 Altitude Profile Comparison	195
Figure 11-30	Shadow 200 Velocity Profile Comparison.....	196
Figure 11-31	Shadow 200 Velocity-Altitude Envelope Used	196
Figure 11-32	Shadow 200 Specific Fuel Consumption Comparison.....	197
Figure 11-33	Shadow 200 Lift to Drag Ratio Comparison.....	197
Figure 12-1	Global Hawk Geometry Trends – Top View, Years (Left to Right): 1994, 2000, 2005, 2010, 2015, 2020, 2025.....	199
Figure 12-2	Global Hawk Geometry Trends – Side View, Years (Left to Right): 1994, 2000, 2005, 2010, 2015, 2020, 2025.....	199
Figure 12-3	Global Hawk Geometry Trends – Isometric View, Years (Left to Right): 1994, 2000, 2005, 2010, 2015, 2020, 2025.....	200
Figure 12-4	Global Hawk Wing Span Trends	200
Figure 12-5	Global Hawk Aspect Ratio Trends	201
Figure 12-6	Global Hawk Wing Sweep Trends.....	201
Figure 12-7	Global Hawk Thickness to Chord Ratio Trends	201
Figure 12-8	Global Hawk Wing Parameter Comparisons	202
Figure 12-9	Global Hawk Fuselage Length Trends.....	202
Figure 12-10	Global Hawk Uninstalled Thrust Trends	203
Figure 12-11	Global Hawk Thrust to Weight Ratio Trends	203
Figure 12-12	Global Hawk Weight Trends	204
Figure 12-13	Global Hawk Mass Fraction Trends	204
Figure 12-14	Design Gross - Obligated Weights Trends.....	204
Figure 12-15	Global Hawk Avionics Weight Trends.....	205
Figure 12-16	Global Hawk Subsystems Weight Trends.....	206
Figure 12-17	Global Hawk Payload Weight Trends.....	206
Figure 12-18	Global Hawk Structures Weight Trends	207
Figure 12-19	Global Hawk Altitude Profile Trends	208
Figure 12-20	Global Hawk Mach Profile Trends	208
Figure 12-21	Global Hawk Mission Lift to Drag Ratio Trends.....	208

Figure 12-22 Global Hawk Mission Fuel Consumption Trends.....	209
Figure 12-23 Global Hawk Design Gross Weight Sensitivity to Technology.....	210
Figure 12-24 Predator Geometry Trends – Top View, Years (Left to Right): 1994, 2000, 2005, 2010, 2015, 2020, 2025.....	212
Figure 12-25 Predator Geometry Trends – Side View, Years (Left to Right): 1994, 2000, 2005, 2010, 2015, 2020, 2025.....	212
Figure 12-26 Predator Geometry Trends – Isometric View, Years (Left to Right): 1994, 2000, 2005, 2010, 2015, 2020, 2025.....	213
Figure 12-27 Predator Wing Span Trends	213
Figure 12-28 Predator Aspect Ratio Trends	214
Figure 12-29 Predator Thickness to Chord Ratio	214
Figure 12-30 Predator Wing Area.....	214
Figure 12-31 Predator Fuselage Length Trends.....	215
Figure 12-32 Predator Uninstalled Power Trends	215
Figure 12-33 Predator Power to Weight Ratio	216
Figure 12-34 Predator Weight Summary Trends.....	216
Figure 12-35 Predator Summary Mass Fraction Trends.....	217
Figure 12-36 Predator Design Gross – Obligated Weight Trends.....	217
Figure 12-37 Predator Avionics Weight Trends.....	218
Figure 12-38 Predator Subsystems Weight Trends	218
Figure 12-39 Predator Payload Weight Trends	219
Figure 12-40 Predator Structures Weight Trends	219
Figure 12-41 Predator Altitude Profile Trends	220
Figure 12-42 Predator Velocity Profile Trends	221
Figure 12-43 Predator Mission Lift to Drag Ratio Trends	221
Figure 12-44 Predator Mission Fuel Consumption Trends.....	222
Figure 12-45 Predator Design Gross Weight Sensitivity to Technology	222
Figure 12-46 Shadow 200 Geometry Trends – Top View, Years (Left to Right): 2000, 2005, 2010, 2015, 2020, 2025.....	223
Figure 12-47 Shadow 200 Geometry Trends – Side View, Years (Left to Right): 2000, 2005, 2010, 2015, 2020, 2025.....	223
Figure 12-48 Shadow 200 Geometry Trends – Isometric View, Years (Left to Right): 2000, 2005, 2010, 2015, 2020, 2025.....	224
Figure 12-49 Shadow 200 Wing Span Trends.....	224
Figure 12-50 Shadow 200 Aspect Ratio Trends.....	225
Figure 12-51 Shadow 200 Fuselage Length Trends	225
Figure 12-52 Shadow 200 Wing Loading – Aspect Ratio Relationships	226
Figure 12-53 Shadow 200 Uninstalled Power Trends	226
Figure 12-54 Shadow 200 Power to Weight Ratio Trends	227
Figure 12-55 Shadow 200 Weight Trends.....	227
Figure 12-56 Shadow 200 Summary Mass Fraction Trends	228
Figure 12-57 Shadow 200 Design Gross – Obligated Weights Trend.....	228
Figure 12-58 Shadow 200 Avionics Weight Trends.....	229
Figure 12-59 Shadow 200 Subsystems Weight Trends	229
Figure 12-60 Shadow 200 Payload Weight Trends.	230
Figure 12-61 Shadow 200 Structures Weight Trends.....	230

Figure 12-62 Shadow 200 Altitude Profile Trends.....	231
Figure 12-63 Shadow 200 Velocity Profile Trends	231
Figure 12-64 Shadow 200 Mission Lift to Drag Ratio Trends	232
Figure 12-65 Shadow 200 Mission Fuel Consumption Trends	232
Figure 12-66 Shadow 200 Design Gross Weight Sensitivity to Technology	233
Figure 13-1 General Atomics Gnat-Predator Family Evolution	237
Figure A-1 Wing Geometry Parameters	239
Figure B-1 Comparison Between Two and Three Bladed Propeller Designs.....	248

List of Tables

Table 3-1 Universal Design Variables	16
Table 3-2 Jet Propulsion Design Variables.....	17
Table 3-3 Reciprocating Engine Propulsion Design Variables	17
Table 3-4 Constraints	18
Table 3-5 Mission constraint types	18
Table 4-1 Technology Attributes	22
Table 4-2 Attribute Ranking Description	22
Table 4-3 Aerodynamics Technology Attributes.....	25
Table 4-4 Airfoil Characteristics.	28
Table 4-5 Avionics and Subsystems Technology Attributes.....	30
Table 4-6 Design Technology Attributes.....	35
Table 4-7 Payload Technology Attributes	36
Table 4-8 Propulsion Technology Attributes.....	39
Table 4-9 Structures Technology Attributes.....	43
Table 6-1 Primary aerodynamics product list.....	60
Table 6-2 Lift Distribution Methods.....	63
Table 6-3 Profile Drag Methods	73
Table 6-4 Low Reynolds number airfoil database.....	80
Table 6-5 High Reynolds number airfoil database.....	81
Table 6-6 Empirical equation airfoil database.....	82
Table 8-1 Component Categories and Types.....	107
Table 8-2 Flight Control Systems Weight Methods	111
Table 8-3 Flight Control System Weight Method Functional Dependencies.....	112
Table 8-4 Environmental Control System Weight Methods.....	113
Table 8-5 ECS System Weight Method Functional Dependencies	113
Table 8-6 Electrical System Weight Methods	114
Table 8-7 Electrical System Weight Method Functional Dependencies	114
Table 8-8 Fuel System Weights Methods.....	115
Table 8-9 Fuel System Weight Method Functional Dependencies	115
Table 8-10 Air Data System Factors.....	117
Table 8-11 Wing Weight Methods	118
Table 8-12 Wing Weight Method Functional Dependencies	118
Table 8-13 Tail Weight Methods.....	123
Table 8-14 Horizontal Tail Weight Method Functional Dependencies.....	123
Table 8-15 Vertical Tail Weight Method Functional Dependencies	123
Table 8-16 Fuselage Weight Methods	123
Table 8-17 Fuselage Weight Method Functional Dependencies	124
Table 10-1 Global Hawk Geometry.....	144
Table 10-2 Global Hawk Propulsion	144
Table 10-3 Global Hawk Design Technology Levels.....	154
Table 10-4 Predator Geometry Characteristics.....	155
Table 10-5 Predator Propulsion Characteristics	156
Table 10-6 Predator Design Technology Levels	165
Table 10-7 Shadow 200 Geometry Characteristics	166

Table 10-8 Shadow 200 Propulsion Characteristics	167
Table 10-9 Shadow 200 Calibration weight comparison.....	172
Table 10-10 Shadow 200 Design Technology Levels	176
Table 11-1 Global Hawk Design Variables	178
Table 11-2 Predator Design Variables.....	185
Table 11-3 Shadow 200 Design Variables.....	192
Table C-1 Autopilot Factors	250
Table C-2 INS Factors	251
Table C-3 Camera Factors	252

Nomenclature

a	Axial interference factor
	Thrust ratio
a'	Rotational interference factor
$A(i,j)$	Influence coefficient in lift distribution methods
ACFunc	Normalized distance from wing AC to trailing edge
alt	Altitude, ft
alt_{max}	Maximum prescribed altitude, ft
AR	Aspect ratio
AR_w	Wing aspect ratio
$a_{surface}$	Surface lift curve slope, 1/deg or 1/radian
a_{tail}	Tail lift curve slope, 1/deg or 1/radian
a_{wing}	Wing lift curve slope, 1/deg or 1/radian
$b(i)$	Influence coefficient in lift distribution methods
BHP	Brake Horsepower, HP
BHP_0	Brake Horsepower at sea level, HP
BHP_h	Brake Horsepower at altitude, HP
b_{ref}	Reference wing span, ft
BSFC	Brake specific fuel consumption, lb/HP*hr
$BSFC_0$	Brake specific fuel consumption at sea level, lb/HP*hr
$BSFC_h$	Brake specific fuel consumption at altitude, lb/HP*hr
b_w	Wing span, ft
c	Local chord of interest (interference drag), ft
	Blade section chord, ft
$c(i)$	Local chord (paneling), ft
$c(\bar{a})$	Mean aerodynamic chord length, ft
C	Cooling power, Watts
C_d	Section drag coefficient
C_D	3-D drag coefficient
C_d	2-D drag coefficient
$C_{D,cavity}$	Landing gear bay cavity drag coefficient
$C_{D,cool}$	Cooling drag coefficient
$C_{D,door}$	Landing gear door drag coefficient
$C_{d,frict}$	2-D friction coefficient
$C_{D,gear}$	Landing gear drag coefficient
$C_{di}(i)$	Local induced drag coefficient
C_{Di}	Induced drag coefficient
C_{Dint}	Interference drag coefficient
$C_{Dint,wall}$	Interference drag coefficient due to perpendicular wall
$C_{Dint,lift}$	Interference drag coefficient increment due to lift
$C_{Dint,sweep}$	Interference drag coefficient increment due to sweep
$C_{Dint,incline}$	Interference drag coefficient increment due to inclination
$C_{d,press}$	2-D pressure drag coefficient
$C_{D,strut}$	Landing gear strut drag coefficient
$C_{D,wheel}$	Landing gear wheel drag coefficient

$c_{\text{flap}}(i)$	Local flap chord, ft
C_l	Section lift coefficient
$C_{l(i)}$	Local 2-D lift coefficient (paneling)
C_L	Total 3-D lift coefficient per surface or total vehicle
$C_{L,\text{Max}}$	3-D maximum lift coefficient
$C_{L,\text{stall}}$	3-D stall lift coefficient
$C_{l,\text{stall}}$	2-D stall lift coefficient
C_{l0}	2-D minimum drag lift coefficient
C_M	Total pitching moment coefficient
$C_{M,CL}$	Pitching moment coefficient due to lift
$C_{M,\text{Flap}}$	Pitching moment coefficient due to flap deflections
$C_{M,\text{fuselage}}$	Fuselage pitching moment coefficient
$C_{M,\text{Fuse,Nac}}$	Pitching moment coefficient due to fuselages and nacelles
$C_{M,0L}$	Pitching moment coefficient due to airfoil sections at zero lift
$C_{m,0L}(i)$	Pitching moment coefficient of local airfoil
C_p	Coefficient of power (conventional- normalized by rotation terms)
C_{PV}	Coefficient of power (normalized by V terms)
$c_r c_{r,w}(j)$	Segment root chord to wing root chord ratio
$c/R_p(j)$	Propeller radius-normalized chord length
$c_{r,w}$	Wing root chord, ft
C_T	Coefficient of thrust (conventional- normalized by rotation terms)
$c_t c_{r,w}(j)$	Segment tip chord to wing root chord ratio
C_{TV}	Coefficient of thrust (normalized by V terms)
c_{wing}	Wing chord
C_x	Torque force coefficient
C_y	Thrust force coefficient
D	Propeller diameter, ft
	Drag, lbs
D_{Cool}	Cooling Drag, lbs
D_{Dish}	Communications dish diameter, ft
D_{Jet}	Jet engine diameter, ft
D_{Pow}	Power Extraction Drag, lbs
D_{Ram}	Ram drag, lbs
D_{Tire}	Tire width, ft
e	Span efficiency factor
E_{seg}	Segment endurance, hrs
E_{subseg}	Subsegment endurance, hrs
F	Prandtl momentum loss factor
$\text{fact}(i)$	Interpolation factor
$\text{factpen}(i)$	Penalty factor
F_{BHP}	Brake horsepower altitude correction factor
F_{BSFC}	Brake specific fuel consumption altitude correction factor
F_{Design}	Design level factor
FF	Airfoil form factor
FF_{Fuse}	Fuselage form factor
$\text{flap}(j)$	Flap function designator, 1=flap, 2=elevator, 3=aileron

F_{Tech}	Final technology factor
$f_{type(j)}$	Flap type, 1=split, 2=plain, 3=slotted flap, 4=double slotted
$F_{Vol,Install}$	Installation volume factor
$F_{Wt,Install}$	Weight installation factor
G	Circulation function
H_{Eng}	Engine height, ft
h_n	Neutral point normalized by the MAC
inc_w	Wing incidence, degrees
I_{xx}	XX area moment of inertia, ft ⁴
$I_{yy,mass}$	YY mass moment of inertia, lbm*ft ²
J	Advance ratio
K	Goldstein momentum loss factor
K	Lift dependent profile drag constant
k_a	Aspect ratio correction factor for downwash derivative
k_{tr}	Taper ratio correction factor for downwash derivative
k_h	Tailplane height correction factor for downwash derivative
$L_{AC-VT,TE}$	Length from the wing AC to the tail root trailing edge, ft
L/D	Aircraft lift to drag ratio
L/D_{fuse}	Fuselage length to maximum diameter ratio
L_{Door}	Length of landing gear door, ft
L_{Elec}	Electrical wiring length, ft
L_{Eng}	Engine length, ft
L_{fuse}	Fuselage length, ft
L_H	Horizontal tail moment arm, ft
L_{Jet}	Length of jet engine, ft
$Load_w$	Lifting load of a wing, lbs
$L_{Overall}$	Overall vehicle length, ft
L_{Tail}	Average tail moment arm, ft
L_V	Vertical tail moment arm, ft
$m(\dot{)}_{cool}$	Cooling air mass flow rate
M	Flight Mach number
mac_w	Wing mean aerodynamic chord, ft
M_{crit}	Critical Mach number
M_{DD}	Drag divergent mach number
MF_{Fuel}	Fuel mass fraction
M_{max}	Maximum Mach number
n	Index number in Prandtl LLT
	Curve fit parameter in parametric airfoil method
	Propeller revolutions per second, 1/sec
N	Maximum value of index n in Prandtl LLT
N_{Crew}	Number of crew members in aircraft
N_{blade}	Blade count
N_{FCS}	Number of flight control systems
N_{Gen}	Number of generators
N_{LLF}	Limit load factor
N_{strut}	Number of struts

N_{Surf}	Number of control surfaces
N_{Tanks}	Number of fuel tanks
$N_{\text{tire/strut}}$	Number of tires per strut
N_{Ult}	Ultimate load factor
P	Power absorbed by propeller, HP
	Component power, Watts
P_{abs}	Absorbed power, HP
P_{Dish}	Power used by dish antenna, Watts
P_{Eng}	Engine power, HP
P_{Max}	Maximum power draw of electrical system, Watts
P_{rot}	Wing rotation 3-D point (ft, ft, ft)
$P_{\text{r,w}}$	Wing segment root point (ft, ft, ft)
P_{Shaft}	Shaft horsepower, HP
$P_{\text{t,w}}$	Wing segment tip point (ft, ft, ft)
P_{w}	Wing root 3-D point (ft, ft, ft)
P/W	Uninstalled sea level horsepower to design gross weight, HP/lb
q	Dynamic pressure, lb/ft ²
Q_{cool}	Cooled power, Watts
q_{max}	Maximum dynamic pressure, lb/ft ²
Q_{seg}	Segment interference drag factor
q_{Shear}	Shear flow
r	Radial distance, L
	Distance in 3-D parameter space for airfoil interpolation
R	Propeller tip radius, ft
	Range, nmi
Re/L	Reynolds number per unit length, ft ⁻¹
ROC	Rate of climb, ft/min
ROC_{min}	Minimum rate of climb, ft/min
R_p	Propeller radius, ft
$r/R_p(j)$	Propeller radius-normalized radial distance
R_{seg}	Segment range, nmi
R_{subseg}	Subsegment range, nmi
R_{Year}	Average technology ratio per year between two reference dates
s	Semispan, L
S_c or S_{Cont}	Control surface area, ft ²
SF	Wing shape factor
	Scale factor
sm	Static margin
S_{ref}	Reference area (defined as planform area of wing 1), ft ²
S_{seg}	Wing panel span increment, ft
S_{tip}	Wing tip semispan distance, ft
$S_{\text{V-Tail}}$	V-tail area, ft ²
S_w	Wing area, ft ²
$S_{\text{wet,Fuse}}$	Fuselage wetted area, ft ²
T	Thrust, lbs
T_{air}	Air temperature

t_{Bend}	Bending material thickness, ft
t/c	Thickness to chord ratio
T_{comp}	Component temperature
Tech	Technology parameter
Tech ₁	Technology parameter at data point 1
Tech ₂	Technology parameter at data point 2
Temp	Absolute static temperature at altitude
Temp _{SL}	Absolute static temperature at sea level
throt	Throttle setting
T_{Jet}	Jet static thrust rating, lbs
T_{max}	Maximum installed thrust in flight, lbs
T_{min}	Minimum installed thrust in flight, lbs
$T_{\text{max,SL}}$	Maximum installed thrust at sea level static conditions, lbs
T_{Pan}	Panel thickness, ft
T_{req}	Required thrust, lbs
TSFC	Installed in-flight thrust specific fuel consumption, lbm/lb-hr
TSFC _{rat}	Installed thrust specific fuel consumption ratio
TSFC _{ref}	Ref. sea level static thrust specific fuel consumption, lbm/lb-hr
TSFC _{SLS}	Installed sea level static thrust specific fuel consumption, lbm/lb-hr
t_{Shear}	Skin thickness of shear material, ft
TVC	Tail volume coefficient
T/W	Uninstalled SLS thrust to design gross weight ratio
u_m	Local velocity in the streamwise (X) direction, kts or ft/sec
U_{∞}	Total flight velocity at infinity, kts or ft/sec
V	Freestream velocity, kts or ft/sec
	Flight velocity, kts
v'	Vortex displacement velocity, kts or ft/sec
$V_{\text{eq,Max}}$	Maximum equivalent velocity, kts
V_{Install}	Installation volume, ft ³
v_m	Local velocity in the spanwise (Y) direction, kts or ft/sec
Vol _{Avail}	Volume available, ft ³
Vol _{Dish}	Radome volume occupied by dish antenna, ft ³
Vol _{Eng}	Engine volume, ft ³
Vol _{Internal}	Internal fuel tank volume, ft ³
Vol _{Jet}	Volume occupied by jet engine, ft ³
Vol _{Margin}	Volume margin, ft ³
Vol _{Tank}	Total fuel volume required, ft ³
Vol _{Tot}	Total fuel tank volume, ft ³
$V_{\text{Uninstalled}}$	Uninstalled volume, ft ³
W	Local total velocity, kts or ft/sec
	Weight, lbs
W_{ADS}	Air data system weight, lbs
$W_{\text{Anti-Ice}}$	Anti-ice system weight, lbs
W_{Attach}	Wing attachment weight, lbs
W_{ATC}	Air traffic control system weight, lbs
W_{Avion}	Total avionics weight, lbs

W_{Bend}	Bending material thickness, lbs
W_{Box}	Weight of wing box, lbs
W_{Camera}	Camera weight, lbs
W_{Comms}	Communications system weight, lbs
$W_{\text{CS,Secondary}}$	Weight of control surfaces and secondary structure, lbs
W_{DG}	Design gross weight, lbs
W_{Dish}	Parabolic dish weight, lbs
W_{Door}	Width of landing gear door, ft
W_{ECS}	Environmental Control System (ECS) weight, lbs
W_{Elec}	Electrical system weight, lbs
$W_{\text{EO/IR}}$	EO/IR payload weight, lbs
W_{f}	Final weight, lbs
W_{fuel}	Total fuel weight, lbs
W_{fuelb}	Fuel burned, lbs
W_{Fuels}	Fuel system weight, lbs
$W_{\text{Fuel,wing}}$	Weight of fuel in the wing, lbs
$w_{\text{fuse}(i)}$	Local fuselage width, ft
W_{Fuse}	Fuselage weight, lbs
W_{Gear}	Landing gear weight, lbs
W_{GPS}	Global Positioning System (GPS) weight, lbs
W_i	Initial weight, lbs
W_{Eng}	Engine width, ft
W_{INS}	Inertial Navigation System (INS) weight, lbs
W_{Jet}	Jet engine weight, lbs
W_m	Local velocity in the vertical (Z) direction, kts or ft/sec
W_{Nac}	Nacelle weight, lbs
W_{Overall}	Overall vehicle width (usually span), ft
$W_{\text{Processor}}$	Processor weight, lbs
W_{Recip}	Reciprocating engine weight, lbs
W_{Recorder}	Data recorder weight, lbs
W_{Ribs}	Weight of wing ribs, lbs
W_{SAR}	SAR payload weight, lbs
W_{seg}	Mean aircraft weight during segment, lbs
W_{Tails}	Overall tail weight, lbs
W_{tInstall}	Installation weight, lbs
W_{tire}	Width of tire, ft
$W_{\text{tUninstalled}}$	Uninstalled weight, lbs
W_{Wing}	Wing weight, lbs
x	Non-dimensional distance $\Omega \cdot r/V$
$x(i)$	Intermediate coefficient in Prandtl LLT
$X_{\text{AC,wing}}$	Wing aerodynamic center location X-coordinate, ft
$x/c_{\text{flap}(j)}$	Segment flap chord ratio
$x/c_{\Lambda,w}(j)$	Segment reference x/c for wing sweep
$x/c_{\epsilon,w}(j)$	Segment reference x/c for washout
x_{cg}	X coordinate of the center of gravity, ft
$x_{c/4}(i)$	Local X coordinate of the panel quarter chord, ft

$x/c_{\Lambda,p}(j)$	Propeller x/c reference for sweep
$x/c_{\beta,p}(j)$	Propeller x/c reference for twist
X_f, Y_f, Z_f	Fuselage leading edge x, y, z coordinates, ft
$X/L_{AC,wing}$	Fuselage x/L location of wing aerodynamic center
$x/L_f(j)$	Fuselage length-normalized x-distance from reference
X_{NP}	Neutral point X-coordinate, ft
X_p, Y_p, Z_p	Propeller center x, y, z coordinates location, ft
$X_{rot}, Y_{rot}, Z_{rot}$	Wing rotation point x, y, z coordinates, ft
$X_{rot,f}, Y_{rot,f}, Z_{rot,f}$	Fuselage rotation point x, y, z coordinates, ft
$X_{rot,p}, Y_{rot,p}, Z_{rot,p}$	Propeller rotation point x, y, z coordinates, ft
X_w, Y_w, Z_w	Wing root leading edge x, y, z coordinates, ft
y	Y coordinate, ft
$y/b_{flap}(j)$	Segment flap span ratio
Year	Year
Year ₁	Year at data point 1
Year ₂	Year at data point 2
Year _{Ref}	Reference Year
$y/L_f(j)$	Fuselage length-normalized side y-distance from reference
$z/L_{m,f}(j)$	Fuselage length-normalized mid z-distance from reference
$z/L_{t,f}(j)$	Fuselage length-normalized top z-distance from reference
$z/L_{b,f}(j)$	Fuselage length-normalized bottom z-distance from reference
Z_{wing}	Z-coordinate of wing aerodynamic center, ft
Z_{tail}	Z-coordinate of tail aerodynamic center, ft
α	Vehicle angle of attack, degrees or radians
$\alpha_{twist}(i)$	Local washout, degrees or radians
$\alpha_{0L}(i)$	Local zero lift angle of attack, degrees or radians
β	Blade twist angle, degrees
Γ_{V-Tail}	V-Tail dihedral angle, degrees
$\Gamma_w(j)$	Segment dihedral, degrees
$\delta, \delta(i)$	Angle of the VLM CP at zero angle of attack, degrees or radians
$\delta_f(i)$	Flap deflection, degrees or radians
$\delta_{flap,w}(j)$	Flap maximum deflection, degrees
$\Delta C_{l,flap}$	Change in local 2-D lift coefficient due to flap deflections
ΔX	Difference in X direction, ft
$\Delta y(i)$	Local spanwise panel difference, ft
ε	Drag to lift ratio
	Downwash angle, degrees or radians
$\varepsilon(i)$	Local downwash angle, degrees or radians
$\varepsilon_w(j)$	Segment washout relative to wing root, degrees
ζ	Displacement velocity ratio, v'/V
η_f	Flap effectiveness factor based on flap type
η_{gear}	Gear efficiency
η_P	Propeller efficiency
$\eta_{P,ideal}$	Ideal propeller efficiency

$\eta_{P,nonideal}$	Non-ideal propeller efficiency
η_{Rad}	Radiation Efficiency
$\eta_{radiation}$	Efficiency of radiating power
$\eta_{tip,w}(j)$	Spanwise location of segment tip - $y_{tip}/(b_w/2)$
$\theta(i)$	Normalized semispan angle for Prandtl LLT
$\theta_{incline}$	Inclination angle between wing and fuselage side at intersection, degrees or radians
$\theta_{rot,f}$	Fuselage rotation angle, degrees
$\theta_{rot,p}$	Propeller rotation angle, ft
$\theta_{rot,w}$	Wing rotation angle, degrees
κ_a	Transonic airfoil technology factor
λ	Speed ratio
	Taper ratio
λ_{eq}	Equivalent taper ratio
$\Lambda_{c/2}$	Sweep at 50% chord, degrees or radians
$\Lambda_{c/4}$	Sweep at quarter chord, degrees or radians
$\Lambda_p(j)$	Propeller sweep angle, degrees
$\Lambda_{x,w}(j)$	Segment sweep at x chordwise location, degrees
μ	Viscosity
ξ	Non-dimensional propeller radius
ξ_0	Non-dimensional propeller hub radius
π	3.14159...
ρ	Air density, sl/ft ³
$\rho_b(j)$	Bottom conic parameter
ρ_h	Density at altitude, sl/ft ³ or kg/m ³
ρ_0	Density at sea level, sl/ft ³ or kg/m ³
$\rho_t(j)$	Top conic parameter
σ	Local solidity
	Air density ratio
$\tau(i)$	Local flap effectiveness factor based on flap type
τ_{ult}	Ultimate shear stress
ϕ	Flow angle
$\phi(i)$	Local dihedral angle, degrees or radians
ϕ_t	Flow angle at the propeller tip
Ω	Propeller angular velocity, radians/sec

Common Subscripts

0	Zero lift condition
	Sea level
avg	Average
eq	Equivalent
fact	Factor - multiplication

frict	Friction drag
i	Index
max,neg	Maximum negative angle of attack (most negative)
mindat	Point of minimum available data
mindrag	Minimum drag condition
press	Pressure drag
prof	Profile drag
ref	Reference case
seg	Segment
stall	Section, wing, or vehicle stall
table	Table
target	Target case
type	Type

Chapter 1 Introduction

1.1 Background

Unmanned Aerial Vehicle (UAV) systems have taken many names and forms over their long history. Unmanned aircraft have been dubbed drone, Remotely Piloted Vehicle (RPV), UAV, Uninhabited Combat Aerial Vehicle (UCAV), Organic Aerial Vehicle (OAV), Uninhabited Combat Aircraft System (UCAS), and Micro Aerial Vehicle (MAV), to list a few. Whatever called, unmanned aircraft systems have an airborne component that performs at least one mission role without a pilot onboard. Additionally, unmanned aircraft must be capable of controlled and sustained flight, otherwise the first cast stone is also the first unmanned aircraft. For consistency, the acronym UAV is adopted throughout this document, as appropriate. The history of unmanned aircraft is described by Werrell [1985], Wagner [1982 and 1992], Irwin [2000], Holder [2001], McDaid [1997], Goebel [2003], and Munson [1988 and 1999], to name only a few sources.

Cruise missiles and UAVs share a highly common lineage [Werrell 1985], and the distinctions between these types of systems are minor. UAV systems began through cruise missile and target drone developments. The first operational experiments with cruise missiles began in World War I [Werrell 1985, McDaid 1997], but these attempts met with little success. During World War II, Germany developed and employed numerous V-1 cruise missiles with unprecedented results [Werrell 1985]. A model of the V-1 is shown in Figure 1-1. Although representing the state of the art for unmanned aircraft, the V-1 is generally considered a cruise missile. Over 5,000 V-1s were launched by the Germans [Werrell 1985]. The United States developed many cruise missiles from the mid-1940's through the late 1960's with generally disappointing results [Werrell 1985]. The combined Air-Launched Cruise Missile (ALCM) and Surface Launched Cruise Missile (SLCM) programs of the 1970's produced the first practical cruise missile programs [Werrell 1985].



Figure 1-1 Model of German V-1 Cruise Missile

The first golden era of U.S. UAV systems was made possible by the Teledyne Ryan (now Northrop Grumman) Firebee/Firefly drones [Wagner 1982 and 1992]. The first version of what became the Firebee drone, shown in Figure 1-2, was initially developed in 1950,

and variants are still in service today [Wagner 1982 and 1992]. Over 20 distinct variants of this system have been employed [Wagner 1982 and 1992]. The Firefly system evolved into the Firebee, which conducted over 3,400 operational reconnaissance missions over Vietnam and other regions [Wagner 1982 and 1992].



Figure 1-2 AQM-34 Firefly Currently in Operational Service

The U.S. experienced a notable decline in UAV funding and development success during the 1970's and 1980's [Wagner 1982 and 1992, McDaid 1997]. Teledyne Ryan successfully developed two high altitude drones during the 1970's, the AQM-147 Compass Arrow and the Compass Cope, that were not fully utilized or pursued due to the changing political climate of the early post-Vietnam era [Wagner 1982 and 1992]. Scale models of the Teledyne Ryan developments are shown in Figure 1-3. The most significant U.S. UAV program of the 1980's was the Lockheed Aquila battlefield surveillance RPV, which cost over \$1 billion to develop, saw significant schedule slips, and was ultimately never fielded due to poor performance [Fahlstrom 1998, Munson 1988, Goebel 1993]. A model of Aquila can be seen on the far right of Figure 1-4. The cancellation of the Aquila program represented the nadir of U.S. UAV capabilities.



Figure 1-3 Models of the Teledyne Ryan Drones (Left to Right: Global Hawk, Compass Cope, AQM-154 Compass Arrow, AQM-147H Firebee, AQM-34 Firefly)



Figure 1-4 Models of Army Battlefield UAVs (Left to Right: Shadow 200, Outrider, Hunter, Aquila)

U.S. UAV systems are now in a second golden era. The Defense Airborne Reconnaissance Office (DARO) and the Defense Advanced Research Projects Agency (DARPA) started, among other UAV efforts, two Advanced Concept Technology Demonstrator (ACTD) programs in 1994. The Tier II+ Global Hawk, developed by Teledyne Ryan, is a High-Altitude Long-Endurance (HALE) UAV that performs reconnaissance missions primarily with Electro-Optical/Infrared (EO/IR) and Synthetic Aperture Radar (SAR) payloads [Drezner 2002, OSD 2002]. A rendering of Global Hawk is shown in Figure 1-5. The Medium-Altitude Endurance (MAE) Predator UAV, developed by General Atomics, flies at a lower altitude and has reduced payload capacity than Global Hawk, but is more affordable [OSD 2002]. A rendering of Predator is shown in Figure 1-6. Both systems are equipped with satellite communications systems to provide Beyond Line Of Sight (BLOS) connectivity with remote ground stations [OSD 2002]. Predator and Global Hawk went into production and have seen extensive operational service [OSD 2002]. Today, these two systems are the backbone of the U.S. UAV arsenal.



Figure 1-5 Global Hawk

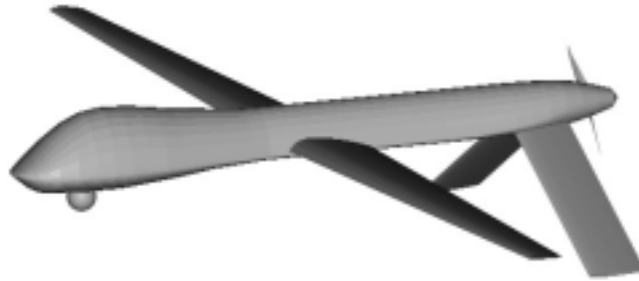


Figure 1-6 Predator

Numerous other UAV programs are either in development or operational today [OSD 2002]. The success of the Global Hawk and Predator demonstrated the maturity of highly effective UAV systems, which helped lead the way for new UAV system developments. While some recent UAV developments experienced failures, others have survived. One example of a surviving UAV system still under development is the tactical AAI Shadow 200 [Palumbo 2000]. Figure 1-7 shows a rendering of the Shadow 200 system.

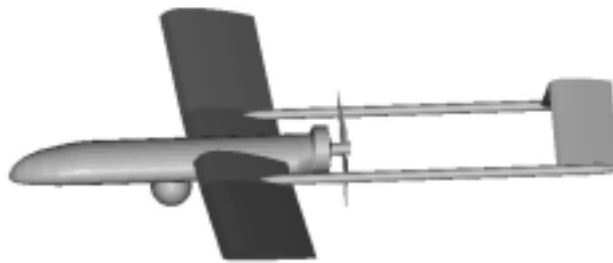


Figure 1-7 Shadow 200

UAVs fill many missions and roles. The obvious distinction from a manned aircraft is the lack of an on-board pilot. Pilots have limitations such as the need for food, water, rest, and the intrinsic value placed on human life. Unmanned aircraft have filled roles for “dull, dirty, and dangerous” [OSD 2002] missions. Dull typically means long reconnaissance and surveillance missions that stress human endurance. Dirty constitutes missions that would endanger human pilots due to exposure to radiation or biological/chemical agents. Dangerous encompasses missions that would place human life at risk. UAVs also offer the potential for significant cost savings over their manned counterparts, though cost savings are not always realized.

Technology has played a key role in UAV success. The first golden era was made possible by analog autopilot advances, lightweight inertial navigation system accuracy enhancements, and early small jet engine technology. The second golden era is enabled by lightweight digital electronics, improved sensor technology, and satellite communications. This effort seeks to explore the implications of potential future technology advances.

The DOD UAV Roadmaps [OSD 2001, OSD 2002], published by the Office of the Secretary of Defense, provide comprehensive guides to UAV needs and technologies projected into the future. These reports integrate existing initiatives and platforms into the plan and projects what new technologies may mature during the same timeframe. These roadmaps constitute the most definitive sources of UAV technology projections available today.

Despite the wealth of technology information brought forward in the UAV roadmaps [OSD 2001, OSD 2002], these sources do not attempt to directly determine the design impacts that may result from insertion of the provided projections through aircraft design and optimization. The descriptive plan focuses on existing systems or currently planned initiatives. The roadmap does not integrate the technology projections into UAV system designs.

Other reports [Carmichael 1996, (1-2) The National Academy of Sciences 2000, Sullivan 1998, Air Force Scientific Advisory Board 1996] describe future requirements, technology, and implementation possibilities. Unfortunately, useful design information and technology trends supporting the technology modeling development are usually not available.

Nearly every UAV system developed underwent an aircraft design effort. However, the design methods employed are rarely published with sufficient detail to provide a complete methodology that can be transferred to other designs. The level of engineering may not be worthy of publication in some cases. Often the design methodologies are closely guarded as proprietary information in the highly competitive UAV industry. Detailed methodologies are occasionally provided on conceptual design studies that do not result in flight hardware.

Boeing provided two noteworthy papers on the design of the Boeing Compass Cope [Brown 1980] and Condor [Johnstone 1990]. Brown [1980] describes the conceptual and preliminary design activities, manufacturing, and flight test of the Boeing Compass Cope, though details on specific design methodologies are limited. Johnstone [1990] describes technical challenges and solutions obtained for the Condor HALE UAV program, but specific design methodologies are not highlighted.

Lockheed Missiles and Space provided a series of highly detailed papers on the Solar High Altitude Powered Platform (HAPP) design studies. Hall [1983] gives extensive conceptual and preliminary design methodologies for the aerodynamics and propulsion system. Hall [1984] describes a method for sizing the structures of this platform, though with some limitations due to proprietary considerations. The Solar HAPP system was intended to fly extended missions at high altitudes using solar power and secondary power sources. Many methods presented in the reports have sufficient detail to be repeatable, though many methods are tailored only to the Solar HAPP application. The Solar HAPP was never built, so the ultimate validity of the methods is unknown.

Gundlach [1-1999] presents the design approach used for the Virginia Tech Forestry UAV. The profile drag strip-build up method and the lifting line theory application described in this source are applied here. Gundlach [1-1999] does not describe the design methodology in sufficient detail to be repeatable. The Forestry UAV flew with demonstrated performance similar to the predictions.

Raymer [2002] presents a method for optimizing UCAV AVs with genetic algorithms. The AV analysis methodology is largely based upon legacy methods from Raymer [1992] and the associated *RDS* software. Raymer [2002] emphasized exploration of GA utility for aircraft optimization. Raymer's research appears to be limited to UCAV cases, which are not covered here.

Naval Research Laboratories (NRL) has advanced the state of the art in Low Reynolds Number (LRN) UAV design. NRL publications [Foch 1992] highlight key technical issues affecting LRN AV design, though no consolidated design synthesis approach is provided.

Sources describing UAV concepts and systems abound. Few describe the design methodologies in sufficient depth to permit re-use. Many sources describe individual design disciplines in isolation, particularly LRN aerodynamics. Existing research is limited to specific design problems that are narrow in scope. There does not appear to be any previous research covering an integrated design and optimization methodology for relatively arbitrary Air Vehicles (AVs).

1.2 Problem Statement

An integrated MDO methodology is developed and applied to subsonic, fixed-wing UAV AV design optimization problems. The methods are calibrated against HALE, MAE, and tactical UAV classes. Technology trends are applied to the requirements of the three calibration cases to evaluate technology impacts on AV design.

1.3 Approach

The AV MDO methodology is applied through a self-contained software application. All geometry, aerodynamics, propulsion, structures, mass properties, and performance algorithms, to name a few, are included in the provided methodology. Wherever practical, multiple methods are provided to trade level of detail, computational speed, and accuracy.

A Genetic Algorithm (GA) is employed to optimize the vehicles for minimum design gross weight. The selected GA is the *GA170* code, developed by David Carrol of UIUC [Carrol 1998]. GA optimizers offer a robust optimization capability that is insensitive to local optima and existence of smooth objective functions, relative to calculus-based

optimization methods. However, this robustness comes at some expense of refinement efficiency.

The flight and payload performance requirements are held constant for all cases. This permits the figure of merit to be minimum design gross weight. Design gross weight is frequently used as a cost analogy by aircraft design codes, since there is a strong correlation between vehicle weight and cost. The presumption is that the evaluated vehicle design gross weight will decrease as technology advances. History shows that the minimum possible AV size for a given mission does decrease with time, but the average weight of AV within a category may actually increase with time due to enhanced capabilities. In other words, UAV requirements typically increase with advancing technology. Determining future requirements is beyond the scope of this effort, since this is largely a function of evolving military doctrine, funding, politics, and technological revolutions.

Three classes of UAV systems were selected for evaluation: the small tactical, Medium Altitude and Endurance (MAE), and High Altitude Long Endurance (HALE), to cover a broad range of vehicles and missions. The small tactical UAV requirement is filled by the AAI Shadow 200 system. The MAE reference system is the General Atomics Predator (A). The HALE reference system is the Northrop Grumman (previously Teledyne Ryan) Global Hawk. The relative size of these systems is shown in Figure 1-8.

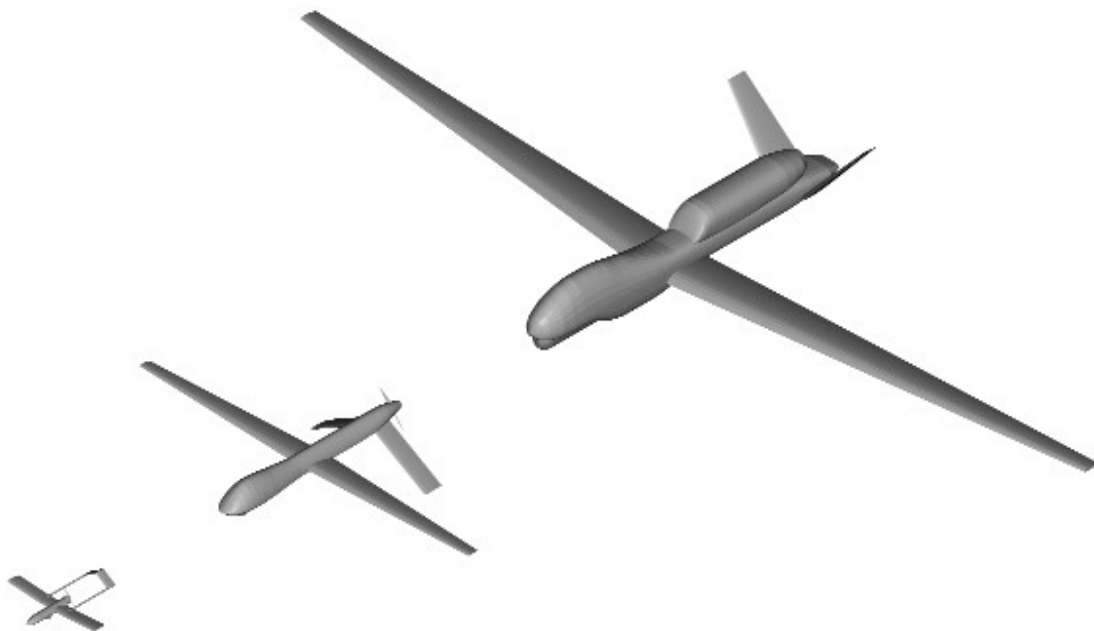


Figure 1-8 Scale Comparison of Shadow 200, Predator, and Global Hawk (Left to Right)

Technology modeling is applied to the AV MDO code to demonstrate the capabilities of the methods employed and to provide insight into technology impacts of AV design. The

direct, derived, and assumed technology trends, based on the roadmaps [OSD 2001, OSD 2002] and other sources, are applied to AV designs in this research. The technology areas explored include aerodynamics, avionics and subsystems, general design, payloads, propulsion, and structures. All technologies are ranked for substantiation, quality and potential design impact.

The technology period under consideration spans 31 years, from 1994-2025. The Global Hawk and Predator systems began development in 1994, and the Shadow 200 system represents year 2000 technology. AV designs for 1994, and every five years from 2000 to 2025 are evaluated.

Technology impacts are evaluated by introducing advancing technologies to a reference technology year. The AV MDO code exploits any advantages gained by the applied technologies. The technologies are considered in combination for all years, and individually at 10-11 years after the reference technology year.

This document provides details of the AV MDO methodology and describes its application to existing and future UAV systems. First, an overview of the methodology and code architecture is presented. Next, the genetic algorithm optimizer and its integration are described. Then, the technology modeling is detailed. The geometry, aerodynamics, propulsion, systems (size, weight and power), and performance analysis methods are presented in the next chapters. The next three chapters describe the application of the methodology to existing UAVs, optimized UAVs with technologies similar to the existing UAVs, and optimized UAVs utilizing advanced technologies. The conclusions chapter summarizes key findings and provides recommendations.

Chapter 2 Methodology

2.1 Methodology Overview

The AV design synthesis is performed with the aid of an integrated Multidisciplinary Design Optimization (MDO) code. The MDO code consists of an AV design code and a GA optimizer. The AV design code includes geometry, weights, propulsion, aerodynamics, performance, structures, systems analysis and other elements.

2.2 Methodology Development

The methodology selection process involved a search of available methods. The strengths and limitations of several methods were evaluated by the author. In several cases, the most promising applicable methodologies were integrated and evaluated. Original methods were developed where none existed or existing methods had unacceptable limitations for this application. The final methods are integrated into the software.

The AV MDO methodology is applied in the *JDES* software. *JDES* is written in the Fortran 90 programming language. This software contains approximately 30,000 physical lines, including spaces and internal documentation. The roughly estimated Source Line of Code (SLOC) count is approximately 8,000. For reference, a typical software development productivity metric is 2,000 SLOCs per equivalent head per year. *JDES*, in its current form, took approximately 4 years to develop, including algorithm re-use.

A spiral development approach was taken to generate the *JDES* software. Important aspects of the code were initially implemented with temporary prototype subroutines. Once the prototype code proved functional, it was gradually replaced by improved versions. The first refined method was the geometry definition, since the outputs are widely used by other methods. The refined aerodynamics followed, since the aerodynamics methods are highly complex and innovative approaches are attempted. Other methods for the other analysis disciplines gradually replaced the prototype placeholder subroutines. Throughout development, full or partial functionality code was run to verify modification effectiveness.

The optimizer proved to be a highly useful tool for identification and isolation of development errors. Throughout development, running the then-current baseline code helped minimize gross errors through developer inspection of results. As the code

became increasingly complex and mature, subtle interactions among subroutines became increasingly difficult to identify. Once the optimizer was integrated, a new mode of error management became possible. The optimizer tends to exploit weaknesses in the code. Through the development and result generation process, the primary aircraft evaluation subroutine *EVAL*, was called by the optimizer approximately 1.5×10^6 times.

2.3 Applied Methodology Architecture

The main subroutine in *JDES* is called *ACMAIN*. The first subroutine called from *ACMAIN* is *FILELIST*, which contains a list of all the evaluation cases. A loop is entered for all the cases considered. The first step within the loop is to call *FILEMANAGER*, which calls all input file reader subroutines. *TEMP* represents a number of subroutines that assigns, stores, and resets temporary values to data that may change during code execution. Next, *GET_OPTFILE* is called to read the optimizer settings. If optimization is required, then the *OPTIMIZER* master subroutine is called to execute the optimization. Otherwise, the *EVAL* design analysis subroutine is called directly with the input design variable settings. After the aircraft is evaluated or optimized, graphics are generated for the final vehicle by the *DXF* subroutine. The functional flow is shown in Figure 2-1.

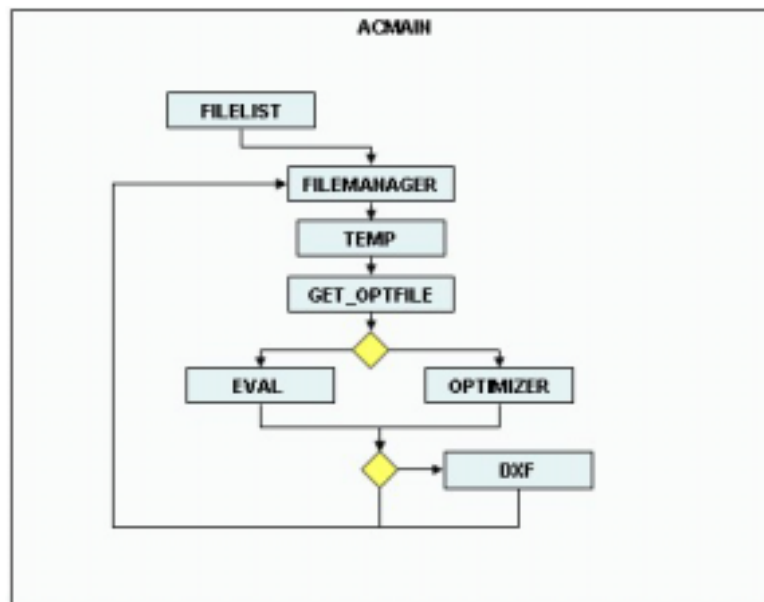


Figure 2-1 ACMAIN Code Architecture

The top-level functional flow of *EVAL*, the primary AV design evaluation subroutine, is shown in Figure 2-2. First, much of the vehicle geometry is calculated in *GEOMETRY*. Next, *WEIGHTS* is called to evaluate the vehicle mass properties and other systems evaluations. Then *AEROC* calculates all of the vehicle aerodynamic tables. Propulsion generates a tabular engine deck. Finally, *PERFORM* is invoked to perform the AV mission performance evaluations and self-optimizations. The methods contained within these subroutines are described in later sections.

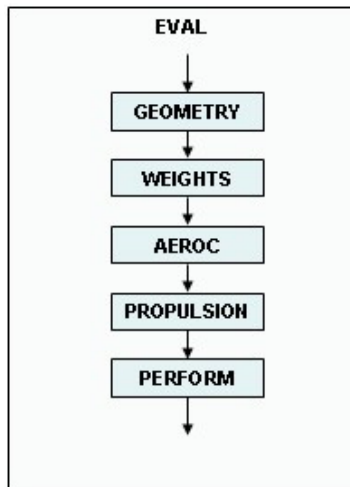


Figure 2-2 *EVAL* Code Architecture

2.4 Methods

Multiple approaches are available for several methods. Many options have origins from prototype methods. The simplified prototype methods were largely supplanted by the more detailed options, but these remain to enhance analysis flexibility. The detailed options were generated when the simple methods did not satisfactorily represent the phenomena of interest. Unfortunately, the detailed methods are typically more computationally demanding. By keeping both simple and detailed methods, the user can trade between detail and computational efficiency. For several disciplines, multiple methods are available with similar levels of detail. In this case, final method selection for this research is based upon inspection of results and assessed appropriateness of functional dependencies.

The aircraft design code represents a large body of original development. Some algorithms were developed by the Author as early as 1993. The graphics file generator, piecewise linear beam wing bending material weight estimator, and the ideal lift distribution method algorithms are strongly inspired by the VPI&SU Strut-Braced Wing (SBW) transonic transport research publications. Other influences and applied methods are cited throughout the methodology chapter.

The methodology chapter describes the methods utilized. Special emphasis is placed on the methods that are applied to generate the results for this research effort. Latent code capabilities are covered, though not extensively. Occasionally, unused procedures are given coverage to highlight limitations to these approaches.

2.5 Calibration

The integrated code is calibrated against the Global Hawk, Predator, and Shadow 200. In all cases, the empty weight, take-off gross weight, and mission performance are matched to the target values available from various sources. Other data is obtained for calibration, such as component lists, subsystem descriptions, payload types, flight envelope limitations, loading, and structural material information, to name a few. Various design levels, technology factors, and penalty factors are applied as appropriate to facilitate the calibration process.

Individual methodologies are validated whenever practical. Applicable experimental data and test case references are assembled to evaluate the method validity. Some methodologies are new or incorporate modifications that make calibration difficult, since experimental data or method test cases are unavailable. For these new or modified cases, calibration often occurs through comparison with alternative competing methods that are included in the code.

Chapter 3 Optimization

3.1 Optimization Overview

The aircraft design code, *JDES*, operates under both analysis and optimization modes. The analysis mode uses inputs provided in the input files with no optimized variable changes except for automatic internal convergence loops. The optimization mode uses the data from the input files and user-defined design variables.

A Genetic Algorithm (GA) is employed to optimize the AV designs. GAs are highly capable of finding global optima within challenging design spaces. However, this comes at some expense of efficiency in finding the refined optima. To help contend with this limitation, custom refinement algorithms are optionally available.

A GA is used to flexibly handle a wide range of design problems, where calculus-based methods may have limitations. The utility and limitations of GAs can be elucidated best by comparison with the competing calculus methods. Calculus-based methods rely on derivatives of the objective function with respect to the design variables, known as gradients. Calculus methods require the existence of derivatives and smooth design space. The optimal solution is the local optima, not necessarily the global optima. Calculus methods start from a point in the design space, and the end result is typically highly dependent on the starting conditions. Within the vicinity of local optima, calculus methods can be very efficient at finding the refined local optima.

Genetic algorithms handle the design problem in a significantly different manner. GAs do not require the existence of gradients. A non-smooth design space with discontinuities is acceptable. GAs are adept at finding the global optima, since the search is based on a population of design points, not a single point. However, refinement of the global optima is inefficient relative to calculus methods within the vicinity of the optima.

GAs do not operate on design variables, called parameters, directly. The parameters are coded in binary strings of zeros and ones, and combined in larger strings. The GA operates on the strings, and then decodes the strings into the parameters prior to evaluating the objective function, called the fitness function. The string operators are reproduction, crossover, and mutation. Each string represents a member of the population. There are multiple individuals in the population for each generation. The design variables are selected to be powerful and intuitive in driving the optimizer to the global optima.

GAs do not handle constraints directly. Violated constraints must be converted to penalty functions that are applied to the objective function. By comparison, many calculus methods may handle constraints directly.

David Carrol's *GA170* [Carroll 1998] optimizer was selected for this research. This code, developed at University of Illinois at Urbana Champaign (UIUC), is freeware and written in Fortran 77, both key attributes contributing to its selection. The code was originally written in Fortran 77, but the language was modified to Fortran 90 by the Author for this application. The *GA170* code is a true GA, using the methods described above.

The basic principles of GAs are well-established. A more extensive treatment of GA theory similar to that applied here can be found in Goldberg [1989].

3.2 Optimization Code Architecture

David Carrol's *GA170* code required significant modification and additional code to be useful for this application. The standard *GA170* code acts as a main subroutine, but the UAV code has a main subroutine that controls the high level execution of the code. *GA170* was modified to act as a subservient subroutine called by *ACMAIN* via the *OPTIMIZER* subroutine. New code was written for conditioning the design variables, constraints, fitness function, and optimizer search refinement.

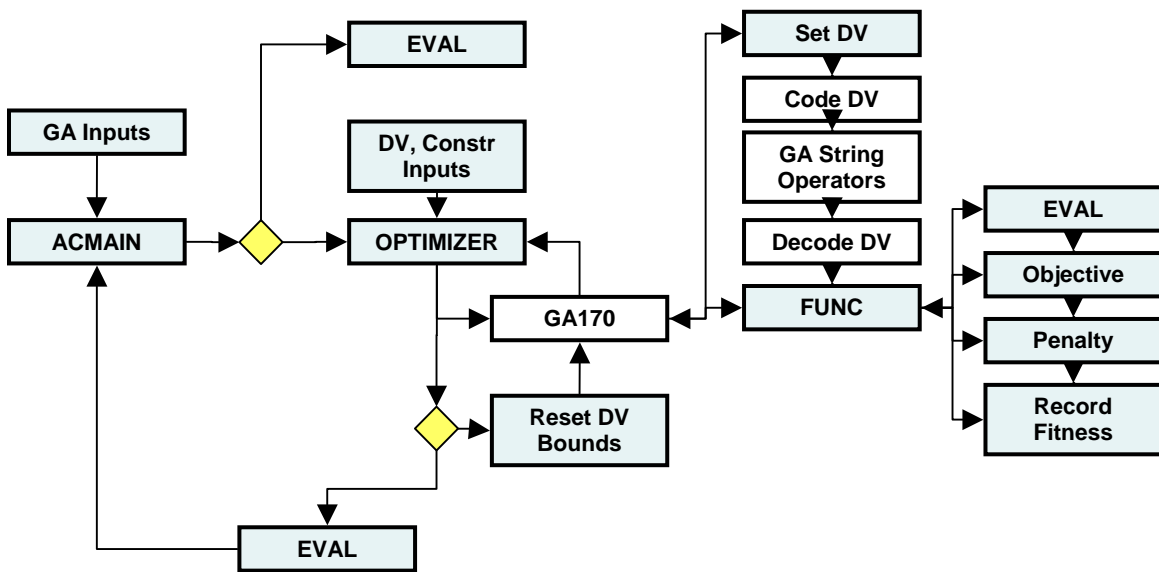


Figure 3-1 Genetic Algorithm Code Architecture

Figure 3-1 shows the GA code architecture. The shaded blocks represent new code developed by the Author, and the white blocks represent existing or slightly modified code contained within David Carrol's *GA170*. The functions represented by the blocks are not necessarily contained within a single subroutine or as a distinct subroutine.

The *ACMAIN* code, the main subroutine, reads the generic GA setting data and controls the execution of the GA. The generic GA setting data includes population size, number of generations, and probability of mutation and crossover settings. The *ACMAIN* code will simply call *EVAL*, the primary aircraft evaluation subroutine, when in the analysis mode. When in the optimization mode, *ACMAIN* will call the *OPTIMIZER* subroutine.

OPTIMIZER is the primary optimization control subroutine. It reads the specialized GA inputs, such as design variable limits and constraint information. Once the GA data is input, *OPTIMIZER* controls the execution of *GA170*. Optimizer can call *GA170* multiple times with refined design variable limits such that the global optima may be refined. Once the best solution is found, *OPTIMIZER* calls *EVAL* to evaluate the best design and write detailed design information to output files.

GA170 contains the GA algorithm. The GA creates an initial population of individuals based on the design variable limitations. These individuals are represented by genotypes of bit strings. *GA170* performs the GA operations on these strings, decodes the strings into design variables, and evaluates the fitness of the individuals. The fitness value for each individual is found in subroutine *FUNC*. This procedure occurs for the specified number of generations. The fittest individual in the final generation is output.

Subroutine *FUNC* combines the objective function and the constraint penalty functions to produce the fitness value for *GA170* to utilize. *FUNC* calls *EVAL* with the design variable settings. *EVAL* calculates the objective function, and evaluates the individual constraint values and penalties. The constraint penalties are summed by *FUNC* and combined with the objective function to produce the fitness function. *FUNC* calls a subroutine to record the most fit members of populations over all generations that do not have violated constraints. The optimized solution and the fit individual array are sent back to Optimizer after the final generation is run.

OPTIMIZER has the option of refining the permissible solution set within the solution space based on the knowledge of the fit individual array. In this scenario, the minimum and maximum design variable limits are brought closer to the minimum and maximum design variable values for the fittest individuals with no violated constraints. This procedure may be performed many times until either the maximum number of iterations is reached or the difference between the minimum and maximum fitness values reaches a specified tolerance. This new feature is not applied to the final cases, since the baseline GA algorithms are sufficient.

The *GA170* code is a highly useful GA. Substantial new code was required to integrate *GA170* into a flexible and user-friendly UAV optimizer. The final product fully satisfies the needs of the research problem set.

Although randomization is used by the GA, the results are repeatable. The random number generator selects the same random numbers starting at the initiation of software execution. The optimized solutions are identical when evaluated in the same order.

3.3 Design Variables

The universally applicable design variables are shown in Table 3-1.

Variable	Description
b_w	Wing span
AR_w	Wing aspect ratio
λ	Wing taper ratio
t/c	Wing thickness to chord ratio
MF_{Fuel}	Fuel mass fraction

Table 3-1 Universal Design Variables

The Global Hawk case additionally provides wing quarter chord sweep as a design variable. Sweep is a unique design variable to this case, because higher Mach-number Global Hawk contends with compressibility effects. Sweep is one way to counteract compressibility impacts on drag.

The geometry is a strong contributor to vehicle weight. The optimizer seeks to minimize the vehicle design gross weight while not violating constraints. The geometry design variables applied here were selected to have the greatest impact. Some of the trades performed by the optimizer with the design variable selections are described here.

The aspect ratio drives aerodynamic efficiency at the expense of structural weight. High aspect ratio wings have lower induced drag and higher available total lift coefficient for a given wing area than low aspect ratio wings. Exclusive of high lift devices and for a fixed airfoil, higher aspect ratio wings tend to have lower wing areas due to the increase in maximum lift coefficient. High aspect ratio wings have a higher structural weight than low aspect ratio wings of the same area due to higher bending moments and shear loads in the wing spar. Aerolastic phenomena are more dominant in high aspect ratio wings, though these effects are not evaluated here.

The taper ratio affects the induced drag and structural efficiency. Wing taper permits a wing to approach the ideal elliptical lift distribution more closely than without taper, which reduces the induced drag. At low Reynolds numbers, the wing tip Reynolds number is lower than the average chord Reynolds number, which can drive up the profile drag. With a constant wing area and wingspan, a reduced taper ratio increases the root chord length, which increases the wing-fuselage fairing size in the parametric geometry. The increased fairing size impact on drag can have positive or negative drag contributions. Taper improves structural weight, because the absolute airfoil thickness is higher where the bending moment is highest. The increased area moment of inertia permits the wing skin thickness to be reduced for a given loading.

Wing sweep can delay the onset of compressibility and reduce the impacts of wave drag, but at the cost of a reduction in laminar flow and less structural efficiency. Wing sweep trades are documented in Gundlach [2-1999].

Increasing the airfoil thickness to chord ratio increases structural efficiency, but tends to adversely affect the wing profile drag and hastens the onset of compressibility effects. Transonic wings tend to manipulate wing sweep and airfoil thickness to chord ratio simultaneously.

The wing, tail, and fuselage weights are impacted by scale. The optimizer tends to minimize fuselage length and wing span such that the volume constraints are not violated. The parametric tail geometry sizes the tail surfaces as a function of tail moment arm, so the fuselage length reduction is tempered by tail size. Additionally, the parametric geometry used for all optimization cases limits the minimum fuselage length via constraints that are functions of span and average chord, as described in the geometry section.

The propulsion design variable for jet aircraft are shown below in Table 3-2. Note that the thrust to weight ratio, T/W , and Sea-Level Static (SLS) thrust, $T_{\max, \text{SLS}}$, may not be used simultaneously. The thrust is evaluated at the uninstalled SLS maximum thrust conditions. Uninstalled refers to the advertised engine characteristics that do not take into account for engine installation impacts due to inlets or nozzles. The weight in T/W is the take-off gross weight of the aircraft.

Variable	Description
T/W	Uninstalled SLS thrust-to-weight ratio at TOGW
$T_{\max, \text{SLS}}$	Uninstalled SLS thrust

Table 3-2 Jet Propulsion Design Variables

The propulsion design variables for reciprocating engines are shown in Table 3-3. Note that P/W and P_{Shaft} may not be used simultaneously. The power is the uninstalled sea level static brake power. Uninstalled refers to the advertised characteristics of the engine that does not account for aircraft installation. The weight in P/W is the take-off gross weight of the aircraft.

Variable	Description
P/W	Uninstalled brake power-to-weight ratio at design gross weight
P_{Shaft}	Uninstalled brake horsepower

Table 3-3 Reciprocating Engine Propulsion Design Variables

3.4 Constraints

Several constraints are used by the optimization code. Unique penalty functions are calculated for violated constraints. The constraint types are listed below in Table 3-4. The user can select which constraints are imposed prior to running the code.

Constraint	Description
Mission Complete	Constraint violated if prescribed mission is not completed due to performance limitations or lack of fuel
Mission Constraints	Constraints violated if the set of mission constraints (Table 3-5) is not fully satisfied over the complete prescribed mission
Fuel Volume	Constraint violated if the required fuel volume is greater than the available allocated volume

Table 3-4 Constraints

The mission constraint types are listed in Table 3-5.

Constraint Number	Description
1	Stall ($C_L > C_{L,Max}$)
2	Insufficient thrust for minimum specified rate of climb
3	Insufficient thrust for level flight
4	Dynamic pressure limit ($q > q_{Max}$)
5	Mach limit ($M > M_{Max}$)
6	Engine operating limits (type dependent)
7	Altitude limit
8	Weight error (Weights < 0)
9	Lift lower limit ($C_L < C_{L,Min,Table}$)

Table 3-5 Mission constraint types

The fitness function is a combination of the objective function and the penalty functions. The GA attempts to maximize the fitness. If the objective is to minimize the weight, and the weight is the objective function, then the fitness should be the negative of the objective function. A negative fitness with a lower magnitude is considered a greater number, so lowering the negative magnitude is a means of maximizing the fitness. Similarly, if the violated constraint penalties are represented in terms of weight, then the penalty contribution to the fitness function is the negative of the penalty. The fitness function is:

$$Fitness = -(Objective + \sum Penalty)$$

The objective function is made to be on the order of 10^0 (or unity). When the objective function is purely a function of design gross weight (W_{DG}), then the objective function is:

$$Objective = \frac{W_{DG}}{W_{DG,Ref}}$$

The penalty functions are intended to be referenced to the same order of magnitude. For constraints that vary, the penalty function takes the form of a quadratic equation with a step function starting when the constraint is violated. The step function ensures that there is an immediate penalty for a violated constraint. The quadratic equation increases the penalty more aggressively as the magnitude of constraint violation increases. Each penalty has a user-defined weighting parameter. The variable penalty function is:

$$Param = f(Constraint) \text{ When constraint is violated}$$

$$Penalty = (Step + F1 \cdot |Param| + F2 \cdot Param^2) \cdot Penalty_{wt} \text{ When constraint is violated}$$

Other constraints take the form of discrete differences. In other words, the constraint is either satisfied or not satisfied. There is no variation in the degree of constraint violation. The penalty parameter is:

$$Param = 1$$

when a constraint is violated. Discrete constraint penalty functions take the following form:

$$Penalty = F1 \cdot Param \cdot Penalty_{wt}$$

when a constraint is violated.

The penalty functions for each of the constraints are described below.

Mission Completion

The mission completion penalty function is called when the mission completion is less than unity.

$$Param = MissComp - 1$$

The penalty function is:

$$Penalty = (0.1 + Param + Param^2) \cdot Penalty_{wt}$$

when the constraint is violated

Performance Constraints

The performance constraint penalty function is found by:

$$Param = N_{violated}$$

The penalty function is:

$$Penalty = Param \cdot Penalty_{wt}$$

Fuel Volume Constraints

The wing volume penalty function is found by:

$$Param = 1 + \frac{Vol_{Margin, Type}}{Vol_{Avail, Type}}$$

when the margin for a given type of volume is negative. The type refers to wings and fuselage, and each type is evaluated individually.

$$Penalty = (0.1 + Param + Param^2) \cdot Penalty_{wt}$$

when the constraint is violated.

Chapter 4 Technology Modeling

4.1 Technology Overview

Technology modeling into the future is an art, since technology trends that endure for more than a few short years are rare. One of the most famous exceptions, Moore's Law, states that the number of transistors on a microprocessor doubles approximately every 18 months. This Law has remained notably accurate since 1965, and the form of this projection is expected to hold true into the coming two decades [OSD 2002].

Most technology trends tend to have high levels of uncertainty. Many trends are based upon the possible, not the likely. It is possible to accelerate a technology with aggressive funding, priority, or inspiration. However, technologies may also experience a maturation period prior to garnering sufficient attention to stimulate investment. Predicting enabling funding relationships can be as challenging as predicting technology breakthroughs. Nascent technologies may demonstrate impressive performance under laboratory conditions. However, this does not mean that the embryonic technology is suitable for operational applications. Transforming the laboratory technology into a field-ready product may result in performance alteration due to practical integration considerations.

To counter the time lag between demonstrated technology and operational capability, it is important to capture impacts of technology emphasis and level of design in the predictions. This research attempts to accommodate both considerations. Long term technology projections contain high uncertainty. Expectations of accuracy become increasingly unrealistic as the time into the future extends. In light of the inherent limitations associated with divining the future, this research endeavors to describe what may potentially happen, not what will.

The technologies are grouped into aerodynamics, avionics/subsystems, design, payloads, propulsion, and structures categories. The individual technologies composing the technology categories were qualitatively ranked for substantiation, quality, and aggressiveness. The summation of all technology categories is shown in Table 4-1. Details of each technology are described throughout this section.

	Substantiation	Quality	Aggressiveness
<u>Aerodynamics</u>			
Induced Drag	4	3	2
Interference Drag	3	2	2
Wave Drag	3	2	2
Profile Drag	3	2	3
<u>Avionics/Subsystems</u>			
Autopilot	3	1	1
Inertial Navigation System	3	1	1
Subsystems	2	3	1
Communications	4	3	2
<u>Design</u>			
Weight Growth	4	3	2
<u>Payloads</u>			
Synthetic Aperture Radar Payload	1	1	1
Small Electro-Optic/Infrared Payload	2	2	2
Large Electro-Optic/Infrared Payload	2	2	3
<u>Propulsion</u>			
Jet Propulsion	1	2	1
Reciprocating Engines	1	2	1
<u>Structures</u>			
Structural Factor	2	3	1
Factor of Safety	3	2	2

Table 4-1 Technology Attributes

The ranking standards for each attribute are shown in Table 4-2.

<u>Substantiation</u>	
1	Direct application of trend from other sources with minimal modification
2	Derived from existing trends in other sources
3	Original trend developed from available sources with data
4	Assumption with little substantiation
<u>Quality</u>	
1	High relative chance of success (i.e. Moore's Law)
2	Moderate relative chance of success
3	Low relative chance of success
<u>Aggressiveness</u>	
1	Substantial technology improvement
2	Moderate technology improvement
3	Little technology improvement

Table 4-2 Attribute Ranking Description

As can be seen from the above tables, there is only one directly applicable existing technology trend with a high relative chance of success and anticipated high impact on the optimization objective function.

4.2 Technology Methods

Two primary methods of technology modeling are applied to the design code. These are technology parameter ratios (Method 1) and direct technology parameter lookup (Method 2).

The technology parameter ratio, Method 1, is used whenever the ratio of technologies is multiplied or divided by a baseline value. An example is a technology factor applied to an input baseline avionics weight. The procedure is shown graphically in Figure 4-1 (A-B).

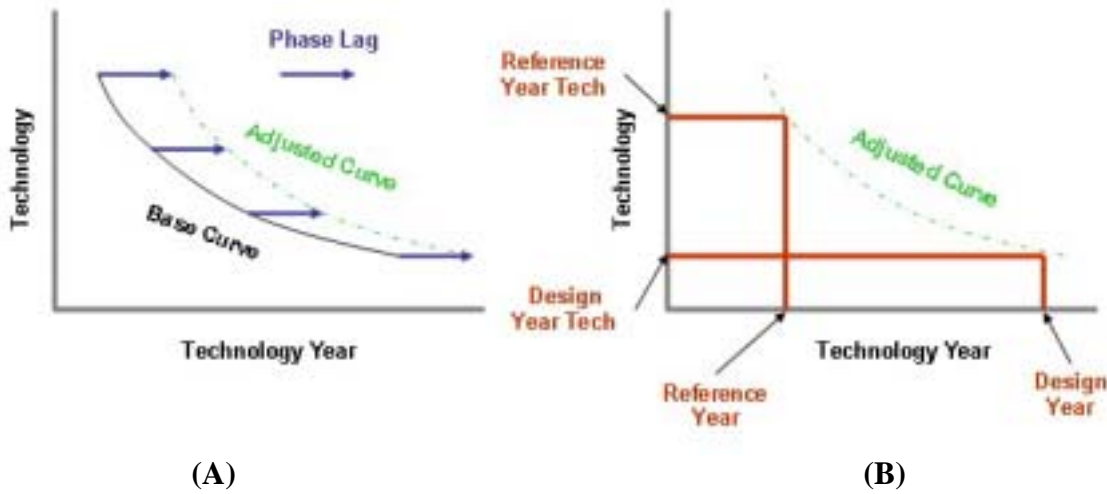


Figure 4-1 Technology Parameter Ratio Model (Method 1)

A single technology curve composed of discrete technology versus technology year data points is used. The technology phase lag, *Phase*, is the time difference between availability of the technology and its application. *Phase* is found through a look-up procedure based on phase lag versus technology level input data. The technology curve is shifted to the future by the time amount *Phase*, to obtain an adjusted technology curve. The technology for a given lookup year is:

$$Tech(Year) = Tech_1 \cdot R_{Year}^{(Year - Year_1)}$$

where *Year* is automatically bound by *Year₁* and *Year₂* in the adjusted technology curve. In the case where *Year* lies beyond the final *Year₂* date, the following extrapolation occurs:

$$Tech(Year) = Tech_2 \cdot R_{Year}^{(Year-Phase-Year_2)}$$

Whenever *Year* is before the earliest *Year₁* date, the technology is set to the earliest technology level without further extrapolation.

The technology ratio between *Year₁* and *Year₂*, *R_{Tech}*, is found by:

$$R_{Tech} = \left(\frac{Tech(Year_2)}{Tech(Year_1)} \right)^{\frac{1}{Year_2 - Year_1}}$$

The technology factor, *F_{Tech}*, is found by:

$$F_{Tech} = \frac{Tech(Year_{Des})}{Tech(Year_{Ref})}$$

where *Year_{Des}* is the design year and *Year_{Ref}* is the reference year of the baseline. For example, the Global Hawk program began in 1994, so the reference year is 1994. If the Global Hawk requirements were evaluated in 2005, then the design year would be 2005. The baseline characteristic of interest is multiplied or divided by the technology factor, as appropriate.

The direct technology parameter lookup model, Method 2, is suitable for design technologies that are not ratios. For example, the structural design factor of safety as a function of design year and design level is appropriate for a look-up function. The design level ranges from 0-1, where 0 represents the lowest design level and 1 is the highest design level. The equivalent of a phase lag is built into the design level, because design level of 1 equates to the minimum phase lag, and design level 0 represents the equivalent of the maximum phase lag. This look-up procedure is shown graphically in Figure 4-2.

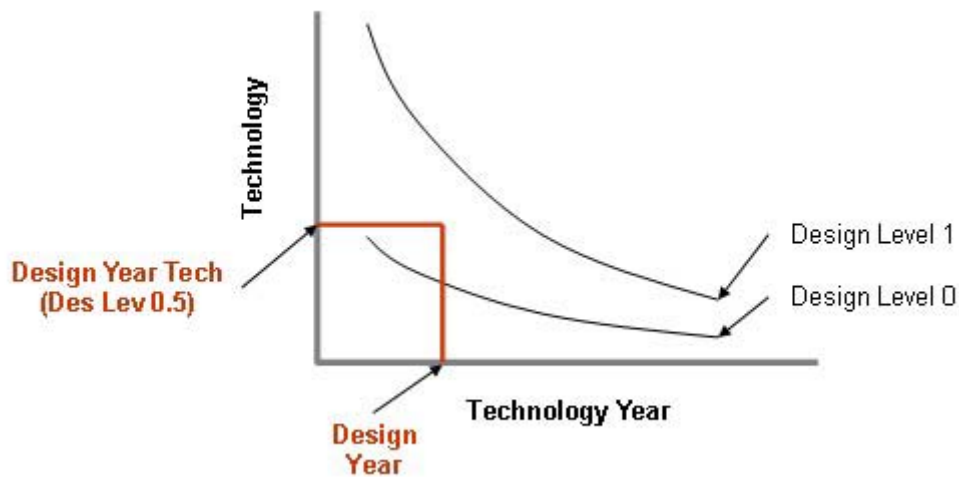


Figure 4-2 Direct Technology Parameter Lookup Model

4.3 Technology Modeling

4.3.1 Aerodynamics

The aerodynamics technologies are divided into induced drag, interference drag, wave drag, and profile drag. For convenience, the attributes of these technologies are repeated in Table 4-3.

	Substantiation	Quality	Aggressiveness
Aerodynamics			
Induced Drag	4	3	2
Interference Drag	3	2	2
Wave Drag	3	2	2
Profile Drag	3	2	3

Table 4-3 Aerodynamics Technology Attributes

Induced Drag

The induced drag technology is modeled as a factor applied to the minimum theoretical induced drag found through the Trefftz plane analysis. The trends are assumed to converge to the ideal as time progresses. This assumption is based on the advancement

of Computational Fluid Dynamics (CFD) in wing design optimization. The assumed technology trends are shown in Figure 4-3.

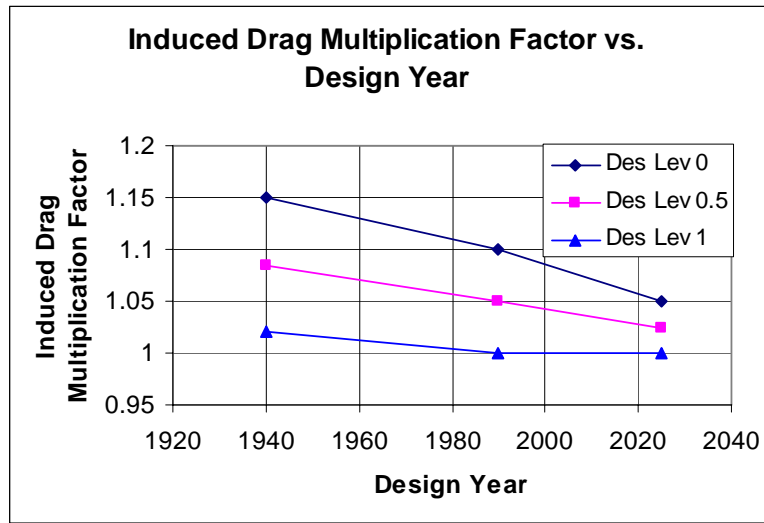


Figure 4-3 Induced Drag Multiplication Factor Technology Trends

Interference Drag

Hoerner [1992] interference drag methods are used, as described later in the aerodynamics section. Hoerner notes that the interference drag of a strut junction may be reduced to 10% of the data presented if properly faired. This trend is assumed to hold for all other interference drag contributors from 1940 through 1995. Some improvement in aggressive design levels are permitted between 1995 and 2025. The general trend is for the interference drag multiplication factors to approach the minimum value as time progresses. This assumption is justified by the proliferation of CFD codes and design methods. Much of Hoerner's data and methods originated in Germany during World War II. Therefore, the starting date is 1940. The interference drag multiplication factor is applied to the standard Hoerner interference drag estimates. The trends are shown in Figure 4-4. Due to the significant impacts of the interference drag on vehicle geometry optimization, the interference drag design level is set to 1 for all cases.

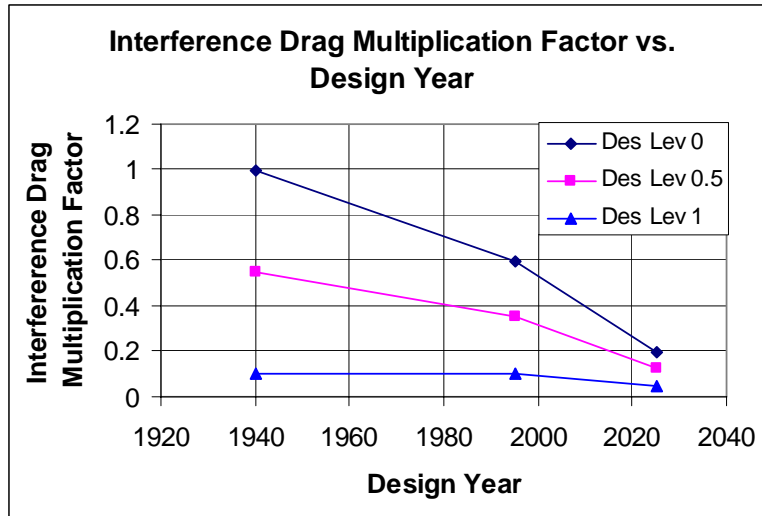


Figure 4-4 Interference Drag Trends

Wave Drag

The wave drag is modeled through the transonic airfoil technology factor used in the Korn equation [Grasmeyer 1998]. The factor for a Boeing 747 is 0.89, and for a Boeing 777 with supercritical airfoil sections of 1995 technology year is 0.955 [Grasmeyer 1998]. These commercial transport values are used to estimate the state-of-the-art trends. One noteworthy assumption is that the lowest technology line for 1995 through 2025 is assumed to be consistent with the technology associated with the 747. The transonic airfoil technology factor trends are shown in Figure 4-5.

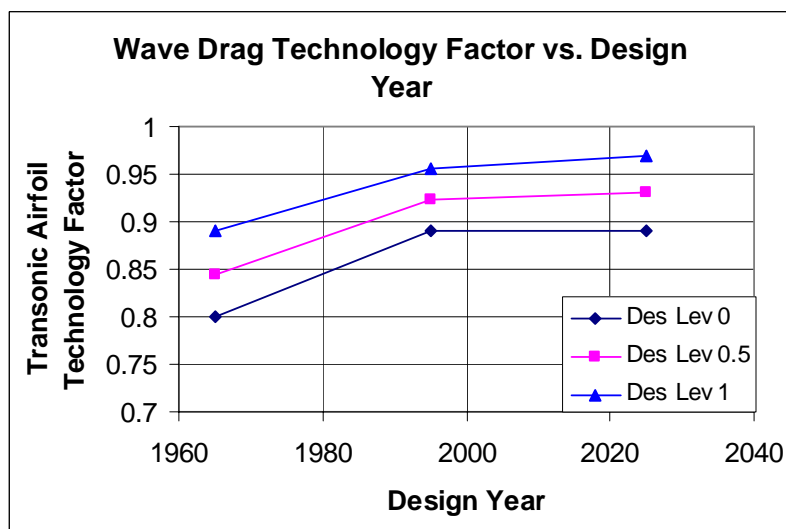


Figure 4-5 Wave Drag Technology Factor Trends

Profile Drag

The profile drag technology is modeled as a multiplication factor to the profile drag. Data was compiled for high performance airfoil sections over a wide time span for three Reynolds numbers covering the majority of the range of interest here. The referenced airfoils represent assumed typical state-of-the-art for the airfoil design year. Table 4-4 shows the selected airfoils.

Airfoil Year	Reynolds Number	Airfoil	L/D max	Source
1949	60,000	NACA 0009	26.3	Selig [1989]
1980	60,000	FX 60-100	45.5	Selig [1989]
1985	60,000	HQ 2.5-9	47	Althaus [1985]
1922	300,000	Clark Y	71	Selig [1989]
1980	300,000	FX 63-137	93	Selig [1989]
1949	3,000,000	NACA 2415	95	Abbot [1949]
1992	3,000,000	SM 701	100	Somers [192]

Table 4-4 Airfoil Characteristics.

The profile drag multiplication factor is the ratio of the inverse of the lift to drag ratios referenced to the starting year condition for a given Reynolds number. These factors for the selected airfoils are plotted in Figure 4-6.

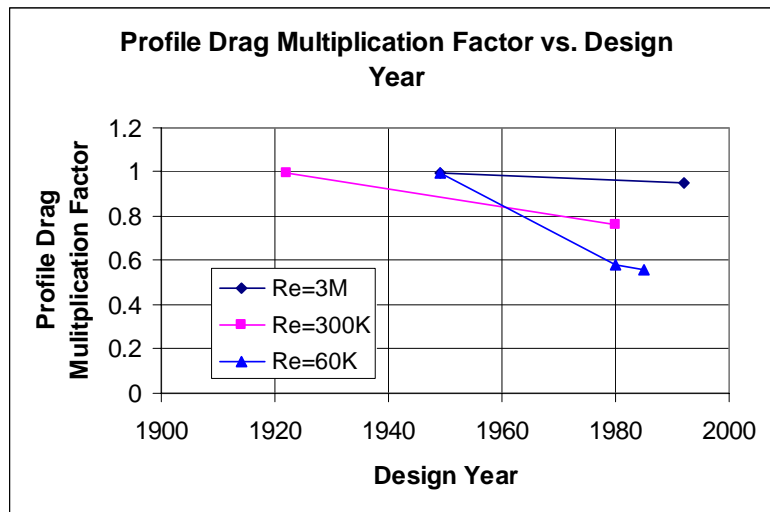


Figure 4-6 Profile Drag Multiplication Factor Trends

The technology trends derived from the available data are highly Reynolds number dependent. The 3 million Reynolds number case represents the flight regime experienced by small, lower speed manned aircraft such as general aviation types. By the first reference date of 1949, much development and testing had been performed on airfoils

operating in these Reynolds numbers, spurred on by two world wars and 44 years of commercial air transportation.

By comparison, the lower Reynolds number airfoils, especially near 60,000, had relatively few applications beyond model aircraft. It was not until the late 1970s that the low Reynolds number regime ($Re < 300,000$) received serious attention by technical hobbyists and engineers. Today, there are multiple, high-quality, low Reynolds number databases available, which are frequently used by competitive model sailplane enthusiasts and UAV developers. Furthermore, high performance boundary layer codes, such as XFOIL, are freely available. These codes can realistically model and aid in the design of low Reynolds number airfoils.

A single function that is Reynolds number independent is desired for the profile drag multiplication factor. The UAVs under consideration typically operate with wing chord Reynolds numbers near the 300,000 to 3,000,000 range. Therefore, a curve approximately splitting the two trends was employed. The level of design was also adopted to bound the variation of design. The profile drag multiplication factor of 1 represents the state of the art in 1949. The presumption is that after the year 1990, the poorest airfoil designs employed on UAVs will be the equivalent of the state-of-the-art in 1949 for an equivalent Reynolds number. The state-of-the-art airfoils in 2025 are assumed to have a 20% improvement over the state-of-the-art in 1949 for a given Reynolds number, as a best judgment. Figure 4-7 shows the resulting assumed airfoil technology trends.

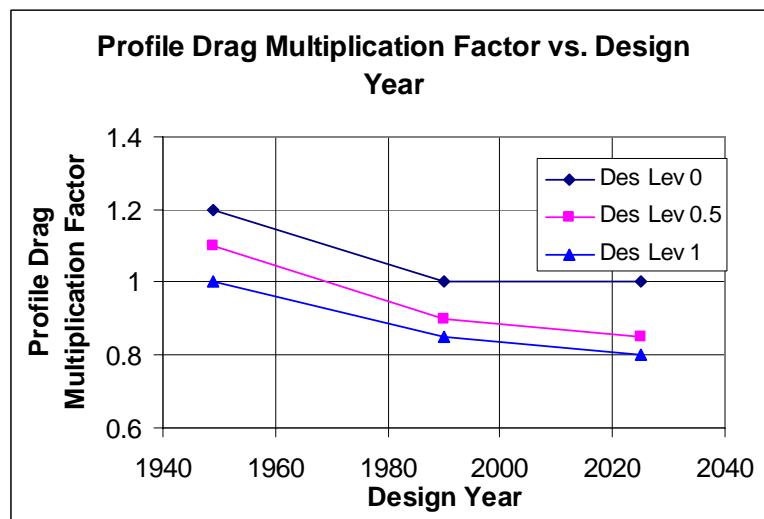


Figure 4-7 Final Profile Drag Multiplication Factor Trends.

The ratio of profile drag multiplication factors is applied as a multiplication factor to the calculated profile drag at a given design level.

Laminar Flow

The laminar flow technology affects transition for 2-D airfoils and 3-D wings with sweep. The applied technologies are independent of year, and the formulation takes a different form than other technologies. The laminar flow technology impacts are described in the Aerodynamics section.

4.3.2 Avionics and Subsystems

Technology trends for various types of avionics are evaluated. The attributes of these technologies are repeated in Table 4-5.

	Substantiation	Quality	Aggressiveness
<u>Avionics/Subsystems</u>			
Autopilot	3	1	1
INS	3	1	1
Subsystems	2	3	1
Communications	4	3	2

Table 4-5 Avionics and Subsystems Technology Attributes

Guidance, Navigation and Control

The Guidance, Navigation and Control (GNC) avionics includes the INS, flight computers, and varying flight critical sensors. Werrell [1985] noted that a 1970 cruise missile GNC weight is 115 pounds. Data for similar functionality GNC systems from manufacturer specification sheets was used to generate the overall GNC trends. Figure 4-8 and Figure 4-9 show the GNC technology phase and technology trends, respectively. The GNC trend is applied to all avionics except for the air data system and INS.

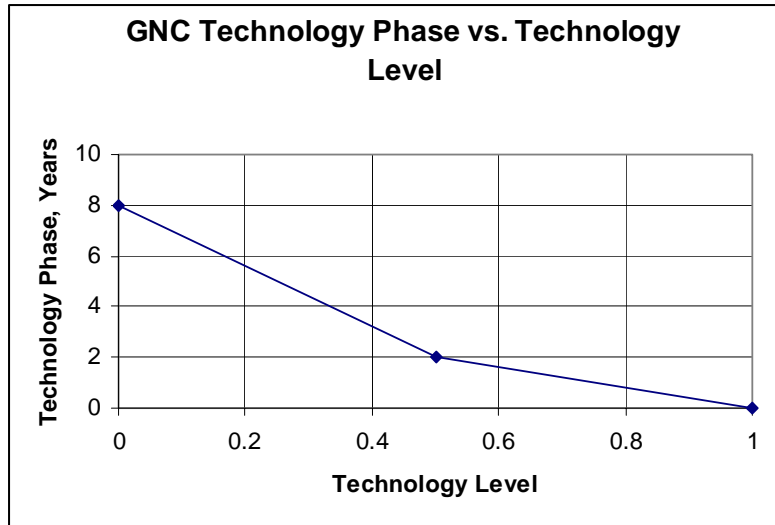


Figure 4-8 GNC System Technology Phase.

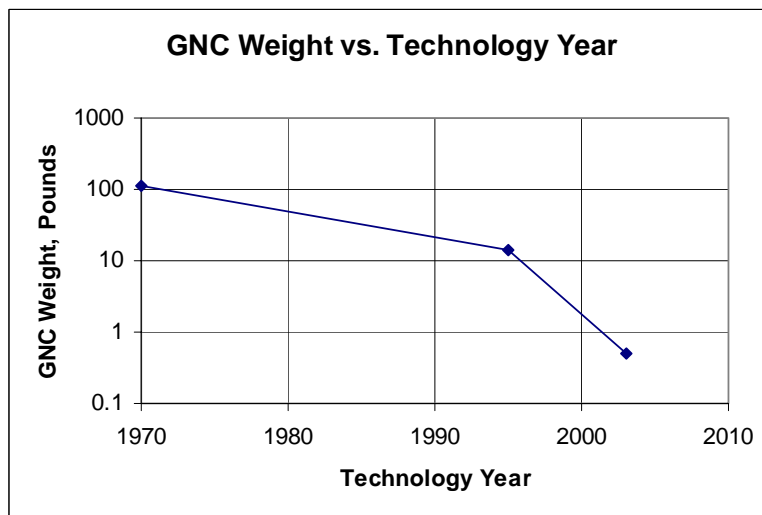


Figure 4-9 GNC System Technology Trends.

Inertial Navigation System

UAV inertial navigation systems (INS) have seen much progress over the past half century. In 1960, a cruise missile INS weighed approximately 300 pounds [Werrell 1985]. By 1970, the same functionality system weighed only 29 pounds, enabling a miniaturized cruise missile revolution [Werrell 1985]. The trends carry the same functionality forward to current technology, using manufacturer specification sheets. The assumed guidance system technology phase and technology trends are shown in Figure 4-10 and Figure 4-11, respectively.

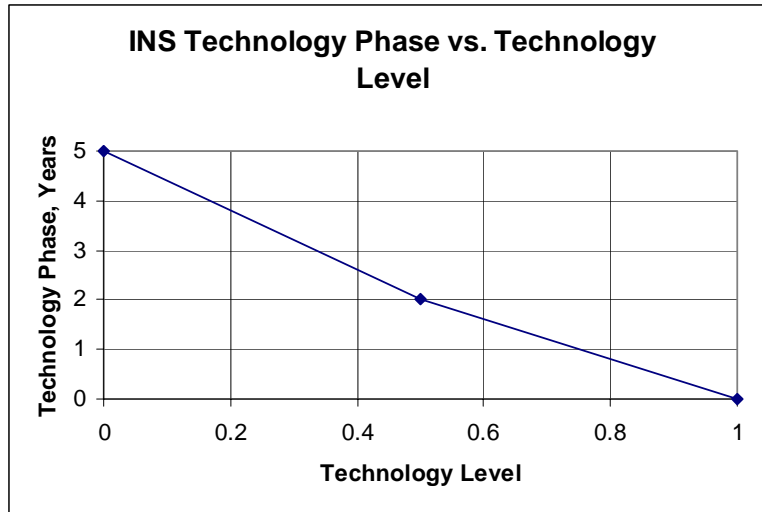


Figure 4-10 INS Technology Phase

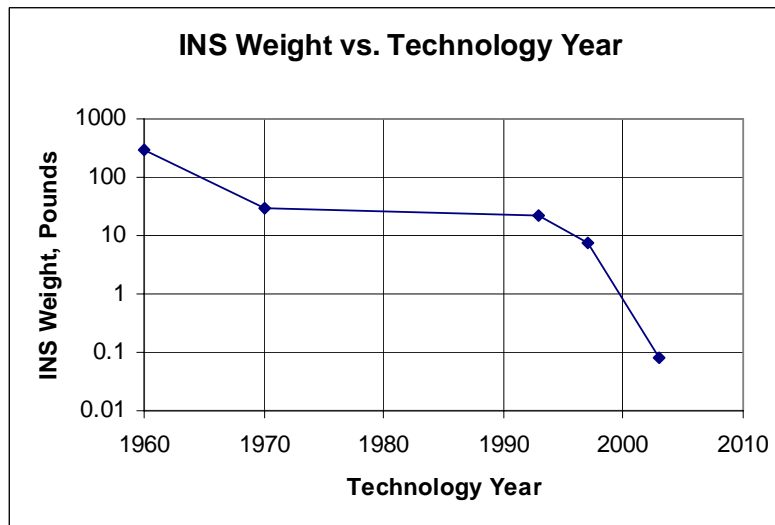


Figure 4-11 INS Technology Trends

Processors

Much of the avionics revolution is made possible through the advancement of processor technology. The DOD UAV Roadmap [2002] has tracked commercial processor speed through time. This technology trend was adopted directly in this research, though not used to generate the results. There is a phase lag between the availability of commercial processors and the application to aircraft.

Although a processor performance trend is available for technology modeling within the design code, it is not utilized here. The INS and GNC weight trends are utilized to estimate avionics weights. The processor speed is not proportional to actual avionics weight, because demand placed on processors increases as processor capability improves.

The demands placed on processors typically increases faster than the improvements in processor speed [Noor 1997]. The GNC weight trends are more representative of attainable weight reductions.

Subsystems

Trends found in Noor [2000], which present Defense and Aerospace study [1995] results, are used for subsystems technology modeling. For long-range, transonic transports, the anticipated total gross weight reduction due to subsystems contributions is estimated at 9% [Defense and Aerospace 1995]. This reduction, however, is not the subsystems weight reduction, but the total synthesized aircraft weight reduction. The subsystems contribution is found by a simple mass fraction analysis. A very simple sizing relationship for a given aircraft class is:

$$\frac{W_{TO}}{W_{Payload}} = \frac{1}{1 - MF_{Fuel} - MF_{E,-Subst} - MF_{Subs} \cdot F_{Subs,Tech}}$$

Numbers representative of the Boeing 777 are used as an estimate for the 1995 mass fraction numbers. The fuel mass fraction is assumed to be 0.4. The mass fraction of the empty weight less subsystems is assumed to be 0.42. The mass fraction of the 1995 subsystems is assumed to be 0.05, when the subsystems weight multiplication factor is equal to 1. In order to achieve a 9% reduction in take-off gross weight due to subsystems contributions, the subsystems weight multiplication factor must equal 0.75. The 1960 subsystems weight multiplication factor is assumed to be 1.1, or 10% greater than the 1995 subsystems weight, since subsystems technology has improved between these dates.

This technology trend is assumed to be applicable to UAVs in absence of better subsystems weight technology models. All UAVs considered here are much smaller than transonic transports, but competing subsystems technology information suitable for a model is unavailable. The assumed subsystems technology phase and multiplication factor trends are shown in Figure 4-12 and Figure 4-13, respectively.

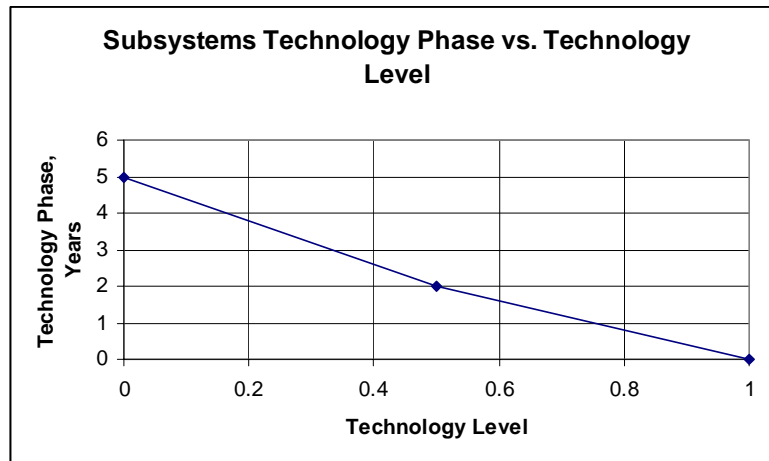


Figure 4-12 Subsystems Technology Phase

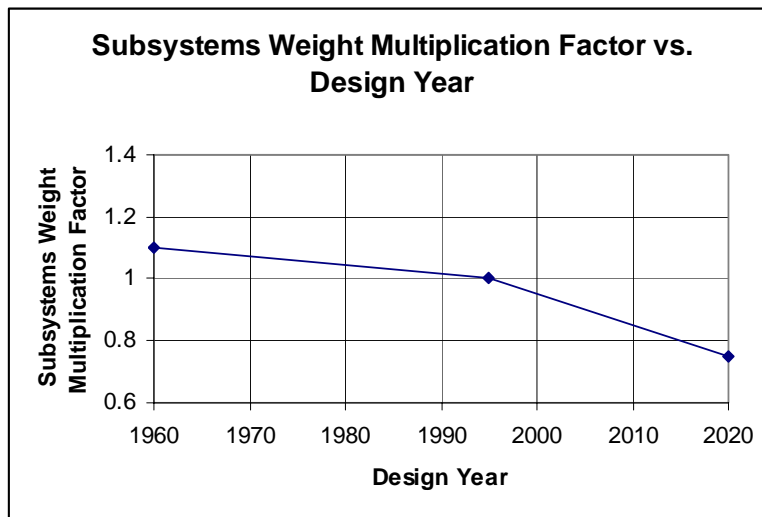


Figure 4-13 Subsystem Weight Technology Trend

Communications

The most significant communications system impact on UAV design is the antenna for satellite communications, if so equipped. In addition to the weight and power of the antenna and gimbals, the antenna takes up considerable volume and drives the shaping of the fuselage. The diameter of dish antennas, as seen on the Global Hawk and Predator, is driven primarily by the antenna gain requirements. The gain requirements are in turn driven by the desired data rates, radiated power, and beam width requirements. These are largely driven by the satellite constellation that the UAV is communicating with.

It is difficult to predict the advancement of communication satellites through 2025. This is largely driven by satellite project funding. It is even more difficult to translate the communication satellite capabilities into UAV antenna diameter. The assumption that there will be no communication satellite or related UAV antenna technology advancement is bolder than assuming that technology will progress. The DOD UAV Roadmap [OSD 2002] predicts that data compression, pre-processed payload data, and more efficient usage of bandwidth will act to relieve the communications challenges facing UAVs. No direct impacts on aperture sizing are provided. In light of the OSD predictions, an assumption was made that for equivalent collection functionality, the dish antenna diameter on UAVs will decrease to 50% of the 1994 values by 2010 and to 25% of the 1994 value by 2025. This relationship is shown in Figure 4-14. It is assumed that no technology phase applies to this assumed trend. This trend affects the Global Hawk and Predator families only.

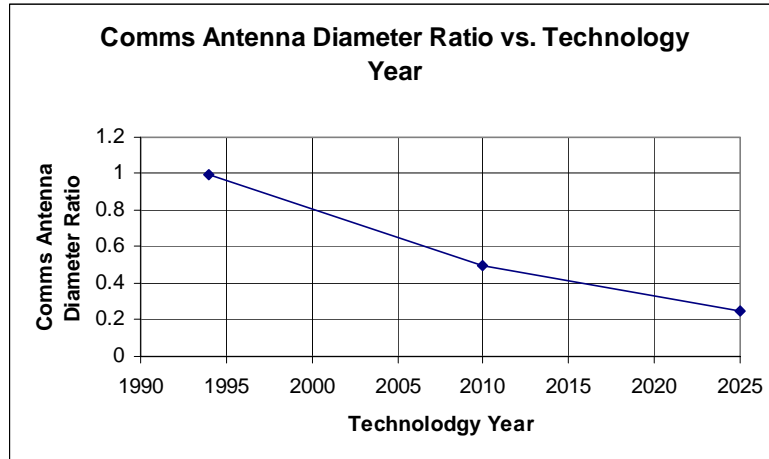


Figure 4-14 Satellite Communications Dish Antenna Diameter Trends

4.3.3 Design

The only technology attribute in the design technology category is weight growth. For convenience, the attributes of this technology are repeated in Table 4-6.

	Substantiation		
	Quality		
	Aggressiveness		
Design			
Weight Growth	4	3	2

Table 4-6 Design Technology Attributes

Weight Growth

The overall vehicle weight growth design technology is assumed to follow the trend presented in Figure 4-15. Nearly every aircraft experiences weight growth in the development process as the aircraft goes from early design to operations. The typical weight growth from project go-ahead to first flight is 7% [SAWE 1996]. The weight growth can be substantially higher than this. The F-111 experienced 17% growth from go-ahead to the end of the first phase research and development, and 23% growth over the first five years after go-ahead [SAWE 1996]. By comparison, the C-5A experienced only 2.9% weight growth from contract award to the delivery date [SAWE 1996]. The assumed lower and upper bounds from 1930 through 1990 from design year to operations are 3% and 20%, respectively. By 2025, the assumed weight growth upper and lower bounds are assumed to change to 1% and 15%, respectively. The technology trend

assumes that the combined impacts of improving integrated mass properties tools and evolving systems engineering practices containing requirements creep will limit the weight growth encountered during development.

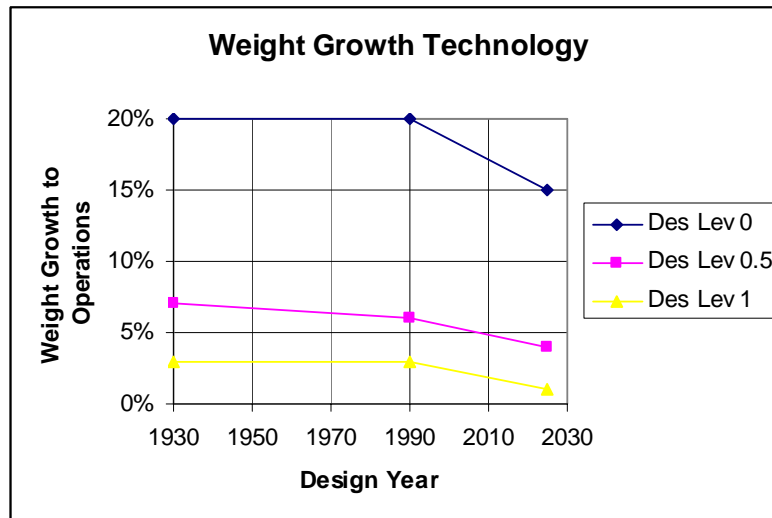


Figure 4-15 Weight Growth Technology

4.3.4 Payloads

Only a small subset of potential payload types is considered for this research. Technology trends for Synthetic Aperture Radar (SAR), Electro-Optical (EO), Long Wave Infrared (LWIR), and Mid-Wave Infrared (MWIR) are incorporated. The source of all payload technology trends is the 2000 DOD UAV Roadmap [OSD 2001].

For convenience, the attributes of these technologies are repeated in Table 4-7.

	Substantiation	Quality	Aggressiveness
<u>Payloads</u>			
SAR Payload	1	1	1
Small EO/IR	2	2	2
Large EO/IR	2	2	3

Table 4-7 Payload Technology Attributes

All payloads are assumed to follow the payload technology phase relationship shown in Figure 4-16. The high technology level phase lag is zero, because it is possible to develop a payload and a UAV concurrently.

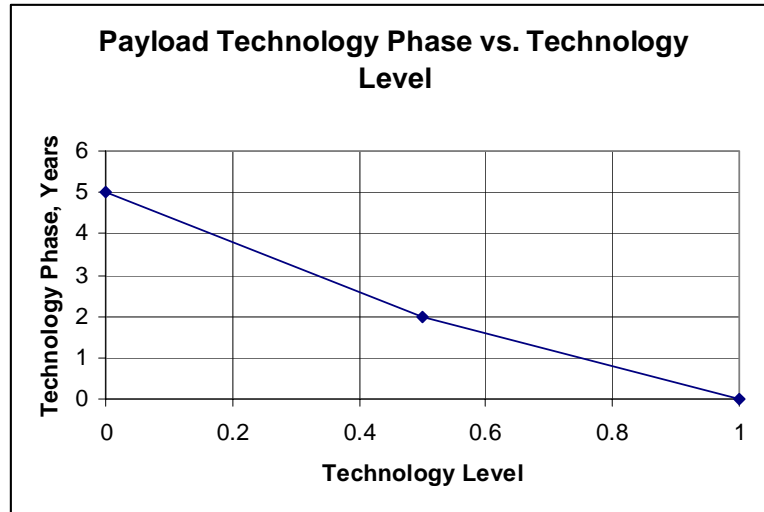


Figure 4-16 Payload Technology Phase

SAR Payloads

The SAR payload technology trends are shown in Figure 4-17. The two trends are the payload relative performance and relative performance to weight. Note that the relative performance to weight improves much faster than the relative performance. The relative performance per weight is used for SAR payload scaling.

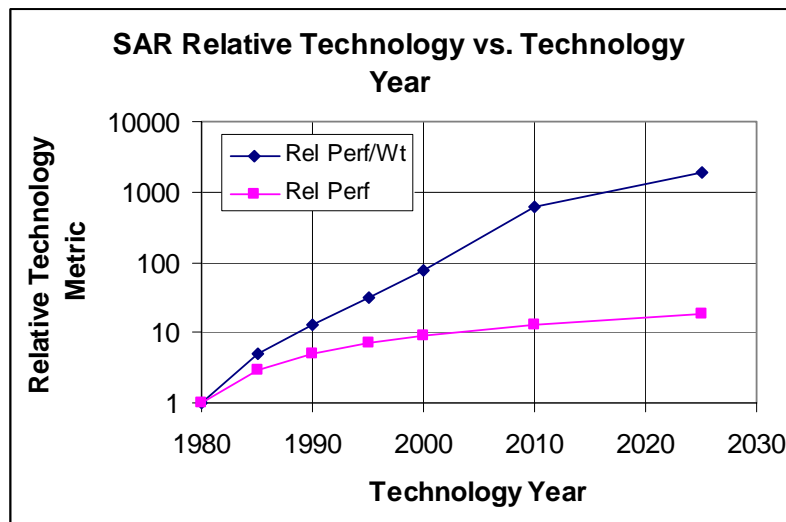


Figure 4-17 SAR Payload Technology Trends

Electro-Optical / Infrared (EO/IR) Payloads



Figure 4-18 EO/IR Payloads

The DOD UAV Roadmap has performance technology trends for large and small Electro-Optical (EO) payloads and large and small Mid-Wave Infrared (MWIR) payloads. The relative performance metric is the ratio of ground resolved distances, a measure of imaging performance, of the initial capability over the new capability. Most EO and Infrared (IR) payloads are combined into single units with an assumed even relative weight and functionality division, so the technology trends were averaged. Two examples of EO/IR balls are shown in Figure 4-18 (A-B). The large EO and large MWIR payload trends were combined for the large EO/IR trend, and the small EO and small MWIR payload trend were combined for the small EO/IR trend. In both cases, the MWIR data was extrapolated to match the first EO technology date. The resulting curves for large and small EO/IR payloads are shown in Figure 4-19 and Figure 4-20, respectively.

The EO/IR payload weight per performance is considered constant. This assumption may be conservative if the EO/IR payload exhibits similar behavior to the SAR.

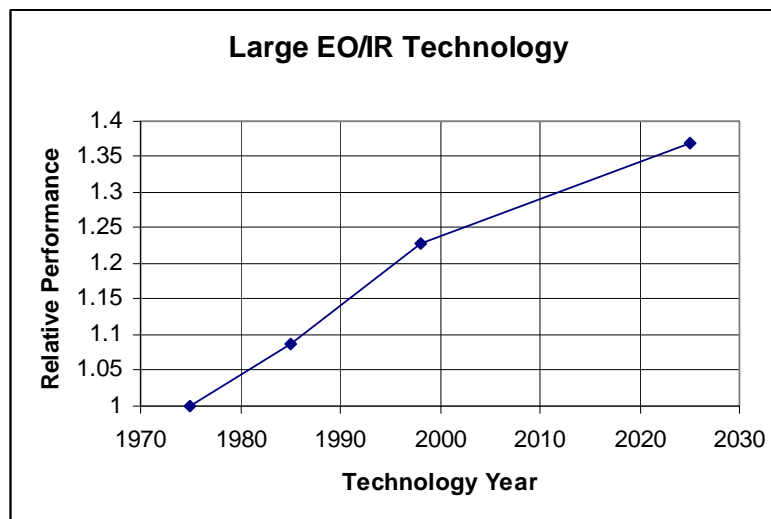


Figure 4-19 Large EO/IR Payload Performance Technology Trend

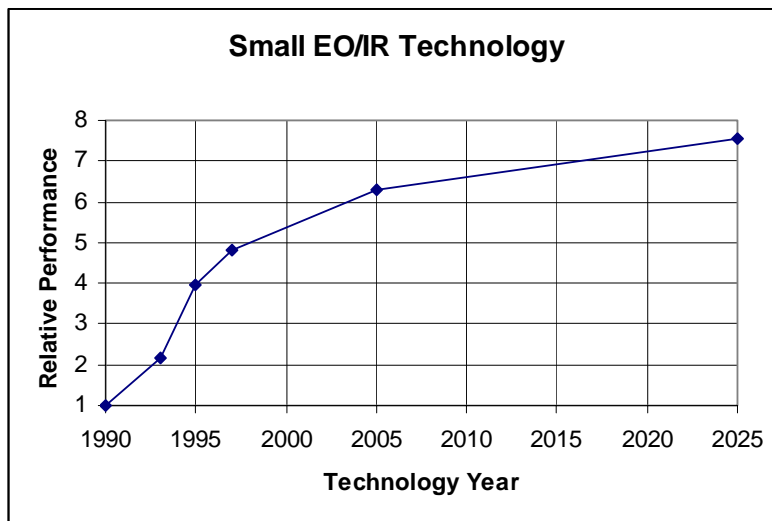


Figure 4-20 Small EO/IR Payload Performance Technology Trend.

4.3.5 Propulsion

The basic propulsion technology trends were derived directly from data provided in the DOD UAV Roadmap [2002]. Both jet engines and internal combustion engine trends are included.

The attributes of these technologies are repeated in Table 4-8.

	Substantiation	Quality	Aggressiveness
Propulsion			
Jet Propulsion	1	2	1
Reciprocating Engines	1	2	1

Table 4-8 Propulsion Technology Attributes

Jet Engines



Figure 4-21 UAV Jet Engine

The HALE family considered here uses jet engines for propulsion, so appropriate technology trends must be applied. An example of a jet engine intended for UAV application is shown in Figure 4-21. The jet engine technology phase and trends are presented in Figure 4-22 and Figure 4-23, respectively. The jet engine technology phase is based on the assumed time from engine technology development to fielding in an aircraft.

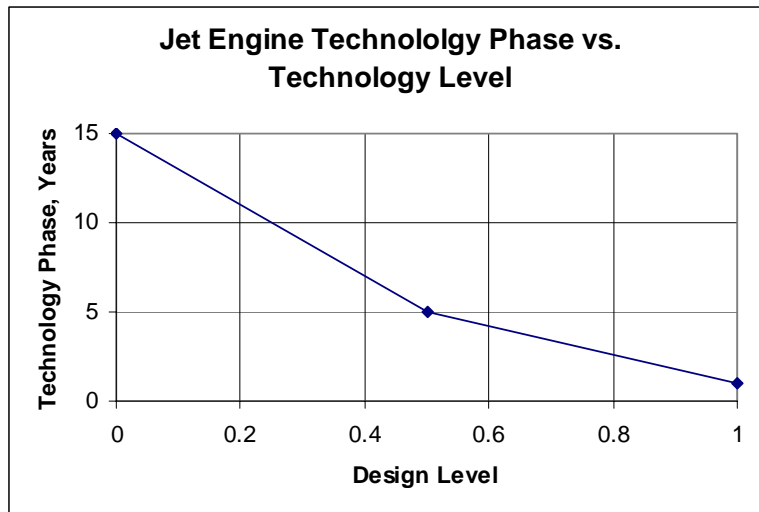


Figure 4-22 Jet Engine Technology Phase

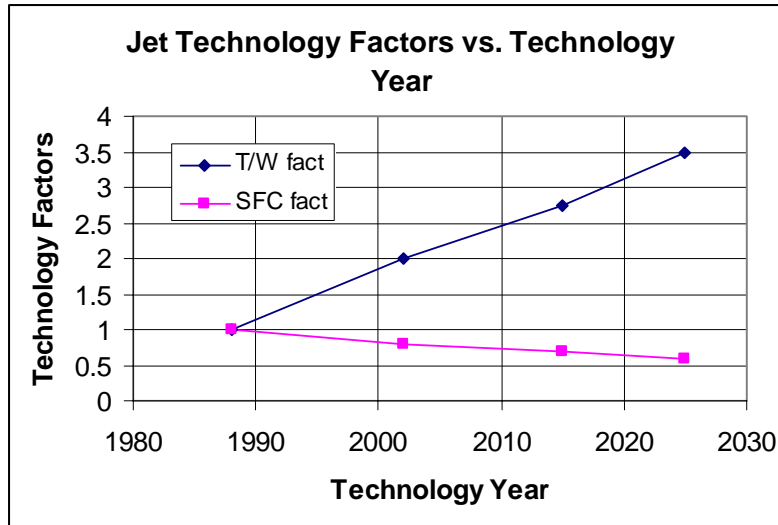


Figure 4-23 Jet Engine Technology Trends

Internal Combustion Engines



Figure 4-24 UAV Internal Combustion Engine

The tactical and MAE UAV classes considered here utilize internal combustion engines. An example of an internal combustion engine intended for UAV applications is shown in Figure 4-24. The internal combustion technology phase and technology trends are presented in Figure 4-25 and Figure 4-26, respectively. The internal combustion engine technology phase is based on the time from development of internal combustion technology and fielding in an aircraft. Note that the lowest technology level phase is 50 years, because many UAV and general aviation engines use internal combustion engines with highly mature technologies.

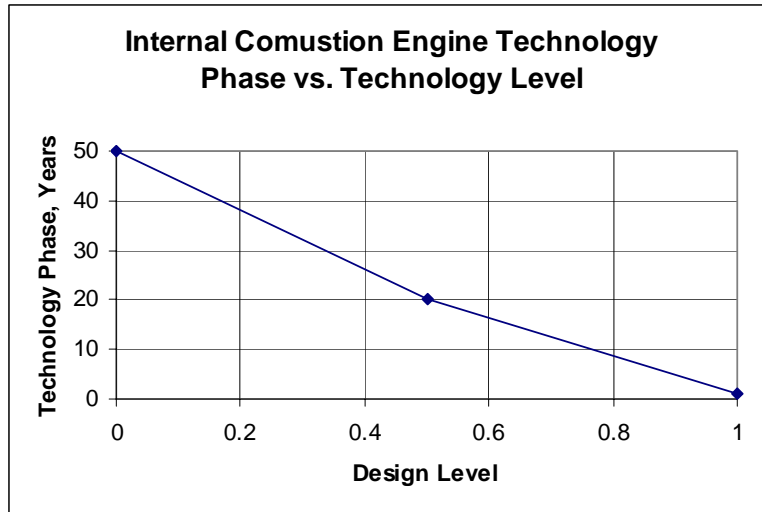


Figure 4-25 Internal Combustion Engine Technology Phase

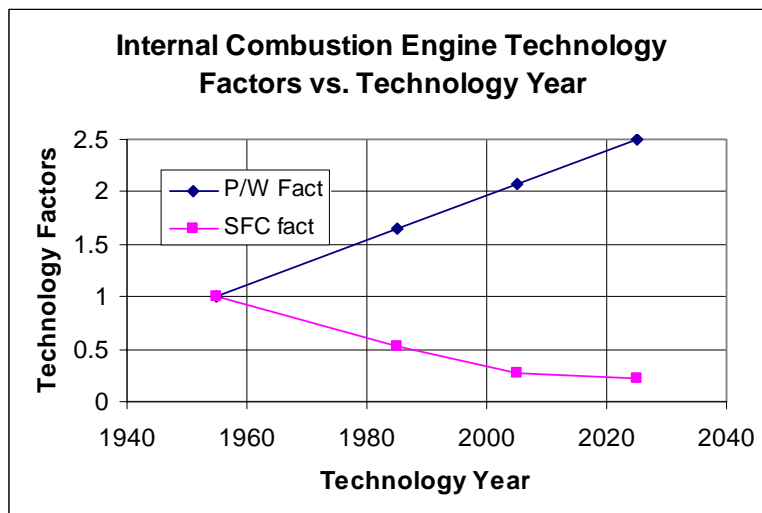


Figure 4-26 Internal Combustion Engine Technology Trends

4.3.6 Structures

Two approaches are used for estimating structures technologies - Factor of Safety (FOS) and direct structural weight reductions. The attributes of these technologies are repeated in Table 4-9.

	Substantiation	Quality	Aggressiveness
Structures			
Structural Factor	2	3	1
Factor of Safety	3	2	2

Table 4-9 Structures Technology Attributes

Factor of Safety

The factor of safety for UAV structures was reduced from 1.5 to 1.25 as late as 1994. This was done to account for the absence of a pilot and the associated safety considerations. A standard UAV minimum factor of safety is assumed to hold constant until 2005. This trend is then assumed to become more aggressive into the future, but for different reasons. By 2025, the factor of safety is assumed to be reduced due to improved structural analysis methods and improved manufacturing quality control. The 2025 factor of safety for high technology UAVs is assumed to be 1.15. Figure 4-27 shows the factor of safety technology trends.

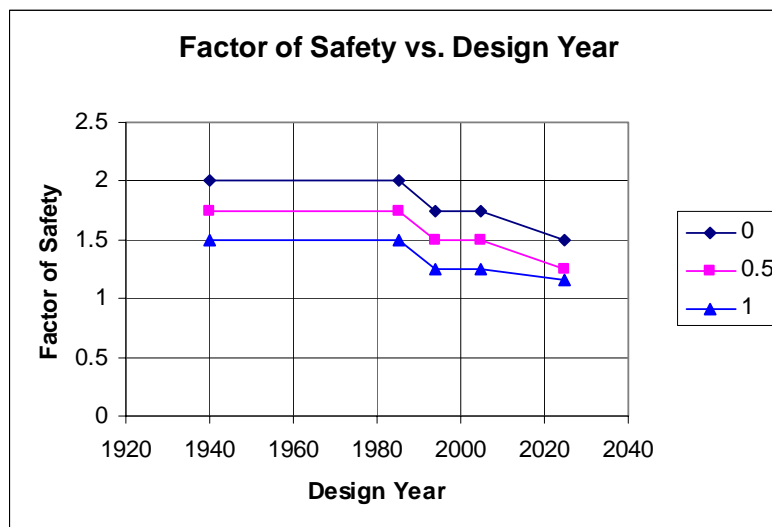


Figure 4-27 Factor of Safety Technology Trends

Structural Weight Factors

The second structural technology factor relates to structural weight directly. Noor [2000] provides relevant results of Defense and Aerospace [1995] study, which predicts aircraft weight reduction due to various technologies from 1995 to 2020. For long range transonic transports, the anticipated total gross weight reduction due to structural

contributions is estimated at 24%. This reduction, however, is not the structural weight reduction, but the total synthesized aircraft weight reduction. The structural contribution is found by a simple mass fraction analysis similar to that performed on the subsystems. A very simple sizing relationship for a given aircraft class is:

$$\frac{W_{TO}}{W_{Payload}} = \frac{1}{1 - MF_{Fuel} - MF_{E,-Struct} - MF_{Struct} \cdot F_{Struct,Tech}}$$

Numbers representative of the Boeing 777 were used as an estimate for the 1995 mass fraction numbers. The fuel mass fraction is assumed to be 0.4. The mass fraction of the empty weight less structure is assumed to be 0.25. The mass fraction of the 1995 structure is assumed to be 0.2, when the structural weight multiplication factor is equal to 1. In order to achieve a 24% reduction in take-off gross weight due to structural contributions, the structural weight multiplication factor must equal 0.765. The 1960 structural weight multiplication factor is assumed to be 1.1, or 10% greater than the 1995 structural weight, since advanced finite element structural design was introduced between these dates. This technology trend is assumed to be applicable to UAVs. The structural weight multiplication factor and factor of safety are applied independently. The structural technology phase and technology multiplication factors are found in Figure 4-28 and Figure 4-29, respectively.

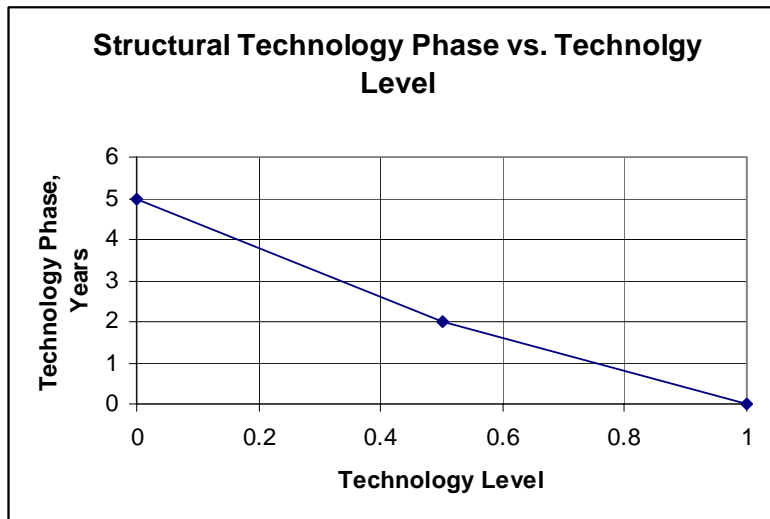


Figure 4-28 Structural Technology Phase

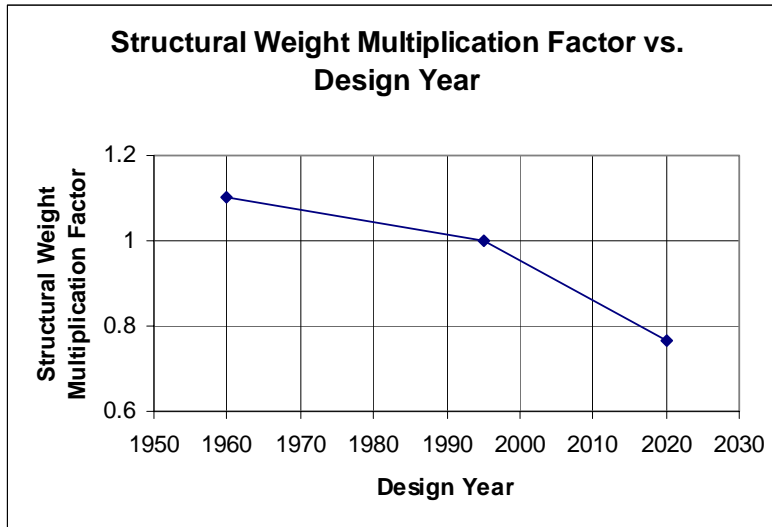


Figure 4-29 Structural Weight Multiplication Factor Technology Trend

Chapter 5 Geometry

5.1 Geometry Overview

Several geometry definitions are required for various analyses within the AV design code. The aerodynamics, structures/weights, and graphical generators all require specialized geometry evaluations. A parametric geometry model is employed to facilitate the optimization process.

5.2 Geometry Definition

The geometry definition is used to define aircraft geometry in detail. The complex geometry definition takes general and specialized forms. The general form will be discussed first. The specialized forms are essentially customized paneling that supports aerodynamics and structures analysis.

5.2.1 Wings and Tails

To streamline the code, the wing, horizontal tail, and vertical tail definitions are combined, since all are aerodynamic surfaces with almost identical geometric properties. The wing geometry equations presented in Appendix A apply to all three surface types unless specified otherwise.

The airfoil coordinates may be input directly from a designated airfoil coordinate file or generated parametrically. The airfoil coordinate files take the form of the UIUC airfoil coordinate database data files to increase utility. The airfoil coordinate file approach is applied only to the graphics file generator, and not the analysis procedures. The parametric airfoil generation uses the NACA 4 and 5 series airfoil equations. The NACA parametric airfoil method is available to all applicable subroutines that require airfoil geometric information.

It is necessary to know the wing span, root chord, area and aspect ratio. However, these parameters are not independent. If any two are known, then the remaining two can be determined through a set of equations. The user selects which two are input. This approach permits the greatest flexibility.

5.2.2 Fuselage

A robust yet simple fuselage geometry formulation is applied. The goal is to minimize the quantity of data needed to describe a wide range of fuselage geometries. The selected method employs conic sections applied across multiple fuselage stations. Conic sections

are extremely useful for metal aircraft, because conic sections describe shapes that 2-dimensional sheets may attain through simple wrapping. A conic curve may be described by three points and a shape parameter. Composite aircraft often have complex curvature that does not require conic sections, yet the flexibility in geometry description still makes conic sections a useful geometry analysis tool.

Each fuselage file data contains geometry descriptions in the following format:

x/L	z/L_m	z/L_t	z/L_b	y/L_s	ρ_t	ρ_b
0.000	0.000	0.000	0.000	0.000	0.414	0.414
0.005	0.000	0.003	-0.003	0.003	0.414	0.414
.....
$x/L_f(j)$	$z/L_{m,f}(j)$	$z/L_{t,f}(j)$	$z/L_{b,f}(j)$	$y/L_f(j)$	$\rho_t(j)$	$\rho_b(j)$

The x-coordinate moves from the nose to the tail, the y-coordinate moves out the right wing, and the z-coordinate is positive in the up-direction. All x, y, and z data are normalized to the fuselage length. Three z-coordinate data points are defined for each x-coordinate. The first is a mid-line, which defines the widest portion of the fuselage for a given section. The second is the upper surface of the fuselage, and the third is the lower surface of the fuselage. The single y-coordinate data point defines the maximum width of the fuselage. The ρ parameters define the fullness of the fuselage cross section such that the surface between adjacent fuselage segments is a conic section. A ρ value of 0 corresponds to a straight line (triangle), 1 is a rectangle, and 0.414 is an ellipse. The ρ is defined separately for the upper and lower surfaces.

Figure 5-1 shows the Predator nose region. The upper conic parameter ρ for the main fuselage is 0.35, and the EO/IR ball has a conic parameter of 0.414. The EO/IR ball is the sphere under the Predator fuselage in Figure 5-1. Note that lines of intersection are not shown in these AutoCADTM grid drawings.

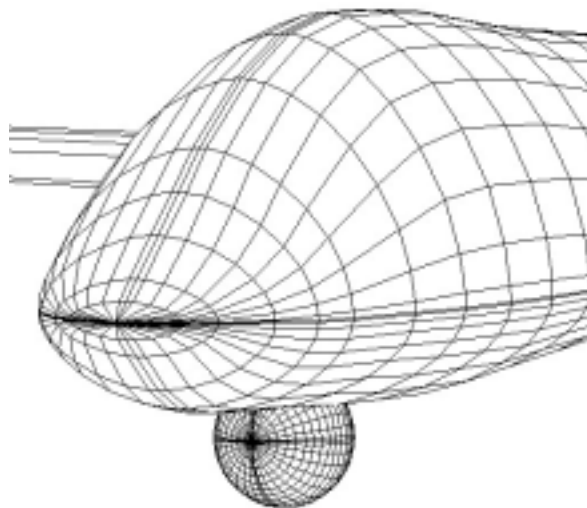


Figure 5-1 Predator Fuselage Nose Region

Figure 5-2 shows the X-45A geometry as represented by this geometry definition. The conic parameter is 0.3 for the entire upper surface.



Figure 5-2 X-45A Geometry

Figure 5-3 shows the Dragon Eye fuselage representation. The selected conic parameter is 0.75 for the center fuselage, giving a boxy appearance.

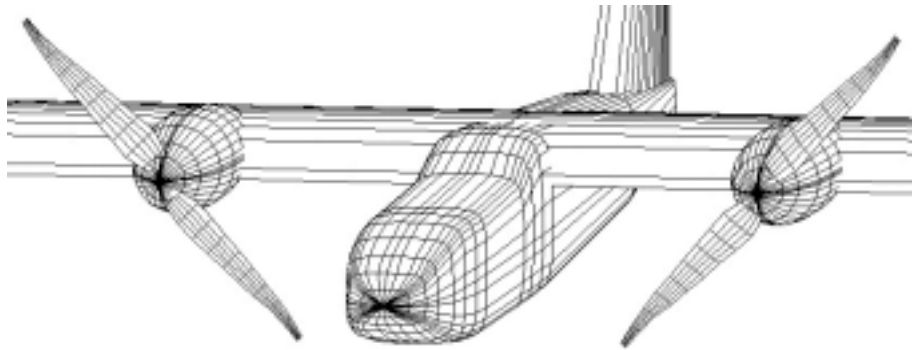


Figure 5-3 Dragon Eye Fuselage Geometry

5.2.3 Propeller

The propeller input is very similar to that of the wing except there are many segments. The first input is the name of the propeller geometry file. The file has the following form:

r/R	c/R	Beta	Sweep	nsweep	ntwist
0.0	0.08	35.	0.	0.25	0.25
0.05	0.08	35.	0.	0.25	0.25
....
$r/R_p(j)$	$c/R_p(j)$	$\beta(j)$	$\Lambda_p(j)$	$x/c_{\Lambda,p}(j)$	$x/c_{\beta,p}(j)$

All dimensions are normalized to the propeller radius. The radial position r/R_p goes from 0 to 1. β is the blade twist angle relative to the rotational plane. $x/c_{\Lambda,p}$ is the reference chordwise location for the blade sweep. $x/c_{\beta,p}$ is the reference chordwise location for the wing blade twist. The propeller chord and twist distribution geometry used for graphics generation and the detailed propeller analysis models are not linked. However, this does

not affect the results because the propeller radius is consistent throughout the code and the detailed propeller design methods are not directly utilized here. The only negative outcome is that the graphical output of the chord and twist distribution do not match.

5.3 Parametric Geometry

The analysis of a known aircraft with a fixed geometry lends itself well to detailed geometry inputs described above. However, optimization requires that geometry components, such as wings, tails and bodies, move together in a sensible manner. For example, the tails and wings should remain attached to the fuselage when so configured. Simply making the wing geometry and fuselage length design variables does not guarantee the resulting optimized geometry solution is reasonable. Geometry sizing laws must be established.

5.3.1 Parametric Fuselage

A parametric fuselage formulation is used for all optimization cases considered. The geometry selected supports both jet and propeller configurations. For the propeller case, the propeller is centered at 96% of the fuselage length. Pusher propellers are applied to the parametric geometry for propeller-driven aircraft, because both the Shadow 200 and Predator use pusher propellers. For jets, the engine nacelle is located on top of the fuselage such that the rear of the nacelle is located at 95% of the main fuselage length, for configuration similarity to the Global Hawk. Figure 5-4 and Figure 5-5 show how propellers and jets are applied to the generic fuselage, respectively.

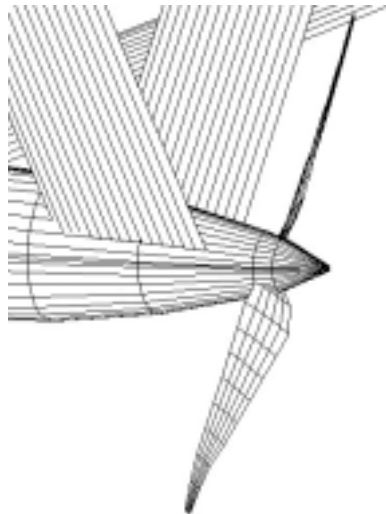


Figure 5-4 Propeller Integration on Generic Fuselage

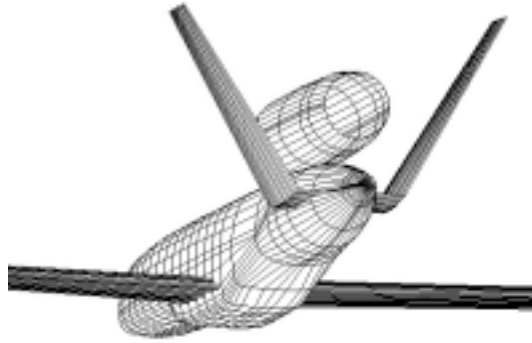


Figure 5-5 Jet Integration on Generic Fuselage

The aerodynamic center of the wing is fixed to 48% of the main fuselage length, regardless of sweep in order to keep a reasonable tail moment arm for tail sizing. 48% appears to be a reasonable number based on visual inspection and from experience with early sizing attempts. The wing root leading edge will shift forward relative to the fuselage as wing sweep increases. The wing root leading edge is always defined as the origin. The wing root leading edge rests at the bottom of the fuselage at the point of intersection.

The parametric fuselage permits blending with other bodies. The most-outside dimension at a given point for two bodies is selected as the final outer geometry for the resultant body. This holds true for upper and lower heights and the width. The maximum conic parameter of the two bodies is applied for same-half upper or lower surfaces.

The wing fairing is one example of fuselage blending. A fairing body with a length twice the wing root chord and centered about the wing is blended with the main fuselage. The resultant blended fairing geometry can be seen in Figure 5-6.

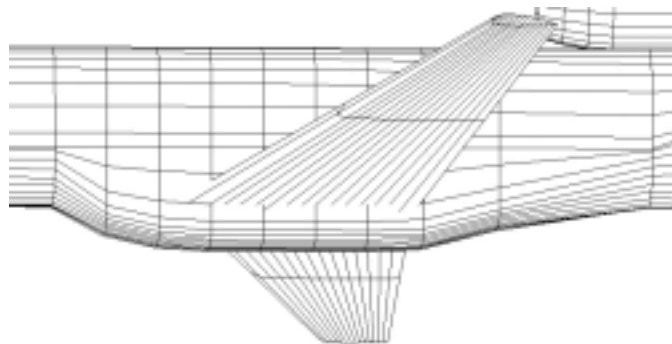


Figure 5-6 Wing Fairing Geometry

Two of the three vehicle classes have radomes to house dish antennas for satellite communications. The proportions of the radome relative to the fuselage vary, and a single fuselage geometry that represents the radome geometry impacts is not possible. A

parametric radome body is applied, which is parametrically linked to the dish diameter. Figure 5-7 shows the radome geometry impact on the fuselage.

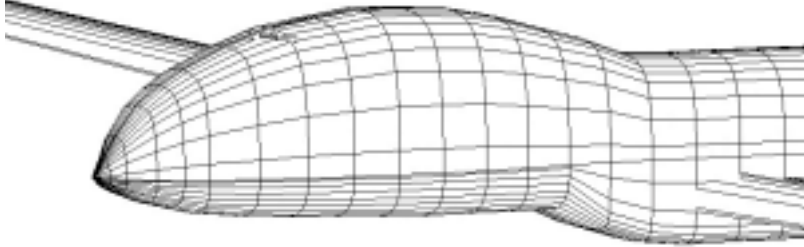


Figure 5-7 Radome Impacts on Fuselage Geometry

If unconstrained, the optimizer tends to minimize the fuselage length such that volume constraints are satisfied. This raises the possibility of creating an infeasible solution for tail sizing, as will be discussed shortly. A fuselage minimum length constraint is necessary. Rather than creating a constraint with a penalty function for the optimizer, the fuselage length is automatically set to the minimum length if the input fuselage length is too low. There are two minimum fuselage length definitions, and the fuselage length must be greater than the greatest of the two. First, the fuselage minimum length is 35% of the wing span. Second, the fuselage length is:

$$L_{fuse} = 4 \cdot \frac{C_{Wing,avg}}{1 - x / L_{AC,Wing}}$$

The first minimum fuselage length protects the fuselage minimum length for high aspect ratio wing cases, and the second minimum protects the fuselage length for low aspect ratio wing cases.

An EO/IR ball is attached to, but not blended with, the main fuselage. The diameter of the ball is found through the EO/IR payload calculations. The ball is fixed at 10% of the fuselage length and approximately 20% of the ball height is submerged in the main fuselage. The relative location of the ball is inspired by the Predator configuration and based on visual inspection. Figure 5-8 shows the EO/IR ball geometry.

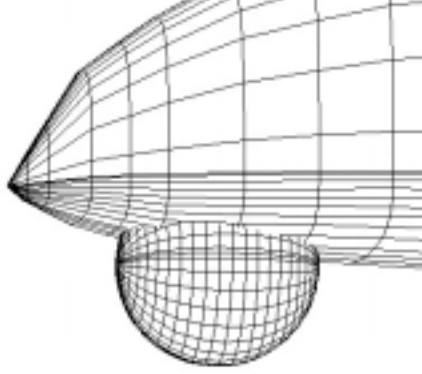


Figure 5-8 EO/IR Ball Geometry

The jet engine nacelle, partially described earlier, is another body that is attached to the main fuselage but not blended. The nacelle length to diameter ratio is assumed to be 1.1 times greater than the jet engine length to diameter ratio. The nacelle length is assumed to be 1.8 times greater than the jet engine length. The nacelle length to diameter and overall length relative to the engine is based on visual inspection of appropriate proportions.

5.3.2 Parametric Tails

The parametric tail geometry uses a tail volume coefficient methodology applied to a V-tail. V-tails are used here, because all three calibration cases use variants this tail configuration. Conventional tails or other alternative tail configurations could also be applied in a similar fashion. A closed form solution to the tail sizing for a fixed tail trailing edge location is not forthcoming, so a convergence approach is used. First, the dihedral angle of the V-tail is found by:

$$\Gamma_{V-Tail} = \tan^{-1} \left(\frac{TVC_V \cdot b_w}{TVC_H \cdot MAC_w} \right)$$

The length between the wing aerodynamic center and the V-tail trailing edge, $L_{AC-VT,TE}$, is found such that the V-tail trailing edge is located at 93% of the fuselage length. The secant method is employed to solve for tail area such that:

$$S_{V-Tail} - TVC_H \cdot \left(\frac{S_w \cdot MAC_w}{(L_{AC-VT,TE} - AC_{Func} \cdot \sqrt{S_{V-Tail}}) \cdot \cos(\Gamma_{V-Tail})} \right) \cdot (\sin(\Gamma_{V-Tail}) + \cos(\Gamma_{V-Tail})) = 0$$

where AC_{Func} is the distance from the V-tail root chord aerodynamic center to the trailing edge normalized by the square root of with V-tail area.

This tail sizing approach permits the tails to automatically scale with the wing and tail moment arm. The tail root vertical height is fixed to the maximum width location on the fuselage at the attachment location, which automatically has vertical separation from the wing. The vertical separation combined with upward-canted V-tails ensures that the lift distribution methods will not have artificial interference leading to singularities.

5.4 Wing Lift Distribution Paneling

Three lift distribution methods are employed: vortex lattice method, lifting line theory, and Trefftz plane analysis. All are described further in the Aerodynamics section. Each of the methods require specific geometric paneling, but sufficient commonality exists for a single geometry definition subroutine to handle all three cases.

There are two primary methods of paneling the wing. The first method panels each segment individually. The second method panels the entire wing by blending segments. Further discussion of these methods can be found in Appendix A.

First, reference parameters are defined. The lifting line theory analyzes wings sequentially rather than simultaneously, so the reference wing area and span is for each individual wing. The reference area for the other methods is the wing area of the main wing. The total average chord for the Trefftz plane analysis is the ratio of the first wing planform area to the first wing's span.

Figure 5-9 and Figure 5-10 show the Virginia Tech Forestry UAV and its wing paneling for lift distribution methods, respectively. The front two faces of the triangles are $xyz1$ and $xyz2$. The rear triangle points are $xyzm$. The first paneling method was used. Note that the panels on the inboard portion of the main wing are evenly spaced and the outboard segment has sinusoidal spacing.



Figure 5-9 Virginia Tech Forestry UAV

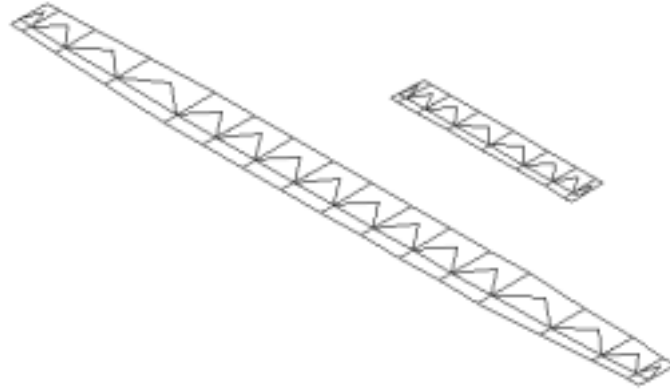


Figure 5-10 Wing Aerodynamic Paneling for Virginia Tech Forestry UAV

5.5 Wing Structures Paneling

The code shares many wing paneling methods for aerodynamics and structures. The wing is broken up into multiple discrete panels. The structural contours for the skins are then determined using the NACA airfoil generator. The wing box for each panel begins after a specified leading edge chord-wise distance and ends at the control surfaces, if any are present. Properties at the root and tip of the panel are calculated, and the average value is used for the panel calculations. The properties under consideration are described below.

The NACA airfoil coordinate generator calculates the 2-D coordinates of the upper and lower surface of the skin. Each skin is composed of straight line segments connecting discretized points on the surface. The coordinate system used here is the same as the aircraft coordinates. The length of each element is found by:

$$L_{elt}(i) = \sqrt{(X_{pt}(i) - X_{pt}(i+1))^2 + (Z_{pt}(i) - Z_{pt}(i+1))^2}$$

The midpoint of each element is found by:

$$X_{mid}(i) = \frac{X_{pt}(i) + X_{pt}(i+1)}{2}$$

$$Z_{mid}(i) = \frac{Z_{pt}(i) + Z_{pt}(i+1)}{2}$$

The angle of the element from the x-axis in the x-z plane is found by:

$$\theta_{elt}(i) = \tan^{-1} \left(\frac{Z_{pt}(i+1) - Z_{pt}(i)}{X_{pt}(i+1) - X_{pt}(i)} \right)$$

The total length of the wing box surface excluding the front and back walls is found by:

$$L_{Surf,tot} = \left(\sum_{i=1}^{nelt} L_{elt}(i) \right)_{Top,Bottom}$$

The centroid calculations neglect wing thickness because the model assumes that the wing skin thickness is uniform. The wing box centroid is found by:

$$X_{cent} = \left(\frac{\sum_{i=1}^{nelt} X_{mid}(i) \cdot L_{elt}(i)}{L_{Surf,tot}} \right)_{Top,Bottom}$$

$$Z_{cent} = \left(\frac{\sum_{i=1}^{nelt} Z_{mid}(i) \cdot L_{elt}(i)}{L_{Surf,tot}} \right)_{Top,Bottom}$$

The X and Z distance from each point is found by:

$$\Delta X_{cent}(i) = X_{cent} - X_{mid}(i)$$

$$\Delta Z_{cent}(i) = Z_{cent} - Z_{mid}(i)$$

The area moments of inertia divided by the skin thickness are found by:

$$I_{XX,t} = \left(\sum_{i=1}^{nelt} \left(\frac{L_{elt}(i)^3}{12} \cdot \sin(\theta_{elt}(i))^2 + L_{elt}(i) \cdot \Delta Z_{cent}(i)^2 \right) \right)_{Top,Bottom}$$

$$I_{ZZ,t} = \left(\sum_{i=1}^{nelt} \left(\frac{L_{elt}(i)^3}{12} \cdot \cos(\theta_{elt}(i))^2 + L_{elt}(i) \cdot \Delta X_{cent}(i)^2 \right) \right)_{Top,Bottom}$$

$$I_{XZ,t} = \left(\sum_{i=1}^{nelt} \left(\frac{L_{elt}(i)^3}{12} \cdot \sin(\theta_{elt}(i)) \cdot \cos(\theta_{elt}(i)) + L_{elt}(i) \cdot \Delta X_{cent}(i) \cdot \Delta Z_{cent}(i) \right) \right)_{Top,Bottom}$$

The shear flow at the centroid divided by thickness considers only the contribution of the wing skins. Shear web contributions are neglected for the purposes of the calculations. The shear flow divided by thickness is found by:

$$q_{Shear,t} = \left(\sum_{i=1}^{nelt} L_{elt}(i) \cdot \Delta Z(i) \right)_{Top}$$

The above calculations were performed on both the root and tip sections of the wing panel. Next, the average panel characteristics must be calculated. The coordinates of the panel centroid are simply the average of the root and tip coordinates. The skin thickness corrected area moments of inertia for the panel is the average of the root and tip values. The skin thickness corrected shear flow is the average of the root and tip values. The total thickness of the panel wing box is the average of the root and tip thicknesses. For the geometry calculations, k is the index for the structural panels. The structural sweep of the panel is found by:

$$\Lambda_{cent}(k) = Tan^{-1} \left(\frac{X_{cent,Tip}(k) - X_{cent,Root}(k)}{Y_{cent,Tip}(k) - Y_{cent,Root}(k)} \right)$$

The centroid dihedral of the panel is found by:

$$\Gamma_{cent}(k) = Tan^{-1} \left(\frac{X_{cent,Tip}(k) - X_{cent,Root}(k)}{Z_{cent,Tip}(k) - Z_{cent,Root}(k)} \right)$$

The structural span of the panel is found by:

$$b_{Struct}(k) = \sqrt{(X_{cent,Tip}(k) - X_{Cent,Root}(k))^2 + (Y_{cent,Tip}(k) - Y_{Cent,Root}(k))^2 + (Z_{cent,Tip}(k) - Z_{Cent,Root}(k))^2}$$

The total surface area of the skins for each panel is found by:

$$S_{Pan}(k) = \frac{(L_{Surf,Tip}(k) + L_{Surf,Root}(k))}{2} \cdot b_{Struct}(k)$$

The results of the structural paneling are shown in Figure 5-11 and Figure 5-12. The shear web is not included.

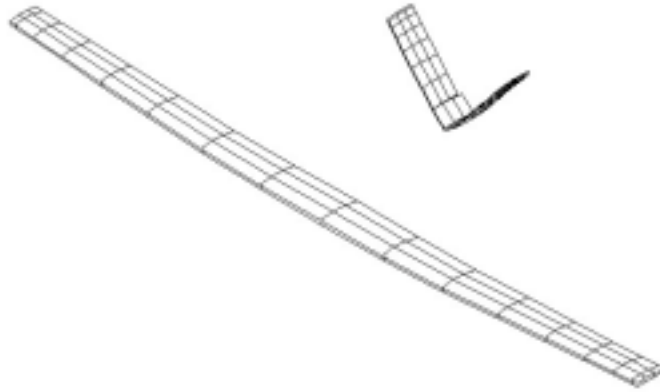


Figure 5-11 Vehicle Structural Paneling Example

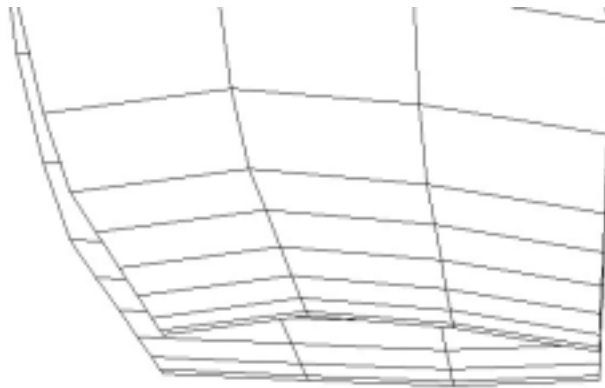


Figure 5-12 Wing Tip Paneling Detail

5.6 Graphics File Generator

The graphics file generator outputs data exchange format (DXF) drawing files that can be accessed by Computer Aided Drawing (CAD) software. The purpose of the graphics file generator is to provide nearly photo-realistic 3-D renderings of the designs. The graphical outputs provide a means of rapidly evaluating the configurations for fundamental flaws. The graphics also provide an effective means of communicating the behavior of the optimization results, where tables and plots become cumbersome. The graphics file generator automatically outputs the geometry of the vehicle of interest.

The graphics file generator has the ability to evaluate a wide variety of configurations. Not all of this functionality is utilized in this research. The graphics generating capabilities are inspired by the work of Libeau [1999]. Figure 5-13 shows one unconventional configuration.



Figure 5-13 Example Unconventional Configuration

The wing, nacelle, and propeller rotation options allow the listed components to be rotated such that the incidence is modified about some point P_{rot} . This is necessary to graphically represent tilt-wing V/STOL configurations as shown in Figure 5-14.

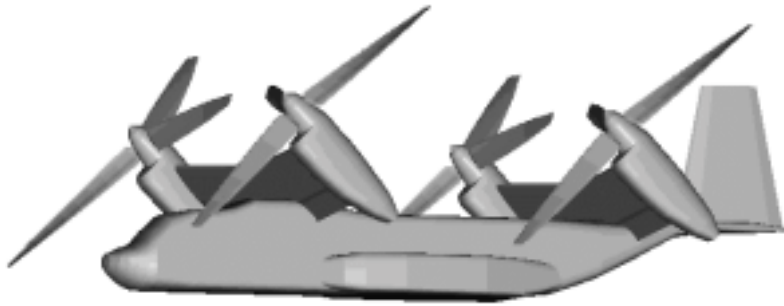


Figure 5-14 Tilt-Wing Graphics Option

The rotation feature and other capabilities facilitate rapid drawings of new concepts. Typically, any new aircraft concept can be graphically represented within 2 hours.

Chapter 6 Aerodynamics

6.1 Aerodynamics Overview

The aerodynamics code models a large variety of aircraft shapes in the subsonic and low transonic flight regimes over a wide Reynolds number range. Both simple and complex methods are employed with varying degrees of accuracy, computational efficiency, and flexibility. The primary product of the aerodynamics code is a drag polar for use in the mission analysis subroutine.

The aerodynamics code utilizes a number of methodologies to evaluate the aerodynamic characteristics of relatively arbitrary vehicles. The various approaches permit different types of questions to be answered, depending on the analysis objectives. The methods also vary in robustness and computational efficiency. All methods must operate in Reynolds numbers ranging from less than 100,000 to very large numbers on the order of 20,000,000 and Mach number between zero and the low transonic region where the drag rise begins.

Early conceptual design work does not require the level of detail necessary in early preliminary design. Early conceptual design focuses on simple sizing, and it does not require exact definition of characteristics such as wing twist, thickness and camber distribution or tail incidence. Early preliminary design generates much more detailed information and, therefore, must model the impacts of detailed inputs. This research focuses on both conceptual and early preliminary design aerodynamics methods.

The problem is decomposed into an incompressible solution with an additive compressible correction. The incompressible solution is assumed to be equivalent to Mach zero at a given Reynolds number, with no compressibility effects on lift or drag. The compressible correction is zero until the critical Mach number is reached, after which the drag rises with Mach number according to the Korn equation [Grasmeyer 1998]. Lift is not corrected for compressibility, which reduces the number of aerodynamics tables that must be generated. There is no consideration for Mach-Reynolds number interactions.

The incompressible drag is composed of induced drag, aerodynamic surface induced drag, profile drag, fuselage drag, interference drag, landing gear drag, and miscellaneous drag. Induced drag contains both traditional drag due to lift and some trim drag. The profile drag is the additive combination of the friction and pressure drag on aerodynamic surfaces such as wings and tails. Interference drag consists of drag at intersections of the wings and bodies, and drag reductions due to reduction of wetted areas at the intersections. Gear drag is calculated in the extended and retracted positions, and consists of the tire, strut, door, and cavity contributions, as appropriate.

The various methodologies book keep drag in different ways. For example, induced drag can also include profile drag due to lift and profile trim drag, where these components are subtracted from the profile drag.

Aerodynamics interacts with propulsion and other systems. Propulsion interactions are captured as drag penalties in the propulsion section. Propulsion effects on lift and pitching moment are neglected. Cooling drag is captured as a drag penalty in the propulsion analysis during mission execution, though these influences will be described in the aerodynamics chapter.

The philosophy adopted for this research is to place the greatest emphasis on the largest contributors to the aerodynamic behavior of interest. The lift methods are quite detailed to provide detailed lift distribution information to determine local stall, usable total lift coefficient, trim requirements, and induced drag. The lifting surface profile drag is another significant drag driver that is given much attention.

The inputs for the aerodynamics code include vehicle geometry and paneling, aerodynamics parameters, flight regime limitations, method selections, drag polar array size parameters, and technology data.

The primary output is a drag polar and an additive compressibility correction array. The drag polar consists of angle of attack and Reynolds number dependent lift and drag arrays and a suitability array. The suitability array determines if the drag array element is usable by considering elevator deflection and local stall constraints. The compressibility correction array consists of a Mach array starting with the critical Mach number, and a drag rise array corresponding with the Mach array. The primary products are shown in Table 6-1.

Product	Description
$C_L(\alpha, Re)$	Total lift coefficient array
$C_D(\alpha, Re)$	Total drag coefficient array
Allow (α, Re)	Permissible data point flag array
$C_{Dw}(\alpha, M)$	Total wave drag coefficient array

Table 6-1 Primary aerodynamics product list.

6.2 Aerodynamics Code Architecture

This section describes the aerodynamics code architecture and its components at a high level. Subsequent sections will discuss the methodologies used in the subroutines in more detail.

Much information is required prior to running the *AEROC* aerodynamics analysis routine. Airfoil data input and considerable geometry definition occurs beforehand. The *MISSPARAM* subroutine estimates the minimum and maximum flight Reynolds number

per unit length based on the flight envelope boundaries. The *CGLOC* subroutine estimates the aerodynamic center based on the geometry and locates the center of gravity based on the aerodynamic center and static margin. Once the inputs are properly conditioned, the *AERO* subroutine is called by *EVAL*.

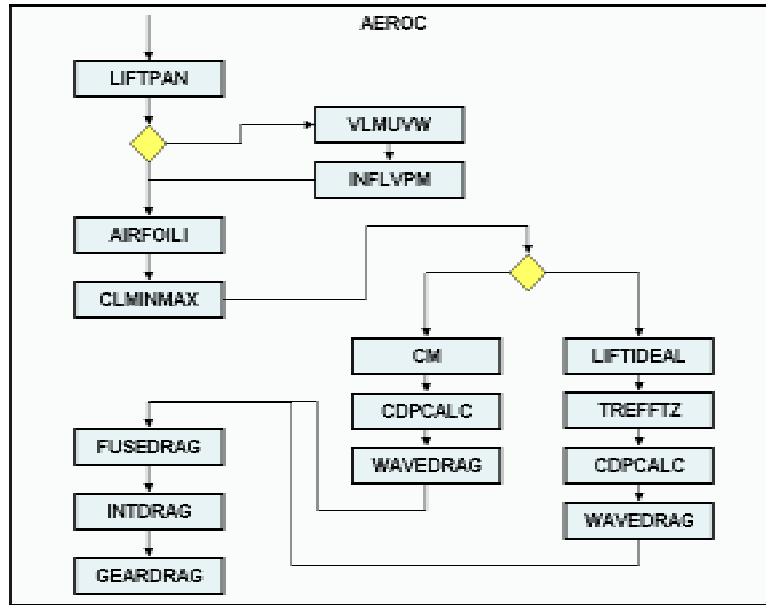


Figure 6-1 AERO code Architecture

Figure 6-1 shows the *AERO* code architecture. The first step is to generate the final paneling used for the lift distribution methods, which was described in the Geometry section. If the vortex lattice method is used, then the velocity influence coefficients are calculated up front with subroutine *VLMUVW* and *INFLVPM*, respectively. The zero lift angle of attack for the panels is determined in subroutine *AIRFOILI*. The positive and negative stall angles of attack for all panels are found in subroutine *CLMINMAX*.

If either the VLM or LLT are selected, then the elevator position to trim the vehicle at a given angle of attack is determined through the secant method by setting the pitching moment about the center of gravity equal to zero. An elevator position and angle of attack, among other inputs, are sent to subroutine *CM*, which then outputs the pitching moment about the center of gravity. If the Trefftz plane analysis is selected, then the lift coefficient is input, and the lift distribution, induced drag, and angle of attack are output.

Once trimmed, the profile drag for each panel is calculated by one of three methods in *CDPCALC*. The wave drag is calculated for a given lift distribution and Mach number in *WAVEDRAG*. The fuselage drag is calculated in subroutine *FUSEDRAG*. The interference drag is calculated in subroutine *INTDRAG*. The retracted and extended landing gear drag contributions are calculated in subroutine *GEARDRAG*.

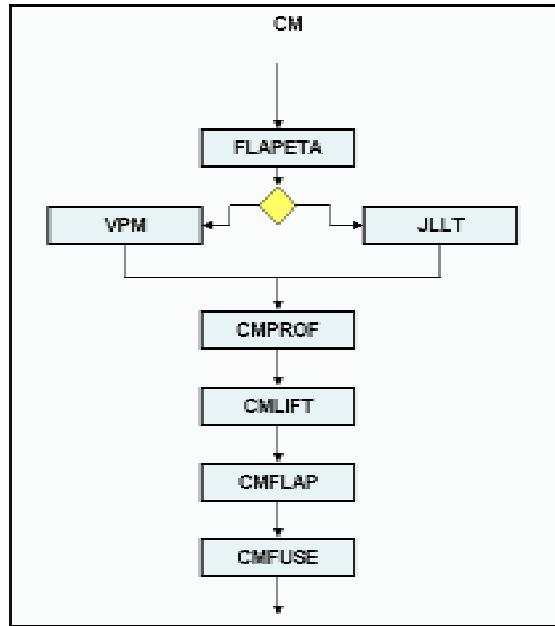


Figure 6-2 Pitching Moment Subroutine Architecture

Figure 6-2 shows the architecture of the pitching moment subroutine, *CM*. First, flap efficiency parameters are calculated in subroutine, *FLAPETA*. Then, either the LLT or VLM subroutines are called to determine the lift distribution as a function of angle of attack and elevator deflection. The airfoil 2-D pitching moment subroutine, *CMPROF*, is called. The pitching moment caused by the lift moment arm about the center of gravity is calculated in subroutine *CMLIFT*. The pitching moment due to flap deflections is determined in subroutine *CMFLAP*. Finally, the fuselage pitching moment is calculated in subroutine *CMFUSE*. These pitching moments are used to help determine how to trim the aircraft, as described in the lift methodology section of this chapter.

6.3 Lift Methodology

6.3.1 Lift Methodology Overview

The lift distribution of a configuration must be determined to evaluate the total lift coefficient, C_L , at which local stall first occurs and induced drag. The lift distribution information is also necessary for determination of profile drag and loads for structural analysis.

6.3.2 CG Location Determination

The center of gravity location must be known in order to estimate the trimmed lift distribution. The key inputs to the center of gravity location are the vehicle geometry and the static margin.

The geometry definition subroutines calculate the X-coordinates of the aerodynamic center of all lifting surfaces, wing mean aerodynamic chord, and tail volume coefficients. The origin of this coordinate system is the front of the main wing root chord, and X is positive moving towards the rear of the aircraft.

The end equation for the X-coordinate of the center of gravity is:

$$X_{CG} = X_{NP} - sm \cdot \bar{c}$$

where the neutral point for the aircraft is defined as:

$$X_{NP} = X_{AC, wing} + (h_n - 0.25) \cdot \bar{c}$$

The wing aerodynamic center is found through standard multi-segmented trapezoidal wing methods. The aircraft neutral point is found using standard methods found in Etkin [1996] and other stability and control texts. The derivative of the fuselage pitching moment with respect to angle of attack is found using methods described in Nelson [1989]. The fuselage is broken into a number of horizontal strips perpendicular to the X-axis.

6.3.3 Lift Distribution Methods

Three lift distribution methods are employed in this code: Prandtl lifting line theory (LLT), vortex lattice method (VLM), and a Trefftz plane analysis. The first two methods take a detailed geometry definition, including camber effects (α_{0L} shift and elevator deflections) and washout. The elevator deflections are adjusted at a given angle of attack to trim the vehicle. The Trefftz plane analysis calculates the minimum induced drag trimmed lift distribution for a given planform geometry without determining how the distribution was generated. The Trefftz plane analysis was applied to generate all results for this research, as shown in Table 6-2.

Method	Applied Here
1. Prandtl Lifting Line Theory	No
2. Vortex Lattice Method	No
3. Trefftz Plane Analysis	Yes

Table 6-2 Lift Distribution Methods

6.3.3.1 Prandtl Lifting Line Theory

The wing lift distribution is determined by using Prandtl's line theory as presented in Davenport [1998]. This method allows varied chord, camber and twist distributions along the span. The method provided in Bertin and Smith [1989] describes only a single taper ratio directly. In the method used, sweep and dihedral cannot be accounted for and it is assumed that the wing is tapered about the quarter chord. The matrix formula takes the form:

$$\frac{\pi c}{4s}(\alpha + \alpha_{twist} - \alpha_{0L})\sin \theta = \sum_{n=1, odd}^{\infty} A_n \sin(n\theta) \left[\frac{\pi \cdot c \cdot n}{4s} + \sin \theta \right]$$

where

$$\theta = \cos^{-1}(-y/s)$$

y is divided up into N segments between 0 and $\pi/2$ radians, and n assumes odd integer values from 1 to $2N-1$. Note that in effect the integer $2N-1$ replaces y in the above equation. The chord at the given y , c , is found through linear interpolation across the semispan.

The following matrix formula is solved:

$$[A(i, j)][x(i)] = [b(i)]$$

where

$$n = 2 \cdot j - 1$$

$$A(i, j) = \sin(n \cdot \theta(i)) \cdot \left(\frac{\pi \cdot c(i) \cdot n}{2 \cdot b_w} + \sin(\theta(i)) \right)$$

$$b(i) = \frac{\pi \cdot c(i)}{2 \cdot b_w} \cdot (\alpha + \alpha_{twist}(i) - \alpha_{0L}(i)) \cdot \sin(\theta(i))$$

The coefficients $x(i)$ are determined by the matrix operation:

$$[x(i)] = [A(i, j)]^{-1} [b(i)]$$

The total lift coefficient for the wing is:

$$C_L = AR \cdot \pi \cdot x(1)$$

and the induced drag is

$$C_{Di} = \frac{C_L^2}{\pi \cdot AR \cdot e}$$

where

$$e = \frac{1}{1 + \sum_{n=3, odd}^{2N-1} n \cdot (x(n) / x(l))^2}$$

The section lift coefficients at v are:

$$C_l(i) = \frac{8 \cdot s}{c} \cdot \sum_{n=1, odd}^{2N-1} x(n) \cdot \sin(\theta(i))$$

The tip lift coefficient is always zero, so $v = 0$ is not included in the A matrix.

The LLT can only analyze a single wing at a time, so downstream downwash effects on tails can not be evaluated directly. The tail is modeled as a new wing without an upstream wing, which creates inaccuracies. The downstream surface is always more affected by the upstream surface than vice versa, because the upstream wing has trailing vortices. A wing downwash model that creates a new tail effective local angle of attack distribution would improve the tail lift predictions, though this is not explored further here. Because trailing vortices from upstream wings are not considered, there is no possibility for tail calculations to fail due to singularities induced by the other surfaces. The inherent limitations of the LLT are that the tail effectiveness is over-predicted, and the tail contribution to induced drag is under-predicted. Although a selectable option in the code, the LLT method was not used to generate the results for this research.

6.3.3.2 Vortex Lattice Method

The vortex lattice method (VLM) offers the ability to evaluate more complex configurations than the LLT. Sweep and dihedral can now be modeled. Configurations with multiple surfaces can be analyzed simultaneously.

The 2-D and 3-D vortex lattice methods of Bertin and Smith [1989] are used directly in the code. As in the example provided in Bertin and Smith [1989], only one panel per chord length is used. The 3-D formulation determines the streamwise, spanwise and vertical velocities (u_m , v_m , and w_m) induced by the circulation by ensuring that there is no flow passing through each control point m . This can be shown by:

$$-u_m \cdot \sin(\delta) \cdot \cos(\phi) - v_m \cdot \cos(\delta) \cdot \sin(\phi) + w_m \cdot \cos(\phi) \cdot \cos(\delta) = -U_\infty \cdot \sin(\alpha - \delta) \cdot \cos(\phi)$$

The angle of the control point at zero angle of attack, δ , is replaced by the zero lift angle of attack minus local incidence, $\alpha_{0L} - \alpha_{twist}$, because the airfoil geometry is not known for many cases. This yields some inaccuracies, but a direct relationship between δ and α_{0L} cannot be established for both conventional and reflexed airfoils. Also, δ and α_{0L} are intuitively interchangeable on the right hand side of the matrix equation, since a change of δ in the term $(\alpha - \delta)$ should have the same effect on local lift as a change in $\alpha_{0L} - \alpha_{twist}$.

The right hand side of the equation was modified further to account for the fact that the angle of attack has less direct influence on the lift of an airfoil as the local dihedral approaches vertical. Additionally, U_∞ is not necessary to determine the lift coefficient distribution, so all velocities are normalized by U_∞ . Using the matrix form:

$$[A(i, j)][x(i)] = [b(i)],$$

the right hand side of the equation is modified to:

$$b(i) = -\sin(a \cdot \cos(\phi(i) + \alpha_{twist}(i) - \alpha_{0L}(i)))$$

The $x(i)$ coefficients are determined by the matrix operation:

$$[x(i)] = [A(i, j)]^{-1} [b(i)]$$

The 3-D code is likely to yield unrealistic results if the trailing vortex from an upstream panel approaches a downstream panel control point, so it is important to ensure sufficient vertical separation between tandem aerodynamic surfaces. The user must control this through inspection for arbitrary configurations. The parametric geometry model used for optimization automatically ensures that these singularities do not occur. This is accomplished through surface vertical separation.

The elements of the 2-D and 3-D $A(i, j)$ matrix are presented in Bertin and Smith [1989], and they will not be reproduced here. The matrix represents the influence of the bound and trailing vortices of all panels on all control points.

The 2-D formulation neglects dihedral effects and vertical separation of panels. By eliminating a dimension, the problem is greatly simplified and computation time is shortened. The 2-D formulation increases the risk of panel interference. The 2-D equation becomes:

$$w_m \cdot \cos(\delta) = -U_\infty \cdot \sin(\alpha - \delta)$$

As with the 3-D case, the velocities are made non-dimensional by U_∞ and δ is replaced by $\alpha_{0L} - \alpha_{twist}$.

The local lift coefficient is found by:

$$C_l(i) = \frac{2 \cdot x(i)}{c(i)}$$

The total vehicle lift coefficient is found by:

$$C_L = \sum_{i=1}^N \frac{2 \cdot C_l(i) \cdot c(i) \cdot \Delta y(i) \cdot \cos(\phi(i))}{S_w}$$

where the factor 2 accounts for Δy being summed over only one semispan by assuming symmetry in the lift distribution.

The induced drag is found by evaluating the downwash in the Trefftz plane and then relating it back to the downwash at the wing surface. This is similar to the approach taken in the Trefftz plane analysis, which is described later. The Trefftz plane can be thought of as the conditions associated with the ideal flow at a location infinitely downstream of the lifting surfaces. The downwash on the bound vortex is half that of the associated downwash infinitely downstream. The induced downwash influence coefficient matrix $A_i(i,j)$ is determined for a position 100 main span lengths downstream of the origin. The equivalent non-dimensional velocity in the Trefftz plane is determined by the matrix $b(i)$.

$$[A_i(i, j)][x(i)] = [b(i)]$$

Note that the $A_i(i,j)$ matrix inverse does not need to be evaluated in this operation, since $x(i)$ for this system was previously determined.

The downwash angle, ε , is found by:

$$\varepsilon(i) = \tan^{-1} \left(\sum_{j=1}^N \frac{A_i(i, j) \cdot b(j)}{2} \right)$$

The local induced drag, $C_{di}(i)$, is found by:

$$C_{di}(i) = C_l(i) \cdot \varepsilon(i)$$

The total induced drag is found by:

$$C_{Di} = \sum_{i=1}^N \frac{2 \cdot C_{di}(i) \cdot c(i) \cdot \Delta y(i)}{S_w}$$

As before, the factor of 2 represents symmetry.

The VLM analysis is available to the user, but it was not used to generate the results for the research.

6.3.3.3 Trefftz Plane Analysis

The Trefftz plane analysis offers the advantage of automatically determining the optimal trimmed lift distribution for minimum induced drag at a given C_L . Unlike LLT and VLM, no iterations of elevator deflections are necessary. There are, however, several disadvantages. First, the method does not determine how this optimal lift distribution is attained or if it is even possible to achieve. Second, the twist and camber distribution (if it were determined) for one lift condition may not provide the optimal lift distribution at a second condition. In other words, the method is optimistic by assuming that a single vehicle can generate optimal lift distributions at more than one lifting condition without variable geometry. Third, no angle of attack information is provided to or generated by this method directly.

Despite its limitations, the Trefftz plane analysis is ideal for quickly analyzing and assessing the optimized results of a lifting system with little definition. This makes the Trefftz plane approach ideal for conceptual design. Methods like LLT and VLM become more beneficial when further vehicle definition becomes available.

Grasmeyer [1998] discusses the details of this method in detail. Grasmeyer's general methodology is employed here. The Trefftz plane analysis is used to generate all results of this research.

6.3.4 Pitching Moment

Both the LLT and VLM provide lift distributions and induced drag estimations for a given configuration at a given angle of attack and elevator deflection. However, there is no guarantee that the configuration is trimmed at the given condition. The trimmed flight condition must be known for performance estimation. The primary purpose of the aerodynamics model is to determine the trimmed drag polar for use in the fuel burn calculations in the performance model.

The trimmed condition occurs only when the summation of the pitching moments about the vehicle center of gravity is equal to zero. The pitching moment contributors are the lifting moments, airfoil zero-lift pitching moments, flap pitching moments, and pitching moments due to fuselages and nacelles. Note that the empennage lifting moments for a conventional configuration, or elevator-affected lift distribution on a flying wing, counteract all other contributions to attain the trimmed condition. The means of determining the trim requirements are handled by the lift distribution methods.

$$C_M = C_{M,CL} + C_{M,0L} + C_{M,Flap} + C_{M,Fuse,Nac}$$

The pitching moment due to lift for each panel is determined by:

$$C_{M,CL} = \sum_{i=1}^N 2 \cdot C_L(i) \cdot \frac{c(i) \cdot \Delta y(i)}{S_w} \cdot \frac{x_{CG} - x_{c/4}(i)}{mac_w} \cdot \cos(\phi(i))$$

The zero-lift pitching moment of the airfoil sections is determined by:

$$C_{M,0L} = \sum_{i=1}^N 2 \cdot C_{M,0L}(i) \cdot \frac{c(i) \cdot \Delta y(i)}{S_w} \cdot \cos(\phi(i))$$

The flap pitching moment is estimated by a series of empirical equations developed from data of several flap types found in McCormick [1995]. The flap/elevator pitching moment increment is estimated by:

$$\frac{\partial C_{M,flap}}{\partial C_L}(i) = -0.259 + 0.40 \cdot \left(\frac{c_{flap}}{c}(i) \right) - 0.141 \cdot \left(\frac{c_{flap}}{c}(i) \right)^2$$

The flap/elevator 2-D lift increment due to deflection is:

$$\Delta C_{l,flap}(i) = 2 \cdot \pi \cdot \delta_f(i) \cdot \eta_f \cdot \tau(i)$$

where η_f is found through interpolation of data found in McCormick [1995], and τ is determined by an empirical equation from the same source.

The profile pitching moment contribution due to flap deflection is:

$$C_{M,flap} = \sum_{i=1}^N 2 \cdot \frac{\partial C_{M,flap}}{\partial C_l}(i) \cdot \Delta C_{l,flap}(i) \cdot \frac{c(i) \cdot \Delta y(i)}{S_w} \cdot \cos(\phi(i))$$

The pitching moment due to fuselages and nacelles is determined by methods found in Nelson [1989]. Note that fuselage and nacelle pitching moment contribution methods are treated identically in this code, so the typical fuselage and nacelle subscript is covered by the fuselage subscript alone. The pitching moment is:

$$C_{M,fuse} = \sum_{Fuselages} \left(C_{M0,fuse} + \frac{\partial C_{M,fuse}}{\partial \alpha} \cdot \alpha \right)$$

The derivative of the fuselage pitching moment with respect to angle of attack was discussed previously. The reference line used to determine fuselage angle of attack is the zero-incidence fuselage reference. The zero-lift fuselage pitching moment estimation approach is the element method used by Nelson [1989]. Due to the order in which the aerodynamics subroutines are called, the aircraft zero lift angle of attack is unknown when this fuselage pitching moment contributor is invoked, so the zero lift angle of attack is assumed to be zero.

For a given angle of attack, the only means of trimming the vehicle is through flap/elevator deflections. Though deflections create profile pitching moments directly, their greatest contribution comes from redistributing the lift on the surfaces. This creates a pitching moment due to lift. The elevator deflection that creates a zero pitching moment about the CG is found via the secant method. If the required elevator deflection falls outside the permissible bounds, the solution is infeasible, and an error flag is set to indicate the condition. Similarly, if the local C_l is greater than $C_{l,max}$, an error flag is set to indicate the local stall condition. No post-stall evaluations are performed, so the maximum lift coefficient occurs when the first wing panel is stalled.

The Trefftz plane analysis requires a pitching moment input prior to calculating the trimmed lift distribution. The zero-lift profile pitching moment and fuselage pitching moment coefficients are input into the method, and the trimmed lift distribution solution ensures that the total pitching moment about the center of gravity is zero. No flap pitching moments are included.

6.4 Drag Methodology

6.4.1 Drag Methodology Overview

A traditional conceptual design wing drag polar equation takes the following parabolic form:

$$C_D = C_{D0} + \frac{C_L^2}{\pi \cdot AR \cdot e}$$

where

$$C_{D0} = \frac{1}{S_{ref}} \sum C_{d0seg} \cdot FF_{seg} \cdot Q_{seg} \cdot S_{seg}$$

Recall that FF_{seg} is the shape form factor, Q_{seg} is the interference factor, and S_{seg} is the wetted area of the body or aerodynamic surface of interest.

Note that wave drag contributions are not under consideration for the purposes of this discussion. This formulation requires that all lift-dependent drag sources are included in the second term on the right hand side of the first equation. The span efficiency factor, e , is usually considered to be independent of lift, but it may vary with geometry. C_{D0} accounts for the profile drag, which is usually held constant at the average Reynolds number. C_{D0} is also considered to be independent of lift.

The above formulation works reasonably well for aircraft with all-turbulent or fixed transition boundary layers, but it is not suitable for many practical applications. A more suitable model is as follows:

$$C_D = C_{Dprof} + \frac{C_L^2}{\pi \cdot AR \cdot e}$$

where

$$C_{Dprof} = \frac{1}{S_{ref}} \sum C_{d,prof,seg} \cdot Q_{seg} \cdot S_{seg}$$

and

$$C_{d,prof} = C_{d,frict} + C_{d,press}$$

The profile drag is readily obtainable from airfoil wind tunnel test results.

6.4.2 Profile Drag Overview

The profile drag is composed of both friction and pressure drag contributions. Significant attention is given to profile drag, because it is a major drag contributor, especially at low Reynolds numbers. Using a realistic profile drag will yield an aircraft drag polar that generally does not have a parabolic form at all Reynolds numbers. The upper and lower transition locations are a strong function of lift coefficient and Reynolds number. The transition location strongly affects the friction drag. The pressure drag coefficient is also a function of lift coefficient and Reynolds number.

Initially, an Excel spreadsheet was developed to help formulate a series of parametric drag polar functions. The desired equation would take the following form:

$$C_d = C_{d0}(Re, t/c) + \Delta C_{d0} + a \cdot (C_l - C_{l,min drag})^2 + b \cdot (C_l - C_{l,min drag})^n$$

where equations for ΔC_{d0} , a , b , and n are found from regression analysis and may be dependent upon Reynolds number, camber and thickness. This equation worked well for high Reynolds numbers ($Re > 3,000,000$). At low Reynolds numbers ($Re < 300,000$), the drag polar behavior becomes erratic and no suitable formulation could be derived. At very low Reynolds numbers ($Re < 100,000$), no simple formulation with acceptable accuracy is possible for most airfoils.

Figure 6-3 shows data for the NACA 0009 airfoil at very low, low and high Reynolds numbers. Note that the parabolic features of the drag polar become much more pronounced as the Reynolds number decreases. Finally, at a Reynolds number of 60,000, the parabolic nature collapses. The NACA 0009 is a very predictable airfoil compared to most that were investigated. The data is based on Abbot and Von Doenhoff [1959] and the UIUC low Reynolds number wind tunnel tests [Selig 1995].

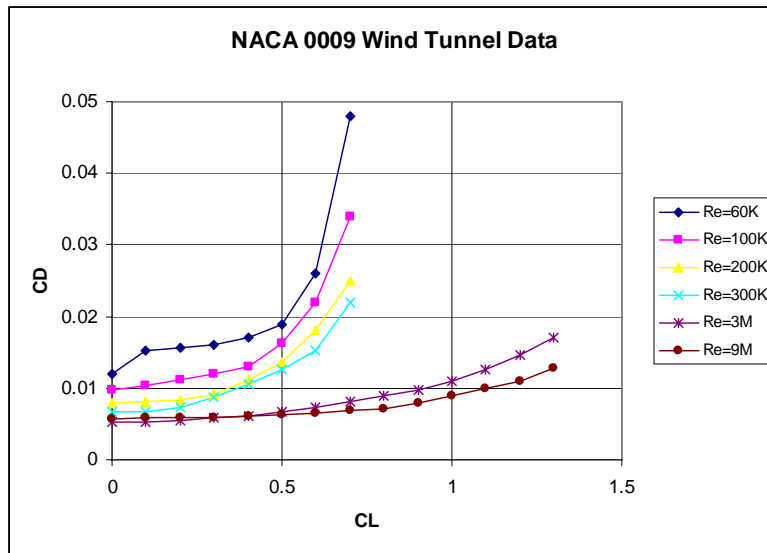


Figure 6-3 NACA 0009 at Several Reynolds Numbers

Figure 6-4 is more representative of most airfoils in the lower Reynolds number range. This airfoil, the Selig-Donovan 7032, is relatively predictable at Reynolds numbers above 200,000. The shape of the drag polar at lower Reynolds numbers differs greatly between airfoils. The data is based on the UIUC low Reynolds number wind tunnel tests [Selig 1995].

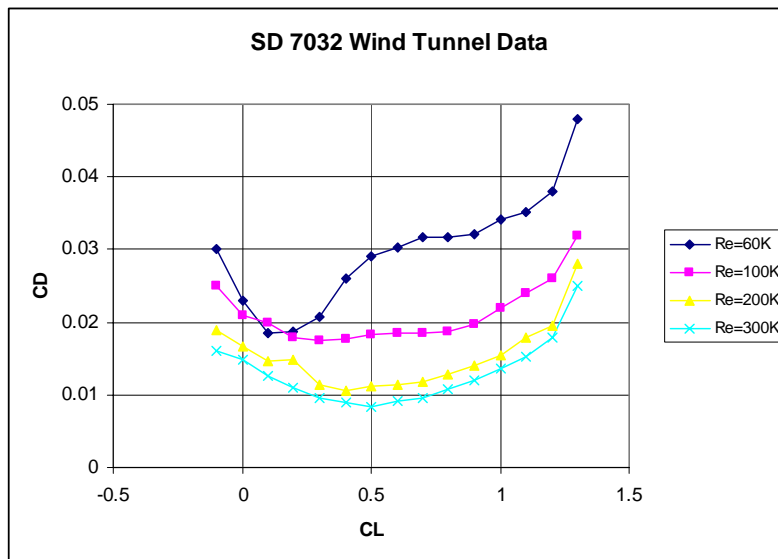


Figure 6-4. Selig Donovan SD7032 at Low Reynolds Numbers

After expending considerable effort pursuing a parametric function, it became clear that a different approach was necessary. The subroutine must work for all Reynolds numbers

encountered by several classes of UAV. Sacrificing fidelity at small UAV Reynolds numbers is not acceptable.

Three methods of determining the profile drag were developed for this research, as shown in Table 6-3. The direct airfoil data method interpolates from databases of airfoil data. The parametric airfoil method applies parametric relationships for the pressure drag and friction drag of several airfoils. Finally, the simplified airfoil method uses simple relationships to relate profile drag to equivalent flat plate skin friction drag. The airfoil interpolation and extrapolation methods can be applied to the direct airfoil data method and the parametric airfoil method.

Profile Drag Method	Applied Here
1. Direct Airfoil Data Method	No
2. Parametric Airfoil Method	Yes
3. Simplified Airfoil Method	No

Table 6-3 Profile Drag Methods

6.4.2.1 Airfoil Interpolation

Unfortunately, aerodynamic data is not always available for an airfoil with the desired thickness, camber and pitching moment. A method was developed to determine the drag polar characteristics for an arbitrary airfoil given data from a variety of other airfoils. Ideally, characteristics of the arbitrary airfoil should be bounded by those of the reference airfoils. The data is interpolated for a fixed Reynolds number and incompressible flow. Compressibility effects are described separately. Figure 6-5 shows a graphical representation of the problem.

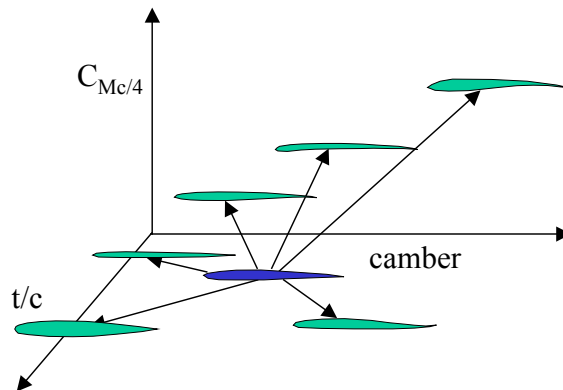


Figure 6-5 Airfoil 3-D Interpolation Space

Traditional multi-dimensional interpolation would require all but one of the independent parameters to remain constant while the dependent variable is found for the non-constant independent parameter. Assume that, for a given Reynolds number and lift coefficient, the drag coefficient must be determined for an airfoil of a certain thickness, camber and

pitching moment. The last three characteristics are independent parameters, and their values for the target airfoil must be bounded by the reference airfoils surrounding it. An interpolation in one parameter requires two reference data points. Using regular parameter increments, a two-parameter interpolation would require four data points. Assuming regular parameter increments, the number of required reference airfoils is 2^n , where n is the number of independent variables. Thus, there must be exactly eight reference airfoils for three independent parameters if regular parameter increments are assumed.

The volume of airfoil data required to perform such an interpolation for all Reynolds numbers of interest would be difficult to obtain within the scope of this research. The goal of the methodology applied here is to find a way of interpolating between relatively few reference airfoils.

First, a reference 'radius' is determined between the characteristics of the target airfoil and those of the reference airfoils. For the above example, the airfoil characteristics are transformed into weighted lengths as follows:

$$\begin{aligned} x_i &= t / c_{fact} \cdot \frac{(t / c_{target} - t / c_{ref,i})}{t / c_{max}} \\ y_i &= camb_{fact} \cdot \frac{(camb_{target} - camb_{ref,i})}{camb_{max}} \\ z_i &= C_{m,fact} \cdot \frac{(C_{m,target} - C_{m,ref,i})}{C_{m,max}} \end{aligned}$$

These lengths are then converted into equivalent radii:

$$r_i = \sqrt{x_i^2 + y_i^2 + z_i^2}$$

The algorithm takes a series of sequential weighted factors and penalties based on the equivalent radii and the number of preceding cases. If the radius between a reference and target airfoil is zero, then the two airfoils are identical. The factor for this reference airfoil is equal to 1 and all others are zero. Assume that there are four airfoils, and the target airfoil is equidistant from all, then the factor for all four is 0.25. The sum of the factors is always equal to unity.

For a given airfoil drag polar, the drag coefficient for that airfoil is found by interpolating first by lift coefficient (for two bounding Reynolds numbers) to get two drag coefficients. These two drag values are then interpolated between the two bounding Reynolds numbers.

The zero-lift angle of attack, maximum lift coefficient and drag coefficient for each airfoil are found via the airfoil look-up function. The target airfoil maximum lift coefficient is the sum of the products of the factors and reference airfoil maximum lift

coefficients. The look-up lift coefficient is scaled from each reference/target airfoil maximum lift coefficient ratio. The target airfoil drag coefficient at a given lift coefficient is the sum of the products of the factors and reference airfoil drag coefficients. Figure 6-6 shows the interpolation plane. For this case, the factor for polar 1 and 2 is about 0.25 and 0.75, respectively. This procedure may be performed for any number of reference airfoils greater than 1.

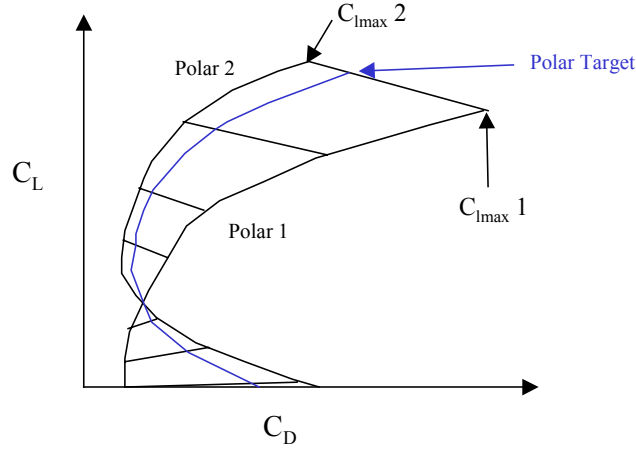


Figure 6-6 Drag Polar Interpolation Diagram for Two Airfoils

The procedure for determining the interpolation factors is relatively straightforward. First, the initial weighting factors for airfoils 1 and 2 relative to one another are assessed:

$$fact_{beg}(1) = 1 - \frac{r(1)}{r(1) + r(2)}, \quad fact_{beg}(2) = 1 - \frac{r(2)}{r(1) + r(2)}$$

Next, the initial weighting factors and initial penalties for the remaining airfoils are assessed:

$$fact_{beg}(i) = 1 - \frac{(i-1) \cdot r(i)}{(i-1) \cdot r(i) + r_{eq}(i-1)}$$

$$pen_{beg}(i-1) = 1 - \frac{r_{eq}(i-1)}{(i-1) \cdot r(i) + r_{eq}(i-1)}$$

Where $r_{eq}(i)$ is the smallest equivalent radius up to reference airfoil i . Next, the factor penalty is assessed:

$$factpen(i) = \prod_{j=2}^i pen_{beg}(j)$$

Finally, the factor for each airfoil is:

$$fact(i) = fact_{pen}(i) \cdot fact_{beg}(i)$$

The summation of all the factors always equals unity.

The airfoil database has a small population of airfoils. These airfoils span the range of thickness, camber and pitching moment. Much of this data comes from UIUC low-speed wind tunnel test databases [Selig 1989 & 1995]. Other data is obtained from offline X-Foil [Drela 2000] airfoil design and analysis software outputs, which is described later. The current approach is to use data for airfoils designed to operate at a given Reynolds number rather than use a single airfoil over the entire Reynolds number range.

6.4.2.2 Airfoil Extrapolation

The airfoil interpolation subroutines focus on positive lift coefficients below stall. However, most airfoils considered have a substantial non-stalled lifting region at negative lift coefficients for which no data is available. It has been determined from analysis of wind tunnel data that the negative stall occurs at an angle of attack equal in magnitude and opposite in sign to that of the positive stall. This effect is independent of camber, which merely shifts the lift curve up and down but does not impact the stall angles.

The parametric airfoil interpolation subroutine permits lift and drag extrapolation at negative lift coefficients without modification. The predicted transition locations and pressure drag terms exhibit no undesirable behavior under extrapolated conditions. The stall angle of attack is assumed to be symmetric about the $\alpha=0^\circ$ axis.

The direct-data airfoil interpolation subroutine presents more challenges than the parametric case. Again, the stall angle is assumed to be symmetrical. Assuming that the behavior of the lift curve is symmetrical as well, with the change in slope opposite in sign on either side of the axis, the maximum negative lift coefficient is:

$$C_{l\max,neg} = 2 \cdot C_l(\alpha = 0^\circ) - C_{l\max}$$

and the pre-stall extrapolated lift coefficient is:

$$C_l = C_l(\alpha = \alpha_{\min dat}) - [C_l(\alpha = -\alpha) - C_l(\alpha = -\alpha_{\min dat})]$$

where $\alpha_{\min dat}$ is less than 0° and may correspond to a positive lift coefficient.

The drag bucket is not assumed to be symmetric about the $\alpha=0^\circ$ axis, but the minimum drag coefficient is assumed to lie near $\alpha=0^\circ$. This assumption is quite suitable in practice. The extrapolation formula is as follows:

$$C_d = C_d(\alpha = \alpha_{\min dat}) + [C_d(\alpha = -\alpha) - C_d(\alpha = -\alpha_{\min dat})]$$

The lift and drag airfoil data behavior as functions of angle of attack are shown in Figure 6-7 (A-B), respectively.

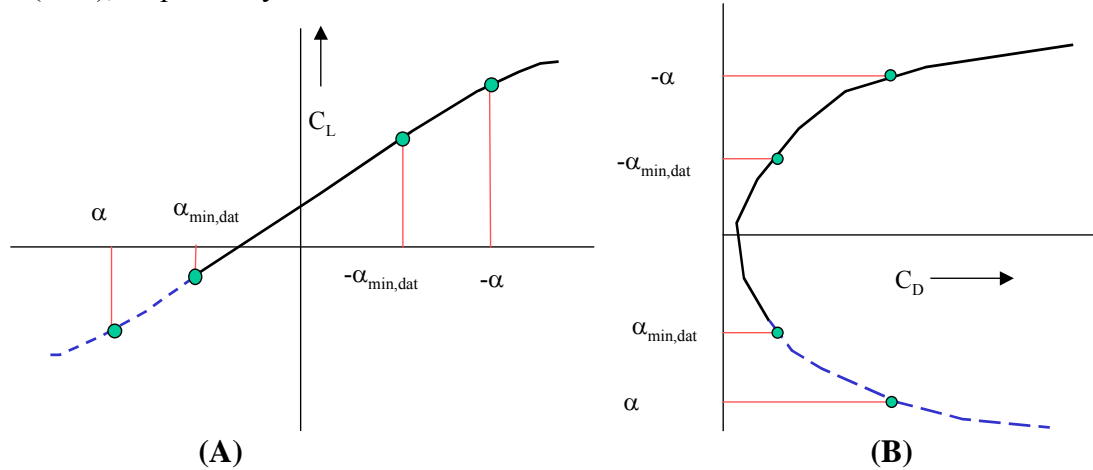


Figure 6-7 Angle of Attack Symmetry Diagram

A report by Sheldahl and Klimas [1981] provides the lift, drag, and pitching moment data of symmetric airfoil sections through $0 \leq \alpha \leq 180^\circ$ at low Reynolds numbers. By symmetry, the results can be applied to a full 360° angle of attack range. Only lift and drag are considered here.

The numerical data was downloaded and analyzed. It was found that the post-stall behavior may be modeled as modified trigonometric functions. Unlike the pre-stall angles of attack, the post-stall lift and drag are functions of angle of attack alone, and are insensitive to Reynolds number and thickness. A regression analysis was used to help determine a curve-fit to the post-stall data. The results are shown in Figure 6-8 (A-B).

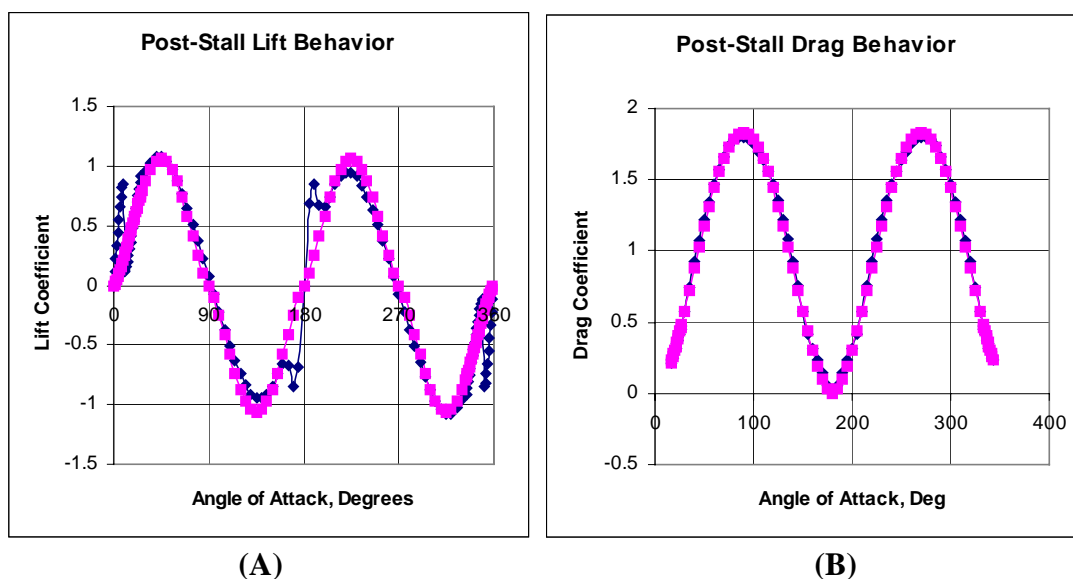


Figure 6-8 Curve Fit for 360-Degree Angle of Attack Sweep

The drag coefficient is:

$$C_d = 1.8332 \cdot (\sin(\alpha))^{1.6729}$$

If $\sin(2\alpha)$ is greater than or equal to 0, then the lift coefficient is:

$$C_l = 1.0617 \cdot (\sin(2 \cdot \alpha))^{1.3548}$$

Otherwise

$$C_l = -1.0617 \cdot (\sin(2 \cdot \alpha))^{1.3548}$$

After the onset of stall, the lift coefficients decrease and the drag coefficients increase relative to their pre-stall values. To have the airfoil prediction code jump from the pre- to post-stall values without any blending would create a discontinuity that may prove troublesome for some design problems. It is therefore desirable to create some smoothing function in a transition region. A sinusoidal function was selected for a transition region of 5° angle of attack. The transition function for the upper stall is as follows:

$$C_l = C_{l,stall} + (C_l(\alpha = \alpha_{stall} + 5^\circ) - C_{l,stall}) \cdot \frac{1 + \sin\left(\frac{\alpha - \alpha_{stall}}{5^\circ} \cdot \pi - \frac{\pi}{2}\right)}{2}$$

The lower stall function takes the same form. It is recognized that some airfoils have an abrupt stall and that a transition function may not be the best representation for those cases. However, the flexibility afforded by this methodology is considered ample justification for any modeling inaccuracies of a phenomenon that is inherently rife with uncertainty. The post-stall data covers only symmetrical airfoils, and the effects of camber are not known at this time.

The drag transition function takes the same form as the lift transition function.

The post-stall subroutine is applied to both the direct-data and parametric airfoil interpolation subroutines. Results for the direct-data interpolation subroutine are presented in Figure 6-9 (A-B). Note that the drag is on a logarithmic scale.

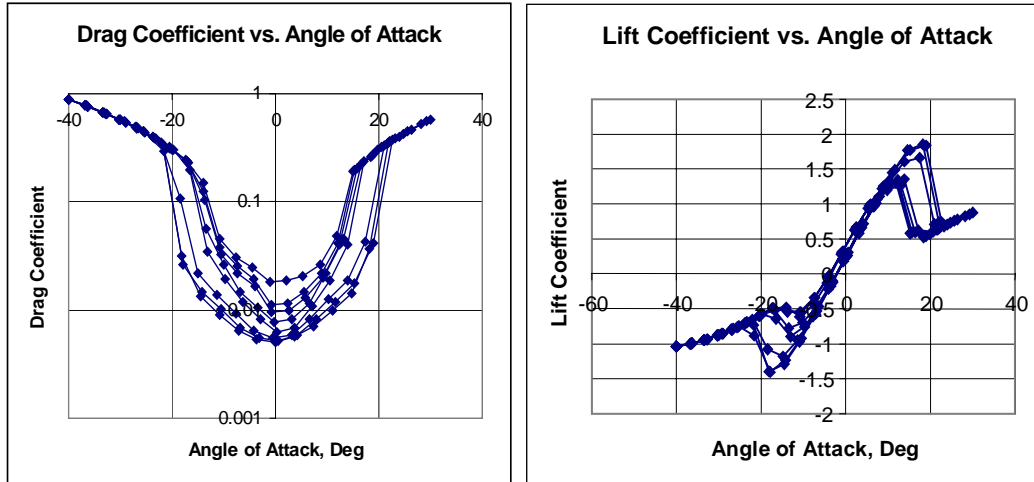


Figure 6-9 Example Drag polar and Lift Curve of an Airfoil Through a Large Angle of Attack Sweep

6.4.2.3 Direct Airfoil Data Method

The direct airfoil data method interpolates airfoil lift and drag data taken from an airfoil database. The database contains airfoils designed for a specific Reynolds number. In other words, the airfoil set changes with reference Reynolds number. The current airfoil database contents are listed in Table 6-4 and Table 6-5.

Reynolds Number	Airfoil	t/c (%)	Camber (%)	C_{m0}	Source
100,000	S1223	11.93	8.67	-0.290	XFOIL
	SD8020	10.10	0.00	0.000	Selig
	S823	21.00	2.49	-0.150	Selig
	SD7032	9.95	3.66	-0.099	Selig
	MH46	11.35	2.85	0.0100	XFOIL
200,000	MH64	8.61	1.91	-0.005	XFOIL
	S1223	11.93	8.67	-0.290	XFOIL
	SD8020	10.10	0.00	0.000	Selig
	S823	21.00	2.49	-0.150	Selig
	SD7032	9.95	3.66	-0.099	Selig
	MH46	11.35	2.85	0.0100	XFOIL

	MH64	8.61	1.91	-0.005	XFOIL
300,000	S1223	11.93	8.67	-0.290	XFOIL
	SD8020	10.10	0.00	0.000	Selig
	S823	21.00	2.49	-0.150	Selig
	SD7032	9.95	3.66	-0.099	Selig
	MH46	11.35	2.85	0.0100	XFOIL
	MH64	8.61	1.91	-0.005	XFOIL
500,000	S823	21.00	2.49	-0.150	Selig
	MH46	11.35	2.85	0.010	XFOIL
	MH64	8.61	1.91	-0.005	XFOIL
	MH78	14.4	2.6	0.050	XFOIL
	MH20	9.02	2.1	0.010	XFOIL
	NACA 2412	12.00	2.	-0.0575	XFOIL
	NACA 4412	12.00	4.	-0.1065	XFOIL

Table 6-4 Low Reynolds number airfoil database.

Reynolds Number	Airfoil	t/c (%)	Camber (%)	C_{m0}	Source
1,000,000	MH46	11.35	2.85	0.010	XFOIL
	MH64	8.61	1.91	-0.005	XFOIL
	MH78	14.4	2.6	0.050	XFOIL
	MH20	9.02	2.1	0.010	XFOIL
	NACA 0012	12.00	0.00	0.00	XFOIL
	NACA 2412	12.00	2.	-0.0575	XFOIL
	NACA 4412	12.00	4.	-0.1065	XFOIL
3,000,000	NACA 0012	12.00	0.00	0.00	XFOIL
	NACA 2412	12.00	2.	-0.0575	XFOIL
	NACA 4412	12.00	4.	-0.1065	XFOIL
9,000,000	NACA 0012	12.00	0.00	0.00	XFOIL
	NACA 2412	12.00	2.	-0.0575	XFOIL
	NACA 4412	12.00	4.	-0.1065	XFOIL
20,000,000	NACA 0012	12.00	0.00	0.00	XFOIL
	NACA 2412	12.00	2.	-0.0575	XFOIL
	NACA 4412	12.00	4.	-0.1065	XFOIL

Table 6-5 High Reynolds number airfoil database.

The accuracy of the direct airfoil data interpolation is only as good as the number and type of airfoils in the database. Some of the provided airfoils represent different technologies, such as standard versus natural laminar flow airfoils. The variety of airfoils is important to ensure that the target airfoil is bound within the parameter space. The direct data airfoil method was not used to generate the results of this research.

6.4.2.4 Parametric Airfoil Method

The parametric airfoil method uses empirical equations to generate smooth and adaptable airfoil lift, angle of attack, and drag data. This method divides the drag into skin friction and profile drag components, which facilitates the application of technology corrections to each component. All equations are based upon XFOIL [Drela 2000] outputs over a Reynolds number range of 60,000 to 20,000,000. Equations were generated for airfoils of symmetrical, single camber, and reflexed camber sections.

This method differs from the direct airfoil data interpolation in another regard. The first method uses the data for airfoils that may be designed for the Reynolds numbers of interest. The empirical equation method models the behavior of a given airfoil over a very wide range of Reynolds numbers. Since airfoils are designed for a relatively small Reynolds range, most of the Reynolds numbers in the second method are not at the design condition. Despite this limitation, the empirical equations are very useful for describing the behavior of airfoils as a function of Reynolds number. The list of airfoils for which empirical equations are written is provided in Table 6-6.

Airfoil	t/c (%)	Camber (%)	C _{m0}
SD7032	9.95	3.66	-0.099
MH18	11.14	3.25	-0.015
NACA 0012	12.00	0.00	0.000
NACA 2412	12.00	2.00	-0.0525
NACA 4412	12.00	4.00	-0.103

Table 6-6 Empirical equation airfoil database.

Quite unexpectedly, a simple set of equations having a similar form can be used to model the behavior of a wide range of airfoil parameters for many airfoil sections. For a given airfoil, first level equations are functions of Reynolds number only. Second level equations are functions of the first level equations and the lift coefficient.

The second level equations are as follows:

$$x / c_{tr,top} = x / c_{tr,top,max} \cdot \left[\cos \left(\frac{c_l - c_{l1,top}}{c_{l2,top} - c_{l1,top}} \cdot \frac{\pi}{2} \right) \right]^{n_{tr,top}} \quad \text{Upper surface transition location}$$

$$x / c_{tr,bot} = x / c_{tr,bot,max} \cdot \left[\sin \left(\frac{c_l - c_{l1,bot}}{c_{l2,bot} - c_{l1,bot}} \cdot \frac{\pi}{2} \right) \right]^{n_{tr,bot}} \quad \text{Lower surface transition location}$$

$$c_{dp} = c_{dp0} + \Delta c_{dp2} \cdot (c_l - c_{l,min d})^2 + \Delta c_{dp6} \cdot (c_l - c_{l,min d})^6 + c_{db} \quad \text{Pressure drag}$$

where

$$c_{db} = c_{db0} \cdot \frac{\left[1 + \sin \left(\frac{c_l - c_{lb1}}{c_{lb2} - c_{lb1}} \cdot 2 \cdot \pi - \frac{\pi}{2} \right) \right]}{2} \quad \text{Laminar separation bubble drag}$$

The factors and exponents given symbols on the right hand side of the second level equations are functions of only Reynolds number for a given airfoil. The factors and exponents described by first level equations are determined through an optimization routine in Microsoft Excel, where the difference between airfoil data and the calculated data is minimized up to stall. The forms of the first and second level equations were selected from visual inspection of the behavior of the data.

The first level equations for the upper surface transition are as follows:

$$\begin{aligned}
x/c_{tr,top,max} &= x/c_{tr,top,max,0} + \Delta x/c_{tr,top,max} \cdot \left[\sin\left(\frac{Re}{Re_{ref}} \cdot \frac{\pi}{2}\right) \right]^{n_{x/c_{tr,top,max}}} \\
c_{l1,top} &= c_{l1,top,0} + \Delta c_{l1,top} \cdot \left[\sin\left(\frac{Re}{Re_{ref}} \cdot \frac{\pi}{2}\right) \right]^{n_{cl1,top}} \\
c_{l,max} &= c_{l,max,0} + \Delta c_{l,max} \cdot \left[\sin\left(\frac{Re}{Re_{ref}} \cdot \frac{\pi}{2}\right) \right]^{n_{c_{l,max}}} \\
c_{l,max,r2} &= c_{l,max,r2,0} + \Delta c_{l,max,r2} \cdot \left[\sin\left(\frac{Re}{Re_{ref}} \cdot \frac{\pi}{2}\right) \right]^{n_{c_{l,max,r2}}} \\
c_{l2,bot} &= c_{l,max,r2} \cdot c_{l,max} \\
n_{tr,top} &= n_{tr,top,0} + \Delta n_{tr,top} \cdot \left[\sin\left(\frac{Re}{Re_{ref}} \cdot \frac{\pi}{2}\right) \right]^{n_{n_{tr,top}}}
\end{aligned}$$

Excluding the maximum lift coefficient, which is evaluated in a separate optimization, the optimization of the second level upper surface transition location formulation involves twelve independent variables.

The first level equations for the lower surface transition are as follows:

$$\begin{aligned}
x/c_{tr,bot,max} &= 1.0 \\
c_{l1,bot} &= c_{l1,bot,0} + \Delta c_{l1,bot} \cdot \left[\sin\left(\frac{Re}{Re_{ref}} \cdot \frac{\pi}{2}\right) \right]^{n_{cl1,bot}} \\
c_{l2,bot} &= c_{l2,bot,0} + \Delta c_{l2,bot} \cdot \left[\sin\left(\frac{Re}{Re_{ref}} \cdot \frac{\pi}{2}\right) \right]^{n_{cl2,bot}} \\
n_{tr,bot} &= n_{tr,bot,0} + \Delta n_{tr,bot} \cdot \left[\sin\left(\frac{Re}{Re_{ref}} \cdot \frac{\pi}{2}\right) \right]^{n_{n_{tr,bot}}}
\end{aligned}$$

The lower surface transition location formulation optimization involves nine independent variables, since the maximum transition location is set to 1.0 for all Reynolds numbers.

The first level equations for the pressure drag are as follows:

$$\begin{aligned}
c_{dp0} &= c_{dp00} + \Delta c_{dp0} \cdot \left[\sin\left(\frac{\text{Re}}{\text{Re}_{ref}} \cdot \frac{\pi}{2}\right) \right]^{n_{cdp0}} + \Delta c_{dp, \text{Re}} \cdot \left(\frac{100,000}{\text{Re}}\right) \\
c_{l, \min d} &= c_{l, \min d0} + \Delta c_{l, \min d} \cdot \left[\sin\left(\frac{\text{Re}}{\text{Re}_{ref}} \cdot \frac{\pi}{2}\right) \right]^{n_{cl \min d}} \\
\Delta c_{dp2} &= \Delta c_{dp20} + \Delta \Delta c_{dp2} \cdot \left[\sin\left(\frac{\text{Re}}{\text{Re}_{ref}} \cdot \frac{\pi}{2}\right) \right]^{n_{\Delta cdp2}} \\
\Delta c_{dp6} &= \Delta c_{dp60} + \Delta \Delta c_{dp6} \cdot \left[\sin\left(\frac{\text{Re}}{\text{Re}_{ref}} \cdot \frac{\pi}{2}\right) \right]^{n_{\Delta cdp6}}
\end{aligned}$$

The optimization of the pressure drag formulation, excluding the bubble drag, involves thirteen independent variables.

The first level equations for the laminar separation bubble drag are as follows:

$$\begin{aligned}
c_{db0} &= c_{db00} + \Delta c_{db0} \cdot \left[\sin\left(\frac{\text{Re}}{\text{Re}_{ref, bub}} \cdot \frac{\pi}{2}\right) \right]^{n_{cdb0}} \\
c_{lb1} &= c_{lb10} + \Delta c_{lb1} \cdot \left[\sin\left(\frac{\text{Re}}{\text{Re}_{ref, bub}} \cdot \frac{\pi}{2}\right) \right]^{n_{clb1}} \\
c_{lb2} &= c_{lb20} + \Delta c_{lb2} \cdot \left[\sin\left(\frac{\text{Re}}{\text{Re}_{ref, bub}} \cdot \frac{\pi}{2}\right) \right]^{n_{clb2}}
\end{aligned}$$

Typically,

$$n_{clb1} = n_{clb2} = 1$$

and

$$\Delta c_{db0} = -c_{db00}$$

All parameters for the bubble drag are selected via manual inputs, since the optimizer will otherwise exploit the parameters in areas where the bubble drag is not relevant. The bubble drag term does not fully capture the bubble drag, but merely large deviations from the polynomial drag growth characteristics of the pressure drag equation.

The above first level equations are applicable for a Reynolds number range of 60,000 to the reference Reynolds number. After the reference Reynolds number is exceeded, the values are held fixed at:

$$param = param0 + \Delta param$$

The reference Reynolds number for all first level equations except for the bubble drag is 20 million. The bubble drag reference Reynolds number is dependent upon the characteristics of the airfoil.

Due to the nonlinear nature of the first level equations, the airfoil interpolation subroutine interpolates the first level left-hand-side (LHS) parameters versus the more numerous right-hand-side (RHS) parameters. The following pseudo-code shows the interpolation process:

```
Param = 0.
Do i=1,nAirfoils
  Param = Param+LHS(i)*Fact(i)
End Do
```

Where

$$\sum_{i=1}^{nAirfoils} Fact(i) = 1$$

The interpolated LHS of the first level equations are used to evaluate the second level equations.

The total drag of the airfoil is given by:

$$c_d = c_{dfri} + c_{dp}$$

where the pressure drag is found directly from the above second level equation. The friction drag is found using standard laminar and turbulent flat plate skin friction equations found in Raymer [1992]. The overall skin friction coefficient for a surface that transitions from laminar to turbulent flow is:

$$c_f = x/c_{tr} \cdot c_{f_{lam}} + (1 - x/c_{tr}) \cdot c_{f_{turb}}$$

The airfoil skin friction coefficient is the summation of the upper and lower skin friction coefficients.

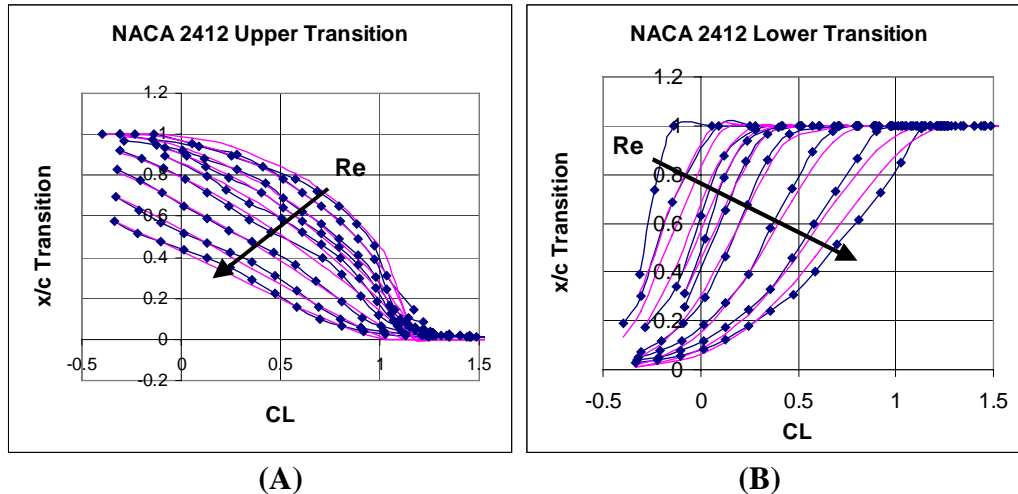


Figure 6-10 Upper and Lower Transition Location vs. Lift Coefficient Comparison Between *XFOIL* and Empirical Equation Matching for the NACA 2412 Airfoil

Figure 6-10 (A-B) show the correlation between the *XFOIL* and parametric boundary layer transition locations as a function of Reynolds number and lift coefficient. The lines without markers represent the curve fit, and the lines with markers represent *XFOIL* data. Agreement is quite good for most Reynolds numbers.

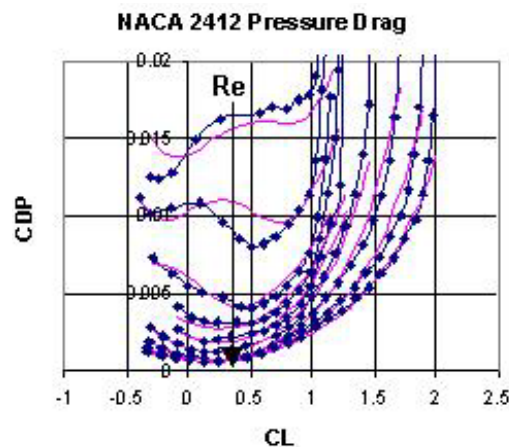


Figure 6-11 The Pressure Drag Comparison Between *XFOIL* and the Empirical Equation Matching for the NACA 2412 Airfoil

Figure 6-11 shows the correlation between *XFOIL* and parametric pressure drag coefficients over a large range of Reynolds numbers and lift coefficients. The laminar separation bubble drag occurs at lower Reynolds numbers. Correlation is quite good for this case as well.

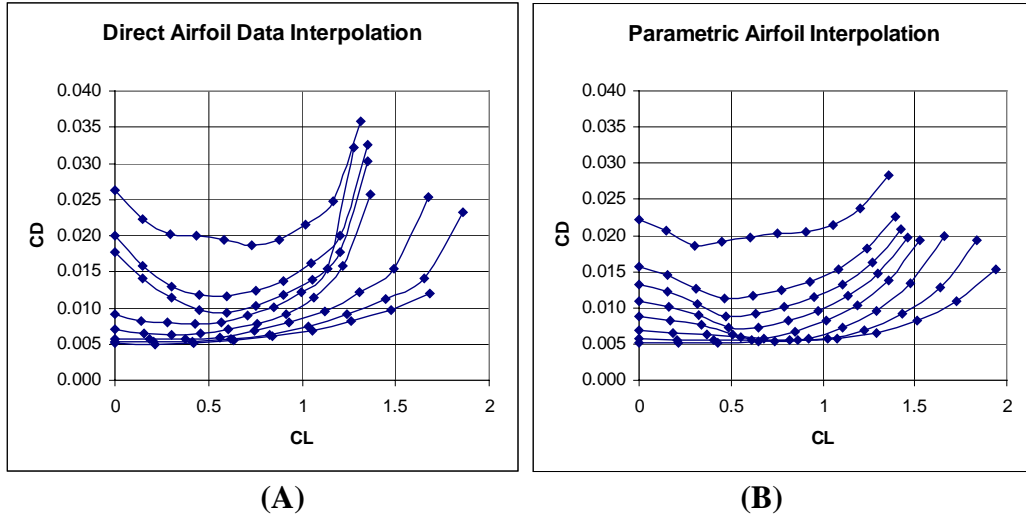


Figure 6-12 Comparison of Drag Polars Between the Direct Data and Parametric Airfoil Interpolation Methods

Figure 6-12 (A-B) shows the difference in drag polars for a general airfoil between the direct airfoil data interpolation (method 1) and the parametric airfoil interpolation (method 2). The magnitude of the minimum drag is in close agreement, but the profile drag grows more slowly with method 2. This is caused by three factors. First, the database for method 1 is presently populated by more airfoils at low Reynolds numbers. Second, method 1 uses wind tunnel data at low Reynolds numbers that has a stronger pressure drag rise than XFOIL data. Third, the interpolation of first level equation results in method 2 has some non-linear effects in the second level equations.

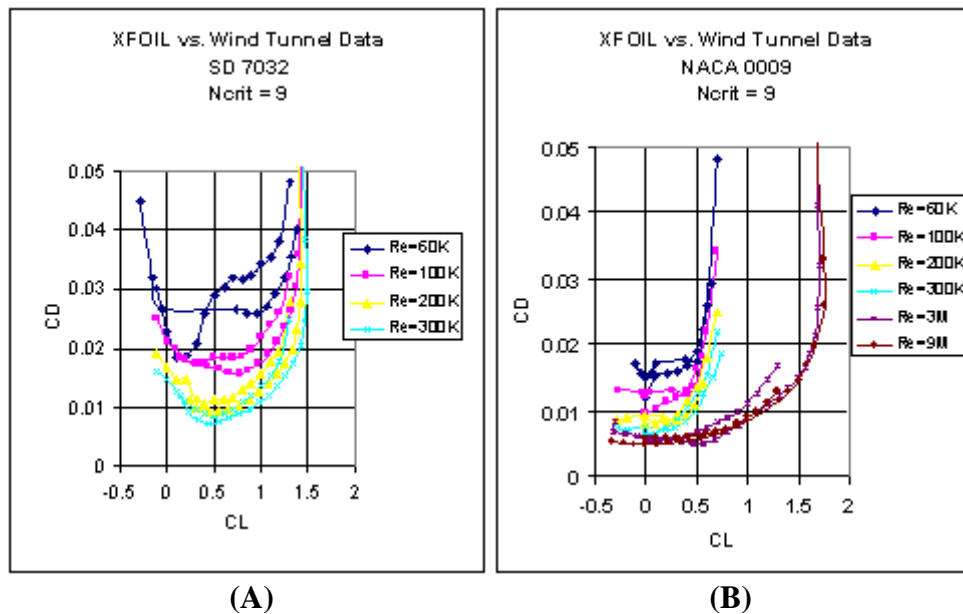


Figure 6-13 Comparison Between XFOIL and Wind Tunnel Data.

Figure 6-13 (A-B) show the correlation between *XFOIL* and wind tunnel data for cambered and symmetrical airfoils. Figure 6-13 (A) shows the correlation for a Selig Donovan SD 7032, and Figure 6-13 (B) shows results for a NACA 0009. All wind tunnel data for Reynolds numbers of 300,000 and below come from Selig's low speed wind tunnel tests at University of Illinois or Princeton [Selig 1989]. The high Reynolds number runs for the NACA 0009 are from the NACA tests as reported in Abbot and Von Doenhoff [1959]. Both series of tests describe the tunnel conditions as 'low turbulence'. According to the *XFOIL* manual [Drela 2000], the e^N turbulence model corresponds to an average turbulence wind tunnel when $N_{crit} = 9$.

In general, the *XFOIL* results tend to underestimate the drag measured in a wind tunnel. Correlation suffers with increasing camber, as can be seen on the SD 7032 graph in Figure 6-13 (A). *XFOIL* does capture the laminar separation bubble effects on pressure drag, though the behavior does differ.

Decreasing the value of N_{crit} does improve the correlation with the available wind tunnel data, but the wind tunnel data does not necessarily correspond to the conditions encountered during flight. A N_{crit} value of 9 is low compared to the flight conditions encountered by some aircraft types. Due to these considerations, N_{crit} is set to 9 for all *XFOIL* runs, even if the results do not match the wind tunnel data most closely.

The parametric airfoil method was used to generate all results for this research effort.

6.4.2.5 Simplified Airfoil Method

The two detailed airfoil methods both require a database and a large number of calculations. In order to reduce memory requirements and to speed computation time, a simplified airfoil method was developed. This is close to the more traditional methods employed in conceptual design. The airfoil profile drag takes the form:

$$C_d = C_{dfrict} \cdot FF + K \cdot (C_l - C_{l0})^2$$

Special functions were created for the minimum drag lift coefficient, C_{l0} , and the parabolic parameter, K , using curve fits to airfoil data and *XFOIL* results. While the detailed airfoil methods were under development, the simplified airfoil method was used to satisfy the profile drag needs. This method is available within the code, but it was not used to generate any results for this research.

6.4.2.6 Laminar Flow Technology

The impacts of 2-D laminar flow due to design level and laminar flow influence on transition are covered. The 2-D transition multiplication factor, $TR_{2-D,Fact}$, is found using:

$$TR_{2-D,Fact} = 1 + 2 \cdot (Tech_{Lam} - 0.5)$$

The $TR_{2-D,Fact}$ transition multiplication factor behavior described by this equation is assumed in the absence of other models. Future research could investigate laminar flow improvements relative to a baseline airfoil through experimental or CFD efforts to further develop this function. The transition factor is multiplied by the upper and lower x/c transition locations for the parametric airfoil model. For other airfoils, the ratio of the flat plate skin friction drag for an assumed fixed transition location multiplied by the transition multiplication factor and the flat plate skin friction drag for an assumed fixed transition location is multiplied by the profile drag.

The effect of sweep on transition is modeled by a curve fit to the laminar flow versus sweep technology curve used by Grasmeyer [1998]. The slope of the curve is:

$$Slope = \frac{9}{15} \cdot (1 + 0.4 \cdot (0.5 - Tech_{Lam}))$$

The transition multiplication factor due to sweep is:

$$TR_{Sweep,Fact} = 1 - Slope \cdot \Lambda_{c/4} \cdot \frac{60}{\pi}$$

This factor is applied to the profile drag just like the 2-D factor.

6.4.3 Interference Drag

The interference drag model is built upon that used by Grasmeyer [1998] on the SBW project, which is a modified version of the Hoerner [1990] method. The interference drag is broken down into several components that can be summed. The total interference drag is:

$$C_{D\ int} = C_{D\ int\ FACT} \cdot \sum (C_{D\ int, wall} + C_{D\ int, lift} + C_{D\ int, sweep} + C_{D\ int, incline})$$

$C_{D\ int, FACT}$ is a multiplication factor to account for improvements possible with a good design. Hoerner [1990] suggested that 0.1 is a suitable value.

The interference drag of a straight wing perpendicularly intersecting a flat wall with no lift is estimated by Grasmeyer [1998] as:

$$C_{D\ int, wall} = (0.8 \cdot t / c^3 - 0.0003) \cdot \frac{c^2}{S_{ref}}$$

The interference drag increment due to lift is estimated by Grasmeyer [1998] as:

$$C_{D \text{ int, lift}} = 0.1 \cdot C_l^2 \cdot \frac{c^2}{S_{ref}}$$

The interference drag increment due to wing sweep relative to the flat wall is estimated by Grasmeyer [1998] as:

$$C_{D \text{ int, sweep}} = \left(-0.00018 \cdot \Lambda_{c/4}^2 + 0.0009 \cdot |\Lambda_{c/4}| \right) \cdot \frac{c^2}{S_{ref}}$$

The interference drag increment due to inclining the wing relative to the flat wall is estimated by Grasmeyer [1998] as:

$$C_{D \text{ int, incline}} = \left(0.00006 \cdot \theta_{incline}^2 + 0.0015 \cdot |\theta_{incline}| \right) \cdot \frac{c^2}{S_{ref}}$$

The Hoerner [1990] formulation as modified by Grasmeyer [1998] has limitations. The flat wall assumption may not hold for fuselages of small diameter. Fuselage overall size never enters into the formulation. In other words, a fuselage length equal to the chord length will produce the same interference drag as a fuselage a hundred times this length. Detailed geometry inputs are required for this formulation, but the overall accuracy is questionable.

The sweep interference drag formulation is suspect because it produces negative drag coefficients at moderate sweep angles.

The interference drag of two intersecting wings is not included in this formulation.

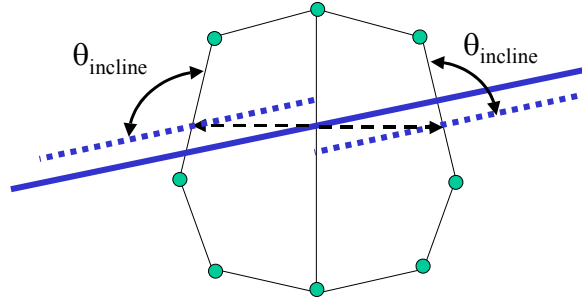


Figure 6-14 Wing-Fuselage Interference Geometry

Determining the interference geometry is not trivial. Figure 6-14 shows the basic wing-fuselage interference geometry. An algorithm determines which wing segments intersected each fuselage. Once the intersection is confirmed, the spanwise point on the wing panel that intersects the fuselage and the height along the centerline of the fuselage are determined. The height of the intersection along the fuselage is translated sideways

to the right and left, but the wing dihedral angle is preserved. A number of fuselage points are defined within the conic section formulation, and straight lines between these points are assumed to represent the fuselage adequately. The difference between the wing dihedral angle and the slopes of the fuselage walls is assumed to be the inclination angle. If the wing ends in the fuselage, then the inclination angle is taken only for the relevant side. Otherwise, if the wing passes through the fuselage, then the average of the right and left-hand side inclination angles is used.

The above geometry calculations are performed on the leading and trailing edges. The amount of span covered by the fuselage for the leading and trailing edges are averaged and multiplied by the chord to estimate the amount of covered wing planform area. This area is divided by the total planform area of the given surface to provide a profile drag multiplication factor. This factor is always less than unity, so it can be considered a constructive interference drag.

6.4.4 Fuselage Drag

The fuselage drag subroutine calculates the drag of generic bodies ranging from slender fuselages to spheres to flat plates normal to the freestream. The fuselage cross section may be circular or have squared edges at the higher fineness ratios. The sphere and slender fuselage formulations are smoothly blended together.

The general equation for fuselage drag is:

$$C_{D,Fuse} = (C_{D,frict} + C_{D,press}) \cdot \frac{S_{ref1}}{S_{ref}}$$

For a slender fuselage this formulation becomes:

$$C_{D,Fuse} = C_{D,frict} \cdot FF_{Fuse} \cdot (\sum Penalty) \cdot \frac{S_{wet,Fuse}}{S_{ref}}$$

where the pressure drag is accounted for by the form factor and the penalty factors.

The form factor equation presented in Raymer [1992] for circular cross sections is applied.

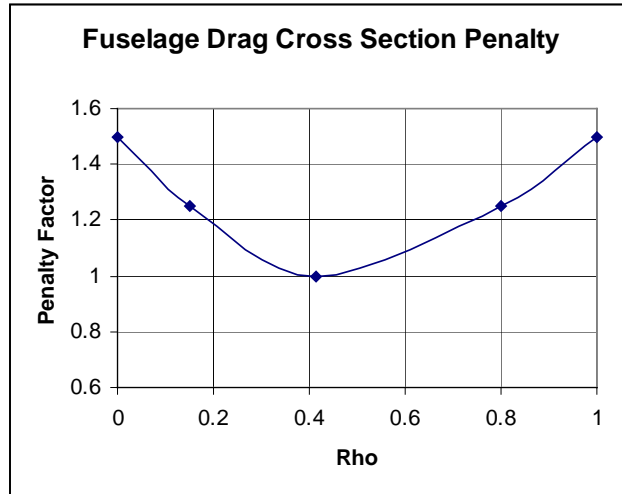


Figure 6-15 Fuselage Drag Cross Section Penalty

Not all fuselage sections of interest are circular in cross sections. Ritchie [1968], provided drag penalties for cross sections ranging from ovals to rectangles. This data was modified to correspond with the conic parameter, ρ (rho). Figure 6-15 shows the penalty factors. The ρ value associated with a circular cross section is 0.414. The volume-averaged ρ value for the fuselage is used to find the penalty through interpolation of the data.

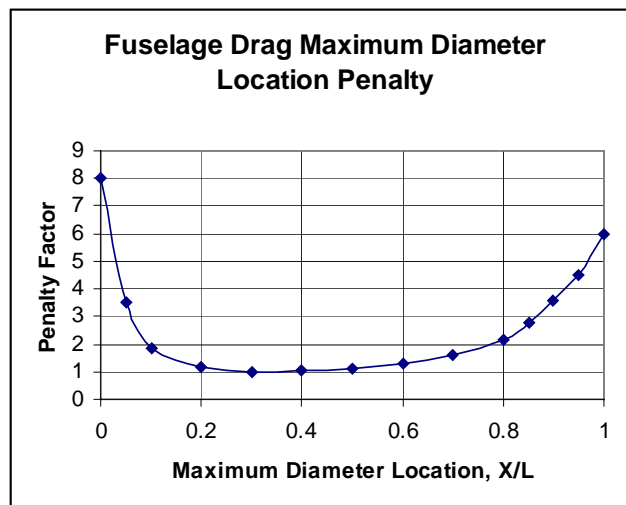


Figure 6-16 Fuselage Drag Maximum Diameter Location Penalty

Ritchie [1968] provides drag penalty data associated with the location of the maximum equivalent diameter location of the fuselage. This data is presented in Figure 6-16. The penalty can be quite high for fuselages with the maximum equivalent diameter located too far forward or too far aft.

Unfortunately, the thickness location function was exploited by the optimizer to artificially drive sweep. Because the wing was affixed to the fuselage by a parametrically blended wing fairing, the wing root would shift forward to align the fairing with the radome of some configurations. The aerodynamic center is fixed on the fuselage in the parametric geometry, so the wing would sweep. The wave drag is the real-world driver for wing sweep. The artificial wing sweep justified setting the factor equal to unity at all times.

The drag coefficient for a sphere is found by:

$$C_{D, fuse} = C_{D, sphere} \cdot \frac{S_{frontal}}{S_{ref}}$$

where the friction and pressure drag are accounted for in $C_{D, sphere}$. Note that the sphere drag coefficient is referenced to the sphere frontal area, so the ratio of the sphere frontal area to the wing reference area is applied to be consistent with other drag contributions. The sphere drag coefficient is 0.41 when below a Reynolds number of 400,000 and 0.15 when above.

A flat plate is assumed to have a drag coefficient of 1.18 referenced to the frontal area regardless of shape.

The three cases are blended together as a function of length to diameter ratios. Above a L/D_{Fuse} value of 2, the slender fuselage formulation is used. Between 2 and 1, the solution is linearly blended between the slender fuselage and sphere. Between 1 and 0, the sphere and flat plate are blended together.

6.4.5 Wave Drag

The wave drag formulation is the same method used by Grasmeyer [1998], which is based on the Korn equation. The drag divergent Mach number is found for a number of panels through the following equation:

$$M_{DD}(i) = \frac{\kappa_a}{|\cos(\Lambda_{c/2}(i))|} - \frac{t/c(i)}{\cos^2(\Lambda_{c/2}(i))} - \frac{Cl(i)}{10 \cdot |\cos^3(\Lambda_{c/2}(i))|}$$

where the airfoil technology factor, κ_a , is estimated by Grasmeyer [1998] as 0.87 for a NACA 6-Series section and 0.95 for a supercritical section. The selection of the airfoil technology factor is described in the technology modeling chapter. The critical Mach number is defined found by:

$$M_{crit}(i) = M_{DD}(i) - \left(\frac{0.1}{80} \right)^{1/3}$$

If the flight Mach number is above the critical Mach number, then the local wave drag coefficient is:

$$C_{d,wave}(i) = 20 \cdot (M - M_{crit})^3$$

and the total wave drag coefficient is:

$$C_{D,wave} = \sum C_{d,wave}(i) \cdot \frac{S_{segment}}{S_{ref}}$$

If the flight Mach number is below the critical Mach number, then the wave drag is zero.

The wing wave drag is assumed to become a major driver at a lower Mach number than the fuselage. Since the wave drag increases so rapidly with Mach number, the impacts of fuselage wave drag in the lower transonic region are considered to be unimportant in the determination of cruise Mach number. Therefore, the fuselage wave drag is not incorporated into the formulation.

6.4.6 Landing Gear Drag

The landing gear drag is broken into two phases of flight: cruise and landing/take-off. The cruise condition has all the gear in the full retraction position, if the configuration has retractable gear. The landing/take-off condition has the gear fully extended.

The gear drag is composed of combinations of tires, struts, streamwise doors, and body cavities. This geometry is passed to the gear drag subroutine prior from the complex geometry definition subroutines. The landing gear drag coefficient is defined as:

$$C_{D,gear} = \sum (C_{D,tire} + C_{D,strut} + C_{D,door} + C_{D,cavity})$$

The tire drag is estimated for the nose and main gear by:

$$C_{D,tire} = 0.25 \cdot N_{tire / strut} \cdot N_{strut} \cdot \frac{D_{tire} \cdot W_{tire}}{S_{ref}}$$

where the size of the nose and main gear may be different. Note that 0.25 is a typical frontal area based drag coefficient. Hoerner [1990] shows a variation in drag coefficient between 0.12 and 0.35, depending on tire type. The above drag coefficient is then modified by a multiplication factor for rear fairing, forward fairing, or wheel pants cases, based upon factors derived from Hoerner [1990].

The strut drag is treated as a circular cylinder perpendicular to the freestream or as a faired strut. The circular cylinder drag coefficient varies with Reynolds number, assuming natural transition, with the critical Reynolds number centered about 3×10^6 . The faired strut assumes a t/c of 0.33, and the simple airfoil method is employed for calculating the drag.

If retractable landing gear is used, then gear door drag is calculated for the extended gear case. The gear doors are assumed aligned with the flow. The equivalent flat-plate turbulent skin friction on the door is calculated on both sides to yield the drag coefficient.

For retractable landing gear, the gear bay cavity drag is calculated for the extended gear case. The drag of the open gear bay cavity is found in Hoerner [1990]. The drag coefficient is:

$$C_{D,cavity} = 0.0083 \cdot N_{strut} \cdot \frac{W_{door} \cdot L_{door}}{S_{ref}}$$

where the value for the nose and main gear well cavities may be different.

The total drag for the up and down position depends on the gear configuration. If a gear is retractable, then the retracted drag coefficient is zero and the extended drag includes the tire, strut, door, and cavity. If the gear is permanently extended, then both drag values include the strut and tire, but not the gear well cavity or the gear door. The retraction scheme can be different for the nose and main gears.

6.4.7 Cooling Drag

The cooling drag associated with the engine and systems is book kept as in the propulsion section. The cooling can be accomplished from an environmental control system (ECS) driven by bleed air from the engine or by a ram air ECS system. Regardless of the cool air source, the engine and systems require a cooling mass flow.

For ram air ECS systems, the total drag associated with cooling is found by:

$$D_{Ram} = \dot{m}_{Ram} \cdot U_{\infty} \cdot \left(1 - \frac{U_e}{U_{\infty}}\right)$$

The ram air mass flow rate (kg/hr) [Sloan 1985] is found by:

$$\dot{m}_{Ram} = 3.59 \cdot \frac{Q_{cool}}{T_{comp} - T_{air}}$$

where the temperatures are in degrees Celsius, and the heat load is in Watts. To put the ram cooling equation in convenient units, the following is attained:

$$D_{Ram} = 0.0012686 \cdot \frac{Q_{cool}}{T_{comp} - T_{air}} \cdot U_{\infty} \cdot \left(1 - \frac{U_e}{U_{\infty}} \right)$$

where the drag is in pounds, the heat load is in Watts, the temperatures are in degrees Fahrenheit, and the velocity is in knots. The velocity recovery, U_e/U_{∞} , is assumed to be only 0.2 due to pressure losses in the ECS system.

The cooling drag for an air cycle machine ECS system is assumed to be the same as a ram air ECS system for the purposes of this code. A fuel-cooled ECS system, like the one used on Global Hawk, is assumed to have no drag penalties.

6.4.8 Miscellaneous Drag

There are inevitably many drag contributors that are not accounted for in the above formulations. A user-input miscellaneous drag factor can be applied to scale the drag polar. This factor is a direct multiplier, so it scales the minimum drag value and the drag due to lift by the same ratio. In other words, the factor acts as a simultaneous minimum drag shift and increases the parabolic behavior of the drag polar. A 5% miscellaneous drag is used for all cases.

Chapter 7 Propulsion

7.1 Propulsion Overview

The propulsion code evaluates the performance of turbofans, turboprops, and piston-props. Each engine type has specialized analysis methods. The primary output of the propulsion code is an engine deck, which is used by the performance analysis.

The engine deck has a common format, because the performance code must adapt to multiple different engine types without modifying its formulation. The burden falls on the propulsion methods to generate this single format deck. The engine deck consists of the following arrays:

```
Altitude(altmin:altmax)  
Velocity(altmin:altmax, velmin:velmax)  
Thrust(altmin:altmax, velmin:velmax, throtmin:throtmax)  
TSFC(altmin:altmax, velmin:velmax, throtmin:throtmax)  
Allow(altmin:altmax, velmin:velmax, throtmin:throtmax)
```

The one-dimensional altitude array varies from the minimum altitude, typically sea level, to a specified maximum altitude for the engine deck. The two-dimensional velocity array varies with altitude and velocity setting. The three-dimensional thrust, Thrust Specific Fuel Consumption (TSFC) and allowable arrays vary with altitude, velocity, and throttle setting. The thrust specific fuel consumption is in jet engine format. The allowable array indicates whether or not a given point in the engine deck violates a propulsion constraint, such as being outside the permissible altitude, velocity, or thrust bounds.

The engine is scaled as a rubber engine, meaning that many engine characteristics are independent of scale. The jet thrust to weight and specific fuel consumption are assumed to stay constant. The piston engine power to weight ratio and brake specific fuel consumption remain constant. The optimizer freely scales the engines to meet the demands of a given solution. Scaling engines is a bold assumption. This implies that the appropriate engine is either available or can be produced in time to meet the UAV development schedule. This may not always be reasonable due the high cost of engine development and the typically fast-paced UAV development schedule. Despite the real-world limitations, the rubber engine assumption is applied here.

7.2 Code Architecture

The propulsion code is broken into multiple subroutines based upon propulsion type. Figure 7-1 shows the top level propulsion code architecture. The initial propulsion data is retrieved from *PROPDATIN* which is called by *INFILES*. *ACMAIN* calls *INFILES* prior to any optimizations on analyses. *ACMAIN* calls *EVAL*, which then calls

PROPULSION. *PROPULSION* can call the propulsion category subroutines: *GASPROP* for piston and turboprops, and *TURBOFAN* for turbojets and turbofans.

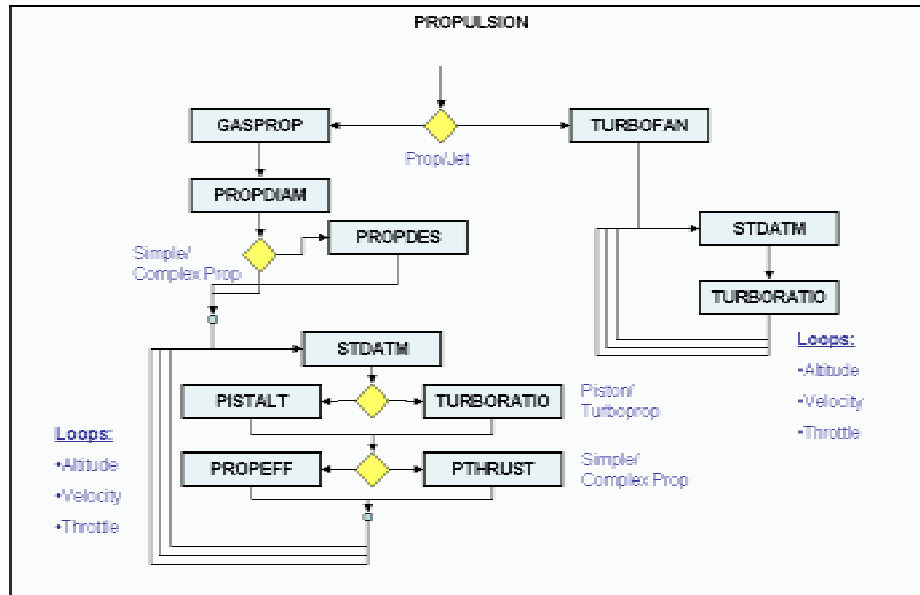


Figure 7-1 Propulsion Code Architecture

GASPROP combines piston-propellers and turboprops because of a high degree of commonality. The first step is to calculate the propeller diameter in *PROPDIAM* using empirical formulas for a specified design condition. If a complex propeller design method is chosen, then the propeller is designed in *PROPDDES*. The tabular engine deck is then calculated. A loop is entered where the altitude, velocity, and thrust levels (throttle) vary. The propulsion system is evaluated at each point. The atmospheric conditions are found by standard atmosphere routine, *STDATM*. The engine power and fuel consumption characteristics are found by *PISTALT* for piston engines and by *TURBORATIO* for turboprops. The propeller efficiency is found by *PROPEFF* if the disk actuator model is used or by *PTHRUST* if the complex propeller analysis method is used.

The *TURBOFAN* subroutine creates engine decks for turbojets and turbofan propulsion systems. The engine deck loop is then entered. The jet engine thrust and fuel consumption characteristics at each altitude, velocity, and throttle are found via the *TURBORATIO* subroutine. The *JETON* detailed jet on-design performance subroutine is integrated but was not used here.

7.3 Propeller Methods

Common propeller design and evaluation methods are used, because piston-prop, electric-prop, and turboprop propulsion systems all utilize propellers. Two propeller analysis methods are employed. A simple disk actuator method provides corrected

theoretical efficiencies with little computation time. A detailed blade element model designs propellers and provides highly fidelity propeller analysis outputs. The propulsion code has the ability to size propeller diameters based on empirical formulas.

Unfortunately, the blade element model is computationally expensive relative to the disk actuator model. Therefore, it is only utilized for determining supportable correction factors for the faster disk actuator model. The blade element model is fully integrated into the code, and is available for use. Appendix B describes the blade element methodology in detail.

7.3.1 Propeller Diameter Sizing

Raymer [1992] provides empirical equations for sizing propellers as a function of maximum engine power and the number of blades. These equations are intended for manned aircraft with two or three blades. UAV designs frequently make more extensive use of gearing than manned aircraft to achieve large propeller diameters with high relative efficiency. The Predator and Shadow 200 designs appear to fit within the application of the diameter estimation. Both of these cases use two-blade propellers. Despite the limitations, the Raymer methods are used when the propeller diameter is not specified. Figure 7-2 shows results of the Raymer empirical equations.

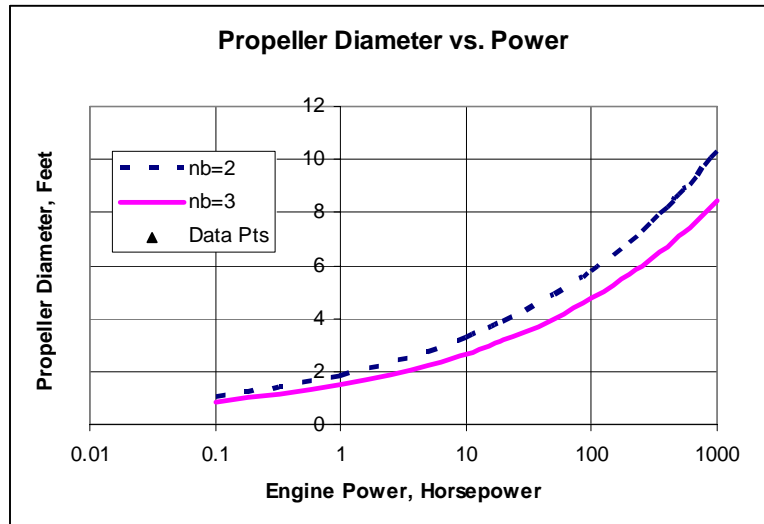


Figure 7-2 Raymer Propeller Sizing Equation Results

The second method for sizing the propellers is scaling from known propeller-engine combination. The Raymer [1993] formulation is used to aid in the scaling.

$$D = D_{Ref} \cdot \frac{D_{func}(BHP)}{D_{func}(BHP_{Ref})}$$

7.3.2 Disk Actuator Model

Two propeller performance models were developed for this effort: 1) a disk actuator model, and 2) a blade element model. Only the disk actuator model was applied here to generate the results. Details of the blade element model can be found in Appendix B.

The disk actuator model is a theoretical method of predicting the ideal efficiency of a propeller. The disk swept out by the propeller is assumed to act uniformly on the air that passes through it. Details of the method are well documented [Mattingly 1987] and will not be reproduced here. Important limitations of the model are that viscosity, non-uniform flow characteristics, propeller hubs, and other relevant aspects of propellers are neglected. Importantly, the disk actuator model cannot predict static thrust without significant modifications. The static case is not considered in this research. Corrections were applied to the theoretical model to provide more realistic predictions.

The relevant thrust equation is:

$$T = \dot{m} \cdot (V_e - V) = \dot{m} \cdot \Delta V$$

For a propeller, the thrust equation may be written in terms of the propeller disk area, A_p :

$$T = \frac{1}{2} \cdot \rho \cdot A_p \cdot \Delta V \cdot (2 \cdot V + \Delta V)$$

Solving for the velocity difference yields:

$$\Delta V = \frac{-2 \cdot V + \sqrt{4 \cdot V^2 + \frac{8 \cdot T}{\rho \cdot A_p}}}{2}$$

The exit velocity, V_e , is simply the sum $V + \Delta V$. The theoretical efficiency is:

$$\eta_{p,ideal} = \frac{2 \cdot V}{V_e - V} = \frac{1}{\frac{\Delta V}{2 \cdot V} + 1}$$

With the above equations, the ideal efficiency can be found for a given propeller diameter at any altitude, airspeed (except static case), or thrust condition. This powerful result is achieved at little computational expense. However, inescapable practical inefficiencies are neglected in the disk actuator model. To remedy this deficiency, a non-ideal efficiency correction is included. The total propeller efficiency of a non-ideal propeller is:

$$\eta_p = \eta_{p,ideal} \cdot \eta_{p,nonideal}$$

where the non-ideal efficiency ranges from approximately 85-95% based on comparisons with the blade element model. A nominal value of 90% is applied.

The propeller thrust can be calculated as a function of shaft horsepower:

$$T = \frac{P_{shaft} \cdot \eta_p}{V}$$

The thrust is a function of the propeller efficiency. The propeller efficiency is a function of the non-ideal propeller efficiency corrections and the ideal efficiency from the disk actuator model. Therefore, the thrust is a function of itself. The ideal efficiency is found iteratively. The initial value of ideal efficiency is set to unity for the starting conditions.

The engine shaft power to produce a given amount of thrust is:

$$P_{shaft} = \frac{T \cdot V}{\eta_p \cdot \eta_{gear}}$$

When the flight velocity is zero, the propeller efficiency is zero, and the power absorbed by the propeller cannot be realistically determined by the disk actuator theory.

A comparison is made in Figure 7-3 between the blade element analysis and the ideal propeller using the disk actuator model. The ideal efficiency plotted below corresponds to the thrust output at each given advance ratio. The ideal efficiency increases as the thrust level decreases over the constant propeller disk area. In the sample case, the blade element design code comes within 7-10% of the ideal theoretical efficiency. Note that the ideal efficiency neglects viscosity and other considerations. A 90% efficiency factor is applied to the disk actuator model based on these results.

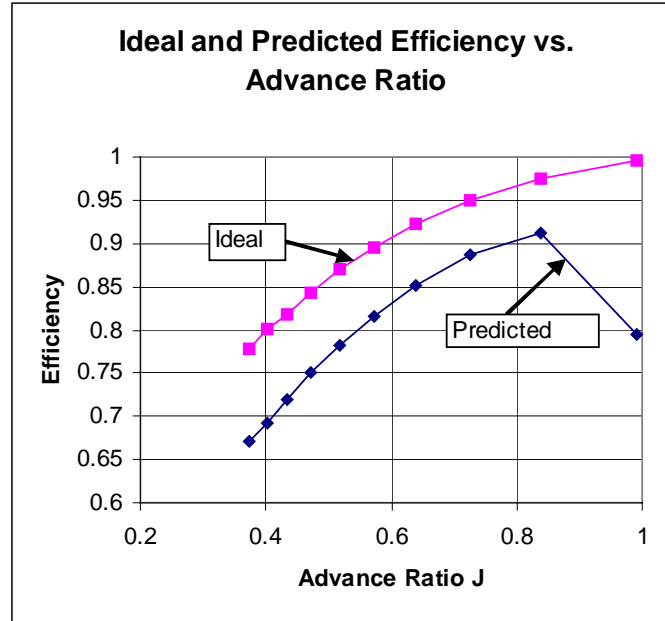


Figure 7-3 Comparison Between Predicted and Ideal Propeller Efficiencies

7.4 Piston-Prop Engines

The piston-prop method generates an engine deck for piston engines that drive a propeller. Although the word *piston* is used, the method applies to rotary engines as well.

A normally aspirated engine relies upon ambient pressure and suction to bring air into the cylinders. This type of engine generates its maximum power at sea level, and performance degrades as altitude increases. The Gagg-Ferrar [Stinton 1995] equation describes this behavior:

$$F_{BHP}(\sigma) = \frac{BHP_h}{BHP_0} = \sigma - \frac{(1 - \sigma)}{7.55}$$

where the subscript h indicates the conditions at flight altitude and 0 indicates sea level conditions. The density ratio is defined as:

$$\sigma = \frac{\rho_h}{\rho_0}$$

The Gagg-Ferrar equation is used for all rotary and reciprocating engines in this code.

Engine power can be restored by means of turbo or supercharging, where the pressure of the intake air is increased by mechanical means. This helps aircraft that fly in hot, humid

conditions or at high altitudes. Neither Predator nor Shadow 200 are known to include turbo or superchargers, so the potential improvements made possible by these devices were not investigated here.

The specific fuel consumption for a piston engine is defined as the ratio of fuel flow to the power, and is usually given in the units lb/HP-hr. Mises [1945] wrote that the typical engine specific fuel consumption ranged from 0.45-0.55lb/HP-hr. It can be assumed that he was speaking of four-stroke engines for manned aircraft applications. The situation has hardly improved since 1945 due to the domination of jet engines. The applied technology trends for reciprocating engines are found in the technology chapter.

The density altitude function $F_{BSFC}(\sigma)$ is estimated by:

$$F_{BSFC}(\sigma) = \frac{\sigma \cdot (1 - C)}{(\sigma^{n\sigma} - C)}$$

where C is about 0.065 and $n\sigma$ is 1.117. The density altitude function $F_{BSFC}(\sigma)$ may be applied directly to the sea level BSFC of a known engine:

$$BSFC_h = F_{BSFC}(\sigma) \cdot BSFC_0$$

The above equation is used for both reciprocating and rotary engines in this code.

Figure 7-4 shows the specific fuel consumption as a function of density ratio for a typical naturally aspirated internal combustion engine.

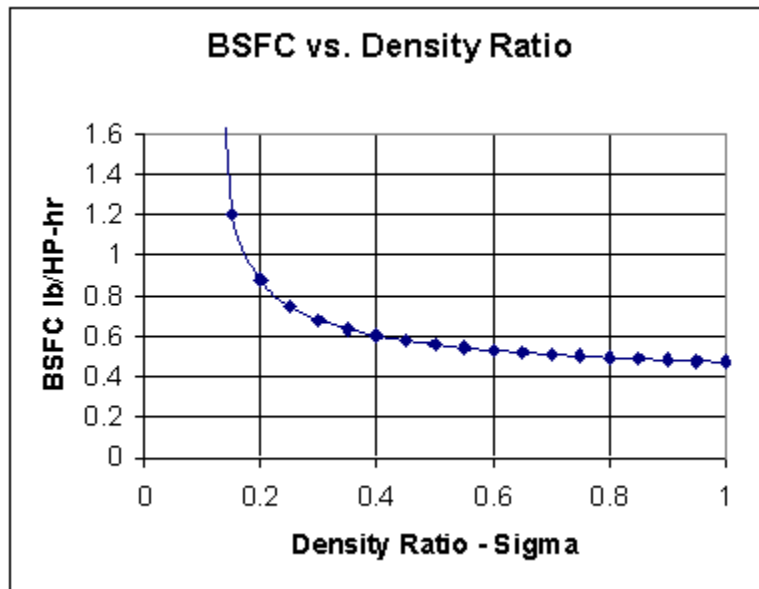


Figure 7-4 Density Ratio Impacts on Brake Specific Fuel Consumption

7.4.1 Piston-Prop Engine Deck

The throttle setting on a piston engine regulates the engine power directly, not the thrust. The power available to the propeller is:

$$P = (P_{0,\min} + \text{throt} \cdot (P_{0,\max} - P_{0,\min})) \cdot F_{BHP}(\sigma) \cdot \eta_{gear}$$

The power available to the propeller is assumed to be equal to the power absorbed by the propeller. This power is passed to either the disk actuator or blade element analysis codes to find the associated thrust and overall propeller efficiency. The engine power is not stored in the engine deck, only the thrust value.

The Brake specific fuel consumption is:

$$BSFC_h = \frac{BSFC_0 \cdot F_{BSFC}(\sigma)}{\eta_p \cdot \eta_{gear}}$$

The engine deck for fueled engines must be written in terms of thrust specific fuel consumption and not brake specific fuel consumption. The conversion for piston engines is as follows:

$$TSFC = BSFC_h \cdot V \cdot \frac{6080}{3600 \cdot 550}$$

where V is in knots, and BSFC_h is in pounds mass per pounds force per hour.

7.5 Turbojets and Turbofans

Turbo-propulsion covers turbojets, turbofans, and turboprops. Complex design methods and simplified off-design performance estimation codes were written for each engine type.

The objective of this research is to estimate the performance of UAVs and to predict the impacts of technology trends on future UAV designs. Unfortunately, technology trends are not available for many jet engine components, only the jet engines as a whole. Because of this, it is fruitless to try to surmise how the technology improvements are divided up into multiple components. The sensible approach is to apply the gross technology trends to simple methods. Simple off-design relationships were established to evaluate how gross engine characteristics vary with operating conditions. The on-design analysis is available to the code, but it was not used here.

The end result is an engine deck composed of specific fuel consumption versus thrust level, altitude and Mach number.

7.5.1 Turbojet/Turbofan Engine Decks

The looping structure for the turbojet/turbofan engine deck model is similar to the piston-prop. There are altitude, velocity, and throttle loops. The throttle loop regulates the thrust. First, the maximum thrust at the given altitude and Mach number is determined using modified Mattingly [1987] equations:

$$a = \left(0.568 + 0.25 \cdot |M - 1.2|^3\right) \cdot \sigma^{0.6} \quad \text{for high bypass ratio (assumed bypass} = 7)$$

$$a = \left(0.88 + 0.245 \cdot |M - 0.4|^{1.4}\right) \cdot \sigma^{0.7} \quad \text{for low bypass ratio (assumed bypass} = 2)$$

$$a = \left(0.907 + 0.262 \cdot |M - 0.5|^{1.5}\right) \cdot \sigma^{0.7} \quad \text{for high bypass ratio (assumed bypass} = 0)$$

The actual thrust ratio is found through a linear interpolation between the thrust ratios based on bypass ratio. The maximum thrust at a given altitude and velocity is found by:

$$T_{\max} = T_{\max, SLS} \cdot a$$

The maximum sea level static installed thrust is provided in an input file or is calculated within the code based upon a thrust to weight ratio or other parameter. The minimum installed thrust in flight is assumed to be 5% of the maximum thrust. The throttled thrust is found by:

$$T = (T_{\min} + \text{throt} \cdot (T_{\max} - T_{\min}))$$

The thrust specific fuel consumption is found using an equation modified from Grasmeyer's [1998] SBW code. This equation is calibrated to work well for high bypass ratio jet engines, though it also works well for low bypass ratio engines and turbojets:

$$TSFC_{rat} = \left(\frac{Temp}{Temp_{SL}}\right)^{0.4704} \cdot \frac{(TSFC_{ref} + 0.4021 \cdot M)}{TSFC_{ref}}$$

The reference thrust specific fuel consumption is 0.5 for a bypass ratio of 7.0, 0.65 for a bypass ratio of 2.0, and 0.85 for a bypass ratio of 0.0. The reference value used in the above equation is interpolated within these values by bypass ratio. The bypass ratio at a given altitude and velocity is found by:

$$TSFC = TSFC_{rat} \cdot TSFC_{SLS}$$

The best installed sea level static thrust specific fuel consumption is provided in an input file.

Chapter 8 Size, Weight, and Power

8.1 Size, Weight, and Power Overview

A systems approach to AV design is essential, since Size, Weight, and Power (SWaP) of all components comprising the aircraft have significant impacts on the overall sizing. The size, as considered here, refers to the component volume. Weight considers both component weights and installation weights. Power contains both power consumed by the component and the cooling power that must be dissipated. These considerations must be addressed for every component on the aircraft whether it falls under structures, avionics, subsystems, propulsion, payload, or fuel categories. A flexible means of evaluating SWaP is provided.

8.2 Generic Systems

8.2.1 Generic Systems Overview

The systems approach to aircraft design is essential for UAV applications. There simply is no way to contend with such a wide range of vehicle sizes and missions using empirical methods alone. The systems method is a core strength of the design code. Consideration of SWaP must be given to every component that enters the air vehicle.

Component and type attributes have been assigned to every component that enters the aircraft. The categories and components comprising the categories are shown in Table 8-1.

Avionics	Subsystems	Structures	Propulsion	Payload
-Autopilot -INS -GPS -Processor -Camera -ADS -Recorder -ATC	-FCS -ECS -Communications -Electrical System -Fuel System -APU	-Generic Struct. -Wing -Tails -Fuselage -Nacelles -Landing Gear	-Generic Prop. -Recip. Engines -Jet Engines	-Generic Payload -EO/IR -SAR

Table 8-1 Component Categories and Types

Multiple options are provided for SWaP. In general, the user may input values directly or select from multiple calculation options. Many component types have specialty input subroutines, and type-specific methods can be entered if available. Though complex, this approach is intended to maximize flexibility over a wide range of problems where

information is often difficult to obtain. Default information for all component categories are input through the defaults file, which may be edited by the user.

8.2.2 Generic Systems Weights

The design code is intended to offer multiple means of calculating weights to enhance flexibility. Weight is divided into two categories: component weight and component installation weight.

Standard methods for calculating the component weights include direct weight input, weight as a fraction of the empty weight, and weight as a fraction of the take-off gross weight. When specialty methods are available and selected, the code calls the specialized weight subroutines for the components. Default component weight categories for all component types are set in the code, but these may be edited by the user.

Standard methods of calculating the installation weights include direct input, a default fraction of the uninstalled weight, and input fraction of the uninstalled weight. The default installation weight factor is a function of the component category and level of design. Default component installation weight categories for all component types are input through the defaults file, which may be edited by the user. The default installation weight factor is found by:

$$F_{Wt,Install} = F_{Wt,Install,Max} + F_{Design} \cdot (F_{Wt,Install,Min} - F_{Wt,Install,Max})$$

where the installation factor is set by component category. Typically, the minimum installation weight factor is 0.15 and the maximum is 0.30 in this research. SAWE [1996] indicates that the installation weight factor usually ranges from 0.25-0.5, but this range was modified as stated to attain sensible calibration results. The installation weight factor is independent of technology year. Installation weight does not apply to fuel, since the fuel system handles all fuel installation considerations. The default structural installation weight factor is set to zero. The installation weight is found by:

$$Wt_{Install} = Wt_{Uninstalled} \cdot F_{Wt,Install}$$

An important aspect of the component weights estimation is determining the location of the weight. In particular, weight in the wing will provide inertia relief that affects wing weight if the piecewise linear beam model is utilized. The location also affects volume margin, as described below. The component location is determined by the user while setting up the input files. A subroutine guides the inputs to ensure the user selects only existing wings, tails, fuselages, and nacelles.

8.2.3 Generic Systems Size

Size, represented here as volume, considerations are very important for many UAV applications. As with manned aircraft, many components on an AV compete for similar locations on the vehicle. A vehicle sized as a point mass may be smaller and lighter than a vehicle that is designed taking volumetric details into account. Volumetric considerations constrain the design in a realistic manner.

There are multiple, user-selectable means of calculating component volumes. The user may input volume directly, calculate volume from an input density, default density, or enter dimensions of various shapes. The density methods allow the user to input component density directly or for default densities to be used.

In limited cases, there are component specialized volume calculations performed in the component weights procedures. These specialized volumes will override density-based volume calculations, but not dimensional inputs or direct volume inputs. The specialized volume calculations are described along with the weight methodology in the weights chapter.

The design code has options for full or partial external volumes. External volumes may occur for antennas and payloads, though almost all components may be mounted externally. The ratio of internal to external volume is input by the user.

Structures are exempt from standard volume calculations, since the volume of the structural outer mold line is calculated separately.

The dimensional inputs for volume calculations permit multiple components and multiple shape types to be input by the user. This is necessary because a single functional item may consist of multiple individual elements. For example, most EO/IR ball payloads consist of the spherical-cylindrical EO/IR ball and separate rectangular driver electronics. Shapes used for calculations include rectangular boxes, spheres, hemispheres, and cylinders.

The default installation volume is a function of component category and level of design. Currently, all default category volume installation factors are a minimum of 0.1 and a maximum of 1.0 of the uninstalled volume. The number used is a linear interpolation between these values with the design level as the interpolation variable. Installation volume factors are independent of technology year. The recommended method is direct user input of installation factors. For the default case, the volume installation factor is found by:

$$F_{Vol,Install} = F_{Vol,Install,Max} + F_{Design} \cdot (F_{Vol,Install,Min} - F_{Vol,Install,Max})$$

The default installation volume is found by:

$$V_{Install} = F_{Vol,Install} \cdot V_{Uninstalled}$$

The code calculates the volume margin for various elements such as wings and bodies. The outer mold line volume is calculated in the geometry subroutines. All bodies and wings have volume calculated. Volumetric decrements to the outer mold line volume due to structures thickness, substructures, routing, and other considerations are estimated. The uninstalled and installation volumes of all components allocated to a given wing or body are summed. The difference between the available volume and the volume of the contents is the volume margin. Fuel may be applied to this margin if fuel is allocated to the element. Violated volume constraints are output, as described in the Optimization section.

8.2.4 Generic Systems Power

The power of all components are divided into mission phases. This enables power sequencing for flight performance fuel burn calculations and sizing of electrical and ECS subsystems. The user also has the option of specifying that the component is powered at all times.

The minimum, nominal, and maximum power are either input by the user or calculated. The power level is selected either for each phase of flight or for the total mission. The calculated power is based on power per weight of the component.

The design code has the ability to calculate minimum, nominal, and maximum power for some component types. These methods are described for the applicable components in the weights chapter.

The performance impacts of power consumption are covered in the mission performance chapter. The nominal power is applied to all mission segments here.

8.2.5 Generic Systems Thermal Management

Component cooling is covered by the code, but component heating is not evaluated. The required cooling of a component is based on the power consumed. This varies for radiating and non-radiating types. Radiating components include RF communications antennas. For non-radiating types, the cooling required is equal to the power consumed. For radiating components the cooling required is calculated by:

$$C = P \cdot (1 - \eta_{Rad})$$

where η_{Rad} is the radiating efficiency of the component.

The design code has the ability to calculate minimum, nominal, and maximum cooling loads for some components. These methods are described for the applicable components in the weights chapter.

The performance impacts of cooling are covered in the Performance and Aerodynamics sections.

8.3 Specialized Size, Weight, and Power Methods

The specialized weights methods are selected by the user when building the system files. In addition to the standard weight methods, the user has the ability to use specialized weights methods when available. Often multiple methods per component type are available. This chapter describes all available methods.

8.3.1 Subsystems

8.3.1.1 Flight Control System (FCS)

The flight control system includes the flight control actuators, and equipment required to support them. The flight control surfaces are not included in this category. Multiple flight controls weight methods are integrated into the design code. The flight control methods and associated functional dependencies are shown in Table 8-2 and Table 8-3, respectively.

Method	Applied Here
1. Roskam[1990] – Cessna General Aviation FCS Weight Equation	No
2. Roskam[1990] – General Dynamics Commercial Transport FCS Weight Equation	No
3. Roskam[1990] – General Dynamics Bomber RCS Weight Equation	No
4. Raymer[1992] Fighter FCS Weight Equation	No
5. Raymer[1992] Transport FCS Weight Equation	No
6. Raymer[1992] General Aviation FCS Weight Equation	No
7. Custom Method	Yes

Table 8-2 Flight Control Systems Weight Methods

Meth.	N _{Crew}	N _{FCS}	N _{Mech}	N _{Surf}	M _{Max}	q _{Max}	V _{eq,Max}	S _{Cont}	L _{Overall}	W _{Overall}	W _{DG}	N _{Ult}	I _{yy,mass}
1	Yes	Yes	-	-	Yes	-	-	Yes	-	-	-	-	-
2	-	Yes	Yes	Yes	-	-	-	Yes	-	-	-	-	Yes
3	-	Yes	-	-	-	-	-	-	Yes	Yes	Yes	Yes	-
4	-	Yes	-	-	-	-	-	-	-	-	Yes	-	-
5	-	Yes	-	-	-	Yes	-	-	-	-	Yes	-	-
6	-	Yes	-	-	-	Yes	-	-	-	-	Yes	-	-
7	-	Yes	-	-	-	-	Yes	Yes	-	-	-	-	-

Table 8-3 Flight Control System Weight Method Functional Dependencies

Method 1 has a severe limitation in that it requires a crew to be present. If no crew is present, then the equation outputs zero weight. In order to preserve some functionality, the number of crew, N_{crew} , is set to one. This is justified because most of the FCS weight is related to crew interfaces.

Method 2 accounts for mechanical functions beyond flight control surfaces. For the purposes of this code, the number of mechanical functions, N_{Mech} , is set to zero. This method is not applied to the cases considered. If integrated later, the mechanical functions of retractable landing gear could be linked.

Method 3 requires that the overall length and width is calculated. The overall length is the distance from the farthest forward point on the vehicle to the farthest aft. The maximum width is typically the wing span.

Method 4 has potential for broad applicability, because it is a function of design gross weight and number of flight control systems only. Many of the listed methods have very complex interactions among many variables that limit applicability beyond their intended use. There is no airspeed dependency, which is largely the reason for elimination here.

Method 7 is based on rough calculations performed on model aircraft electric actuators. The basis of the equation is the assumption that the actuators and other FCS weight contributions are proportional to the dynamic pressure and the total control surface area. The custom flight control system equation developed is:

$$W_{FCS} = 0.00002 \cdot V_{eq,max}^2 \cdot S_{Cont} \cdot N_{FCS}$$

8.3.1.2 Environmental Control System (ECS)

The environmental control system weight includes all equipment necessary to thermally manage the aircraft. Unlike manned aircraft, there is no need for cabin environmental control. The equations have been appropriately modified to reflect this consideration. The environmental control system weight methods and associated functional dependencies are shown in Table 8-4 and Table 8-4, respectively.

Method	Applied Here
1. Roskam[1990] – General Dynamics Fighter ECS Weight Equation	No
2. Roskam[1990] – General Dynamics Low-Subsonic Aircraft ECS Weight Equation	Yes

Table 8-4 Environmental Control System Weight Methods

Method	$W_{\text{Anti-Ice}}$	W_{Avionics}
1	-	Yes
2	Disabled	Yes

Table 8-5 ECS System Weight Method Functional Dependencies

The anti-icing factors in Method 2 have not been applied, because none of the UAVs considered include anti-icing systems.

8.3.1.3 Communications System

The communications system SWaP varies significantly across different applications. For many cases, these values are entered directly by the user through the generalized methods described earlier. One specialized method is applied for dish antennas typically used for satellite communications.

The assumed dish weight equation, which includes the dish, gimbal, and actuators, is:

$$W_{\text{Dish}} = 3 \cdot D_{\text{Dish}}^2$$

The factor of 3 was found through an analysis of terrestrial dishes. The correlation was poor, but the factor of 3 represents highly transportable terrestrial satellite communications dishes. A rough approximation of the volume occupied by the dish is based on estimations from drawings of Global Hawk, which has a 4-foot dish diameter. The assumed dish volume equation is:

$$Vol_{\text{Dish}} = 120 \cdot \left(\frac{D_{\text{Dish}}}{4} \right)^3$$

For a given frequency, the antenna gain, and therefore signal to noise ratio, improves with increasing diameter. The requirements for power to the antenna decrease with improved gain for a given data rate and frequency, because the effective radiated power in the desired direction improves. No link analysis is performed to evaluate these impacts. Furthermore, the frequency and desired data rates are not uniform across currently fielded UAV satellite communication solutions. It is assumed that the selected antenna power input is proportional to the dish diameter, and the data rates and

frequencies are selected as appropriate to meet the aperture size. The assumed dish power equation, based on best-judgment, is:

$$P_{Dish} = 250 \cdot D_{Dish}$$

Further refinement of satellite communications systems SWaP would be beneficial to future UAV research efforts.

8.3.1.4 Electrical System

The electrical system includes all elements of the electrical system including, but not limited to, generators, batteries, converters, and the power distribution elements. Multiple empirical equations have been included in the code. The electrical system weights methods and associated functional dependencies are shown in Table 8-6 and Table 8-7, respectively.

Method	Applied Here
1. Roskam[1990]-Cessna General Aviation Electrical System Weight Equation	No
2. Roskam[1990]-USAF Electrical System Weight Equation	No
3. Roskam[1990]-General Dynamics Transport Electrical System Weight Equation	No
4. Roskam[1990]-General Dynamics Bomber Electrical System Weight Equation	No
5. Roskam [1990] – General Dynamics Navy Fighter Electrical System Weight Equation	No
6. Raymer [1992] Transport Electrical System Weight Equation	Yes
7. Raymer [1992] General Aviation Electrical System Weight Equation	No

Table 8-6 Electrical System Weight Methods

Method	W _{DG}	W _{Fuels}	W _{Avion}	P _{Max}	L _{Elec}	N _{Gen}
1	Yes	-	-	-	-	-
2	-	Yes	Yes	-	-	-
3	-	Yes	Yes	-	-	-
4	-	Yes	Yes	-	-	-
5	-	Yes	Yes	-	-	-
6	-	-	-	Yes	Yes	Yes
7	-	Yes	Yes	-	-	-

Table 8-7 Electrical System Weight Method Functional Dependencies

The Raymer [1992] transport electrical system weight equation, Method 2, requires an estimation of the overall length of the electrical system. This value, L_{Elec}, is assumed to be 50% of the overall vehicle length. The maximum power is calculated for all avionics

and most subsystems prior to the electrical system subroutine call. This method is used because it is a function of system power, not avionics and fuel system weights.

8.3.1.5 Fuel System

The fuel system contains the fuel tanks, fuel pumps, fuel lines, and other components. Several fuel system weight empirical equations have been integrated into the code. The fuel system weight methods and associated functional dependencies are shown in Table 8-8 and Table 8-9, respectively.

Most of the methods are adaptable to external fuel tanks, but this was disabled since none of the UAVs under consideration have external fuel tanks. The parameter $Vol_{Internal}/Vol_{Tot}$ is set to one.

The tank volume is simply the fuel weight divided by the fuel density for the purposes of these calculations. Fuel volume constraint checking is handled in other subroutines.

The total number of tanks, N_{Tanks} , is assumed to be two for the purposes of this code.

Method	Applied Here
1. Raymer [1992] Fighter Fuel System Weight Equation	No
2. Raymer [1992] Transport Fuel System Weight Equation	Yes
3. Raymer [1992] General Aviation Fuel System Weight Equation	No

Table 8-8 Fuel System Weights Methods

Method	Vol_{Tank}	$Vol_{Internal}/Vol_{Tot}$	N_{Tanks}	T_{max}	TSFC	N_{Eng}
1	Yes	Yes	Yes	Yes	Yes	Yes
2	Yes	Yes	Yes	-	-	-
3	Yes	Yes	Yes	-	-	Yes

Table 8-9 Fuel System Weight Method Functional Dependencies

The Raymer [1992] fighter fuel system weight equation originally contained provisions for protected fuel tanks. Factors for this consideration were disabled.

8.3.1.6 Auxiliary Power Unit (APU)

The user may either enter in the APU weight directly or use the APU weight estimation method. The estimation method is an attempt to relate APU weight from the power required of it.

It is assumed that the power required of the APU is 50% of the maximum power experienced by the aircraft. The APU is assumed to weight 1.5 pounds per horsepower, which is between typical values of 2-stroke and 4-stroke engines, and is heavy for a turboshaft. None of the cases considered are believed to contain an APU, so this method was not utilized.

8.3.2 Avionics

Avionics are given substantial consideration in this research, because they can be a dominant weight driver. For example, a small component like a GPS antenna can weigh as much as an optical payload on a very small UAV. The weight of a GPS antenna is within typical weight calculation error levels for a manned aircraft.

A general methodology for avionics weight was attempted. Avionics suites are highly dependent on the mission, vehicle class, design philosophy, and technology. General avionics methods were attempted for autopilots, INS, GPS, processors, cameras, recorders, and ATC avionics. Though providing some utility, these methods were not employed in the final evaluations of the cases of interest. The avionics suites of the vehicles under consideration are simply too divergent and case-specific to be captured in generalized formulations. With the exception of the applied ADS method, all avionics were input directly. The avionics methods are shown in Appendix C for completeness, though the methods are not mature. It is unlikely that an effective, generalized avionics methodology is possible.

8.3.2.1 General Avionics Functions

The weight, volume and power functions all use a common form. The common equation is:

$$Y = Y_0 + a \cdot X^n$$

X_0 (=0) and Y_0 is input. The mid values X_1 (=0.5) and Y_1 (=1) are input. The maximum values X_2 (=1) and Y_2 are also input. The values of n and a are found by:

$$n = \frac{\ln\left(\frac{Y_2 - Y_0}{Y_1 - Y_0}\right)}{\ln\left(\frac{X_2 - X_0}{X_1 - X_0}\right)}$$

$$a = \frac{Y_1 - Y_0}{(X_1 - X_0)^n}$$

If Y_0 is greater or equal to Y_1 , or if Y_1 is greater than or equal to Y_2 , then linear interpolation is used.

8.3.2.2 Air Data System (ADS)

Air data systems are necessary to provide the autopilot with angle of attack, angle of sideslip, pressure altitude, and dynamic pressure, depending on the autopilot. The ADS weight equations used here are based upon best-judgment assumptions. The ADS method is intended to make the ADS estimated weight of the correct order of magnitude for a wide range of UAV AVs. Future research could adjust the factors of these equations based on regression analysis of a custom ADS database. The ADS weights resulting from these methods appear to be reasonable for the purposes of this research, considering that there are no alternative methods available.

Two types of air data systems are considered: ADS booms and integral ADS. The typical ADS boom weight is assumed to be:

$$W_{ADS} = 0.05 \cdot V_{eq,max}$$

The typical weight of an integral ADS system is assumed to be:

$$W_{ADS} = 0.02 \cdot V_{eq,max}$$

If the maximum flight altitude is greater than 15,000 feet, the ADS is assumed to have a heater. The weight of the ADS with heater is assumed to be:

$$W_{ADS} = 1.2 \cdot W_{ADS}$$

The ADS weight is corrected for ruggedness, performance, and miniaturization. The factors are shown in Table 8-10.

Driver	Minimum (0)	Mid (0.5)	Maximum (1)
Ruggedness	0.8	1.0	1.2
Performance	0.8	1.0	1.2
Miniaturization	0.6	1.0	1.4

Table 8-10 Air Data System Factors

The weight and volume are initially calculated by using the boards and boxes formulas. Only 25% of the ADS volume is internal. The weight and volume installation factors are the same as for boards and boxes.

8.3.3 Structures

An attempt has been made to provide multiple options for the various structural weights. Numerous manned aircraft equations have been utilized, but other customized options have been introduced. The new piecewise linear beam structures methods do not have reference UAV cases to draw upon, so fidelity may be low. However, this is often better than using equations for manned aircraft outside their applicable range.

8.3.3.1 Wing

Multiple methods for calculating wing weights have been incorporated into the design code. There are options for three parametric weights and one semi-analytic method. The parametric weights are modified versions of Raymer's [1992] fighter, transport, and general aviation wing weights. The semi-analytic method is a piecewise linear beam model. All wing weight methods are available, but the piecewise linear beam model is believed to have the most general applicability to small AV designs. The piecewise linear beam model was applied to all cases in this work. The wing weight methods and associated functional dependencies are shown in Table 8-11 and Table 8-12, respectively.

The code can handle multiple wings performing lifting functions, so canards, tandem wings and other types may be evaluated. The level flight loading at the design gross weight condition of each wing is found by:

$$Load_{Wing}(i) = \frac{W_{DG} \cdot S_w(i)}{S_{W,tot}}$$

Method	Applied Here
1. Raymer [1992] Fighter Wing Weight Equation	No
2. Raymer [1992] Transport Wing Weight Equation	No
3. Raymer [1992] General Aviation Wing Weight Equation	No
4. Piecewise Linear Beam	Yes

Table 8-11 Wing Weight Methods

Meth.	Load _w	N _{Ult}	S _w	AR _w	t/c _{Avg}	λ _{eq}	Λ _{c/4}	S _c /S _w	q	W _{Fuel,wing}	Tech
1	Yes	Yes	Yes	Yes	Yes	Yes	Yes	Yes	-	-	Yes
2	Yes	Yes	Yes	Yes	Yes	Yes	Yes	Yes	-	-	Yes
3	Yes	Yes	Yes	Yes	Yes	Yes	Yes	-	Yes	Yes	Yes

Table 8-12 Wing Weight Method Functional Dependencies

8.3.3.1.1 Piecewise Linear Beam Model

The wing and tail structure is analyzed using the piecewise linear beam model. The methods were inspired by publications from the Strut-Braced Wing (SBW) research at Virginia Tech [Naghshineh-Pour 1998]. The method applied here is more limited in scope, since only cantilever wings are considered.

Piecewise Linear Beam Load Estimation

The load allocated to each wing is assumed to be proportional to the ratio of the area of the wing to the total wing area. The total load carried by the wing is found by:

$$Load_{Wing} = N_{ult} \cdot W_{DG} \cdot \frac{S_w}{S_{W,Tot}}$$

The design code currently does not calculate the wing load distribution based on the lift distribution methodologies used in the aerodynamics. However, these methods could be adapted in future versions of the code. The lift load distribution method assumes an elliptical distribution. The lift load for each panel is found by:

$$Lift(k) = Load_{Wing} \cdot \frac{b_{Struct}(k)}{b_{Struct,Tot}} \cdot \frac{4}{\pi} \cdot \sqrt{1 - \frac{2 \cdot Y_{Run}(k)}{b_{Struct,Tot}}}$$

where Y_{Run} is the distance of the mid-panel centroid from the root along the path of centroids, and $b_{Struct,Tot}$ is the total structural span of the wing along the path of centroids.

The wing may carry non-structural components such as avionics and subsystems, which provide inertia relief. These are allocated to the wing by the standardized systems subroutines. The total weight of these non-structural components, $W_{Non-Struct,Tot}$, is allocated externally. The load distribution is assumed to be triangular, with the maximum weight at the root. The non-structural weight distribution is found by:

$$W_{Non-Struct}(k) = W_{t_{Non-Struct,Tot}} \cdot \frac{2 \cdot b_{Struct}(k)}{b_{Struct,Tot}} \cdot \left(1 - \frac{2 \cdot Y_{Run}(k)}{b_{Struct,Tot}}\right)$$

The overall shear load and bending moment due to lift and non-structural weight are found by numerical integration from the tip to the root. The wing weight is calculated from tip to root. The shear and moment are corrected for the structural wing weight of outboard panels.

8.3.3.1.2 Piecewise Linear Beam Wing/Tail Weight Estimation

The thickness of the bending material for the panel is found by:

$$t_{Bend}(k) = \frac{Mom_{Bend}(k) \cdot \frac{T_{Box}(k)}{2}}{I_{xx,t}(k) \cdot \sigma_{ult}}$$

If this value is less than the minimum gage value, then the thickness is set to the minimum gage thickness. The total bending material weight of the panel is found by:

$$W_{Bend}(k) = \rho_{Mail} \cdot t_{Bend}(k) \cdot S_{Pan}(k)$$

The total panel area moment of inertia is found by:

$$I_{xx}(k) = I_{xx,t}(k) \cdot t_{Bend}(k)$$

The shear material weight assumes that the majority of the structural material is contained in the wing skins, so the contribution of shear material to the area moment of inertia and the shear flow is small. The area moment of inertia for shear material calculations is identical to that found through the wing bending material calculations. The shear web is assumed to be a single web which occupies the entire maximum thickness of the panel. It is assumed that if multiple webs are used, the total shear material weight will be comparable. The shear flow is found by:

$$q_{Shear}(k) = q_{Shear,t}(k) \cdot t_{Bend}(k)$$

The shear material thickness is found by:

$$t_{Shear}(k) = \frac{Shear(k) \cdot q_{Shear}(k)}{I_{xx}(k) \cdot \tau_{ult}}$$

If the shear material thickness is greater than the minimum gage thickness, then the shear material thickness is set to the minimum gage value. The shear material weight of the panel is found by:

$$W_{Shear}(k) = t_{Shear}(k) \cdot T_{Pan}(k) \cdot b_{Struct}(k)$$

The bending and shear material weights are summed across the wing to provide the total wing weight:

$$W_{Bend,Tot} = \sum_{k=1}^{Nseg} 2 \cdot W_{Bend}(k)$$

$$W_{Shear,Tot} = \sum_{k=1}^{Nseg} 2 \cdot W_{Shear}(k)$$

The wing box weight is found by summing the total bending and total shear weights:

$$W_{Box} = W_{Bend,Tot} + W_{Shear,Tot}$$

The wing box is only part of the wing weight. Other weights components include:

- Attachments for engines, undercarriage, and miscellaneous items, W_{Attach}
- Leading and trailing edge control surfaces and secondary structure, $W_{CS,Secondary}$
- Rib Weight, W_{Ribs}

Empirical equations for these components are difficult to find. Detailed weight statements for aircraft, manned or unmanned, are much more scarce. Macchi [1995] developed a semi-analytical method for estimating wing weight. While this method is not directly employed here, the results of the analysis are helpful in determining the weight of wing components. Figure 8-1 shows the resulting multiplication factors applied to the wing box for other wing structural elements.

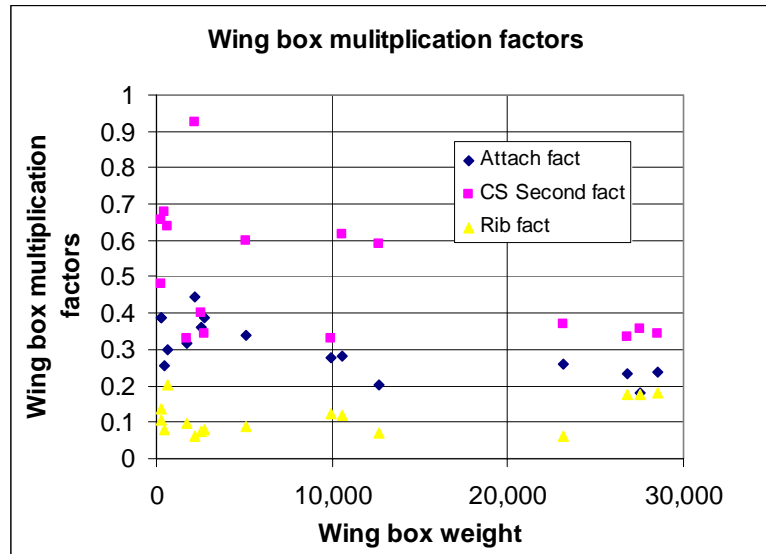


Figure 8-1 Macchi Wing Factors

The average wing box multiplication factor value for each weight type was determined, to give the following weight estimation equations:

$$W_{Attach} = 0.303 \cdot W_{Box}$$

$$W_{CS,Secondary} = 0.500 \cdot W_{Box}$$

$$W_{Ribs} = 0.114 \cdot W_{Box}$$

The overall wing weight is:

$$W_{Wing} = W_{Box} + W_{Attach} + W_{CS,Secondary} + W_{Ribs}$$

8.3.3.1.3 Piecewise linear beam model considerations

The piecewise linear beam model contains both conservative and optimistic assumptions. While these considerations may partially cancel one another, this will vary from case to case. No single parametric wing weight equation is applicable across the wide range of vehicles considered in this research. The hope is that, despite the beam model limitations, it will provide a reasonable estimate across all vehicles where no applicable competing methods exist.

One conservative assumption made in the model is that the wing skin bending material and shear material thicknesses are uniform for a given segment. The thicknesses are calculated at the points of maximum bending and shear stresses for a given wing segment, which means that all other points have more thickness than required. Although conservative, this may reflect reality because of limitations of processes to manufacture variable thickness skins at a given spanwise location.

This model does not account for wing torsion, drag loads, drag moments, rail-launch shock loads, landing loads, off-normal lift load vectors, or axial loads. Also, aerolastic effects, especially flutter, can be a major driver in high aspect ratio wings. No direct consideration of aerolastic effects are considered here.

All of the wings are assumed to be designed for strength rather than for stiffness. Additional weight penalties will be incurred if a stiffness based wing design is necessary. These penalties are not applied in this code.

8.3.3.2 Tails

The tail weight accounting includes all tail structures as a single weight, which simplifies the calculation of multiple tail arrangements. The piecewise linear beam model and Raymer [1992] transport and general aviation tail weight methods are included. The piecewise linear beam model is applicable to horizontal tails and V-tails. All the configurations under consideration have V-tails, so the piecewise linear beam model was employed. The tail weight methods are shown in Table 8-13. The horizontal tail weight methods functional dependencies are shown in Table 8-14. The vertical tail weight methods functional dependencies are shown in Table 8-15.

Method	Applied Here
1. Raymer [1992] Transport Tail Equations	No
2. Raymer [1992] General Aviation Tail Equations	No
3. Piecewise Linear Beam	Yes

Table 8-13 Tail Weight Methods

Meth.	W _{DG}	N _{Ult}	S _H	AR _H	L _H	λ _H	Λ _{c/4,H}	S _c /S _H	q	Tech
1	Yes	Yes	Yes	Yes	Yes	Yes	Yes	Yes	-	Yes
2	Yes	Yes	Yes	Yes	-	Yes	Yes	-	Yes	Yes

Table 8-14 Horizontal Tail Weight Method Functional Dependencies

Meth.	W _{DG}	N _{Ult}	S _V	AR _V	L _V	λ _V	Λ _{c/4,V}	q	Tech
1	Yes	Yes	Yes	Yes	Yes	-	Yes	-	Yes
2	Yes	Yes	Yes	Yes	-	Yes	Yes	Yes	Yes

Table 8-15 Vertical Tail Weight Method Functional Dependencies

For V-tails (also known as butterfly tails), the tail weight is calculated as a combination of horizontal and vertical tail weights when using parametric equations. The V-tail weight is calculated without these manipulations when applying the piecewise linear beam model. All other geometry parameters such as taper ratio, sweep, and thickness to chord ratio are identical. The V-tail weight is found by:

$$W_{V-Tail} = W_{HT} \cdot \cos(\Gamma)^2 + W_{VT} \cdot \sin(\Gamma)^2$$

The aspect ratio for the vertical tail part of the calculation is assumed to be half of the input aspect ratio.

8.3.3.3 Fuselage

Three fuselage methods have been adopted from Raymer [1992]. For many of the smaller UAVs considered, these manned aircraft equations are not working within the intended applicable bounds. The fuselage weight methods and associated functional dependencies are shown in Table 8-16 and Table 8-17, respectively.

Method	Applied Here
1. Raymer [1992] Fighter Fuselage	No
2. Raymer [1992] Transport Fuselage	No
3. Raymer [1992] General Aviation Fuselage	Yes

Table 8-16 Fuselage Weight Methods

Meth.	W_{DG}	N_{Ult}	$S_{wet,Fuse}$	L_{Tail}	L/D_{Fuse}	L_{Fuse}	q	Wing Geom	Tech
1	Yes	Yes	-	-	Yes*	Yes	-	-	Yes
2	Yes	Yes	Yes	-	Yes	Yes	-	Yes	Yes
3	Yes	Yes	Yes	Yes	Yes	-	Yes	-	Yes

Table 8-17 Fuselage Weight Method Functional Dependencies

The Raymer [1992] General Aviation fuselage equation was used for all cases. This method requires special information on the nominal cruise dynamic pressure, tail location on the fuselage, and cabin pressurization. The nominal cruise dynamic pressure, q , is assumed to be 75% of the maximum dynamic pressure. The tail geometry imposes limitations on the design, since many UAVs may not have tails attached to the fuselage or even have tails at all. Nevertheless, the length of the tail from the wing, L_{Tail} , is approximated as 60% of the fuselage length. The fuselage is assumed to be unpressurized, so no pressurization weight penalties are incurred.

8.3.3.4 Nacelles

The Raymer [1992] transport engine nacelle weight was applicable to both pylon and other arrangements. The pylon mounted option is not used, so the associated correction factor, K_{NG} , is set to unity. The equation is dependent upon the engine controller weight, $W_{Engcont}$, but this is not always included in the nacelle. The engine controller weight was set to 10% of the engine weight for the purposes of these calculations, as an assumption.

8.3.3.5 Launch and Recovery Gear

Multiple empirical methods exist for estimation of landing gear weight [Raymer 1992, Roskam 1990], but these methods typically have landing gear geometry functional dependencies. Raymer [1992] landing transport landing gear weights equations were applied to the Global Hawk, Predator, and Shadow 200 in a spreadsheet. The average mass fraction of the landing gear relative to the design gross weight as evaluated was 4.28%. The minimum landing gear mass fraction was 3.26%, and the maximum was 5.16%. Given the limitations of the analysis and large spread of results, 4% was selected as the basic landing gear mass fraction applied to all conventional landing gear in this research.

Recovery-only gear can take the form of non-recoverable (crash landing), skid landing, or parachute recovery. The parachute recovery is considered here. Parachute recovery gear is assumed to weigh 2% of the design gross weight, as a weight index to the conventional landing gear method. The parachute mass fraction method is a best-judgment assumption. The Shadow 200 can use a parachute recovery system. The Global Hawk and Predator use conventional landing gear only.

8.3.4 Propulsion

8.3.4.1 Reciprocating Engines

The engine calculation method multiplies the specific power and the engine power to obtain the engine weight. This is calculated by:

$$W_{Eng} = P_{Specific} \cdot P_{Eng}$$

The overall engine dimensions are found by Roskam [1990] 6-cylinder engine formulas modified to have application beyond general aviation engines:

$$\begin{aligned} L_{Eng} &= 1.56 \cdot P_{Eng}^{0.15} \\ Wid_{Eng} &= 1.5 \cdot \frac{P_{Eng}}{200} + 0.00134 \cdot P_{Eng} \\ H_{Eng} &= 1.7 \cdot \frac{P_{Eng}}{200} + 0.00156 \cdot P_{Eng} \end{aligned}$$

The engine volume is found by:

$$Vol_{Eng} = L_{Eng} \cdot Wid_{Eng} \cdot H_{Eng}$$

The power draw and cooling of the engine are set to zero for the standard component accounting. These are calculated under the mission performance.

8.3.4.2 Jet Engines

A simple thrust to weight method and a parametric method are used to determine the engine weight. A specialized means of calculating the jet engine volume was employed.

Jet engine weight – thrust to weight method

The thrust to weight jet weight calculation method is:

$$W_{Jet} = \frac{T_{Jet}}{T / W_{Jet}}$$

Jet engine weight – Roskam method

The Roskam [1990] jet weight calculation method is available in the code. This method relates the jet engine weight to the thrust level and bypass ratio. This method was not used to generate the results of this effort.

Jet engine weight – default rubber engine method

This method uses a default reference engine to calculate the engine weight, length, and diameter. The thrust scale factor is found by:

$$SF = \frac{T_{Jet}}{T_{Jet,Ref}}$$

The jet engine weight is found by:

$$W_{Jet} = W_{Jet,Ref} \cdot SF$$

Jet engine volume calculations

For the thrust to weight and Roskam [1990] engine weight methods, the engine diameter is found by using a reference thrust/diameter² parameter. The default rubber method uses the length and diameter methods described earlier.

A limited engine database for turbojets and turbofans was used to determine the length/diameter² parameter. Unfortunately, there is little correlation between bypass ratio and the parameter, and there is significant scatter. A nominal value of 500 lb/ft² was used for the purposes of these simple calculations. The jet engine diameter equation is:

$$D_{Jet} = \frac{T_{Jet}}{(T_{Jet} / D^2)_{Ref}}$$

The engine length is found by a length/diameter parameter. The engine database was used to select an appropriate value. Similar to the thrust/diameter² parameter, there was little correlation with aspect ratio, and the data has significant scatter. The jet engine length equation is:

$$L_{Jet} = D_{Jet} \cdot (L / D)_{Jet,Ref}$$

The jet engine volume is then found by:

$$Vol_{Jet} = \frac{\pi}{4} L_{Jet} \cdot D_{Jet}^2$$

Jet engine power and cooling

The jet power consumption and cooling are set to zero in the component calculations. The impacts of engine cooling are calculated in the performance model. These are covered in the mission performance chapter.

Chapter 9 Flight Performance

9.1 Overview

The performance model predicts aircraft fuel burn and optimizes flight trajectories. The mission analysis evaluates a wide array of mission types with an emphasis on flexibility and robustness. Simple performance methods are combined in multiple ways to solve complex performance problems without the need for external flight trajectory optimization.

The performance code is designed to evaluate the fuel burn of the AV as it flies the mission profile and to evaluate associated constraints. Several options exist for evaluating the mission, ranging from direct evaluations of a specified mission to limited mission optimization.

The code evaluates multiple mission segments. These segments can represent climb, cruise, descent, loiter or combinations thereof. The individual segments are further broken into sub-segments. During each segment of flight, several constraints are evaluated. These include stall, specified Mach limits, specified altitude limits, specified dynamic pressure limits, insufficient thrust for level flight, insufficient thrust for prescribed rate of climb, and engine operating limits.

The performance code has the ability to optimize flight velocities. The figures of merit include range efficiency, endurance efficiency, climb efficiency, and maximum rate of climb. These velocities are optimized such that no constraints are violated.

Two possibilities exist for the evaluation of fuel burn. First, standard or arbitrary mission profiles can be evaluated either forwards or backwards to determine the percentage of the mission that could be completed. Second, a loiter segment can be established in the middle of a mission profile with sufficient endurance to use all of the available fuel. The first possibility lends itself well to a mission completion constraint, and the second is suitable for an objective function contributor.

9.2 Performance Code Architecture

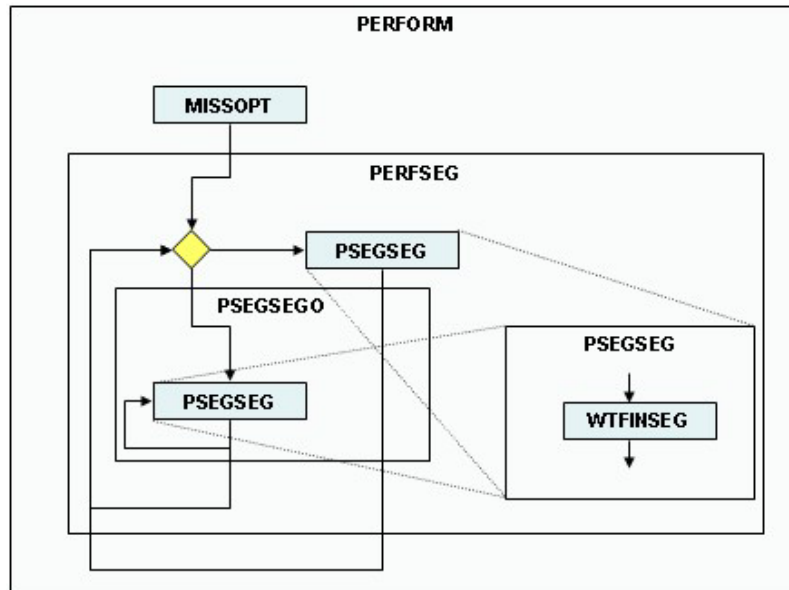


Figure 9-1 Performance Code Architecture

Figure 9-1 shows the performance code architecture. The *PERFORM* subroutine drives the performance evaluation. Prior to calling *PERFORM*, the mission parameters must be input, the aerodynamics and propulsion tables must be generated, and the weights must be determined. Once this is done, *PERFORM* calls the necessary subroutines to evaluate the fuel burn and mission constraints.

ACMAIN initially calls *PERFORMIN* to read and interpret the mission input data files. *ACMAIN* then calls *EVAL* directly or through the optimizer. *EVAL* calls the propulsion, geometry, weights, and aerodynamics subroutines, along with others, to generate the data necessary to drive *PERFORM*.

PERFORM, the main performance subroutine, first calls *MISSOPT* to organize the mission. *MISSOPT* has the ability to drive the evaluation of a normal one-direction mission or an optimized centered mission. With either option, *MISSOPT* calls *PERFSEG* for every mission segment. *PERFSEG* subdivides the mission segment into sub-segments and calls either *PSEGSEG* for prescribed velocities or *PSEGSEGO* to determine optimized velocities. *PSEGSEGO* calls *PSEGSEG* multiple times to determine optimal velocities that do not violate constraints. *PSEGSEG* calls *WTFINSEG* multiple times to determine the fuel burn or performance and any remaining unknowns.

The header of the mission input file has the following format:

Test performance input file

```
2      miss_type (1=non-opt,2=R spec)

0.99   ff_taxi

4      nsegseg

8      nseg
```

The toggle flag *miss_type* specifies the type of mission to be flown. A value of 1 indicates a normal one-direction mission, and a value of 2 indicates that the mission is centered and that all the fuel will be depleted during the mid-mission loiter.

ff_taxi is the fuel fraction that is used during warm-up, taxi, and take-off. This does not include the climb to altitude.

nsegseg is the number of subsegments each segment will be divided into, and *nseg* is the total number segments in the mission.

The remainder of the mission input file represents the individual mission segments. Each segment has the following format:

```
3      segment number
1      fwd_flag (1=fwd, 2=reverse, 3=center)
1      ra_en_flag (1=range inpt, 2=endur inpt, 3=climb)
20.    rangeseg (if ra_en_flag = 1), nmi
1.     endureseg (if ra_en_flag = 2), hrs
3      vm_flag - velocity-Mach flag (1=V,2=M,3=R,4=E,5=h/t,6=h/f)
150.   vel (if vm_flag = 1), kts
0.3    mach (if vm_flag = 2)
1      contig_flag (1=contiguous, 2 = not contig)
0.     alt1 - initial altitude (if contig_flag=2), ft
1      altroc_flag (1=fin alt,2=ROC,3=cruise,4=const)
30000. alt2 (if altroc_flag = 1), ft
500.   roc (if altroc_flag = 2), ft/min
```

The selection flag *fwd_flag* indicates whether the mission is flown forward from take-off (at design gross weight) to landing, backwards from landing (at the empty weight) to take-off, or from a centered mission. A centered mission must follow a centered mission profile described later.

The toggle flag *ra_en_flag* indicates whether range, endurance, or climb is the primary objective of the mission segment. Range, R_{seg} , is input if range is the primary objective. Endurance, E_{seg} , is input if endurance is the primary objective. If climb is the primary objective, then climb between two specified altitudes will be achieved either with maximum rate of climb or maximum fuel efficiency.

The selection flag *vm_flag* indicates how the flight velocity will be determined. The flight velocity or the Mach number may be input directly, where constraints may be violated. The flight velocity may be optimized such that no constraints are violated. The options for optimized flight velocities include the velocities associated with best range, endurance, rate of climb, or most efficient climb.

The toggle flag *contig_flag* indicates whether the mission segment is contiguous with an adjacent mission segment. Either the initial or final altitude may be set to the appropriate altitude of the adjacent segment when contiguous, depending on the direction in which the mission is evaluated. The altitudes must be input directly when the segment is not contiguous.

The selection flag *altroc_flag* indicates whether the final altitude or constant rate of climb is input.

9.3 Performance Methodology

9.3.1 Performance Equations

The heart of the performance modeling for fueled aircraft begins with the Breguet range equation:

$$R = \frac{V \cdot L/D}{TSFC} \cdot \ln \left(\frac{W_i}{W_f} \right)$$

This form of the Breguet equation requires that the product $V \cdot L/D/TSFC$ remains constant, which necessitates a cruise-climb. Many missions are flown at constant altitude or velocity, creating inaccuracies in the Breguet range equation estimation. Climbs differing from the cruise climb can also introduce inaccuracies. The product may not hold constant well if the altitude change is significant. The prediction accuracy can be improved by breaking each mission segment into sub-segments and introducing corrections.

$$R = \sum R_{seg}$$

The equations that follow may be calculated in several different orders, depending on which information is known *a priori*.

The Breguet range equation is modified to account for thrust values differing from the ideal.

$$R_{seg} = \frac{V \cdot \left(\frac{L}{D}\right)}{T_{mult} \cdot TSFC} \cdot \ln\left(\frac{W_i}{W_f}\right)$$

where the thrust multiplication factor, T_{mult} , is found by:

$$T_{mult} = \frac{T_{req}}{D}$$

The required thrust, T_{req} , is found by:

$$T_{req} = \left(\frac{ROC}{V} + \frac{1}{L/D}\right) \cdot W$$

The lift to drag ratio, L/D , is replaced by the ratio of weight over drag. The required thrust becomes:

$$T_{req} = \frac{ROC}{V} \cdot W + D$$

The lift coefficient, C_L , is simply:

$$C_L = \frac{W}{1/2 \cdot \rho \cdot V^2 \cdot S_w}$$

The air density, ρ , is found via a standard atmosphere subroutine. The drag coefficient is found by the aerodynamics table lookup subroutine:

$$C_D = C_D(C_L, M, R_e / L)$$

where,

$$M = \frac{V}{a} \quad \text{or} \quad V = M \cdot a$$

depending on whether Mach number or velocity is known beforehand. The speed of sound, a , is found via the standard atmosphere subroutine. The Reynolds number per unit length, R_e/L , is found by:

$$R_e / L = \frac{\rho \cdot V}{\mu}$$

where the viscosity and density are found via the standard atmosphere subroutine.

The specific fuel consumption, TSFC, is found via the engine deck lookup subroutine. In general,

$$TSFC = TSFC(alt, M, T_{req})$$

The minimum and maximum thrust values at the given altitude, T_{min} and T_{max} , respectively, are also output from the engine deck lookup subroutine.

The time taken to complete the sub-segment range is:

$$E_{seg} = \frac{R_{seg}}{V}$$

The performance modeling must also capture the impacts of cooling drag and power extraction. The cooling drag estimation is described in the aerodynamics chapter. The relationship between drag and power, assuming thrust is equal to drag, is:

$$Pow = D \cdot V$$

If a generator supplies this power, then there will be power generation efficiency, η_{Gen} . When this relationship is rearranged and corrected for units, power extraction equivalent drag is found by:

$$D_{Pow} = 0.43687 \cdot \frac{Pow}{V \cdot \eta_{Gen}}$$

where D_{Pow} is in pounds, Pow is in Watts, and V is in knots. This method is a simple approximation for the equivalent drag resulting from power extraction. The approach lends itself well to reciprocating engines, and is assumed to be applicable to jet engines as well.

The overall drag including all considerations becomes:

$$D = \frac{C_D}{C_L} \cdot W + D_{Pow} + D_{Cool}$$

The weight calculations can occur in different orders, depending on the available inputs and required outputs. For example, the segment range and initial weight can be input and the final weight output. Or, the initial and final weights can be input and the endurance output. The mission performance code is structured such that multiple combinations of inputs and outputs may be accommodated.

For a forward-calculated mission segment, the final weight is found by:

$$W_f = \frac{W_i}{e^{\left(\frac{T_{mult} \cdot R_{seg} \cdot TSFC}{V \cdot \frac{C_L}{C_D}} \right)}}$$

For a reverse-calculated mission segment, the initial weight is found by:

$$W_i = W_f \cdot e^{\left(\frac{T_{mult} \cdot R_{seg} \cdot TSFC}{V \cdot \frac{C_L}{C_D}} \right)}$$

9.3.2 Performance Constraints

There are multiple flight envelope constraints:

- | | |
|---|---|
| 1) $V < V_{stall}$ | Stall constraint |
| 2) $ROC_{avail} < ROC_{min}$ | Minimum rate of climb constraint |
| 3) $D > T_{max}$ | Insufficient thrust for level flight constraint |
| 4) $V > \frac{V_{eq,max}}{\sqrt{\rho / \rho_{SL}}}$ | Dynamic pressure constraint |
| 5) $V > M_{max} \cdot a$ | Mach constraint |
| 6) $T_{req} < T_{min}$ | Minimum available thrust constraint (not set yet) |
| 7) $alt > alt_{max}$ | Maximum altitude constraint |

Figure 9-2 shows potential flight envelope constraints.

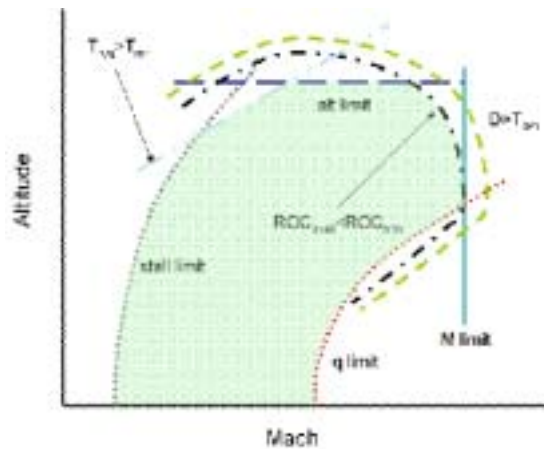


Figure 9-2 Flight Envelope Boundaries

9.3.3 Flight Velocity Optimization

To optimize the velocities, there are several figures of merit:

$FOM = \frac{R_{seg}}{W_i - W_f}$	Range efficiency
$FOM = \frac{E_{seg}}{W_i - W_f}$	Endurance efficiency
$FOM = ROC_{avail}$	Maximum climb rate
$FOM = \frac{ROC \cdot E_{seg}}{W_i - W_f}$	Climb efficiency

A search algorithm finds the optimal velocity for the given figure of merit in the constrained flight envelope. In a trade between speed and robustness, a bisection search algorithm is used.

Figure 9-3 shows how the search is initiated. The initial minimum velocity is the stall speed. The initial maximum velocity is the minimum of the dynamic pressure limit and the Mach limit. In this case, the minimum and maximum velocities fall outside the constraint boundaries. Depending on which constraints are violated, the minimum velocity is incrementally increased or the maximum velocity is incrementally decreased until the boundaries fall within the feasible region.

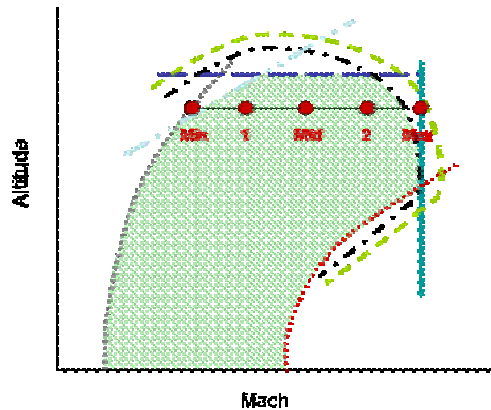


Figure 9-3 Velocity Search Initialization

Once all the velocities fall within the feasible region, the search begins. If the point with best figure of merit does not lie on the end, then the point with the best figure of merit becomes the point *mid*. The case where the best figure of merit lies on the end will be discussed later. The right and left adjacent points become points *min* and *max*, respectively. Point *1* is created halfway between points *min* and *mid*, and point *2* is created halfway between points *mid* and *max*. The process continues through several

iterations. The velocity associated with the best figure of merit at the end of the search is the final velocity selected.

The process is different when the best figure of merit is an end point. In the case where the best figure of merit is point *min*, point *mid* becomes point *max* and point *1* becomes point *mid*. Points *1* and *2* are generated halfway between these points as described above. The process continues with one or more of the processes discussed until the maximum number of iterations is reached.

9.3.4 Climb Performance

The cruise climb altitude change is assumed equal to the altitude change required to keep the lift coefficient constant. The final sub-segment altitude is found through linear interpolation or extrapolation. The reference altitude change is 10,000 feet. The cruise climb altitude change is found by:

$$alt2 = alt1 + 10,000 \cdot \frac{\rho(alt1)}{\rho(alt1 + 10,000) - \rho(alt1)} \cdot \left(\frac{W_f}{W_i} - 1 \right)$$

The rate of climb associated with the cruise climb is estimated. If the cruise climb rate of climb exceeds the 80% of the available rate of climb at the given velocity, the cruise climb rate of climb is set to 80% of the available rate of climb. The 80% factor is applied to account for typical reductions in available rate of climb as altitude is increased. When a cruise climb profile is selected, the fuel burn is first calculated without any rate of climb. The difference in fuel burn for the level flight and cruise climb conditions is found by first estimating the difference in thrust required for cruise climb:

$$\Delta T_{Climb} = \frac{ROC}{V} \cdot W$$

Next, the difference in fuel burn for the cruise climb is estimated by:

$$\Delta W_{Fuel,Climb} = \Delta T_{Climb} \cdot SFC \cdot E_{Seg}$$

Note that E_{Seg} is the endurance of the sub-segment. The optimal cruise velocity is found for each new sub-segment. The initial cruise altitude for the second through final sub-segments is simply the altitude associated with the best cruise condition of the predecessor segment.

For forward-calculated cruise climb segments, the altitude used for calculations is the starting altitude. Similarly, reverse-calculated cruise climb segments use the final altitude. The average altitude is output.

A constant rate of climb may be specified for a mission segment. The flight velocity may be optimized for any figure of merit desired. For a forward evaluation:

$$alt2 = alt1 + ROC_{seg} \cdot E_{seg} \cdot 60$$

For a backwards evaluation:

$$alt1 = alt2 - ROC_{seg} \cdot E_{seg} \cdot 60$$

If the initial and final altitudes are specified, then the rate of climb is found by:

$$ROC_{seg} = \frac{(alt2 - alt1)}{E_{seg} \cdot 60}$$

If the final altitude, $alt2$, exceeds the maximum altitude, then the final altitude is set to the maximum altitude. Unlike the flight velocities, the altitude calculations do not optimize altitudes such that no constraints are violated. The performance code will output the violated constraint value if the required rate of climb is not attainable.

Even if a rate of climb is input, it may not be achievable. The maximum available rate of climb is:

$$ROC_{max,avail} = \frac{(T_{max} - D)}{W} \cdot V \cdot \frac{6080}{60}$$

For descent, the minimum rate of climb (positive rate of descent) is:

$$ROC_{min,avail} = \frac{(T_{min} - D)}{W} \cdot V \cdot \frac{6080}{60}$$

The rate of climb may be reset for missions segments that permit flexibility in the rate of climb. If the required rate of climb exceeds the maximum rate of climb, then the rate of climb will be set to the maximum rate of climb. Similarly, if the required rate of descent exceeds the minimum rate of climb, then the rate of climb is set to the minimum rate of climb.

The mission analysis code can evaluate the climb performance without a prescribed range or endurance. The initial and final altitudes must be input, and the range and endurance will be output. The two desired climb modes are maximum rate of climb and most fuel efficient climb. The associated velocities are found via the outer loop figure of merit search procedure described earlier. For the maximum rate of climb, maximum throttle is used. For most fuel efficient climb, a search procedure is initiated with the following figure of merit:

$$FOM = \frac{ROC_{seg}}{W_i - W_f}$$

The initial and final weights are evaluated with the Breguet range equation with the segment range missing, thus eliminating the range and endurance dependency. The endurance and range are then found by:

$$E_{seg} = \frac{alt2 - alt1}{ROC_{seg} \cdot 60} \quad \text{and} \quad R_{seg} = E_{seg} \cdot V$$

The initial or final sub-segment weight, depending on evaluation direction, is then found via the modified Breguet range equation.

9.3.5 Mission Evaluation

Mission profiles can be either standard or arbitrary. The standard mission profile is useful because it permits an evaluation of available time on station for a given fuel load. Arbitrary missions are much more flexible. These can contain up to 20 segments and the compiler integer limit for sub-segments per segment.

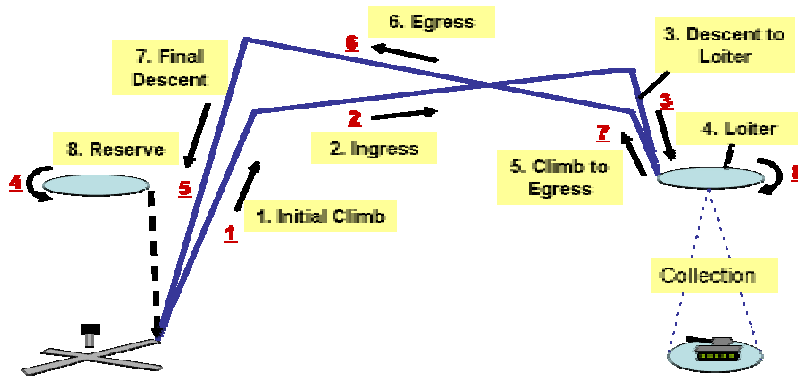


Figure 9-4 Standard Mission Profile

Figure 9-4 shows the standard mission profile used for long-range missions. The boxes identify the mission segment name and the flight order. The arrows indicate the direction of flight. The underlined numbers show the order of calculation for a centered mission. The order of calculation is the same as the order of segments for forward calculations or in the opposite order for backwards calculations.

9.3.6 Mission Completion Criterion

The mission completion criterion is a metric for determining if the air vehicle with the available fuel load can complete the desired mission. The mission completion criterion is handled differently for centered-standard and arbitrary mission profiles.

The centered-standard mission completion criteria depends on the available fuel at the loiter segment. If the loiter segment's final weight is greater than the initial weight, then the time on station will be negative. The mission completion criterion is:

$$misscomp = 1 - \frac{W_f - W_i}{W_i}$$

Otherwise, if the loiter segment initial weight is greater than the final weight, the mission completion criteria is unity. The time on station is a direct result of the available fuel, and this may be an objective function.

The arbitrary mission completion criterion evaluation method depends on if the AV completes the mission. If the AV completes the mission from either the forward or backward analysis direction, the mission completion criterion is found by:

$$misscomp = \frac{W_{fuel}}{W_{fuelb}}$$

A different procedure is used when there is insufficient fuel to complete the arbitrary mission. The mission analysis code keeps track of three different types of mission segment: range, endurance, and climb. Although all three parameters are known for each segment, only one per segment is tracked for the mission completion criteria. First, the total range, endurance, and climb are calculated:

$$\begin{aligned} R_{tot} &= \sum R_{seg} && \text{For all range-type segments} \\ E_{tot} &= \sum E_{seg} && \text{For all endurance-type segments} \\ \Delta alt_{tot} &= \sum |\Delta alt_{seg}| && \text{For all climb-type segments} \end{aligned}$$

Next, the relative weighting of each metric must be assessed. The range, endurance, and climb are all put in terms of distance. Then each distance-normalized parameter is weighted. First, the common denominator is found:

$$Denom = R_{tot} + \left(E_{tot} + \frac{\Delta alt_{tot}}{ROC_{min} \cdot 60} \right) \cdot 0.75 \cdot V_{eq,max}$$

Second, the relative weightings are found:

$$\begin{aligned} R_{wt} &= \frac{R_{tot}}{Denom} \\ E_{wt} &= \frac{E_{tot} \cdot 0.75 \cdot V_{eq,max}}{Denom} \\ alt_{wt} &= \frac{\frac{\Delta alt_{tot}}{ROC_{min} \cdot 60} \cdot 0.75 \cdot V_{eq,max}}{Denom} \end{aligned}$$

If the air vehicle depletes the fuel during any mission segment, then an error flag is output along with the amount of the segment that is completed. All segments that follow

are not completed. There is a running summation of the completed and partially completed segments. The mission completion parameter for non-completed arbitrary missions is:

$$misscomp = R_{wt} \cdot \frac{R_{comp}}{R_{tot}} + E_{wt} \cdot \frac{E_{comp}}{E_{tot}} + alt_{wt} \cdot \frac{|\Delta alt_{comp}|}{\Delta alt_{tot}}$$

Chapter 10 Calibration

10.1 Calibration Overview

Design code calibration is essential to ensuring the validity of a new design analysis. It is highly unlikely that a design algorithm will provide sensible results without adequate tailoring of inputs and methods. The present design code was calibrated for the three UAV classes under consideration. Once calibrated, the technology design impacts may be assessed with a higher degree of confidence.

10.2 Calibration Methodology

Design code calibration is a challenging endeavor. It is possible to reach a point calibration through many different approaches. In this effort, there are more code inputs than available calibration point references.

The primary outputs that must be matched are empty weight, design gross weight, volumetric closure, and mission completion. The empty weight is affected by the avionics and subsystems, structural loading, flight envelope, fuel capacity, payloads, and numerous other inputs. The design gross weight is a function of empty weight and the fuel weight. Volumetric closure is a function of component volumes, fuel volume and available volume. The mission completion is a function of weights, aerodynamics performance, propulsion performance, and the self-optimized mission profile.

The calibration process starts with the following inputs:

1. Vehicle Geometry
2. Loads and flight envelope parameters
3. Component SWaP or SWaP method inputs
4. Fuel fraction input
5. Structural materials characteristics
6. Subsystems parameters and characteristics
7. Mission profile

The vehicle design code is run with all available inputs. If the empty weight is higher than the reference value, then several items may be adjusted:

1. Factor of safety design level (if not specified)
2. Weight growth design level
3. Installation weight design level
4. Avionics and subsystems characteristics (if appropriate)
5. Structural materials characteristics (if appropriate)

Once the empty weight at the reference fuel mass fraction is calibrated, the performance calibration begins. The fuel mass fraction is held constant at the reference value. The following items may be adjusted to ensure that the design mission profile is completed:

1. Uninstalled engine characteristics (if unknown)
2. Propulsion installation losses
3. Aerodynamics design levels

If volumetric constraints are violated, then the volumetric design level must be adjusted. If this is not sufficient, then the external geometry of the vehicle and component volume estimations must be scrutinized for validity.

The parameters adjusted during the calibration process and any unique methods employed are identified for each of the three cases evaluated here. The calibration cases utilized the calibration process outlined above.

10.3 Calibration Cases

10.3.1 Global Hawk

10.3.1.1 Global Hawk Description

The Global Hawk is the first and only operational strategic high altitude UAV. This system began development in 1994. Global Hawk started as an Advanced Concept Technology Demonstrator (ACTD) with many goals, but the only firm requirements was a fixed Unit Fly-away Price (UFP). Many modifications have occurred to improve the system, and it has experienced operational use in wartime. Therefore, the available performance numbers represent the estimated performance of the vehicle as built, not necessarily as designed. As with nearly any aircraft program, the performance changes over time due to weight growth, system modifications, and other considerations. An attempt is made to calibrate the code against a representative Global Hawk.

10.3.1.2 Geometry Characteristics

A rendering of Global Hawk is shown in Figure 10-1, and major geometry characteristics are described in Table 10-1.

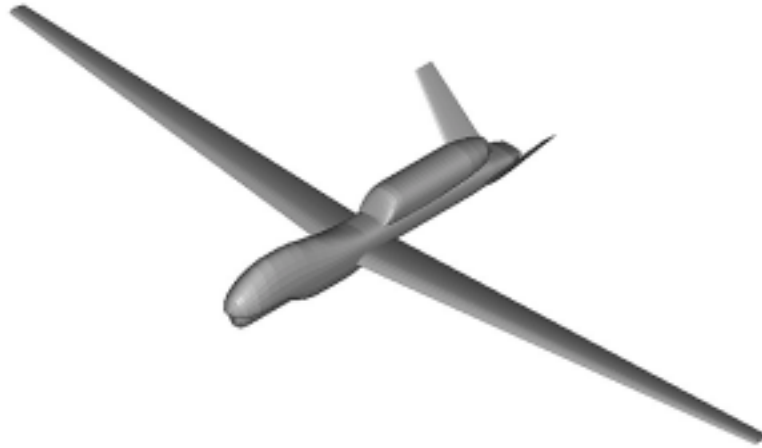


Figure 10-1 Global Hawk

Item	Value	Source
Wing span	116.2 ft	Janes [1999]
Aspect ratio	25	Janes [1999]
Sweep (quarter chord)	5°	Janes [1999]
Fuselage Length	44.4 ft	Janes [1999]

Table 10-1 Global Hawk Geometry

Detailed geometry characteristics were found through scaling of 3-view drawings. The results were integrated into the detailed geometry input files.

10.3.1.3 Propulsion

The Global Hawk engine is the Rolls-Royce 3007H. Major engine characteristics are shown in Table 10-2.

Item	Value	Source
Thrust (T-O S/L)	8,290 lbs	Janes [1999]
TSFC	0.33 lbm/lb-h	Janes [1999]
Weight (Dry)	1,581 lbs	Janes [1999]
Length	8.88 ft	Janes [1999]
Diameter	3.63 ft	Janes [1999]

Table 10-2 Global Hawk Propulsion

In addition to the engine, an additional 50 pounds of propulsion weight was added to account for the engine control electronics and actuators, as an assumption.

The overall propulsion installation thrust installation factor is assumed to be 0.8, and the thrust specific fuel consumption factor is assumed to be 0.65. These calibration factors were selected through the performance matching process.

The calculated propulsion performance is shown in Figure 10-2 and Figure 10-3.

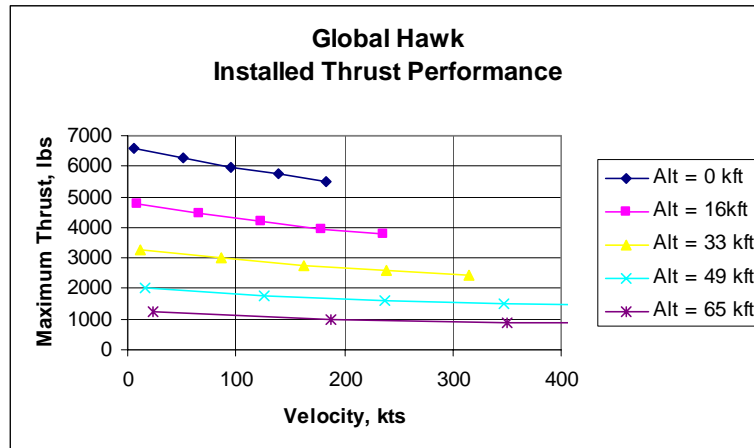


Figure 10-2. Global Hawk Engine Thrust Performance

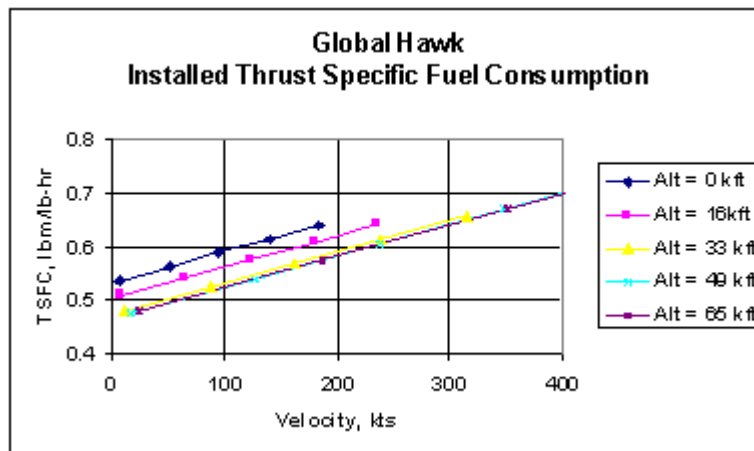


Figure 10-3 Global Hawk Engine Specific Fuel Consumption Performance

10.3.1.4 Avionics

Global Hawk is known to have an extensive electronics suite. Weights for all of the components are not available. Details of some avionics components, such as INS and data recorders, are found in Global Hawk literature and vendor data sheets. The assumed avionics weights use a fragmentary Master Equipment List (MEL), developed from information generated from Altmann [2002] and Janes [1999], as guidance. Figure 10-4 shows the avionics weights determined for the calibration case.

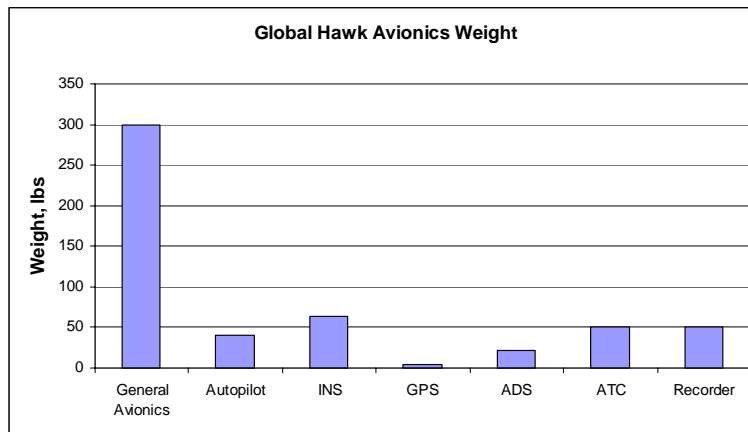


Figure 10-4. Global Hawk Avionics Weights Summary

General Avionics

The general avionics category is intended to capture all avionics components not covered by specific avionics categories. 300 pounds of general avionics was assumed. This weight was the best-judgment assessment of the weight of all avionics for which detailed weight information is not available.

Autopilot

The autopilot weight consists of two Integrated Mission Management Computers (IMMCs). No weights information is readily available on these units. The weight is 40 pounds, as a best-judgment assumption.

INS

The INS weight consists of two LN-100 INS units (21.6 pounds each), and two Kearfott KN-4072 units (10 pounds each).

GPS

The GPS weight consists of the GPS antenna and a GPS processor. The GPS must support Differential GPS (DGPS) functionality. The GPS weight was set to 5 pounds, which is a best-judgment assumption.

Air Data System

The air data system consists of two air data booms on the tails. The custom air data system weight equation was used. The equation is set to have the largest size, most rugged design, and highest performance settings.

Air Traffic Control

Global Hawk has a robust air traffic control system. Global Hawk is the first UAV to gain a type certification, enabling a file and fly capability. Global Hawk is known to have VHF/UHF ATC radios, and Identify Friend or Foe (IFF) avionics [Altmann 2002]. The ATC weight was set to 50 pounds, which is a best-judgment assumption.

Recorder

Global Hawk has a data recorder capability. L-3 claims that its S/TAR family of data recorders is installed on the Global Hawk [L-3 2003]. These recorders have an advertised weight range of 19-33 pounds, and a weight of 25 pounds is selected for the Global Hawk calibration. It is assumed that two of these units are installed, given the significant redundancy on the aircraft.

10.3.1.5 Subsystems

Global Hawk has a complex set of subsystems. A list of known subsystems identified by Altmann and Janes is captured in the simple MEL. Unfortunately, no weights data is available for the subsystems. Therefore, no actual weights were used, only assumed subsystem weights and parametric methods. The resulting subsystems weights are shown in Figure 10-5.

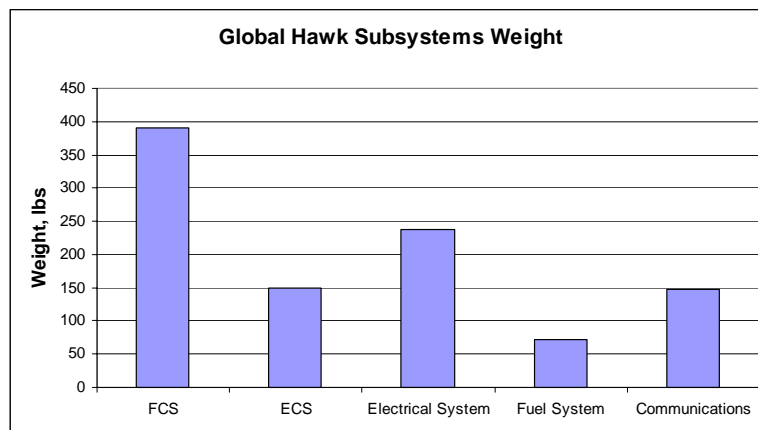


Figure 10-5 Global Hawk Subsystems Weights Summary

Flight Control System (FCS)

Global Hawk has a redundant flight control system. Per vehicle side, Global Hawk has two ailerons, two spoilers, and two ruddervators. Since the flight control system includes the actuators, the weight was assumed to be twice the parametric flight control system weight to account for the redundancy. The custom FCS weight estimation equation (Flight Control Method 7) was used to estimate this weight.

Electrical System

Global Hawk has a redundant electrical power system. There are two flight critical buses, two start buses, three batteries, an AC and a DC generator, power converters, and interfaces to ground power. The Raymer [1992] transport electrical system equation (Electrical System Method 6) was used, with two generators input.

Fuel System

Global Hawk has a sophisticated fuel system that interacts with the environmental control system. The aircraft has two high capacity fuel tanks and one sump tank in the fuselage, and three wing tanks. In addition to feeding the engine, the fuel is routed through various avionics, payload, and other bays to provide thermal management. The fuel is actively pumped through the system. The Raymer [1992] transport fuel system weight equation (Fuel System Method 2) was employed.

Environmental Control System (ECS)

The environmental control system is linked to the fuel system. Fuel cools the avionics and other components via heat exchangers and other means. The Roskam [1990]-General Dynamics low-subsonic aircraft ECS weight method (ECS Method 2) was employed. The performance model takes no drag penalty or propulsion penalty for the ECS system, since there is no ram air or engine bleed air used for thermal management.

Communications System

The Global Hawk communication system consists of multiple communications links and associated equipment. There is a high bandwidth satellite communications link using a 48-inch parabolic dish for payload data downlink. There are two low bandwidth satellite communications links for command and control. Global hawk has air traffic control links that are accounted for under ATC equipment weights. There is a line-of-sight communications link between the aircraft and the launch and recovery element to support launch and recovery operations.

The custom dish weight equation is used to estimate the high bandwidth link parabolic dish weight. Additionally, 100 pounds of communications equipment weight was input to estimate the weight of all other communications equipment, which is a best-judgment assumption used in the absence of better information.

10.3.1.6 Structures

The Global Hawk structure consists of the main wing, tails, fuselage, nacelle, landing gear and installation weight. No direct weights data is available for the structure. However, Altmann [2002] provides useful information to describe the structural design drivers and philosophy. The factor of safety for the structure is 1.25. Altmann provides a

V-N diagram that indicates that the light weight vertical load is approximately 3.6 G, and the heavy weight vertical load is approximately 2 G. Because the wing weight is calculated at gross weight, the vertical load is assumed to be 2 G. The Global Hawk structural weight is presented in Figure 10-6.

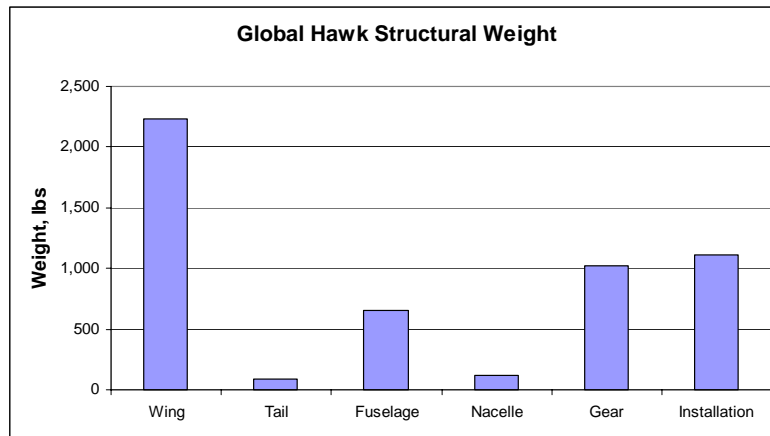


Figure 10-6 Global Hawk Structural Weight Summary

Wing

The wing is made of Carbon Fiber Reinforced Plastic (CFRP) [Jane's 1999]. The piecewise linear beam model is used to estimate the wing weights. A "black aluminum" formulation was used. The base material is the 2017 Aluminum alloy with a minimum gage of 0.02 inches. A composites weight reduction factor of 0.85 was used, as suggested by Raymer [1992].

Tails

The tail consists of a single V-tail made of unspecified composites [Jane's 1999]. The piecewise linear beam model is employed. As with the wing, 2017 aluminum with a minimum gage of 0.02 inches was assumed for the reference material. A composites weight reduction factor of 0.83 was used for the tails, as suggested by Raymer [1992].

Fuselage

The fuselage is essentially an aluminum alloy box structure [Jane's 1999]. The Raymer [1992] General Aviation method was used. No credit was provided for composites.

Nacelle

A single nacelle houses the Rolls Royce 3007H engine. The Raymer [1992] transport nacelle equation was used for weight estimation. The resulting nacelle weight may be low, though there is no available weights information for comparison.

Landing Gear

The Global Hawk landing gear consists of a retractable nose gear mounted in the fuselage and a two-strut retractable main gear mounted in the wing root. The custom gear weight equation was used.

10.3.1.7 Payloads

Global Hawk payloads consist of a Synthetic Aperture Radar (SAR), an Electro-Optical/Infrared (EO/IR) payload, and the supporting electronics. The supporting electronics include an integrated sensor processor, a receiver/exciter/controller unit, transmitter (for SAR, presumably), and a sensor electronics unit. It is unclear if the elements of the communications architecture, INS, or structure are included in the advertised payload weight of 1,900 pounds [Jane's 1999]. The summation of the listed components comes to 797 pounds [Jane's 1999]. There is no available source that clarified this discrepancy. To satisfy the sizing mission profile, 1,900 pounds was assumed for the total payload weight, with an even weight division between SAR and EO/IR.

10.3.1.8 Overall Weights

The available information in Jane's [1999] on Global Hawk weights does not contain any noticeable internal discrepancies. According to Jane's [1999], the empty weight is 9,200 pounds, the maximum fuel weight is 14,500 pounds, the payload weight is 1,900 pounds, and the maximum take-off weight is 25,600 pounds. The sum of the components comprising the maximum take-off weight equals the maximum take-off weight.

There is conflicting information from other sources on Global Hawk weights. Northrop Grumman [2003] lists the gross take-off weight at 26,700 pounds. Due to typical weight growth of aircraft, both weights may be true for the associated reporting time. The Jane's [1999] weight is assumed as correct for the purposes of sizing.

The payload weight of 1,900 pounds, and the fuel fraction associated with Jane's [1999] fuel weight and maximum take-off weight were input. The target design gross weight is assumed to be equal to the maximum take-off weight. The calibration process sought to match the empty weight and design gross weight. The empty weight matches within 0.2%, and the design gross weight matches within 0.2%.

The Global Hawk weight summary is shown in Figure 10-7.

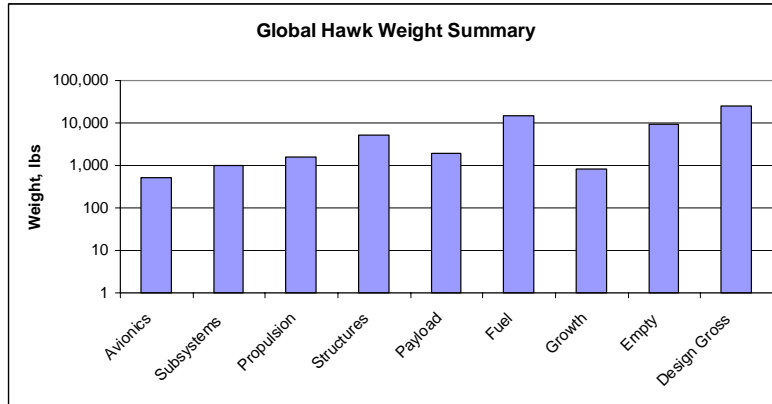


Figure 10-7 Global Hawk Weights Summary

The mass fractions are shown in Figure 10-8.

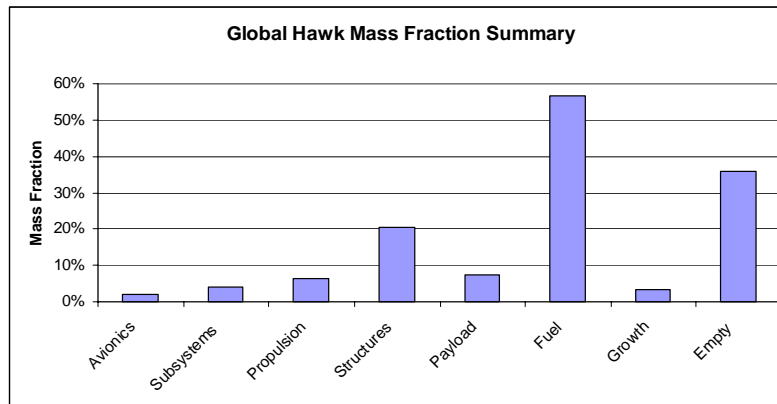


Figure 10-8 Global Hawk Mass Fraction Summary

10.3.1.9 Aerodynamics

The predicted Global Hawk incompressible trimmed Lift to Drag (L/D) over the range of Reynolds number per unit length is shown in Figure 10-9.

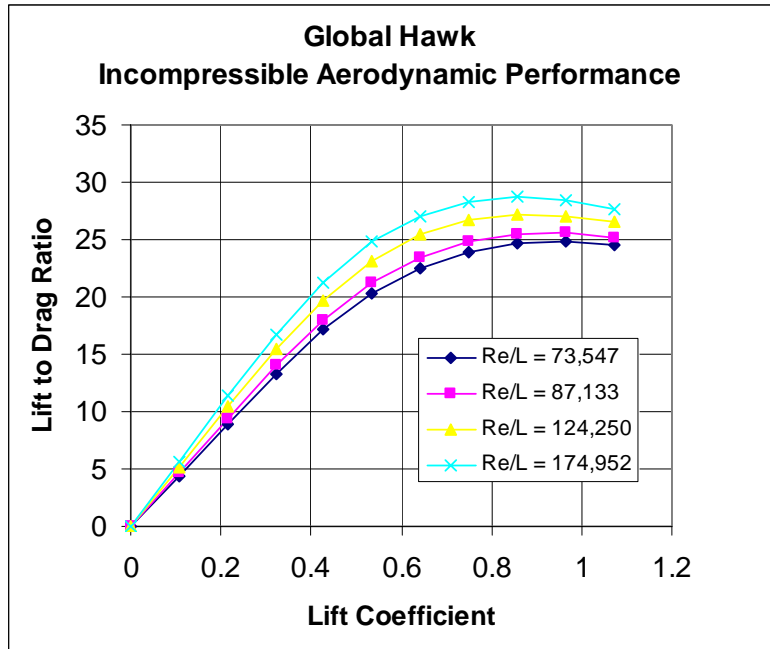


Figure 10-9 Global Hawk Trimmed Incompressible Aerodynamic Performance

The Global Hawk drag contributors by drag type at Mach 0.7 at the maximum bounding Reynolds number are detailed in Figure 10-10.

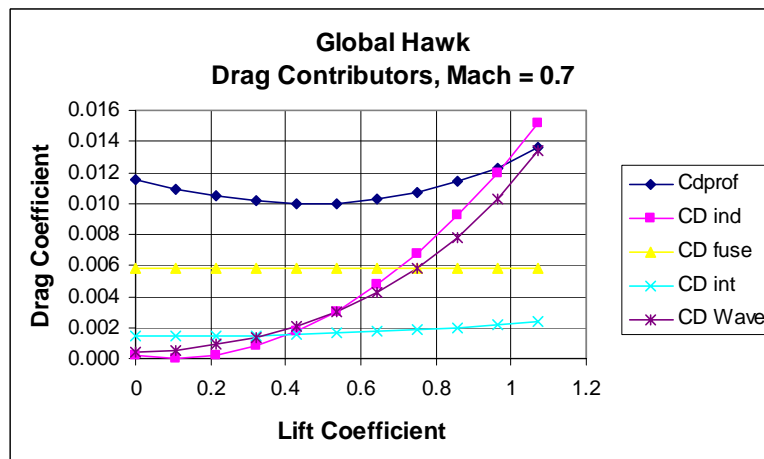


Figure 10-10 Global Hawk Trimmed Drag Contributors

Several aerodynamics methods were used to generate the drag polar. The Trefftz plane analysis was used to determine the trimmed lift distribution and induced drag. The parametric airfoil method was used to determine the profile drag. A static margin of 5% was assumed. A 5% miscellaneous drag factor was applied. All other aerodynamics methods are standard.

10.3.1.10 Performance

Altmann [2002] provides useful information on the Global Hawk performance and flight envelope limitations. The maximum equivalent airspeed is 175 Keas, and the maximum Mach is approximately Mach 0.7.

Northrop Grumman advertises the Global Hawk Performance as 24 hours time on station at 1,200 nautical miles radius [Northrop 2003]. This performance estimate was adopted for sizing. Range credit was assumed to be 100 nautical miles for the initial climb to 50,000 feet, and 200 nautical miles from the end of cruise to the final loiter altitude. A half-hour loiter at 5,000 feet was assumed for airfield operations. Altitude and Mach characteristics are shown in Figure 10-11, Figure 10-12, and Figure 10-13. Note that Figure 10-13 shows the Mach and altitude points flown in the optimized mission profile, not the boundaries of the flight envelope. Figure 10-13 shows the same data points as Figure 10-11 and Figure 10-12. Sudden changes in the Mach-altitude profile occur during transitions from one mission segment to another, such as changing from loiter to egress.

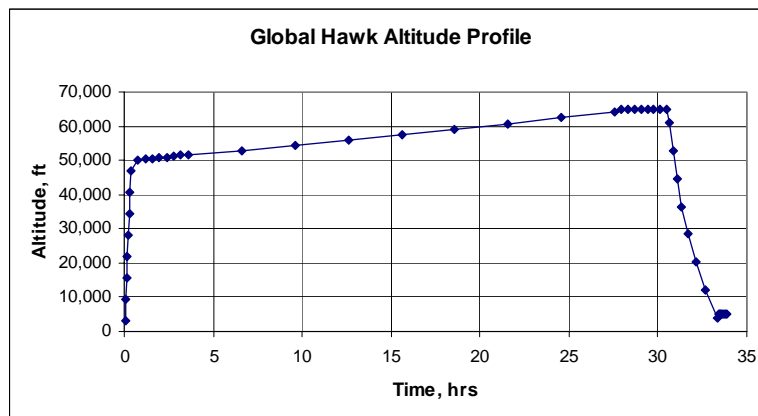


Figure 10-11 Global Hawk Altitude Profile

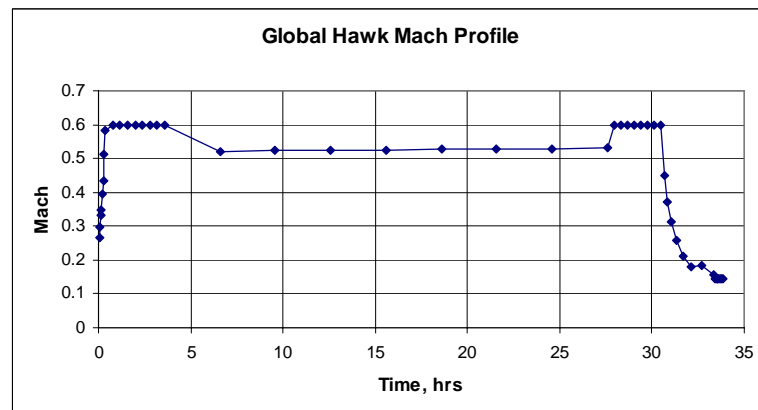


Figure 10-12 Global Hawk Mach Profile

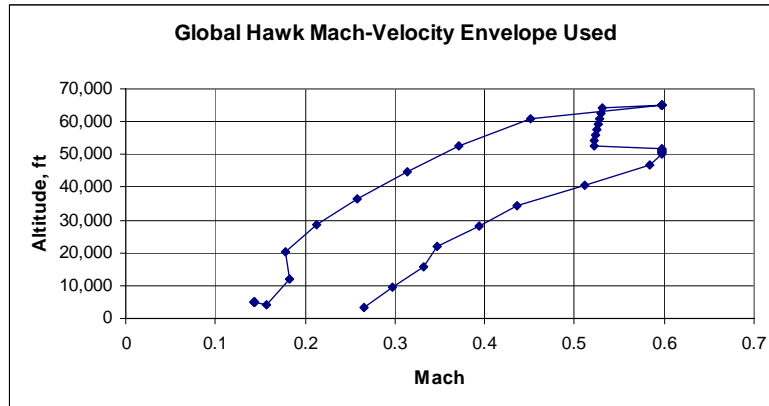


Figure 10-13 Global Hawk Mach-Altitude Envelope

10.3.1.11 Design Technology

The weights and performance calibration process resulted design technology levels are shown in Table 10-3.

Design Item	Tech Level (0-1)
Volume Efficiency	0.5
Induced Drag	0.31
Interference Drag	1.0
Wave Drag	0.31
Laminar Flow	0.31
Factor Of Safety	1.0
Weight Growth	0.35
Installation Weight	0.5

Table 10-3 Global Hawk Design Technology Levels

10.3.2 Predator

10.3.2.1 Predator Description

Predator is a Medium-Altitude Endurance (MAE) UAV designed to provide battlefield surveillance with a beyond line of sight communications capability. This aircraft is an evolution from the General Atomics Gnat UAV. The Predator program began in 1994 as an ACTD. The program transitioned to operational use very early in development.

10.3.2.2 Geometry Characteristics

The Predator key geometry characteristics are shown graphically in Figure 10-14, and numerically in Table 10-4.



Figure 10-14 Predator

Item	Value	Source
Wing span	48.7 ft	Jane's [1999]
Aspect ratio	19.25	Jane's [1999]
Sweep (quarter chord)	0°	Jane's [1999]
Fuselage Length	26.7 ft	Jane's [1999]

Table 10-4 Predator Geometry Characteristics

10.3.2.3 Propulsion

Predator uses the Rotax 914 reciprocating engine to drive a pusher propeller. Major engine characteristics are presented in Table 10-5.

Item	Value	Source
Maximum Power (S/L)	105 HP	Jane's [1999]
BSFC	0.5 lbm/HP-hr	Assumed
Weight	150.4 lbs	Jane's [1999]

Table 10-5 Predator Propulsion Characteristics

The predicted installed predator engine performance is shown in Figure 10-15 and Figure 10-16.

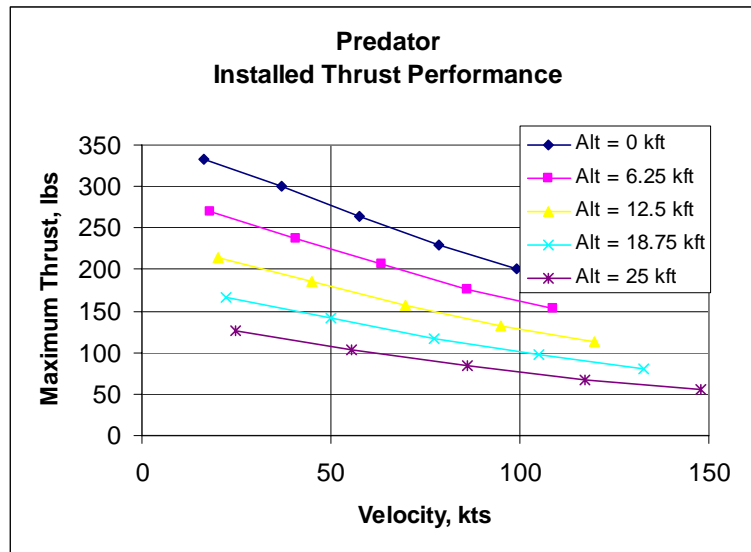


Figure 10-15 Predator Installed Thrust Performance

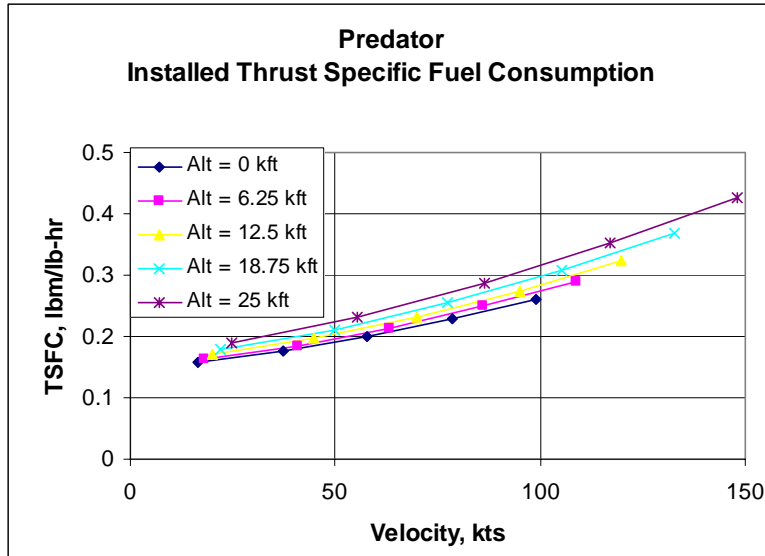


Figure 10-16 Predator Installed Specific Fuel Consumption Performance

10.3.2.4 Avionics

Predator has a relatively simple avionics suite compared to Global Hawk. Predator is largely a single-sting system with little redundancy. A summary of the Predator avionics weights is presented in Figure 10-17.

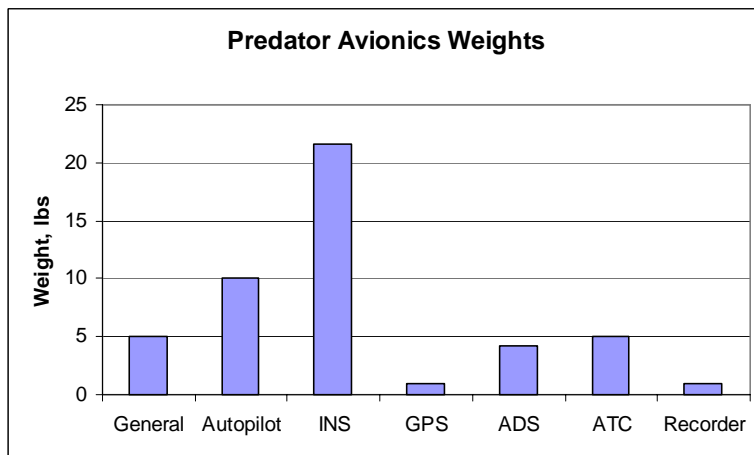


Figure 10-17 Predator Avionics Weights Summary

General Avionics

The Predator general avionics category is intended to capture non-allocated avionics weights. The general avionics weight allocation was 5 pounds, which was a best-judgment assumption used in the absence of better information.

Autopilot

Details of the autopilot physical characteristics are not available. The Predator autopilot must support both autonomous flight and pilot commanded maneuvering. The autopilot weight allocation was 10 pounds, which was a best-judgment assumption used in the absence of better information.

INS

Predator has a single Litton LN-100G INS, weighing 21.6 pounds.

GPS

Predator has a GPS capability, and 1 pound was allocated to the receiver. Unlike Global Hawk, Predator does not land autonomously with the aid of DGPS.

Air Data System

The air data system (ADS) was calculated via the custom method. The ADS is assumed to have medium-low ruggedness, a medium-high level of miniaturization, and medium-low performance. The resulting ADS weight is 4.28 pounds.

Air Traffic Control

Predator has a VHF/UHF ATC radio and an IFF capability [Jane's 1999]. The ATC weight was assumed to be 5 pounds, based on the weight class of simple general aviation aircraft ATC equipment. The ATC weight is assumed to be avionics weight, though it is possible that it may be considered payload weight. The ATC equipment may not be permanent avionics.

Recorder

The data recording capability of the Predator is unknown. The avionics data recorder weight allocation was 1 pound, which was a best-judgment assumption. Any additional data recorder weight is assumed to be covered under payload weights.

10.3.2.5 Subsystems

A summary of the Predator subsystems weights is presented in Figure 10-18.

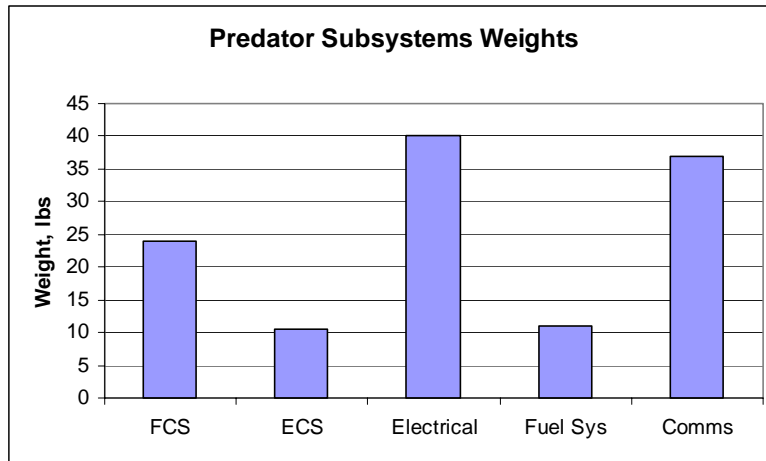


Figure 10-18 Predator Subsystems Weights Summary

Flight Control System

The Predator flight control system consists of inboard and outboard wing trailing edge control surfaces and all-flying ruddervators. All control surfaces are electrically actuated. The custom flight control system method (FCS Method 7) was employed to estimate this weight.

Electrical System

The electrical system consists, at minimum, of a generator and power distribution wiring. The Raymer [1992] transport electrical system weights equation (Electrical System Method 6) was employed. The calculated nominal power load is 2.81 kW.

Fuel System

Little is known from available literature of the Predator fuel system. The Raymer [1992] transport fuel system weight equation (Fuel System Method 2) was used.

Environmental Control System

The Predator ECS system is assumed to be a ram-air system. The performance model includes the impacts of the ram air on aerodynamic efficiency. The Roskam [1990] - General Dynamics low-subsonic aircraft ECS weight equation (ECS Method 2) was used.

Communications

Predator has a sophisticated communications system. The Predator has a satellite communications capability for command and control and imagery downlink. It also has the ability to communicate within line-of-sight range to a launch and recovery ground station.

Predator uses a 30-inch parabolic dish for satellite communications. The custom dish weight estimation method is used to calculate the weight, volumetric, and power impacts.

Predator includes communications equipment. All or part of the equipment is produced by Loral. This equipment is assumed to include the Limited Capability Common Data Link, which weighs 18.3 pounds.

10.3.2.6 Structures

The structure is largely made of carbon/epoxy composites [Jane's 1999]. The smaller Gnat UAV in the Predator family is stressed for 6 G maneuvers at an unspecified weight. Absent of further information, the 6 G loading was applied to the Predator. A summary of the Predator structural weights is presented in Figure 10-19.

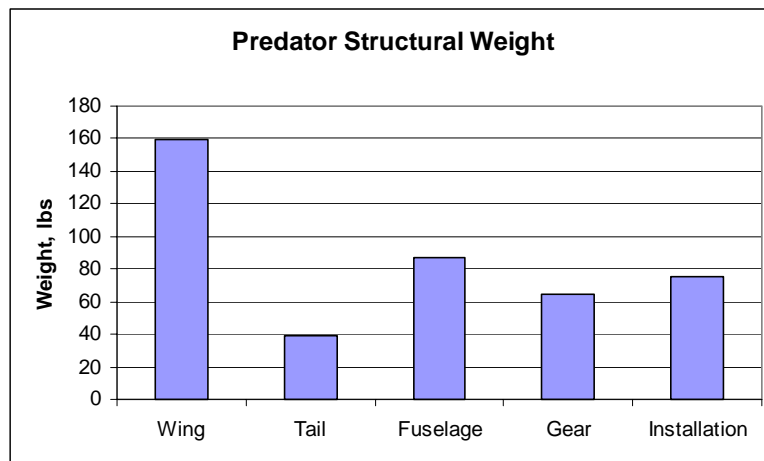


Figure 10-19 Predator Structural Weight Summary

Wing

The piecewise linear beam model was applied to the wing structure. The wing was assumed to weigh 75% of the equivalent aluminum wing with a minimum gage of 0.02 inches. The 75% composites factor was attained through the calibration process, since the empty weight could not be sufficiently reduced through other parameters. The 75% composites multiplication factor applied to the wing, tails, and fuselage was estimated through the calibration process.

Tails

The tail weight was estimated with the piecewise linear beam model. The tail was assumed to weigh 75% of the equivalent aluminum tail with a minimum gage of 0.02 inches. The factor of 75% was matched to the wing factor, since the wing and tails were probably designed by General Atomics with similar methods.

Fuselage

The fuselage weight was estimated with the Raymer General Aviation fuselage weight equation. A factor of 75% was applied to account for the extensive use of composites in the fuselage. Again, the 75% factor was identical to that of the wings and tails due to the assumed similarities in the design approach.

Landing Gear

The landing gear weight was estimated with the custom tricycle landing gear weight method.

Payloads

Predator is known to carry both EO/IR and SAR payloads. The advertised payload capacity is 450 pounds. The weights of the actual payloads appear to be much less than the maximum payload weight. The Versatron Skyball EO/IR payload with supporting electronics weighs 66 pounds. The Lynx SAR payload weighs 115 pounds. These two payloads were incorporated for the purposes of the sizing mission.

10.3.2.7 Overall Weights

Jane's [1999] lists the Predator Empty weight at 772 pounds, a fuel weight of 650 pounds, and a maximum payload weight of 450 pounds. The sum of these weights comes to 1,872 pounds. Jane's lists the maximum take-off weight at 2,250 pounds. Jane's [1999] does not state what payload is carried for the mission. The empty weight and fuel weight from Jane's are assumed to be valid, and these values were applied directly. The payload weight incorporated for the mission profile and the weights sizing is the sum of the known EO/IR and SAR payload weights, which totals 181 pounds. The target design gross weight is 1,603 pounds. The calibrated Predator analysis design gross weight is within 0.5% of this value. The calibrated empty weight is within 0.6% of the target value. The predator weight and mass fraction summaries are presented in Figure 10-20 and Figure 10-21, respectively.

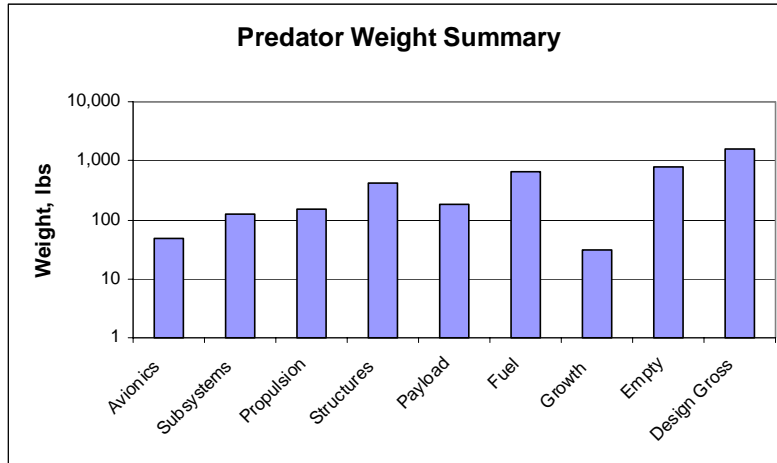


Figure 10-20 Predator Weights Summary

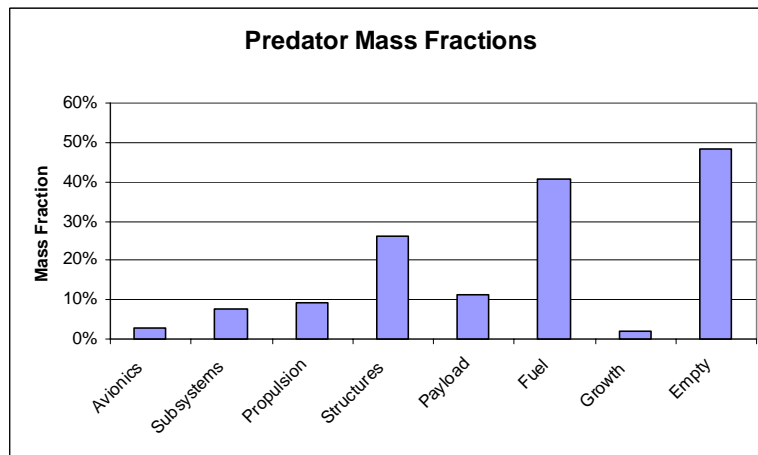


Figure 10-21 Predator Mass Fraction Summary

10.3.2.8 Aerodynamics

The predicted aerodynamics characteristics of the Predator are shown in Figure 10-22 and Figure 10-23.

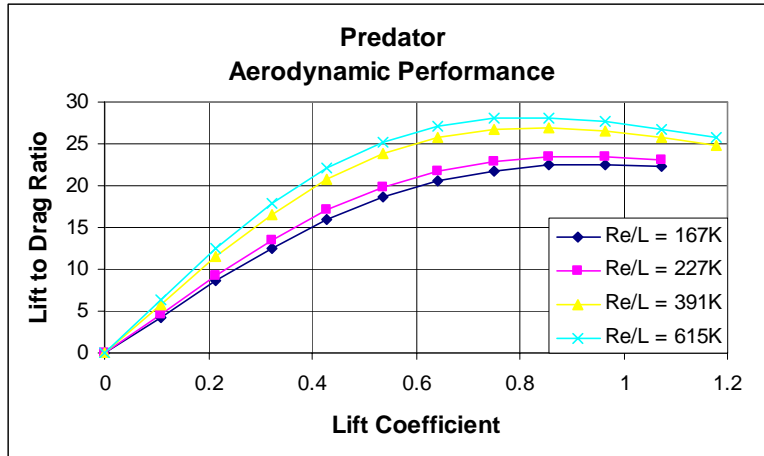


Figure 10-22 Predator Trimmed Aerodynamic Performance

The Predator drag contributors at the maximum bounding Reynolds number are shown in Figure 10-23. Note that wave drag is not shown here, since this is not a consideration at these flight Mach numbers.

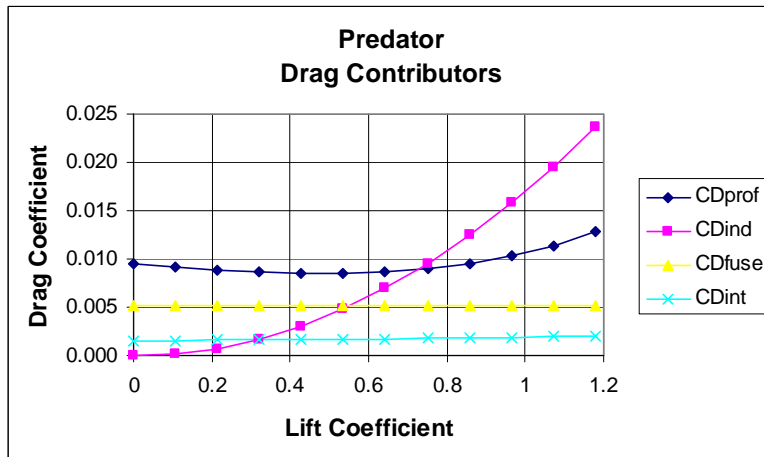


Figure 10-23 Predator Trimmed Drag Contributors

10.3.2.9 Performance

The mission profile for Predator is 24 hours time on station at a 500 nautical mile radius, according to Jane's [1999]. The 2003 General Atomics Predator brochure indicates that the performance is 24 hours time on station at a 400 nautical mile radius. The Jane's [1999] mission profile was used here. The EO/IR-SAR payload combined weight of 181 pounds was used, not the maximum payload capacity. An additional one-hour loiter at sea level is added to account for recovery operations. A ceiling of 25,000 feet was imposed on the mission performance calculation. A climb from sea level to 20,000 feet was included in the ingress segment. The descent from the final loiter point to sea level

was included in the egress segment. The Predator altitude and velocity performance is shown in Figure 10-24, Figure 10-25, and Figure 10-26. Note that Figure 10-26 is a combination of the data points shown in Figure 10-24 and Figure 10-25. Figure 10-26 does not represent the limits of the flight envelope, only velocity-altitude points flown in the optimized mission.

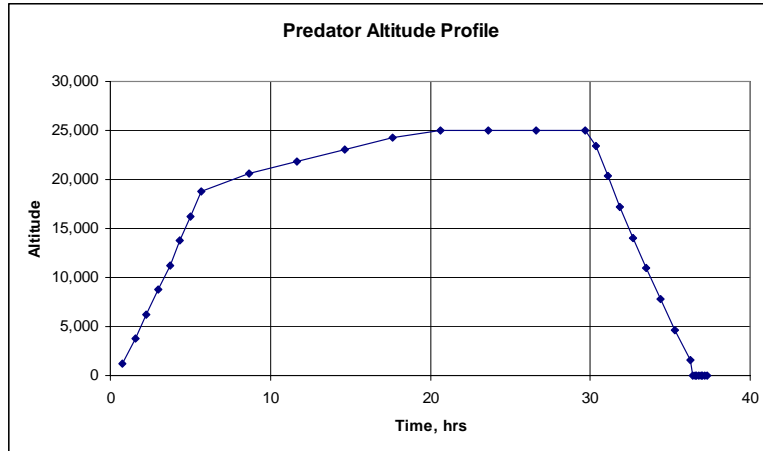


Figure 10-24 Predator Altitude Profile

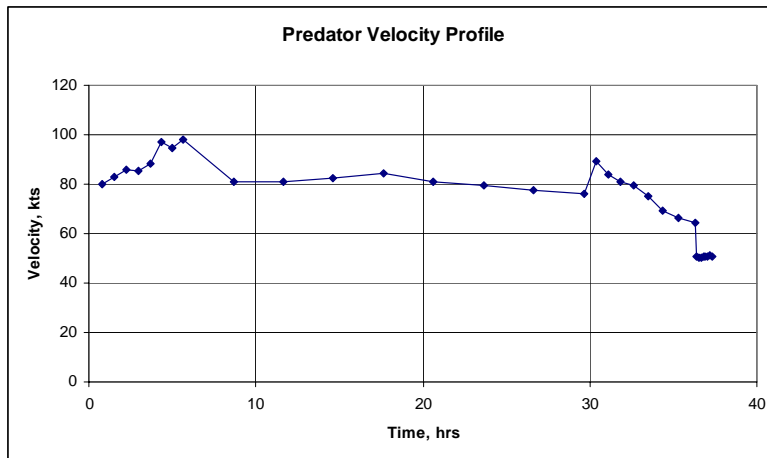


Figure 10-25 Predator Velocity Profile

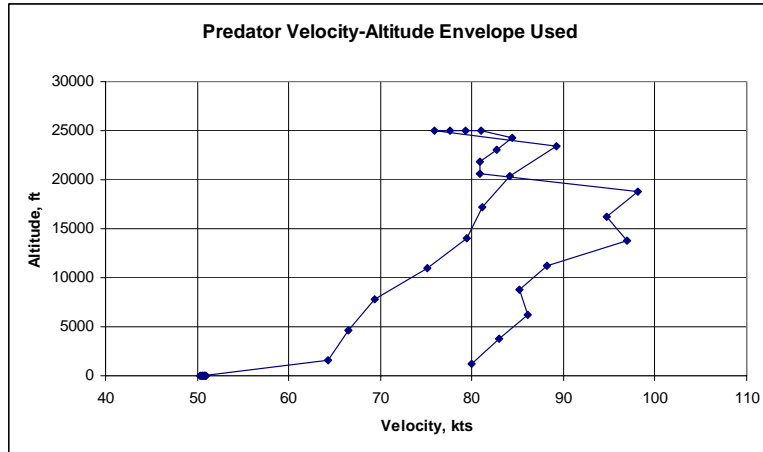


Figure 10-26 Predator Velocity-Altitude Envelope

10.3.2.10 Design Technology

The weights and performance calibration process resulted design technology levels shown in Table 10-6.

Design Item	Tech Level (0-1)
Volume Efficiency	0.5
Induced Drag	0.4
Interference Drag	1.
Wave Drag	1 (No compressibility impacts)
Laminar Flow	0.4
Factor Of Safety	1.
Weight Growth	0.75
Installation Weight	1.

Table 10-6 Predator Design Technology Levels

10.3.3 Shadow 200

10.3.3.1 Shadow 200 Description

Shadow 200 is a small tactical UAV designed to support line-of-sight battlefield surveillance missions. Initial development began in 1990. However, the technology year was assumed to be 2000 due to the extended development time, significant design evolution, requirements changes, and incorporation of more advanced technologies.

Palumbo [2000] is assumed to be the most authoritative source of Shadow 200 data. Palumbo describes an evolutionary design history beginning in 1990 that has not ended. The design attempts to leverage legacy components and tooling, and does not represent a clean sheet design synthesis. For example, the wing configuration is driven by a constraint to re-use Pioneer program wing tooling.

10.3.3.2 Geometry Characteristics

The Shadow 200 geometry characteristics are shown graphically in Figure 10-27, and numerically in Table 10-7.



Figure 10-27 Shadow 200

Item	Value	Source
Wing span	12.75 ft	Jane's [1999]
Aspect ratio	7.07	Jane's [1999]
Sweep (quarter chord)	0°	Jane's [1999]
Overall Length	11.17 ft	Jane's [1999]

Table 10-7 Shadow 200 Geometry Characteristics

10.3.3.3 Propulsion

The Shadow 200 uses a UEL AR 741 rotary engine. The engine drives a two-blade propeller. The engine weight listed includes the alternator. Major characteristics of the Shadow 200 engine are shown in Table 10-8.

Item	Value	Source
Maximum Power (S/L)	38 HP	Jane's [1999]
BSFC (Max power, S/L)	0.57 lbm/HP-hr	Jane's [1999]
Weight	28 lbs	Palumbo [2000]
Propeller Diameter	2.33 ft	Jane's [1999]

Table 10-8 Shadow 200 Propulsion Characteristics

The thrust and efficiency loss factor was found to be 0.59 through the calibration process. The aerodynamics technologies are already very conservative, so the only remaining performance factor for modification is the propulsion losses. Figure 10-28 and Figure 10-29 show the Shadow 200 predicted installed propulsion characteristics.

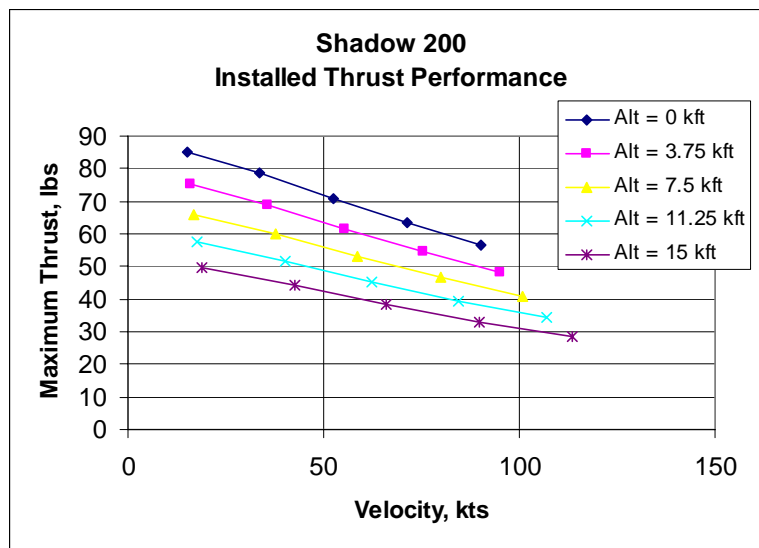


Figure 10-28 Shadow 200 Installed Thrust Performance

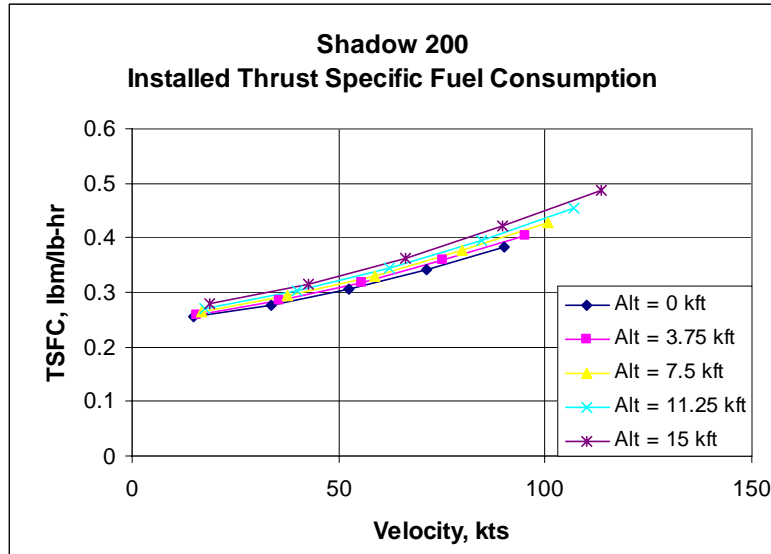


Figure 10-29 Shadow 200 Installed Specific Fuel Consumption Performance

10.3.3.4 Avionics

The Shadow 200 uses a relatively simple avionics suite. There is no indication that any of the avionics components are redundant.

General Avionics

Palumbo does not provide a detailed breakout of avionics weights. The total weight allocated to avionics is 57 pounds, which includes avionics, communications equipment, and elements of the electrical system [Palumbo 2000]. The avionics, at minimum, includes the autopilot and a Mode IV IFF transponder. No further information about the avionics suite is provided by Palumbo.

For the purposes of this analysis, 30 pounds was allocated to avionics and 27 pounds was allocated to communications equipment. The electrical system weight was set to 0 pounds, and the alternator weight was included in the propulsion weight.

The avionics suite apparently has evolved since 2000 to include more modern equipment. The Shadow 200 is known to use the Tactical Automatic Landing System (TALS), which has an airborne component weighing 3 pounds. The Shadow 200 currently uses the Athena GS-211 GuideStar™ autopilot, which weighs 2 pounds. This autopilot includes an INS and air data measurement equipment. The allocated weight of 30 pounds is applied, due to the year 2000 design year assumption.

10.3.3.5 Subsystems

An overview of the Shadow 200 subsystems weight results is in Figure 10-30.

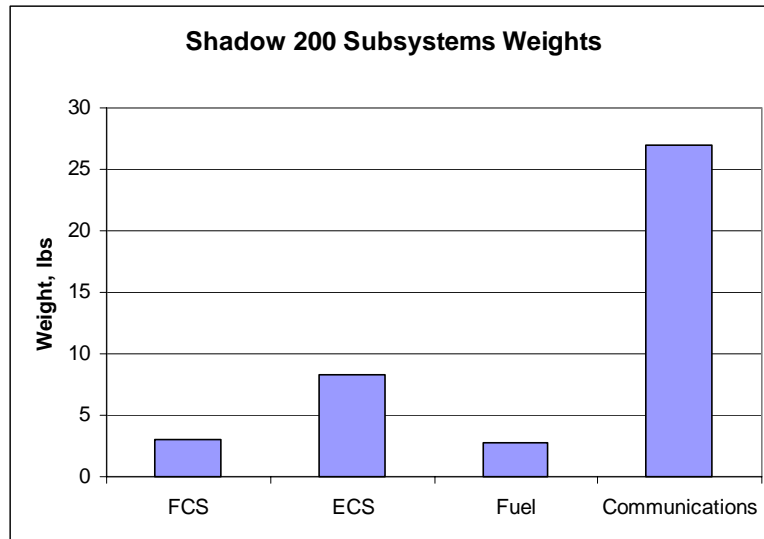


Figure 10-30 Shadow 200 Subsystems Weights Summary

Flight Control Systems

The Shadow 200 Flight Control System (FCS) consists of one aileron per wing and V-tail ruddervators. The custom FCS weight method (FCS Method 7) was used to estimate FCS weight.

Electrical System

The electrical system weight was set to 0 to accommodate the weight accounting system differences between this model and the weights described by Palumbo [2000]. The Palumbo [2000] alternator weight is included in the engine weight. Other elements of the electrical system weights are captured in the avionics weight, due to the weights accounting provided by Palumbo [2000]. The electrical system weight is fully accounted for by the engine and avionics weight categories.

Fuel System

The available literature provides little information on the Shadow 200 fuel system. The Shadow 200 wing tanks are believed to be self-sealing. The Raymer [1992] Transport fuel system weight equation (Fuel System Method 2) was used, despite being outside the applicable range. The fuel system numbers appear to be reasonable.

Environmental Control System

The available literature provides no information on the Shadow 200 Environmental Control System (ECS). A ram-air ECS was assumed, and the associated performance impacts are included in the flight performance model. The Roskam [1990] - General

Dynamics low-subsonic aircraft ECS weight method (ECS Method 2) was used. This weight method appears to scale well to small UAVs.

Communications

The Shadow 200 is equipped with the Tactical Common Data Link, which is a moderate bandwidth line-of-sight communications link. No actual weights information is known for this system, but 27 pounds was assumed, based on the assumed allocation between avionics and communications weights described earlier. Separate communications relay payloads may be integrated, but they are not baseline avionics, and they were not included here.

10.3.3.6 Structures

The Shadow 200 structure is 90% composites, which is primarily composed of graphite and Kevlar epoxy [Jane's 1999]. Jane's [1999] lists the limit load at 3.6 G, and Palumbo [2000] lists the limit load at 3.8 G. The limit load of 3.8 G was applied here. This limit was applied directly at the design gross weight condition, since the fuel fraction is relatively low on this UAV. The Shadow 200 structural weight estimations are summarized in Figure 10-31.

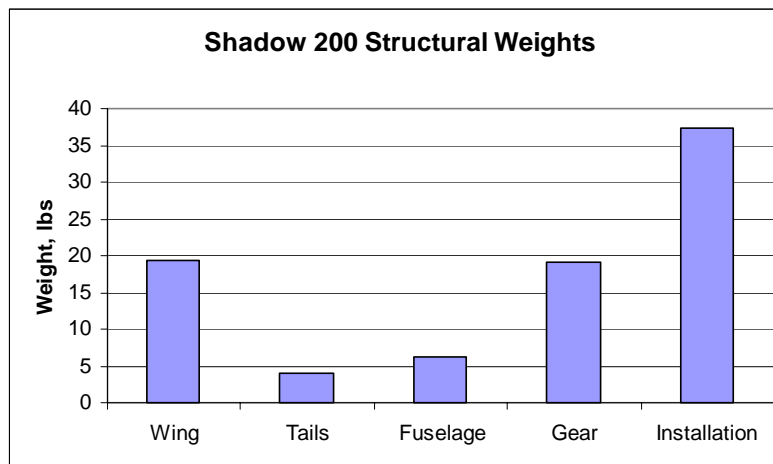


Figure 10-31 Shadow 200 Structural Weight Summary

Wing

The piecewise linear beam model was used to determine the wing weight. The reference material is the 2017 Aluminum alloy with a minimum gage of 0.02 inches. A composites wing weight multiplication factor of 0.85 was used, as suggested by Raymer [1992].

Tails

The piecewise linear beam model was used to determine the tail weight. The reference material is the 2017 Aluminum alloy with a minimum gage of 0.02 inches. A composites tail weight multiplication factor of 0.83 was used, as suggested by Raymer [1992].

Fuselage

The shadow 200 fuselage consists of a main pod and two booms that connect the tail to the wing. The primary contributor to the weight is the main pod. This houses the engine, payload, landing gear, most subsystems, and the avionics. The Raymer [1992] General Aviation fuselage weight equation was used to estimate the fuselage weight. Although this equation is operating outside of its intended application, the resulting weight appears to be reasonable when combined with the overall installation weight. The installation weight was primarily added to the fuselage weight. A 0.9 fuselage weight multiplication factor was applied to account for composites usage, as recommended by Raymer [1992].

Landing Gear

The Shadow has both fixed landing gear and a parachute recovery capability. The standard landing gear weight equation is used to account for the fixed landing gear weight. The gear drag contributions are accounted for in the aerodynamics analysis. The parachute recovery gear was estimated using the custom parachute recovery system weight method.

10.3.3.7 Payloads

The maximum payload weight is 52 pounds [Palumbo 2000]. This weight was assumed to be split evenly between EO/IR and SAR functionality for the purposes of calibration and technology modeling.

10.3.3.8 Overall Weights

Palumbo [2000] provides group weights for structures, avionics, propulsion, payload, and fuel. The structural weight in Palumbo appears to contain many elements of the subsystems weights. 27 pounds of avionics weights are moved to subsystems to account for the communications subsystems assumptions. These parameters as modified for this research, the take-off gross weight (design gross weight here), and the corresponding values from the analysis are provided in Table 10-9. The Shadow 200 weight and mass fraction summaries are presented in Figure 10-32 and Figure 10-33, respectively.

	Palumbo Original/Modified	Analysis	Difference
Structure (struct + subs)	115/142 lbs	144.5 lbs (Includes wt. growth)	1.77%
Avionics	57/30 lbs	30 lbs	0%
Engine/Alternator	28 lbs	28 lbs	0%
Payload/Ballast	52 lbs	52 lbs	0%
Fuel	64 lbs	64.63 lbs	1.0%
Design Gross Weight	316 lbs	319.1 lbs	0.99%

Table 10-9 Shadow 200 Calibration weight comparison

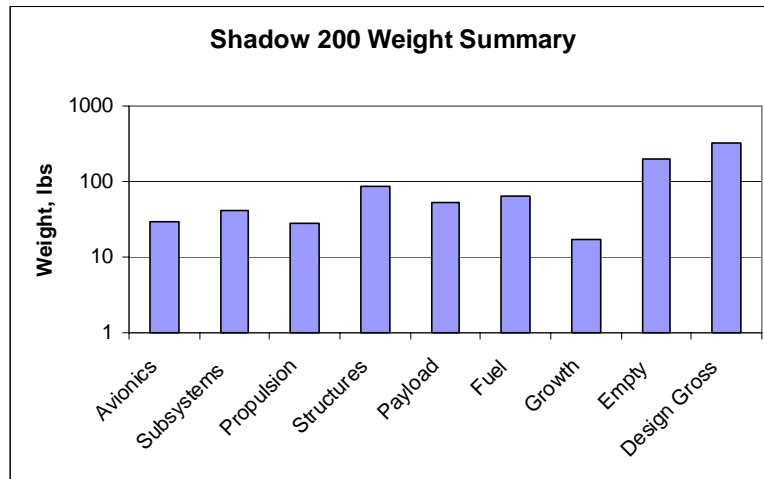


Figure 10-32 Shadow 200 Weights Summary

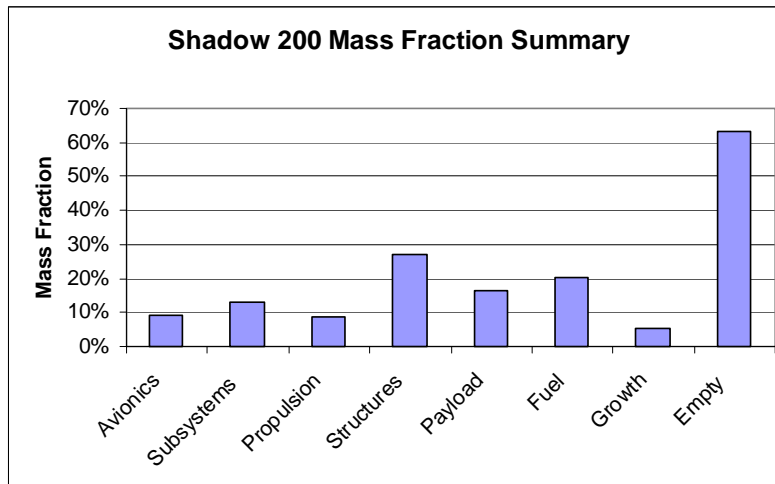


Figure 10-33 Shadow 200 Mass Fraction Summary

10.3.3.9 Aerodynamics

Figure 10-34 and Figure 10-35 show the estimated aerodynamic performance of the Shadow 200.

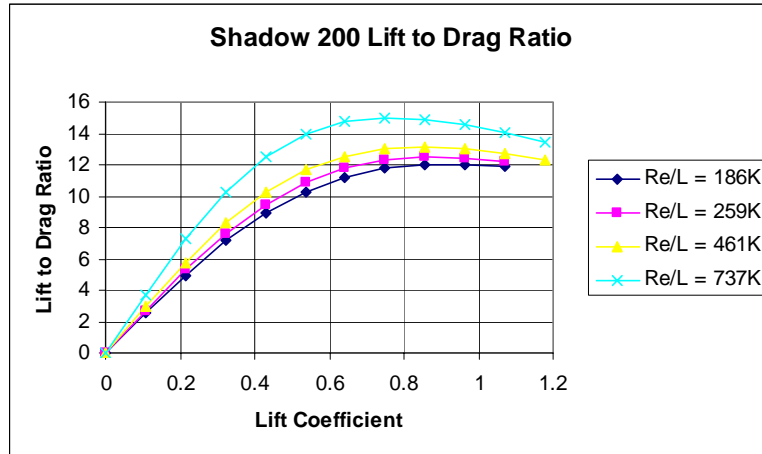


Figure 10-34 Shadow 200 Trimmed Aerodynamic Performance

Note that gear drag was included in the drag contributor summary. The Shadow 200 flies without retracting the landing gear.

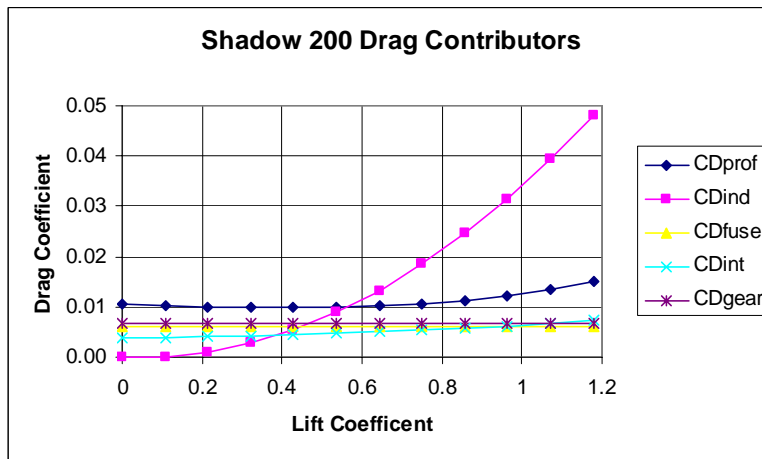


Figure 10-35 Shadow 200 Trimmed Drag Contributors

10.3.3.10 Performance

The Shadow 200 flight performance is described differently by various sources. Jane's [1999] indicates that the Shadow has an operational radius of 43 nautical miles and 6 hours of endurance, though it is not explicitly states that this occurs on the same flight or that the maximum payload weight is included. An AAI Shadow 200 brochure presented

at the Association of Unmanned Vehicle Systems International (AUVSI) conference on or before 2003 states that the performance is 5-6 hours without further details. A second AAI brochure presented at AUVSI at or before 2003 states that the Shadow 200 can fly 50 'clicks' (kilometers) and remain on station up to 4 hours. The second brochure also states (on the opposite side) that the endurance at 100 kilometers is 4 hours.

Palumbo [2000] describes the design mission profile as 4 hours time on station at a 200 kilometer radius. Here, an additional 30 minutes of endurance was added at the end of the mission to account for recovery operations and mission planning uncertainties.

Palumbo [2000] and Jane's [1999] state the Shadow 200 ceiling is 15,000 feet, which was applied here. The ingress segment climb was assumed to be from sea level to 12,500 feet. The aircraft then performed a cruise climb until reaching the ceiling. The aircraft descended from the final loiter altitude to sea level in the egress segment. Figure 10-36, Figure 10-37, and Figure 10-38 show the Shadow 200 altitude and velocity performance. Note that Figure 10-38 is assembled from the data points of the optimized mission profile, and does not represent the boundaries of the flight envelope. Rapid changes in the velocity-altitude profile occur during changes of mission segment, such as transitioning from loiter to egress.

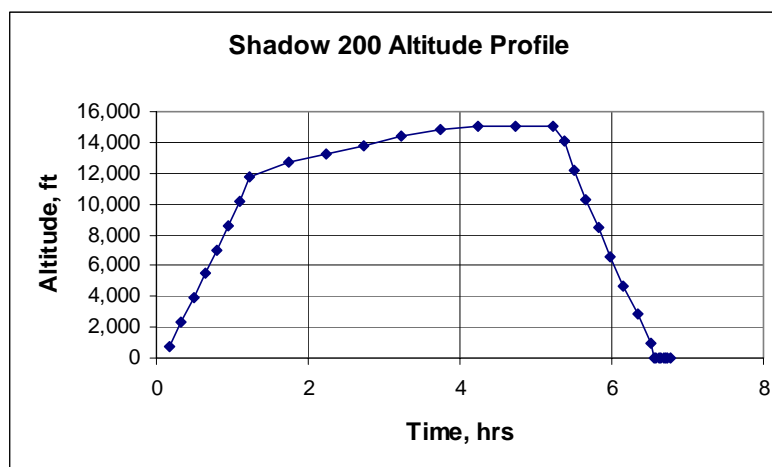


Figure 10-36 Shadow 200 Altitude Profile

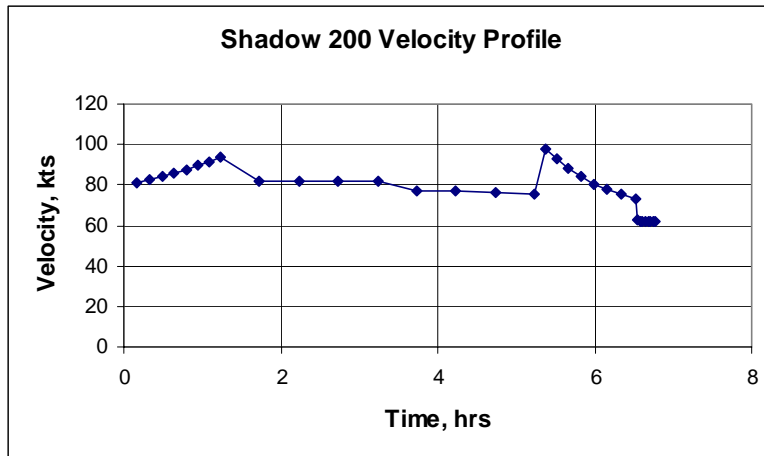


Figure 10-37 Shadow 200 Velocity Profile

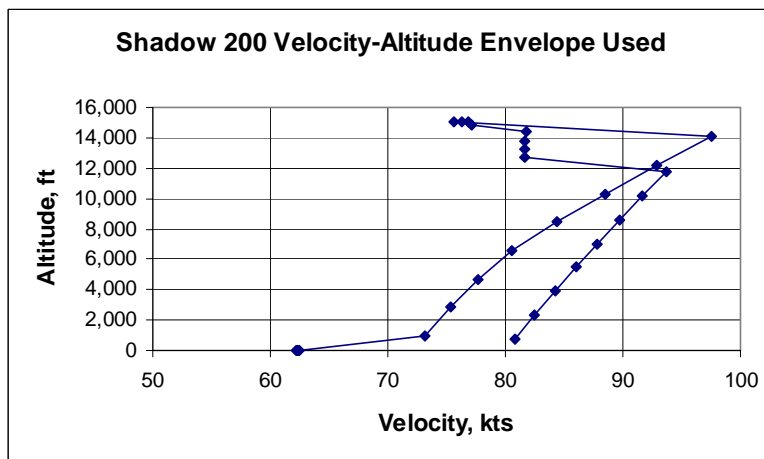


Figure 10-38 Shadow 200 Velocity-Altitude Envelope

10.3.3.11 Design Technology

The weights and performance calibration process resulted in the design technology levels shown in Table 10-10.

Design Item	Tech Level (0-1)
Volume Efficiency	0.5
Induced Drag	0.2
Interference Drag	1.
Wave Drag	1. (No compressible effects)
Laminar Flow	0.2
Factor Of Safety	0.5
Weight Growth	0.35
Installation Weight	0.35

Table 10-10 Shadow 200 Design Technology Levels

Chapter 11 Reference Year Calibration- Optimization Comparisons

11.1 Overview

Optimized designs using the same requirements and same technology levels as the calibration cases were developed. The reference year calibration cases were described in the previous chapter. The reference year calibration and optimization cases are compared in this chapter.

The calibration cases are inappropriate for optimization, so a specialized parametric geometry formulation is necessary. The calibrated fuselage geometry will not re-shape to account for wing junctures, radome changes, or other considerations. The calibrated wings and tails are located and sized based on manual inputs, not parametric relationships. The parametric geometry has similarities among all cases, so it is not customized for any one case. Details of the parametric geometry are described in Chapter 5. The comparison between the reference year optimized parametric and calibrated designs is necessary to better understand the progression of design into the future.

There are more similarities than differences between the calibrated and optimized reference year cases. The avionics, subsystems, and payload inputs are identical. The technology levels and design levels are the same. There are no differences in analysis methods, such as aerodynamics, propulsion, mass properties, and performance analysis. The mission profile and input flight envelope constraints are identical.

The results of the Global Hawk, Predator, and Shadow 200 reference year optimized solutions are presented. Emphasis is placed on the differences between the calibrated and optimized solutions.

11.2 Reference Case Comparisons

11.2.1 Global Hawk 1994 Optimum Design

Table 11-1 shows the Global Hawk active design variables and the associated limiting bounds. These values were used for all optimized Global Hawk cases without modification.

Design Variable	Lower Bound	Upper Bound
MF_{Fuel}	0.4	0.65
b_W	20	140
AR_W	10	30
T/W	0.18	0.4
L_{Fuse}	15	50
t/c_W	0.09	0.17
l_W	0.2	1.
Λ_W	0°	15°

Table 11-1 Global Hawk Design Variables

The optimized Global Hawk geometry has significant differences relative to the calibration case. The comparison of the calibrated and optimized 1994 Global Hawk cases are shown graphically in Figure 11-1, Figure 11-2, and Figure 11-3. The calibrated Global Hawk case is on the left, and the optimum Global Hawk is on the right for these figures. The numeric differences in the geometry between these cases are presented in Figure 11-4.

The parametric fuselage applied to all optimized Global Hawk cases uses the lower fairing to mount the wing, whereas the 1994 calibration case uses the lower fairing to house the SAR payload. The basic parametric fuselage prior to the addition of the radome and wing fairing has a lower length-to-diameter ratio than the calibration fuselage. There is no EO/IR housing in the optimized case. The optimized fuselage has a slightly shorter fuselage length.

The tail configurations for the two cases are essentially identical. The optimized case uses the parametric tail volume coefficient method. The tail moment arm is less on the optimized case, so the tail area is greater.

The optimized wing has a shorter span, lower aspect ratio, and much reduced sweep than the baseline wing. The optimized Global Hawk has a wing loading 3.5% higher than the baseline, permitting an efficient higher speed loiter. The overall wing area went down 8.6%. Compressibility impacts do not appear to limit either case.

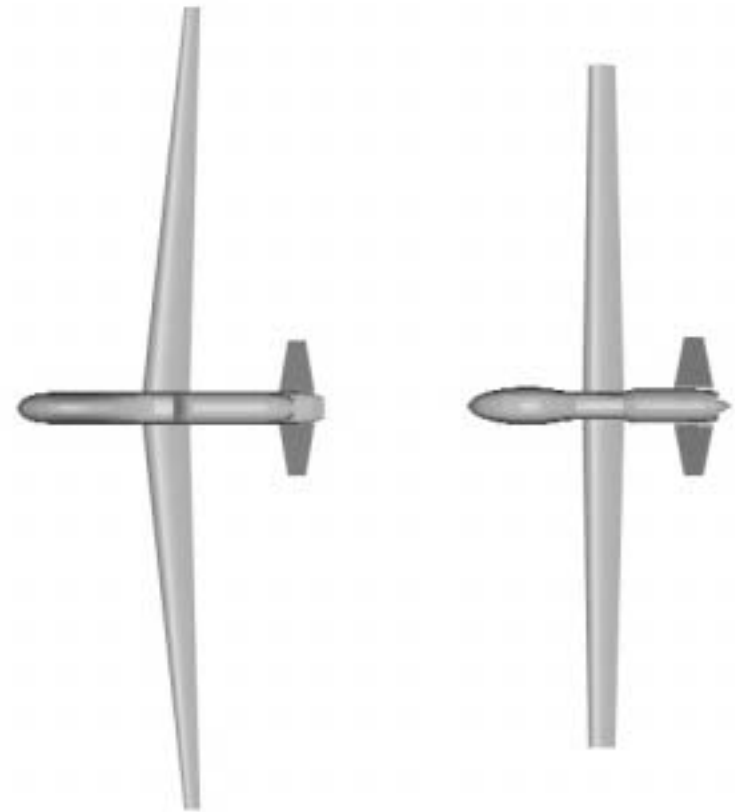


Figure 11-1 1994 Global Hawk Geometry Comparison – Top View



Figure 11-2 1994 Global Hawk Geometry Comparison – Side View



Figure 11-3 1994 Global Hawk Geometry Comparison – Isometric View

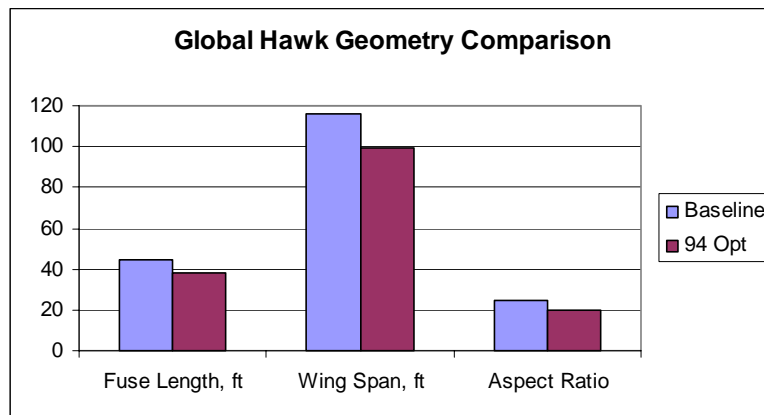


Figure 11-4 Global Hawk Geometry Comparison

The primary weights differences between the optimal and baseline cases reside within the structures and propulsion weights. The optimized Global Hawk has a reduced aspect ratio and shorter wingspan, resulting in reduced aerodynamic efficiency but also a reduced structural weight. The avionics and payload weights are identical. The minor subsystems weight differences are caused primarily driven by the flight control system. The differences in the weight and mass fraction summaries are shown in Figure 11-5 and Figure 11-6, respectively.

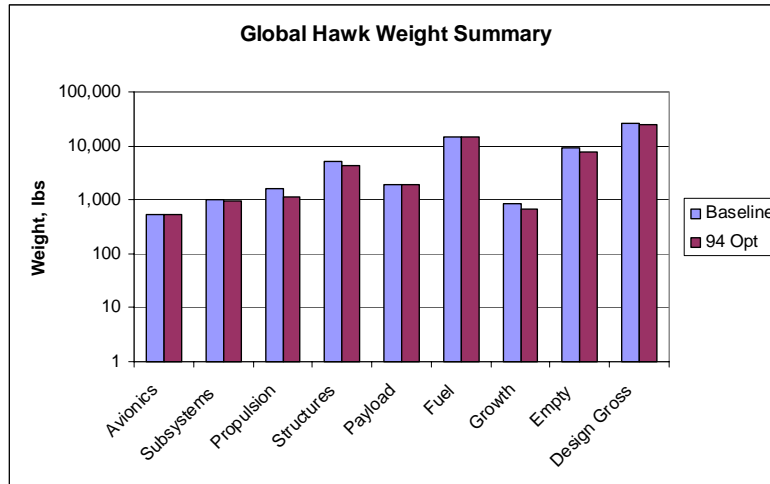


Figure 11-5 Global Hawk Summary Weights Comparison

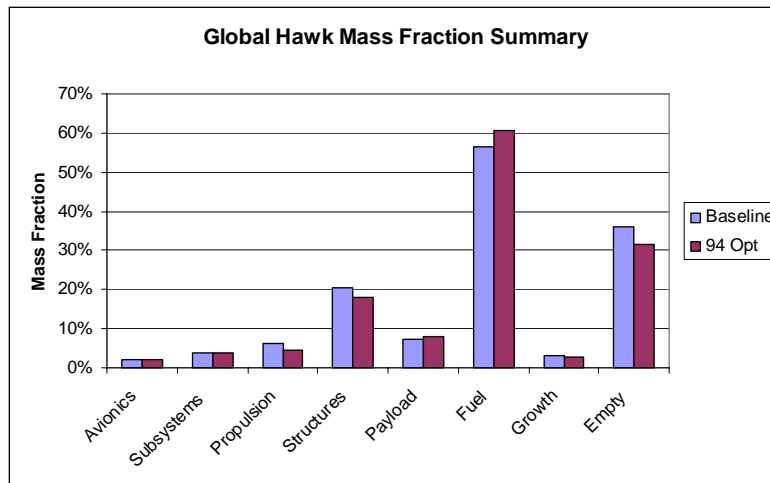


Figure 11-6 Global Hawk Summary Mass Fraction Comparison

There are no significant differences in the mission profiles. The calibration case achieves the maximum altitude of 65,000 feet shortly before the optimized case. The lift to drag ratio of the optimized case is lower than the calibration case, which is compensated for with the higher fuel fraction. The minor differences in specific fuel consumption are caused by the cruise Mach number and altitude experienced at a given point in the mission. The mission performance differences between the calibrated and optimized 1994 Global Hawk cases are presented in Figure 11-7, Figure 11-8, Figure 11-9, Figure 11-10, and Figure 11-11.

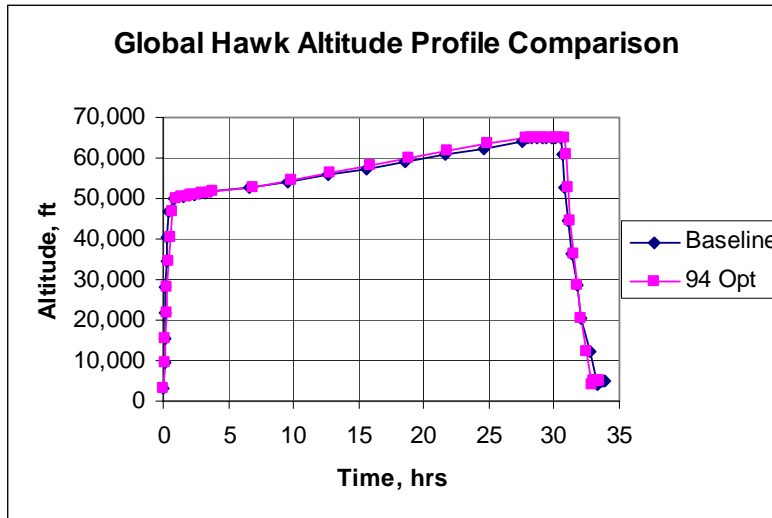


Figure 11-7 Global Hawk Altitude Profile Comparison

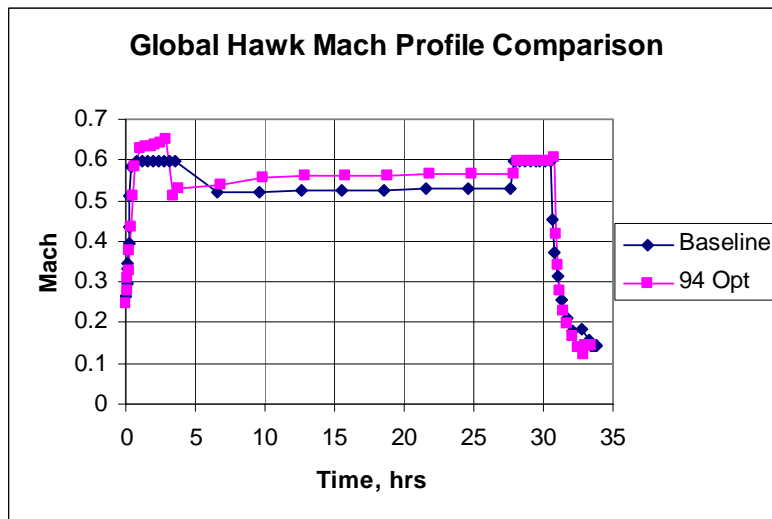


Figure 11-8 Global Hawk Mach Profile Comparison

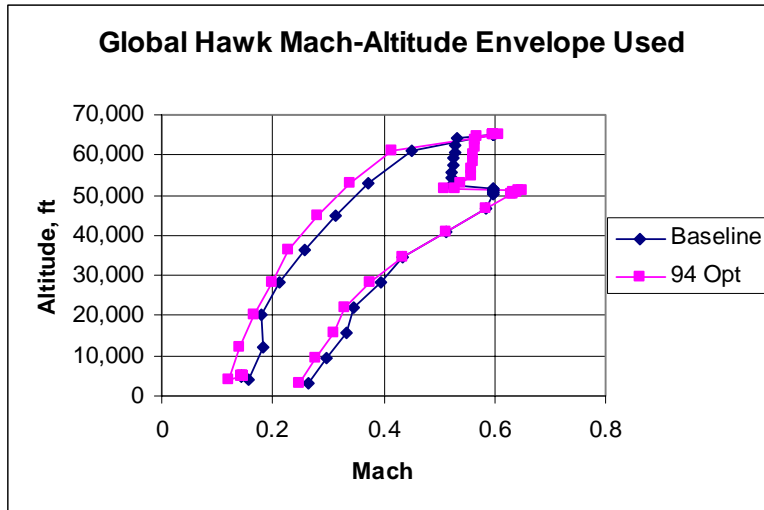


Figure 11-9 Global Hawk Mach-Altitude Envelope Used

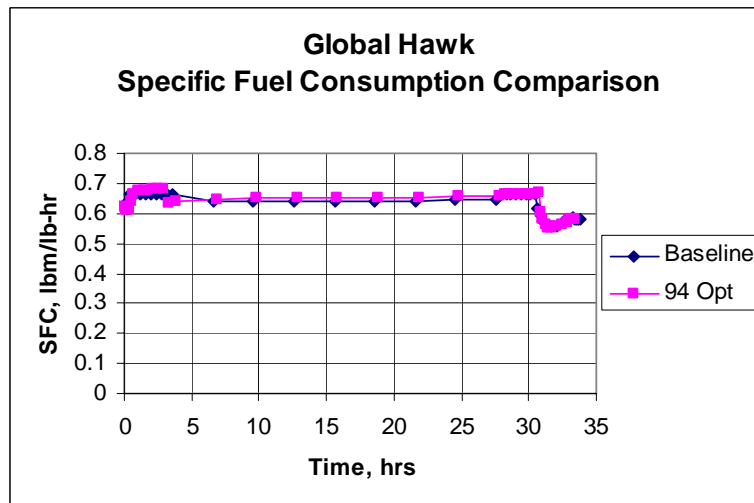


Figure 11-10 Global Hawk Specific Fuel Consumption Comparison

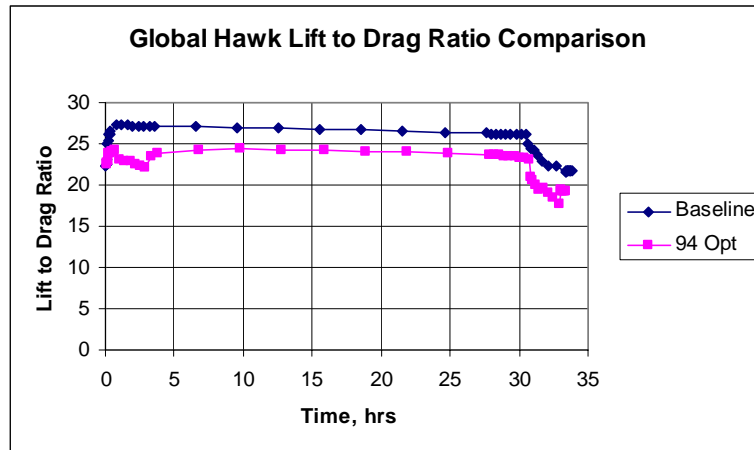


Figure 11-11 Global Hawk Lift to Drag Comparison

11.2.2 Predator 1994 Optimum Design

Table 11-2 shows the Predator active design variables and the associated limiting bounds. These values were used for all optimized Predator cases without adjustment.

Design Variable	Lower Bound	Upper Bound
MF_{Fuel}	0.25	0.45
b_W	6	55
AR_W	10	30
P/W	0.04	0.1
L_{Fuse}	5	30
t/c_W	0.09	0.17
l_W	0.2	0.9

Table 11-2 Predator Design Variables

The Predator 1994 optimal solution exhibits geometry variations relative to the calibration case. The geometry differences between these two cases are presented graphically in Figure 11-12, Figure 11-13, and Figure 11-14. The calibrated Predator is on the left and the optimum Predator is on the right for these figures. Key geometry differences are presented numerically in Figure 11-15.

The Predator parametric fuselage has distinct differences from the calibration case. The parametric Predator and parametric Global Hawk have the same radome sizing relationship, which scales the radome dimensions linearly with the parabolic dish diameter. The parametric Predator fuselage contains a wing fairing on the underside, whereas the calibrated Predator does not.

The optimization process resulted in a significantly lower length-to-diameter ratio and shorter fuselage length for the optimized Predator than for the calibration case. Although less visually pleasing than the calibration case, this is a valid solution.

The parametric Predator tail geometry is different for the two cases. Although still a V-tail configuration, the parametric Predator has a traditional V-tail, and the calibrated Predator has an inverted V-tail. The traditional V-tail was selected to minimize erroneous interference impacts in the Trefftz plane analysis that might be exploited by the optimizer and artificially drive the optimized solutions. The inverted V-tail was found to be free of interference problems on the baseline case, despite the V-tail plane intersecting the wing plane. The dihedral angle is higher on the optimized case because the wing aspect ratio is higher, which drives the vertical component of the tail. The tail proportions of the optimized case appear exaggerated because the tail moment arm is short.

The optimized solution has a slightly shorter span and nearly identical aspect ratio to the calibration case.

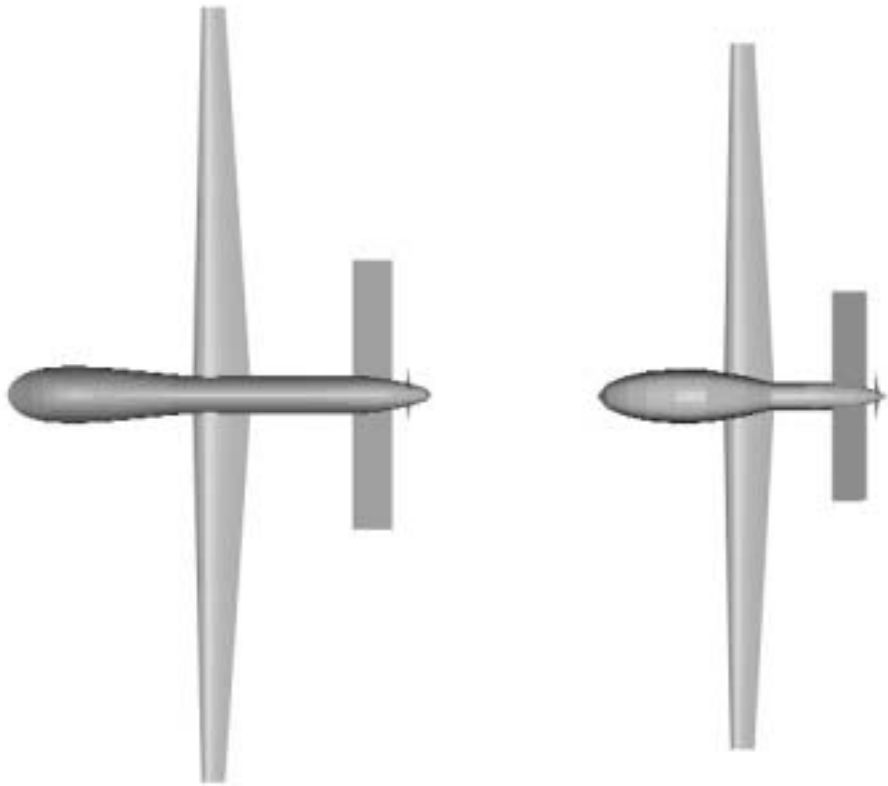


Figure 11-12 1994 Predator Geometry Comparison – Top View



Figure 11-13 1994 Predator Geometry Comparison – Side View

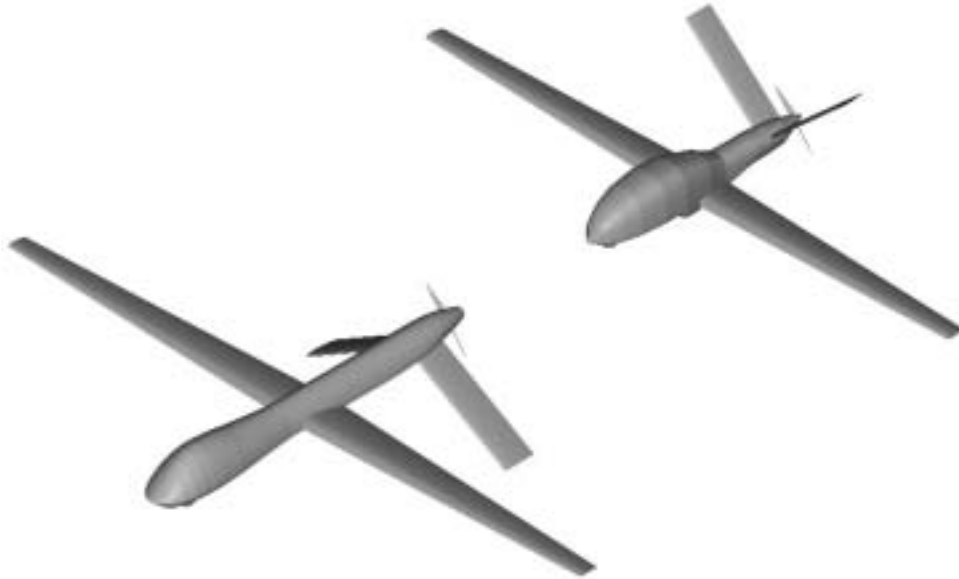


Figure 11-14 1994 Predator Geometry Comparison – Isometric View

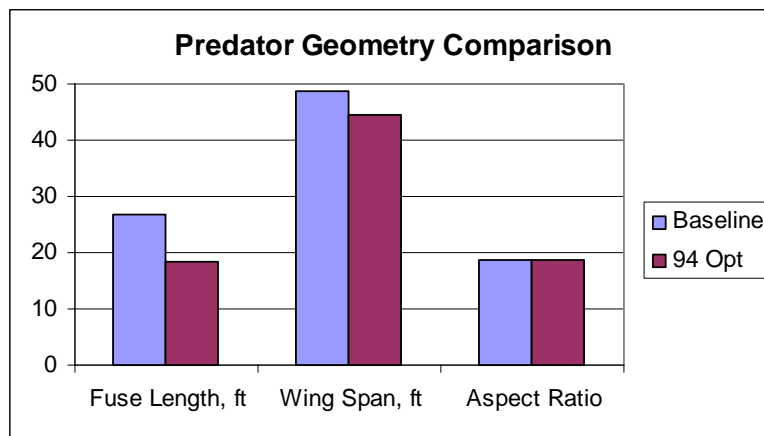


Figure 11-15 Predator Geometry Comparison

A comparison of the calibrated and optimized 1994 Predator weight and mass fraction summary is presented in Figure 11-16 and Figure 11-17, respectively. The optimized Predator has a lower design gross weight than the calibration case. The primary differences reside in structures and propulsion weights. The avionics and payload weights are identical. The differences in the subsystems are driven primarily by reduced flight control system and fuel system weights.

The uninstalled power to weight ratio for the optimized 1994 Predator is 15.5% less than the calibrated case. This directly drives the propulsion weight down, which has significant synergistic effects on the design. This appears to be a driver for the weight difference between the two cases. If a take-off analysis were performed, then a higher power to weight ratio might result.

In addition to the reduced propulsion weight influence, the structures weight reduction also appears to be a function of reduced wing, fuselage, and tail size.

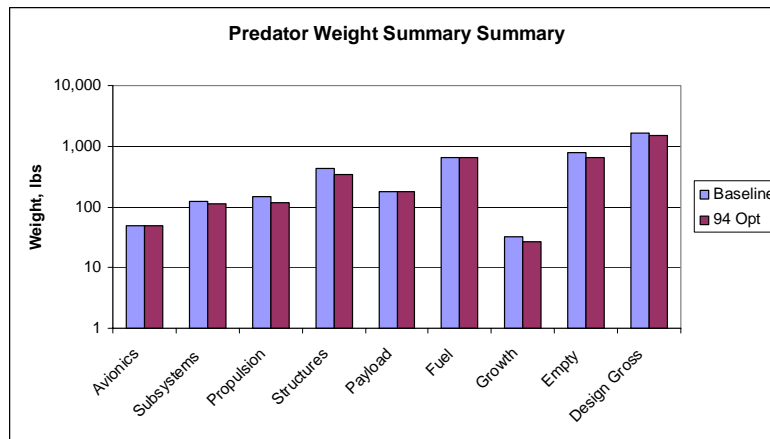


Figure 11-16 Predator Weights Summary Comparison

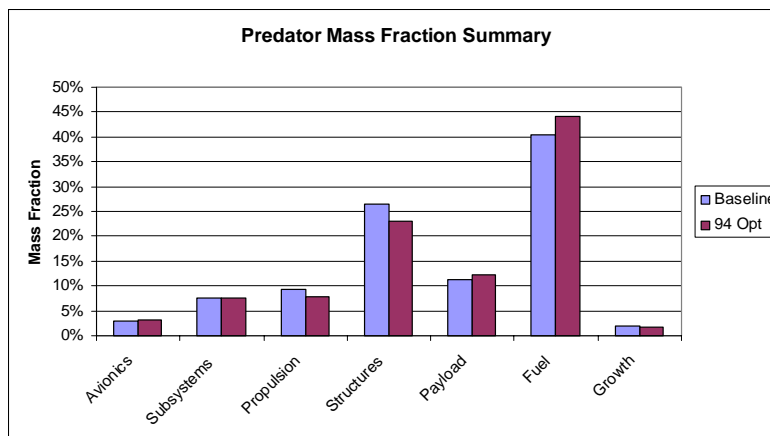


Figure 11-17 Predator Summary Mass Fraction Comparison

The internally optimized mission profiles for the two reference year Predator cases are similar. The mission performance characteristics are compared in Figure 11-18, Figure 11-19, Figure 11-20, Figure 11-21, and Figure 11-22. The optimized Predator has a wing loading 10.9% higher than the baseline case, resulting in higher speeds in some portions of the mission.

The difference in specific fuel consumption appears to be driven by the propeller, which is scaled as a function of engine power. The propeller efficiency is a function of the power required, the altitude, and airspeed.

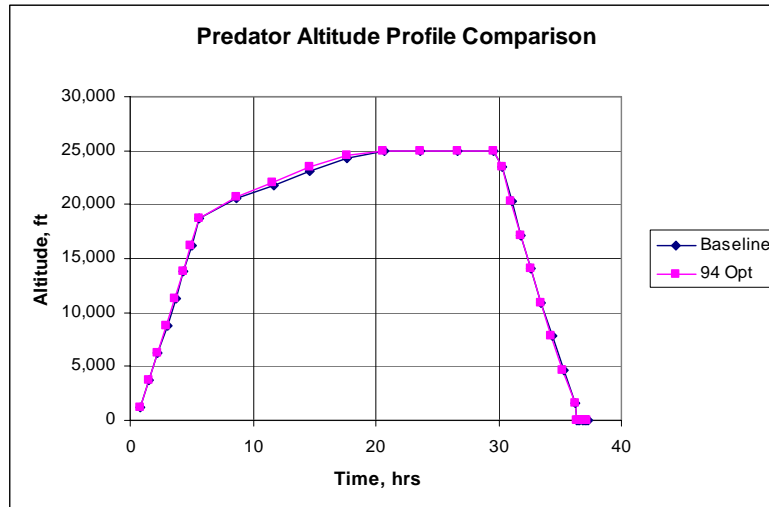


Figure 11-18 Predator Altitude Profile Comparison

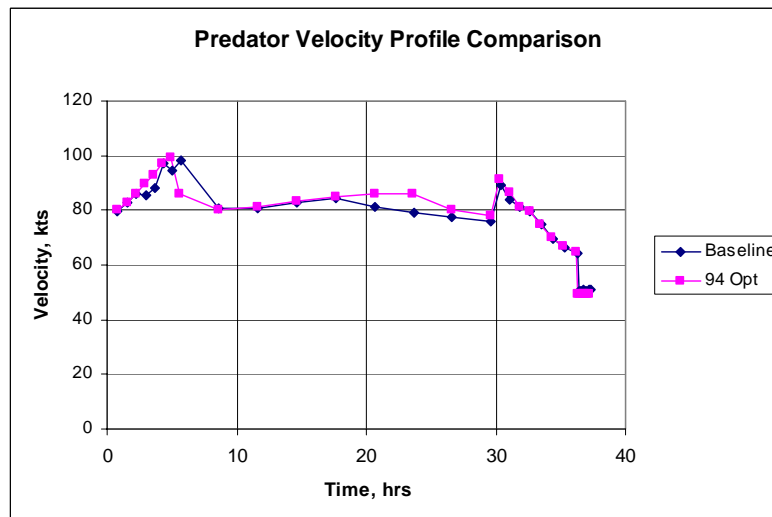


Figure 11-19 Predator Velocity Profile Comparison

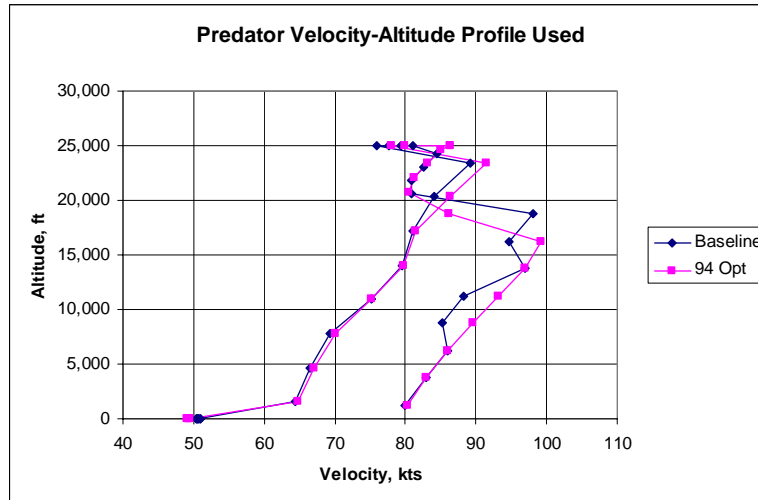


Figure 11-20 Predator Velocity-Altitude Envelope Used

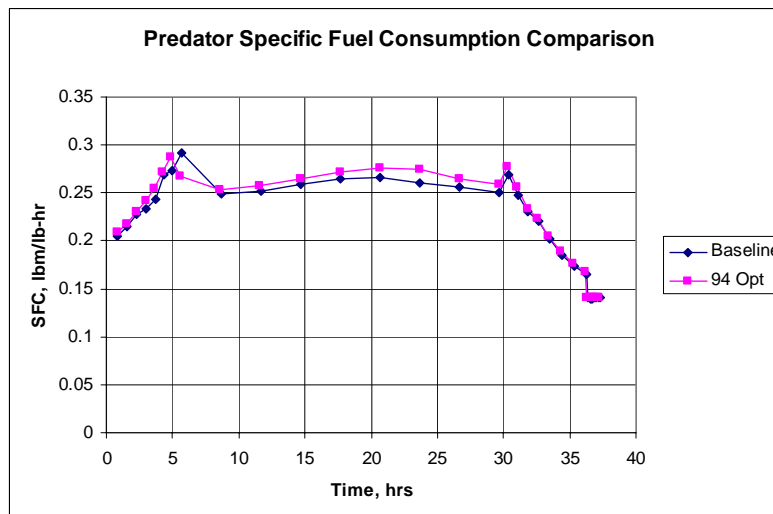


Figure 11-21 Predator Specific Fuel Consumption Comparison

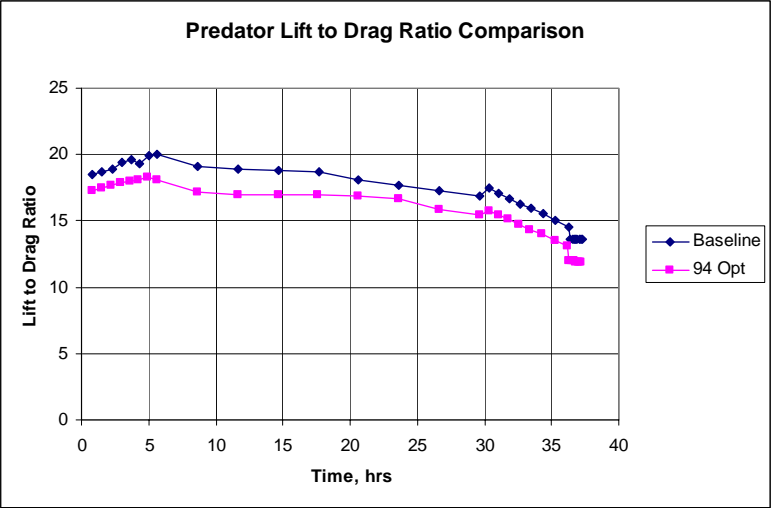


Figure 11-22 Predator Lift to Drag Comparison

11.2.3 Shadow 200 2000 Optimum Design

Table 11-2 shows the Shadow 200 active design variables and the associated limiting bounds. These values were used for all optimized Shadow 200 cases.

Design Variable	Lower Bound	Upper Bound
MF_{Fuel}	0.08	0.25
b_W	3	12.75
AR_W	5	20
P/W	0.05	0.2
L_{Fuse}	3	12
t/c_W	0.09	0.17
l_W	0.2	1

Table 11-3 Shadow 200 Design Variables

The Shadow 200 reference year optimal solution varies significantly from the calibration case. The geometry comparison of these cases is presented in Figure 11-23, Figure 11-24, and Figure 11-25. The calibrated Shadow 200 is on the left and the optimum Shadow 200 is on the right in these figures. The numerical geometry comparison is shown in Figure 11-25.

The fuselage geometry is noticeably different. The calibration Shadow 200 case fuselage has a pod and twin-boom configuration. This configuration is more difficult to integrate parametrically than the parametric fuselage formulation used for the other cases. Additionally, the parametric wing is attached to the lower fuselage with a wing fairing, whereas the calibration case has a mid-wing attachment to the pod fuselage. Future versions of the software could easily integrate a parametric twin-boom configuration.

The tail geometry is also different between the two cases. The calibration case has an inverted V-tail attached at the tips to the booms. The parametric tails are a traditional V-tail configuration attached to the fuselage.

The optimization process resulted in a higher aspect ratio wing than the calibration case. A maximum wingspan constraint of 12.75 feet, the span for the calibration case, was imposed to account for transportation considerations. The optimized case does not reach the wingspan constraint. The Shadow 200 was constrained by AAI to maintain the chord of the available tooling, which largely drove the wing design. The optimal case does not have this restriction, so the aspect ratio and wingspan are free to vary independently. The resulting aspect ratio was much higher than the calibration case. The optimal Shadow 200 flies faster than the calibrated Shadow 200, due to an increased wing loading.

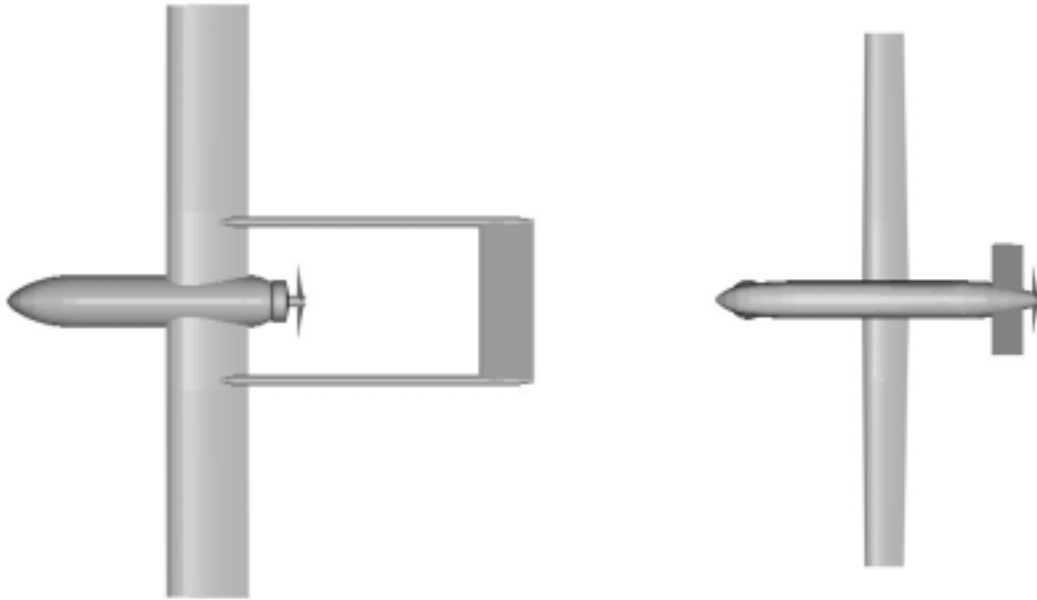


Figure 11-23 2000 Shadow 200 Geometry Comparison – Top View



Figure 11-24 2000 Shadow 200 Geometry Comparison – Side View

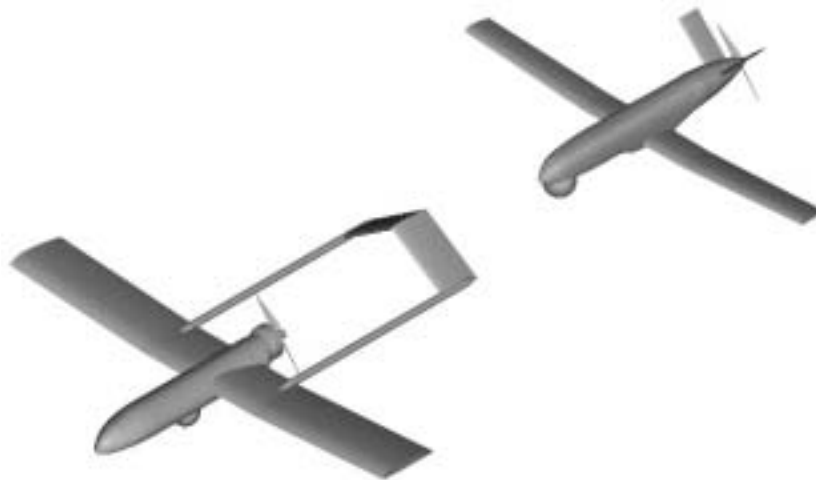


Figure 11-25 2000 Shadow 200 Geometry Comparison – Isometric View

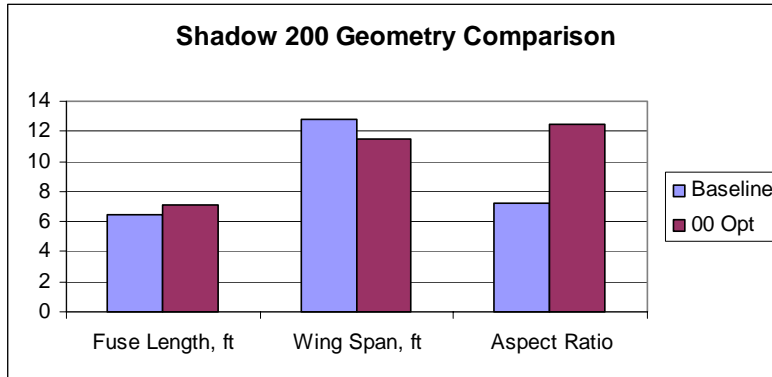


Figure 11-26 Shadow 200 Geometry Comparison

The Shadow 200 2000 weight and mass fraction summary comparisons are presented in Figure 11-27 and Figure 11-28, respectively. The avionics and payload weights between the two cases are identical. The differences in subsystems weights are largely due to flight controls and fuel system weight variations. The payload mass fraction is higher for the optimized case, showing an increase in relative utility. The higher payload mass fraction is made possible by a reduction in structural mass fraction. The fuel mass fractions are similar, which is a result of off-setting effects of the improved lift to drag ratio and degraded specific fuel consumption of the optimized case. The degraded specific fuel consumption is caused by propeller efficiency reduction at higher speeds.

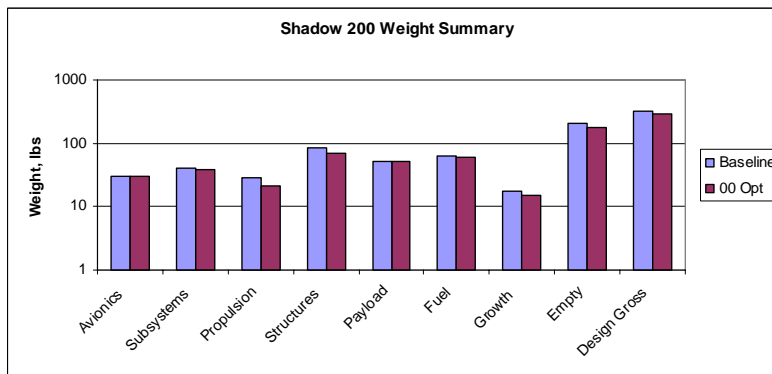


Figure 11-27 Shadow 200 Summary Weights Comparison

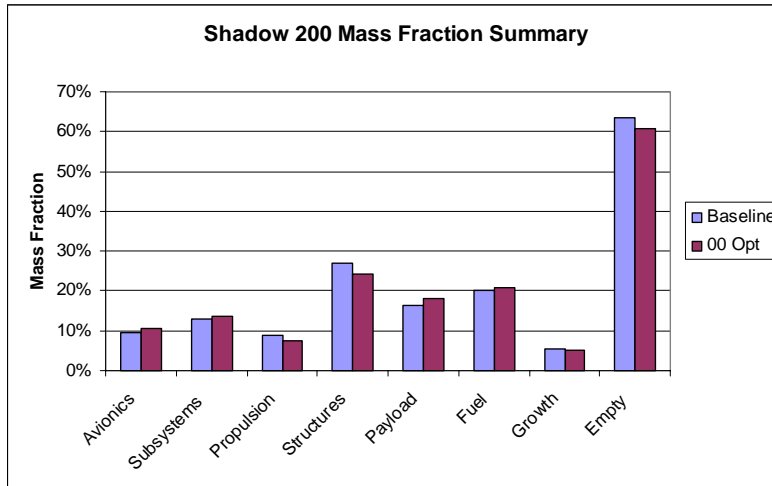


Figure 11-28 Shadow 200 Summary Mass Fraction Comparison

Comparison of the same-year Shadow 200 flight performance characteristics are shown in Figure 11-29, Figure 11-30, Figure 11-31, Figure 11-32, and Figure 11-33.

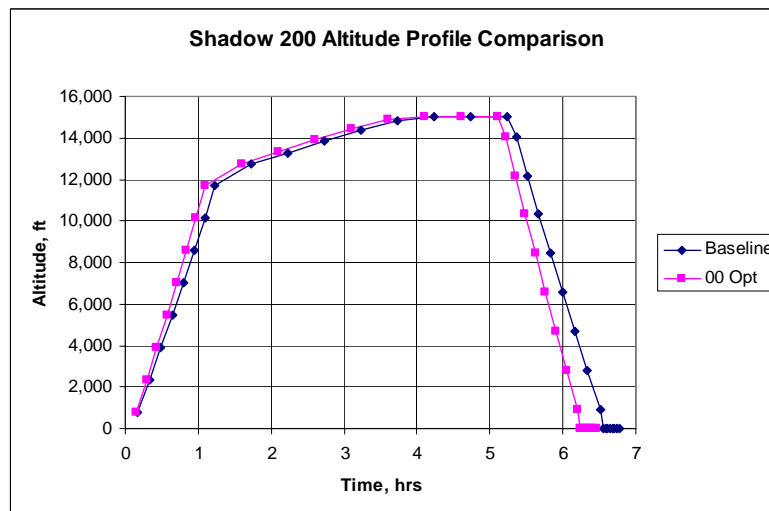


Figure 11-29 Shadow 200 Altitude Profile Comparison

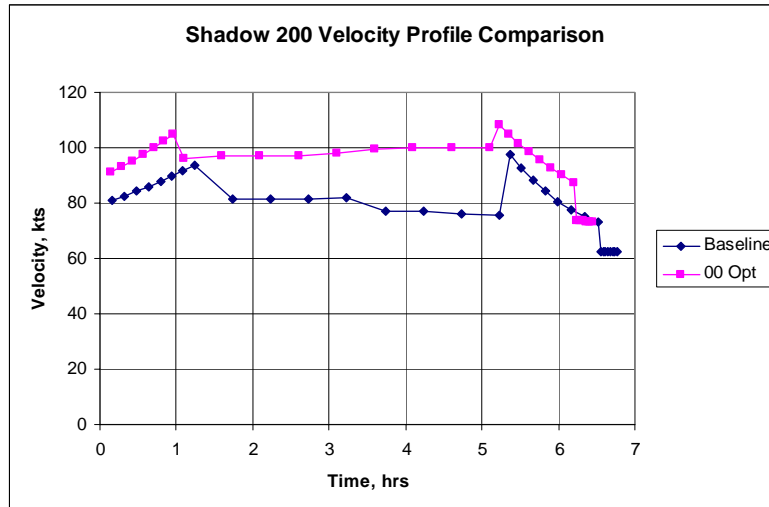


Figure 11-30 Shadow 200 Velocity Profile Comparison

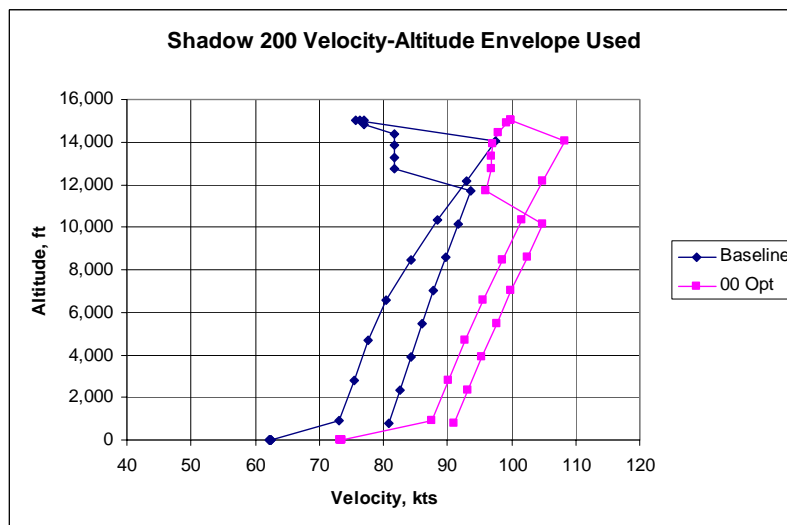


Figure 11-31 Shadow 200 Velocity-Altitude Envelope Used

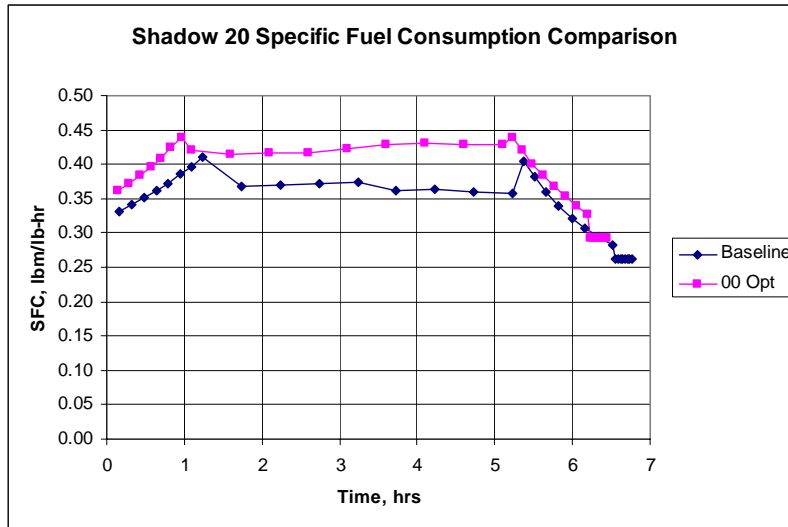


Figure 11-32 Shadow 200 Specific Fuel Consumption Comparison

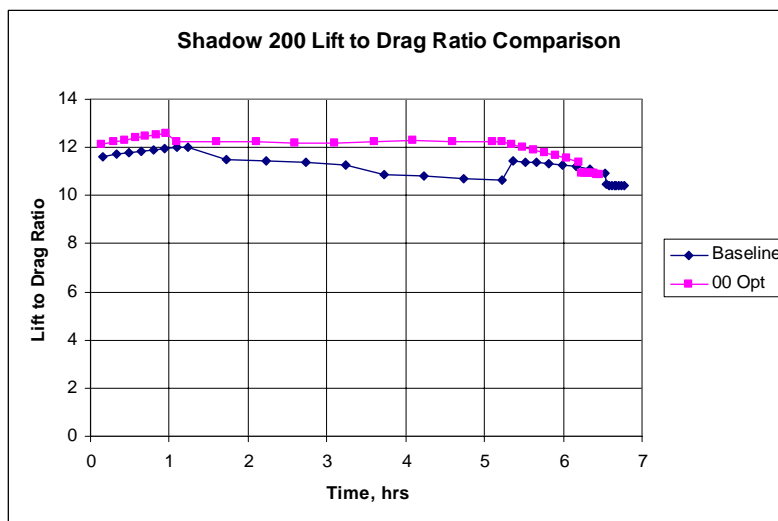


Figure 11-33 Shadow 200 Lift to Drag Ratio Comparison

Chapter 12 Technology Case Optimization Applications

12.1 Overview

The technology impacts investigation evaluated the design synthesis of air vehicles with constant requirements and advancing technologies. Optimization aided the design synthesis substantially. The Global Hawk, Predator, and Shadow 200 technology solutions are presented in this chapter.

12.2 Global Hawk Technology Impacts

12.2.1 Sizing Overview

The Global Hawk optimized cases experienced steady weight reduction through the advancing years. The relative improvement per period steadily diminished through 2010. The improvement degradation began to stabilize near 2015 through 2020. The 2025 optimum design was an unusually good design, taking a significantly different approach than the two preceding cases. The initial advances were mostly driven by the SAR payload weight reduction and propulsion improvements, followed by avionics/ subsystems, structures and aerodynamics. Beyond 2010, the relatively unvarying EO/IR payload weight limited the sizing improvement potential, despite advances in other technologies.

12.2.2 Geometry

The graphical summary of the Global Hawk technology cases is presented in Figure 12-1, Figure 12-2, and Figure 12-3. The earliest-to-latest date progresses from left to right in these figures. Wing geometry trends are shown in Figure 12-4, Figure 12-5, Figure 12-6, Figure 12-7, and Figure 12-8. The fuselage length trend is shown in Figure 12-9.

Global Hawk is the only design class that contends with compressibility effects. The Global Hawk cases can ingress and egress at a low transonic speed, so wing sweep, reduced wing thickness to chord ratio, or both were typically selected by the optimizer to delay the onset of compressibility effects. Two design families, or niches, emerged from the optimization, as shown in Figure 12-8. The 1994, 2010, and 2015 cases took the approach using low aspect ratio wings with little sweep and reduced thickness to chord ratios. The 2000, 2005, and 2025 cases had high aspect ratio wings with some sweep and high thickness to chord ratio wings. For a fixed technology year, the unswept, low aspect

ratio niche has a relatively low structural mass fraction due to the smaller wing size and more efficient structure, but a higher fuel fraction due to the relatively poor aerodynamic performance. For a fixed technology year, the swept, high-aspect ratio niche has a higher aerodynamic efficiency and a lower fuel mass fraction than the competing niche, but this comes at the expense of structural weight.

The wing span and aspect ratio tended to be more significant drivers than taper ratio and wing sweep. The optimizer tended to select wing thickness to chord ratios of 15.7-17%, which was well above the minimum value of 9%. The wing span for same-niche vehicles consistently decreased over time.

The fuselage length decreased from 1994 through 2010, but then remained relatively constant from 2015 through 2020. The radome geometry influence on the fuselage outer loft became insignificant by 2020.

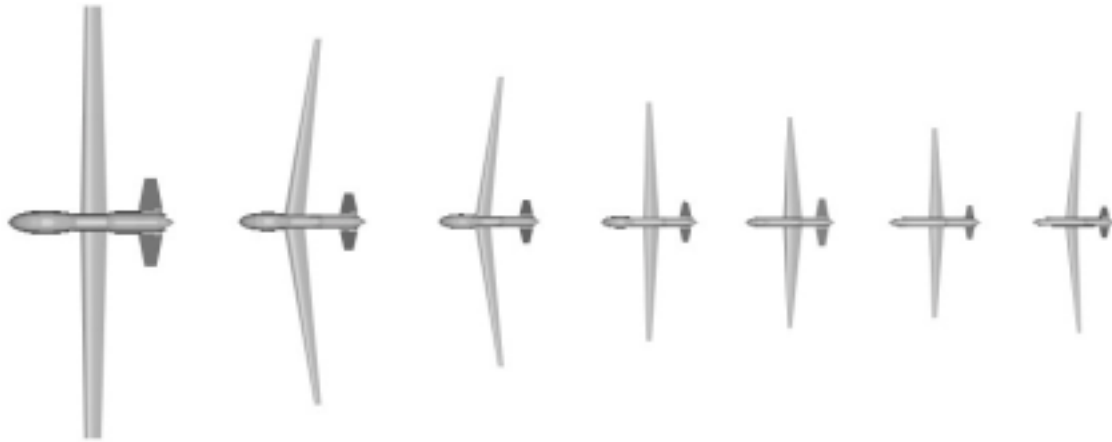


Figure 12-1 Global Hawk Geometry Trends – Top View, Years (Left to Right): 1994, 2000, 2005, 2010, 2015, 2020, 2025



Figure 12-2 Global Hawk Geometry Trends – Side View, Years (Left to Right): 1994, 2000, 2005, 2010, 2015, 2020, 2025

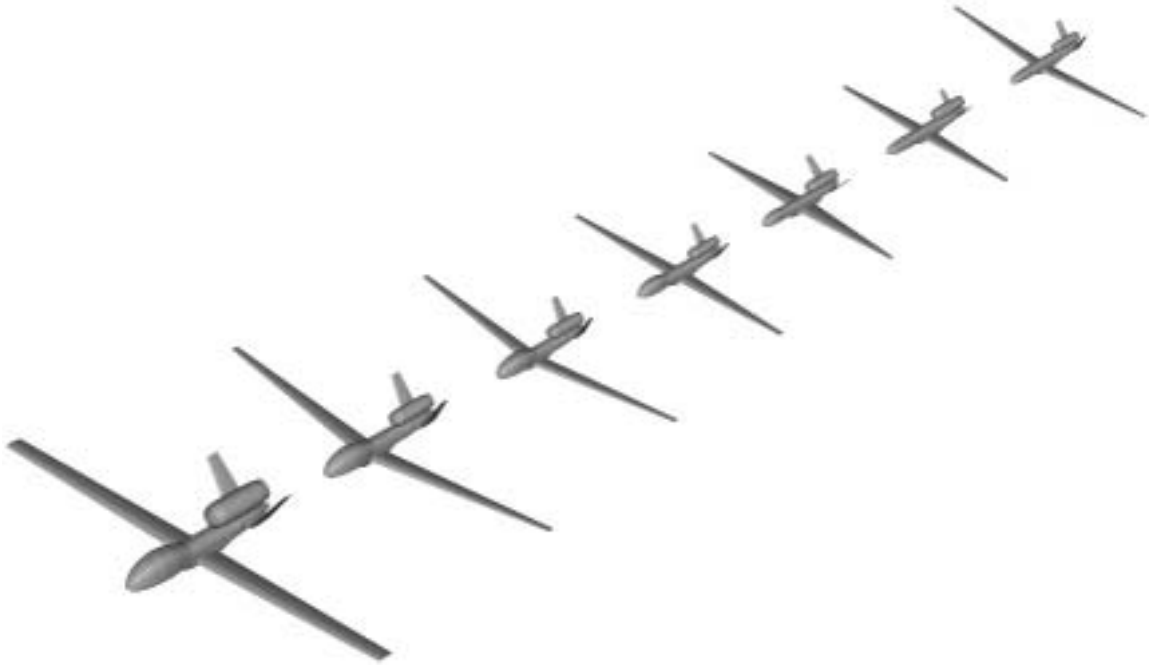


Figure 12-3 Global Hawk Geometry Trends – Isometric View, Years (Left to Right): 1994, 2000, 2005, 2010, 2015, 2020, 2025

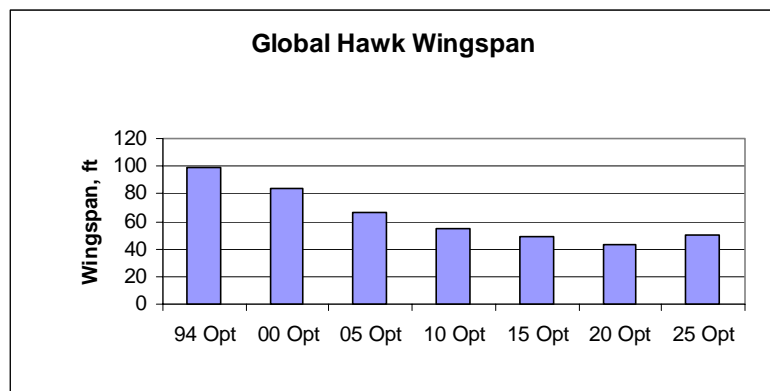


Figure 12-4 Global Hawk Wing Span Trends

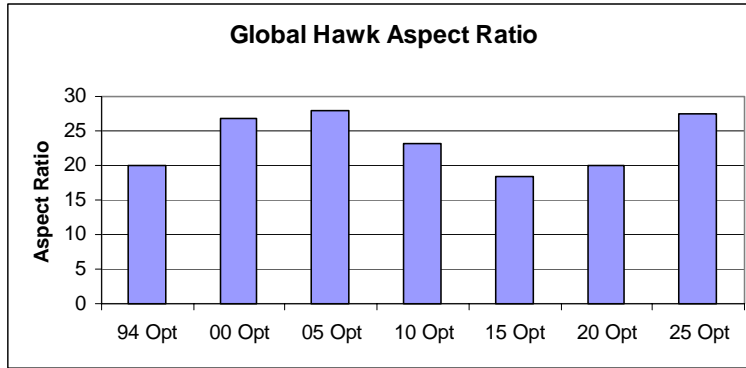


Figure 12-5 Global Hawk Aspect Ratio Trends

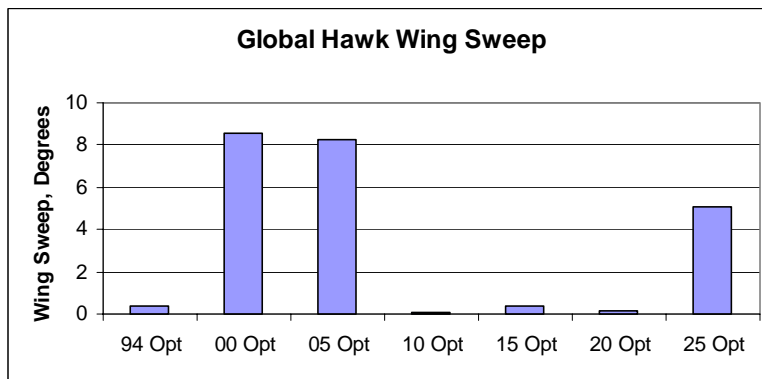


Figure 12-6 Global Hawk Wing Sweep Trends

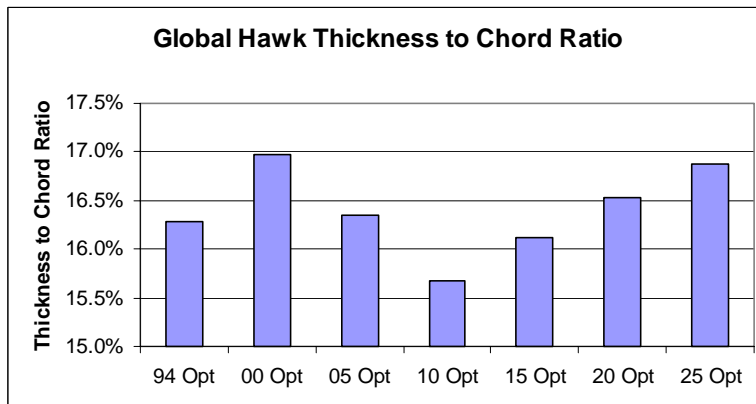


Figure 12-7 Global Hawk Thickness to Chord Ratio Trends

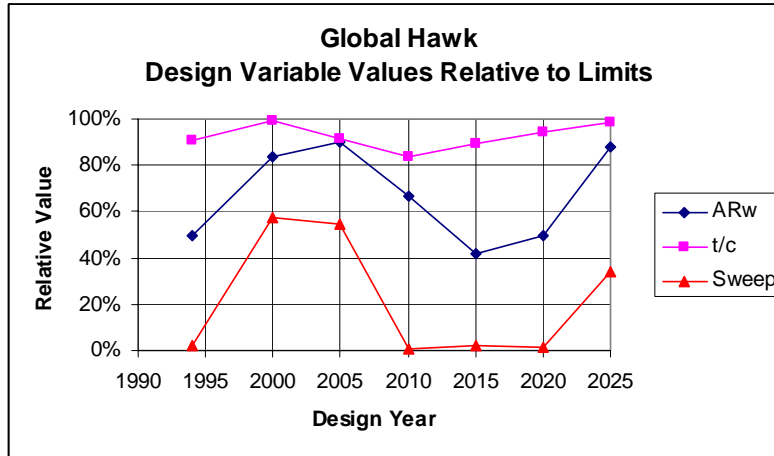


Figure 12-8 Global Hawk Wing Parameter Comparisons

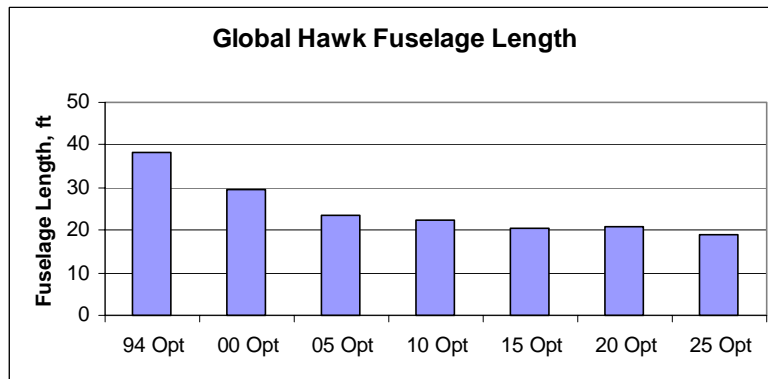


Figure 12-9 Global Hawk Fuselage Length Trends

12.2.3 Propulsion

The global hawk uninstalled thrust and uninstalled thrust-to-weight trends are shown in Figure 12-10 and Figure 12-11, respectively. The Global Hawk uninstalled thrust level rapidly shrank from 1994 to 2000, but then was reduced more gradually and inconsistently from 2000 to 2025. There was no consistent trend for uninstalled thrust to weight ratio referenced to the design gross weight as a function of design year. The vehicle thrust to weight ratio became less costly to the design as time progressed due to engine thrust to weight improvements, so the thrust to weight ratio increased from 2010 to 2020. The decrease in thrust to weight ratio of the 2025 design relative to its predecessor was a result of more aggressive aerodynamic design, such as higher aspect ratio and increased sweep.

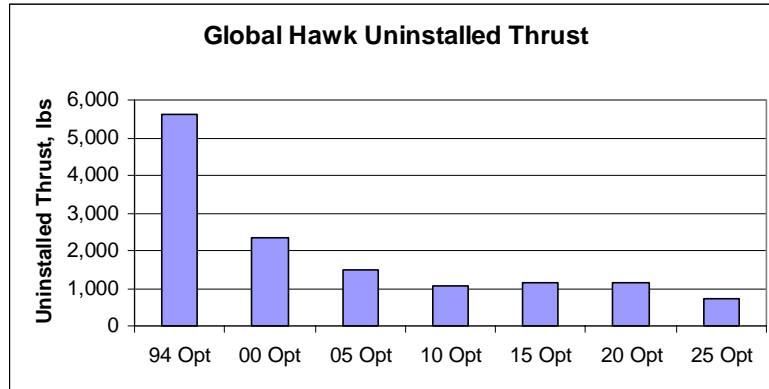


Figure 12-10 Global Hawk Uninstalled Thrust Trends

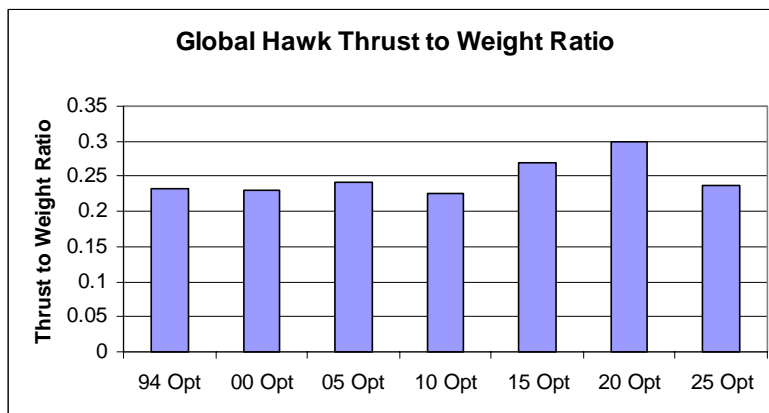


Figure 12-11 Global Hawk Thrust to Weight Ratio Trends

12.2.4 Weights

Weight Summary

The Global Hawk weight and mass fraction trends are shown in Figure 12-12 and Figure 12-13, respectively. The weight improvement trends are shown in Figure 12-14. As expected, the synthesized vehicle weight improved as technology improves. The mass fraction of the payload increased as the mass fractions consumed by fuel, propulsion, and avionics were reduced. Note that the weights in Figure 12-12 are on a log scale, so weight categories such as the growth weight appear exaggerated despite having a relatively constant mass fraction.

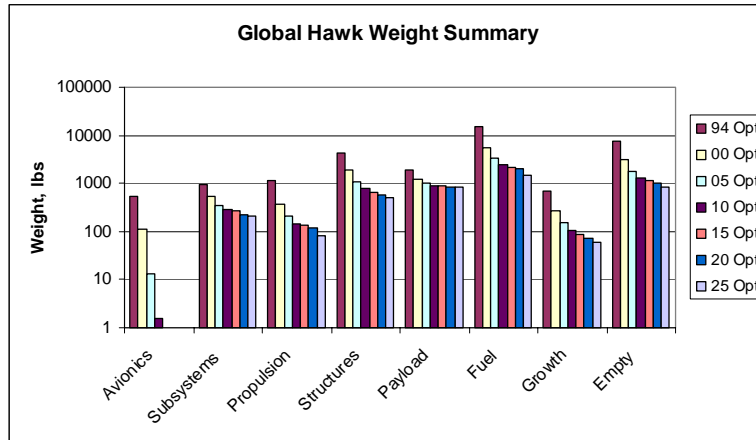


Figure 12-12 Global Hawk Weight Trends

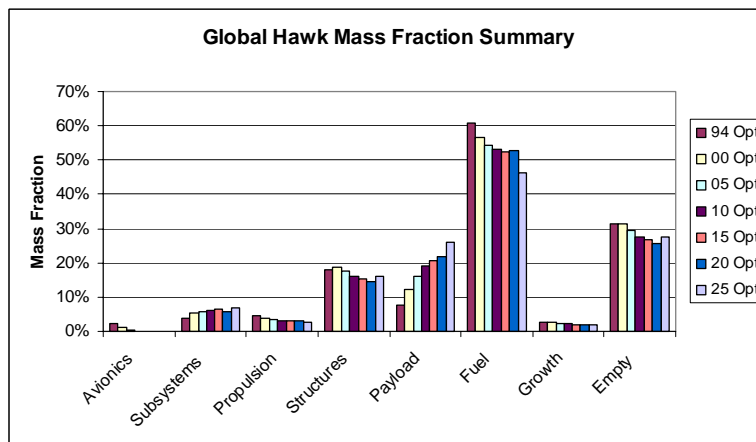


Figure 12-13 Global Hawk Mass Fraction Trends

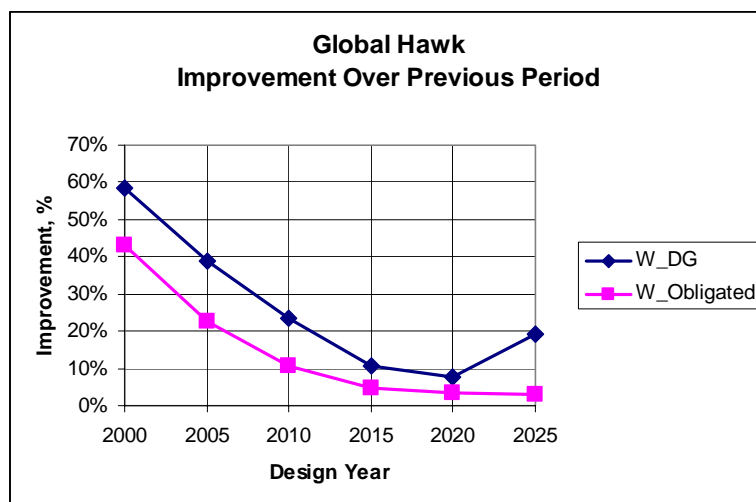


Figure 12-14 Design Gross - Obligated Weights Trends

Avionics Weights

The avionics weights improved dramatically through future years. The results can be seen in Figure 12-15. The relative influence of the overall avionics weight contribution to vehicle sizing compared to the payload weight became less significant as time advanced. The avionics weight reductions follow the technology trends provided in Chapter 4.

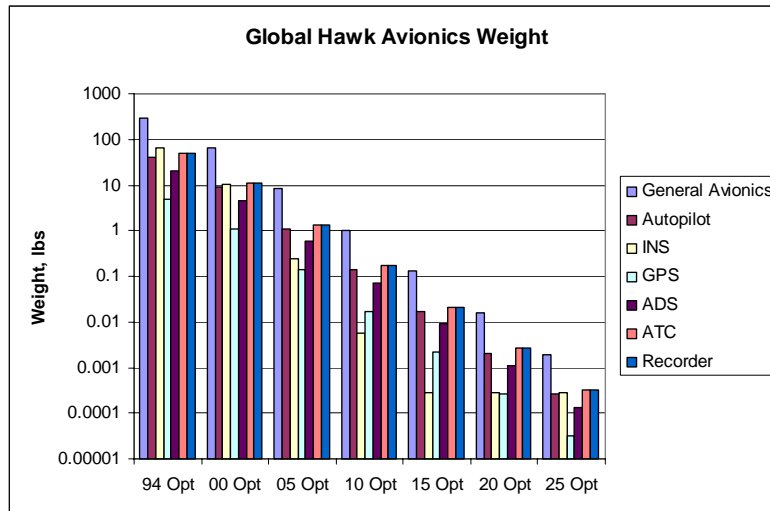


Figure 12-15 Global Hawk Avionics Weight Trends

Subsystems Weights

The subsystems weight trends are shown in Figure 12-16. The relative contribution of the communications system was greater in the future cases when using the assumed technology curves. This was caused by the parabolic dish weight that was a function of dish diameter. The dish diameter and associated dish weight followed a technology trend separate from the subsystems curve.

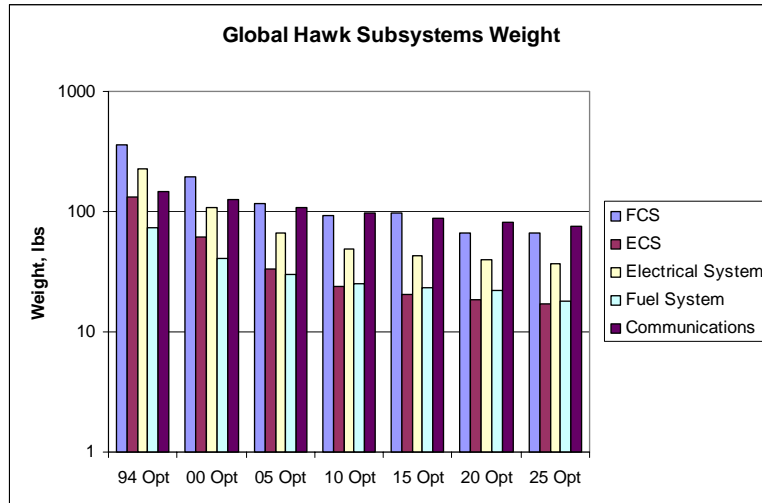


Figure 12-16 Global Hawk Subsystems Weight Trends

Payload Weights

The Global Hawk payload weight trends are shown in Figure 12-17. The SAR payload weight saw aggressive improvement in weight relative to the EO/IR payload. Relative to the 1994 SAR value, the SAR payload weight was reduced by 87.2 % in 2005 and 98.9% by 2025. Relative to the 1994 EO/IR value, the EO/IR payload weight was reduced by only 7.4% in 2005 and 14.6% in 2025. The large-EO/IR payload technology prediction was applied here. The EO/IR payload became the primary vehicle sizing driver in 2025.

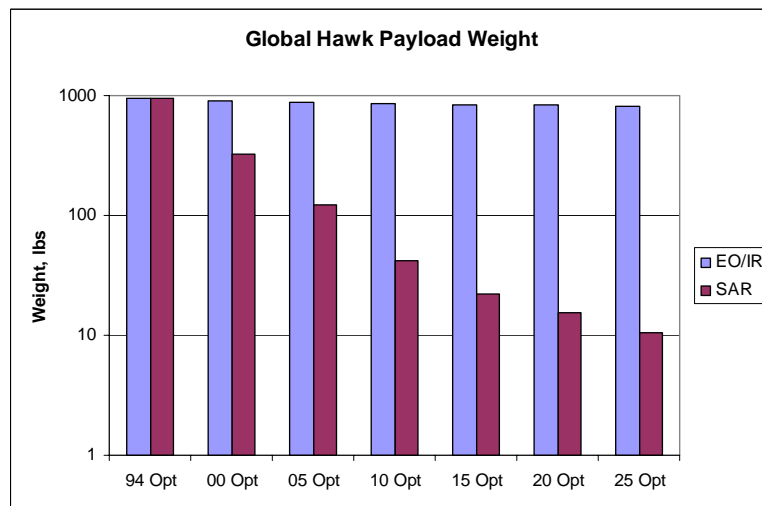


Figure 12-17 Global Hawk Payload Weight Trends

Structures Weights

The Global Hawk structural weight trends are shown in Figure 12-18. The installation weight became the most dominant structural weight contributor in 2005. The physical

size of the structure decreased due to volume reductions of many components, fuel reduction, and general sizing phenomena. The combined relative weight of the obligated weights did not change as rapidly as the major structural components. The installation weight associated with these items was proportional to the component weights, and therefore the installation weight did not decrease rapidly. The wing structural weight trends would likely vary if an aerolastic and stiffness analyses were performed. Future research should fully account for these relevant phenomena.

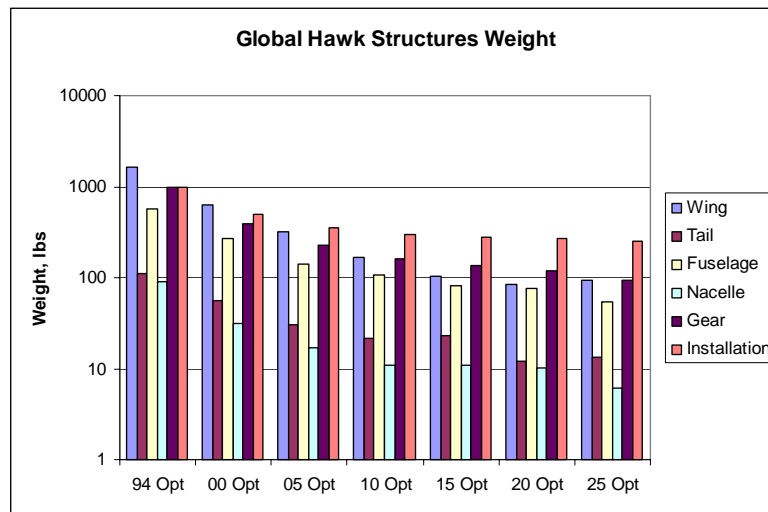


Figure 12-18 Global Hawk Structures Weight Trends

12.2.5 Performance

The optimized Global Hawk mission profiles and related performance data are shown in Figure 12-19, Figure 12-20, Figure 12-21, and Figure 12-22. The internal mission optimization routine selected slightly different flight profiles for the various solutions. The 1994 optimum had the highest average Mach number and reached the maximum altitude quickest.

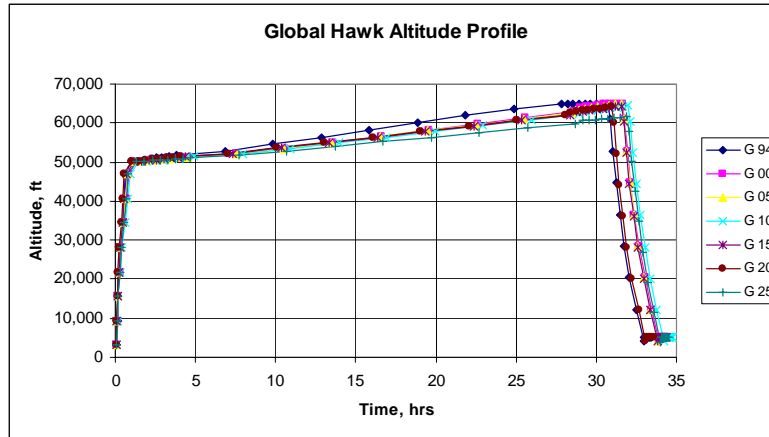


Figure 12-19 Global Hawk Altitude Profile Trends

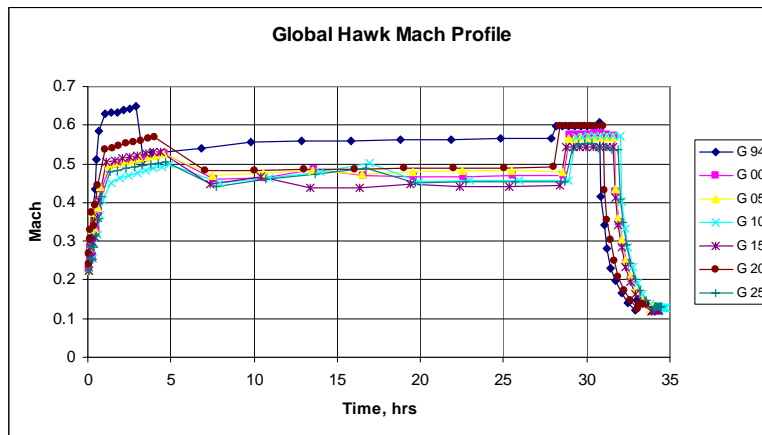


Figure 12-20 Global Hawk Mach Profile Trends

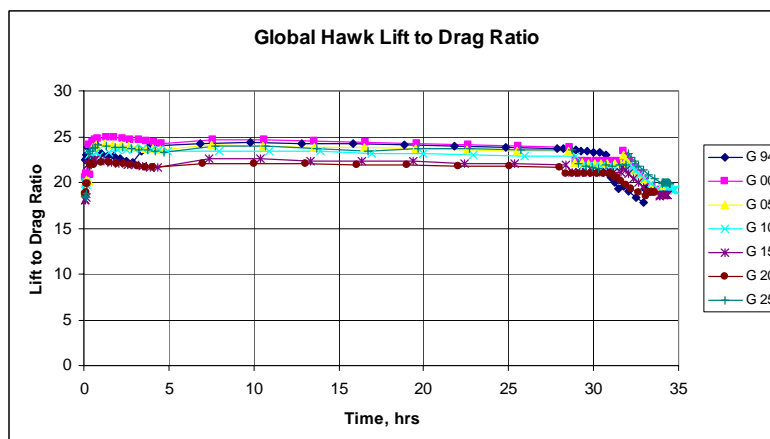


Figure 12-21 Global Hawk Mission Lift to Drag Ratio Trends

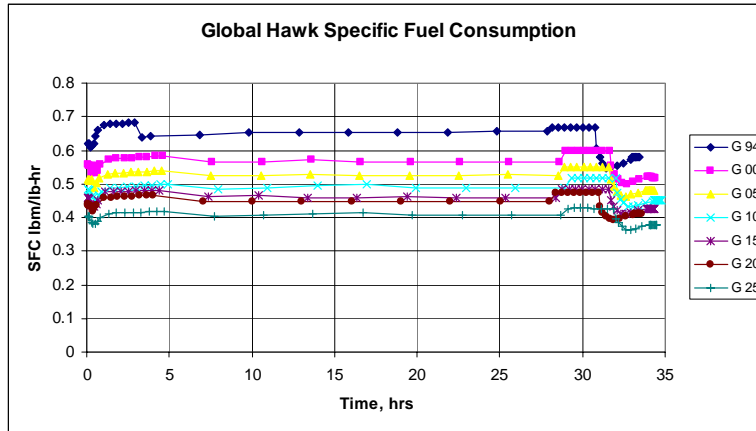


Figure 12-22 Global Hawk Mission Fuel Consumption Trends

12.2.6 Technology Sensitivities

The Global Hawk technology sensitivities are shown in Figure 12-23. The three bars represent different ways of viewing the technology impacts. The total bar is the design gross weight difference between the 1994 optimized Global Hawk and the 2005 optimized Global Hawk with all technologies applied simultaneously in the design. The components bar shows the weight improvement for each individual technology group when applied individually. Finally, the combined bar is the multiplication of all of the improvements from each of the technology groups. The combined bar is found from:

$$Improvement = 1 - \prod_{Components} (1 - Improvement_{Component})$$

Global Hawk was most sensitive to payload and then propulsion technology impacts between 1994 and 2005. The avionics/subsystems technologies also had significant influence. There was overall synergy among the combined technologies. The combined improvement of all individual technology groups is 67.9%, and the total difference in design gross weight from 1994 to 2005 is 74.5%. The overall synergy, defined here as the difference of the total and combined technologies, is 6.68%.

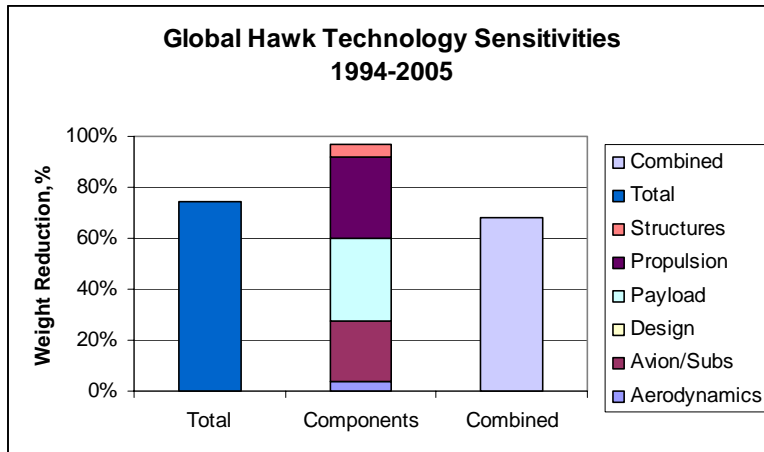


Figure 12-23 Global Hawk Design Gross Weight Sensitivity to Technology

12.3 Predator Technology Impacts

12.3.1 Sizing Overview

Like Global Hawk, Predator sizing was strongly influenced by the payloads and other obligated weights. Predator used the small EO/IR technology trend, which was far more aggressive than the Global Hawk large EO/IR trend. The notable reduction in EO/IR weight throughout the dates considered permitted continuing weight reduction beyond 2005.

12.3.2 Geometry

Graphical representation of the Predator technology case geometry behavior is shown in Figure 12-24, Figure 12-25, and Figure 12-26. Numerical wing geometry trends are presented in Figure 12-27, Figure 12-28, Figure 12-29, and Figure 12-30. The fuselage length trend is provided in Figure 12-31.

The most dominant visual feature of the optimized predator solutions is the radome. The Predator parametric radome strongly affected the aerodynamic performance of the vehicles under consideration. As the assumed satellite communications technology improved, the dish diameter and radome size decreased, permitting the fuselage to assume more visually pleasing and aerodynamically efficient contours. The fuselage length generally decreased with time due to decreasing avionics, subsystems, propulsion, and fuel volume.

The strongest wing geometry contributors to design gross weight were the wing span and aspect ratio, which define the wing area. The wing area tended to decrease with decreasing vehicle weight. The taper and thickness to chord ratios had no correlation with design year, and were not major design drivers.

The optimization process resulted in a relatively low wing taper ratio of 0.81 for the 2015 optima. One possible explanation for this result is the impact of the wing on the fuselage geometry. The parametric wing fairing length is proportional to the wing root chord. The wing root chord may have been reduced to manage the fuselage length to diameter ratio for fuselage drag reduction, given the dominance of the radome. Wing taper provides wing structural weight and induced drag reductions. Apparently, the negative impacts of low taper ratios on the fuselage drag overcame the wing structural and aerodynamic benefits for the 2015 case. The optimizer generally selected more aggressive wing taper for this family of UAV.

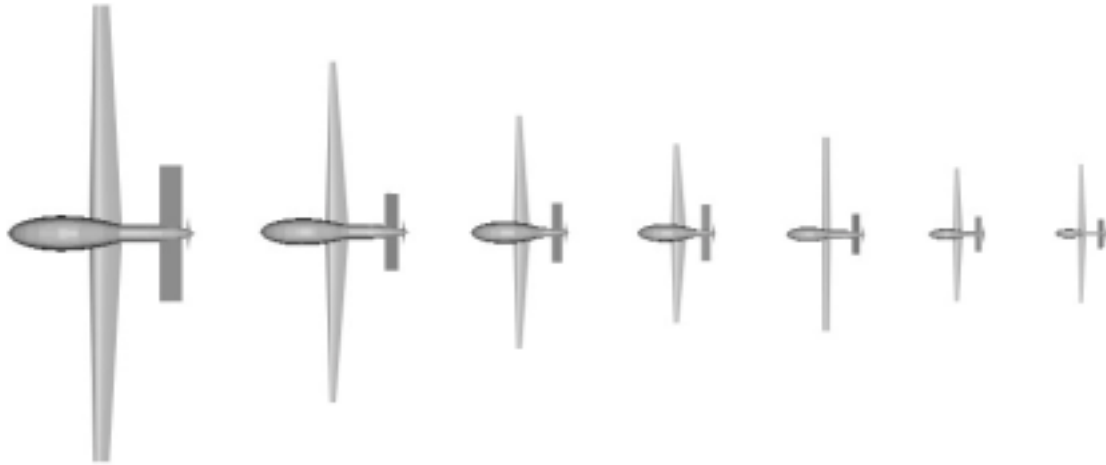


Figure 12-24 Predator Geometry Trends – Top View, Years (Left to Right): 1994, 2000, 2005, 2010, 2015, 2020, 2025



Figure 12-25 Predator Geometry Trends – Side View, Years (Left to Right): 1994, 2000, 2005, 2010, 2015, 2020, 2025

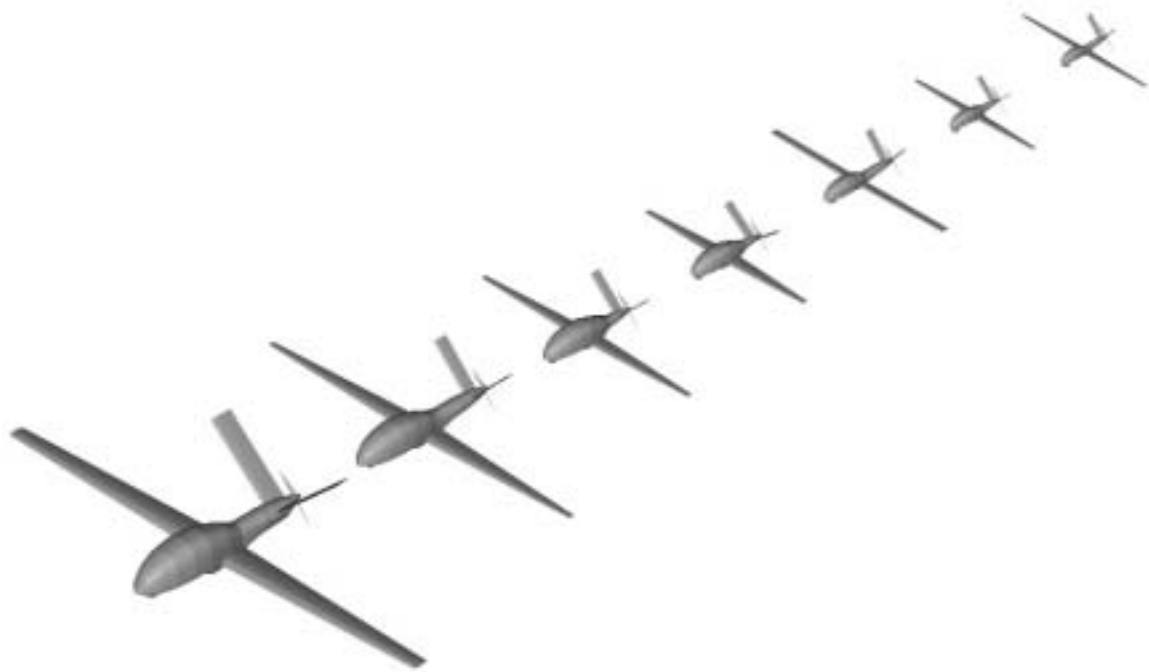


Figure 12-26 Predator Geometry Trends – Isometric View, Years (Left to Right): 1994, 2000, 2005, 2010, 2015, 2020, 2025

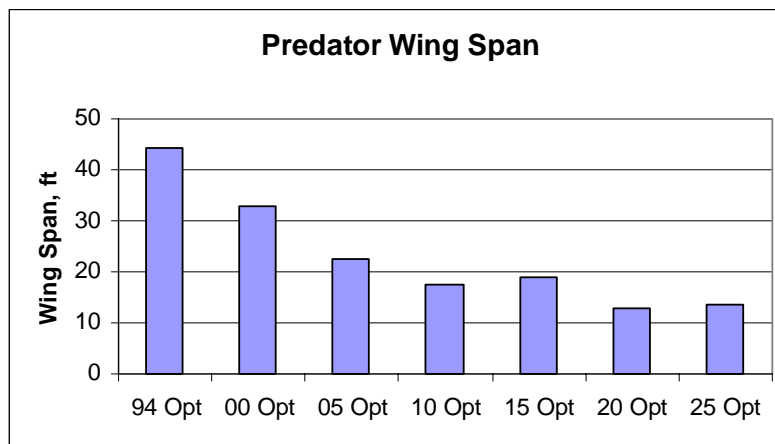


Figure 12-27 Predator Wing Span Trends

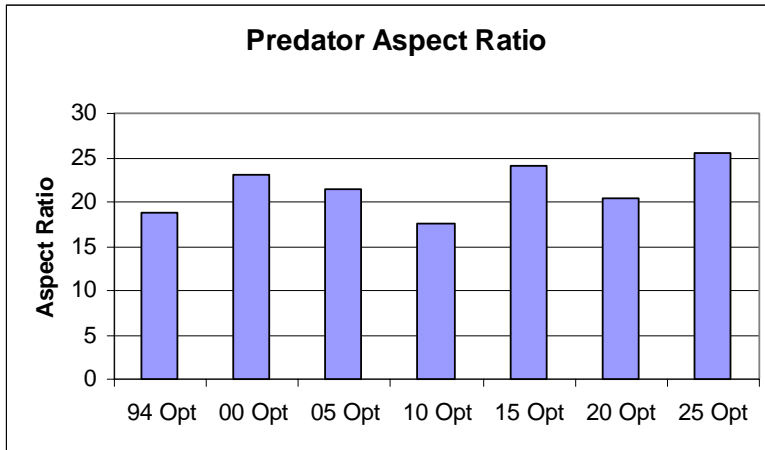


Figure 12-28 Predator Aspect Ratio Trends

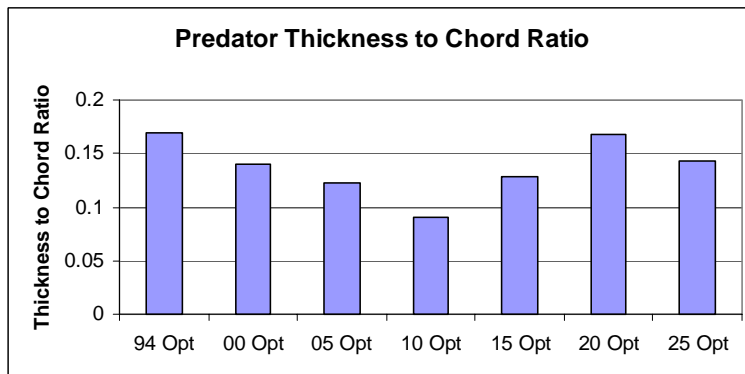


Figure 12-29 Predator Thickness to Chord Ratio

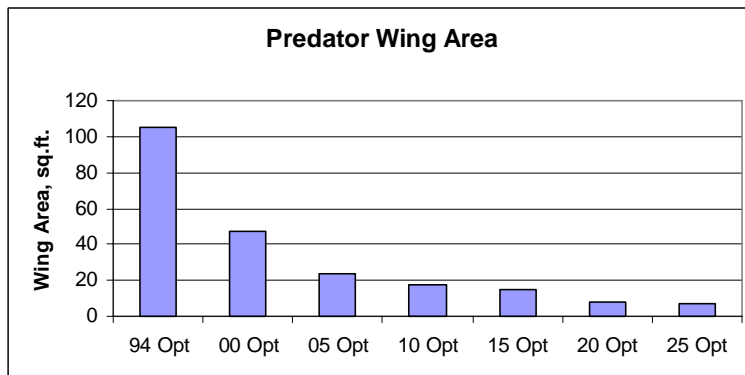


Figure 12-30 Predator Wing Area

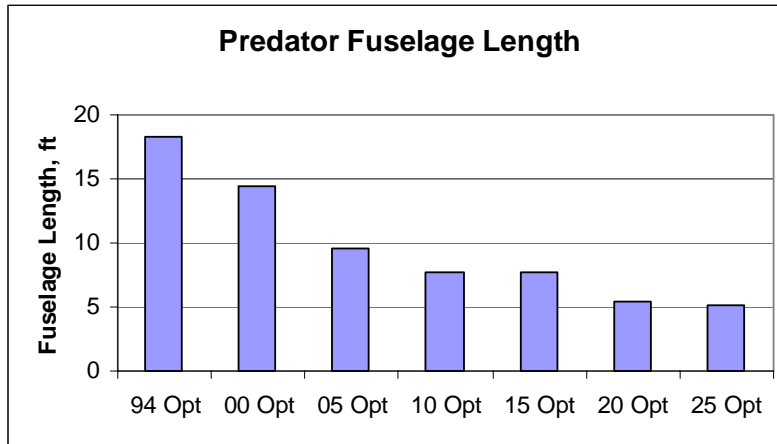


Figure 12-31 Predator Fuselage Length Trends

12.3.3 Propulsion

The Predator uninstalled power and uninstalled power-to-weight trends are shown in Figure 12-32 and Figure 12-33, respectively. As expected, the uninstalled power decreased with vehicle weight as time progresses. The power-to-weight ratio tended to increase as time progressed, since the weight impacts attributable to the propulsion system were less stressing on future designs.

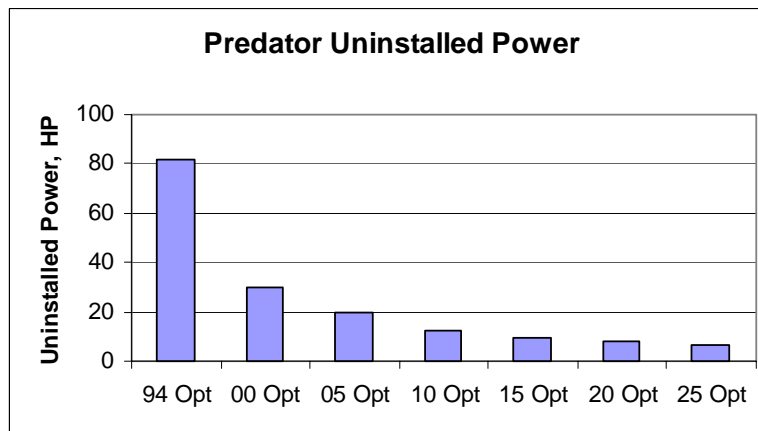


Figure 12-32 Predator Uninstalled Power Trends

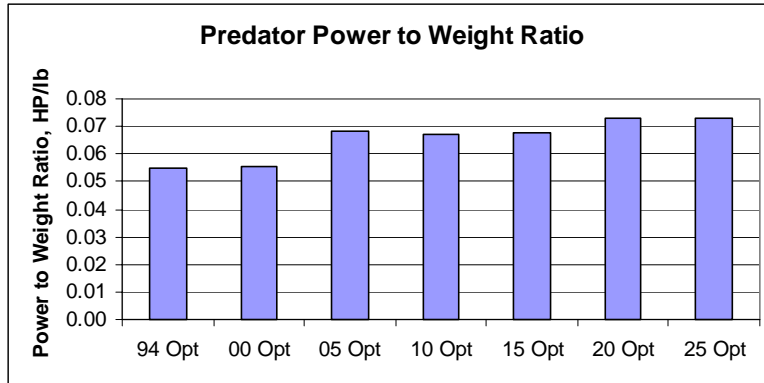


Figure 12-33 Predator Power to Weight Ratio

12.3.4 Weights

Weight Summary

The Predator technology case weight and mass fraction trends are shown in Figure 12-34 and Figure 12-35, respectively. The Predator overall weight improvement trends are shown in Figure 12-36. The Predator weights uniformly decreased with improving technology. The behavior of the mass fractions had variation, but the general trend was for the fuel mass fraction to decrease while the payload mass fraction increased. The overall design gross weight improved faster than the reduction in obligated weights, which revealed that the other technology improvements were providing benefit.

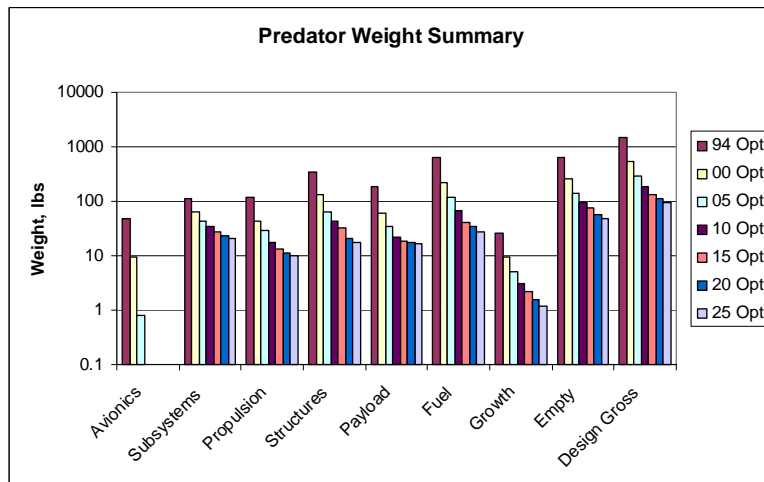


Figure 12-34 Predator Weight Summary Trends

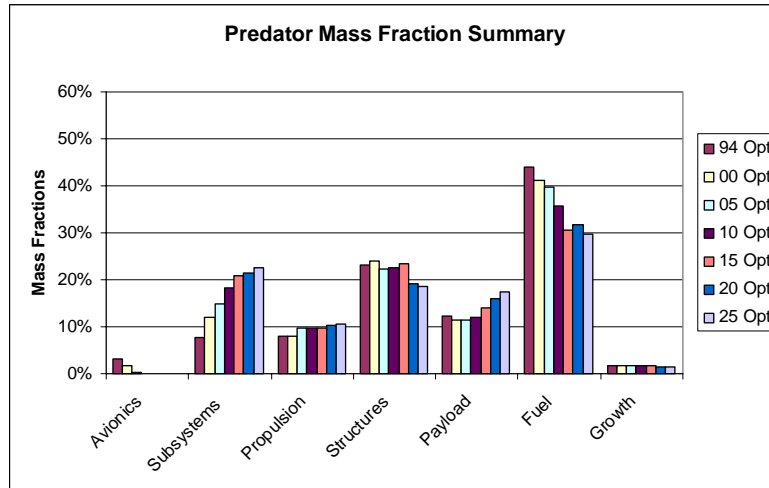


Figure 12-35 Predator Summary Mass Fraction Trends

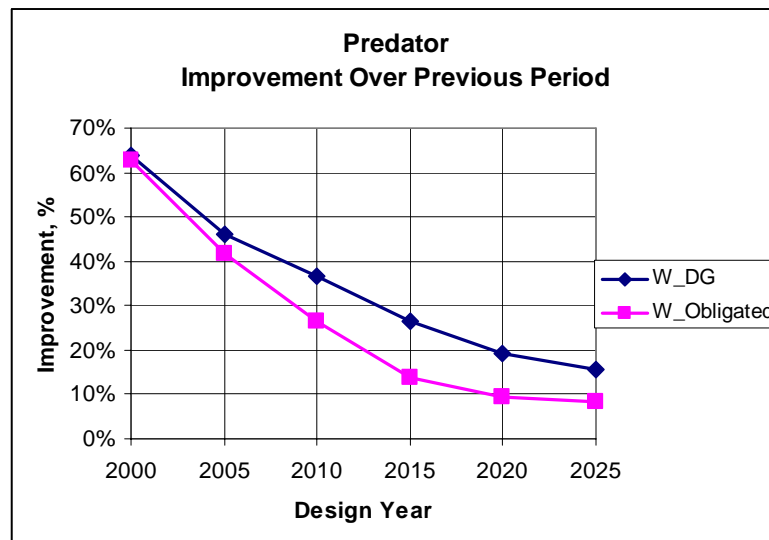


Figure 12-36 Predator Design Gross – Obligated Weight Trends

Avionics Weights

The Predator technology case avionics weights trends are presented in Figure 12-37. As seen on Global Hawk, the avionics weights became negligible as technology advanced.

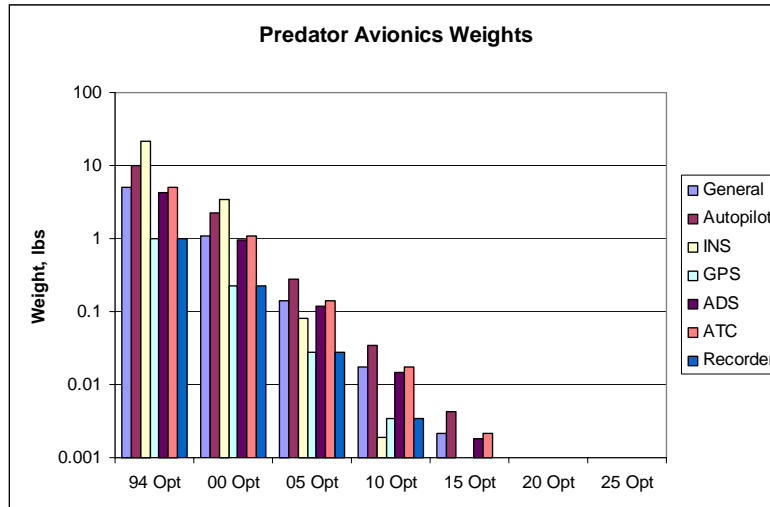


Figure 12-37 Predator Avionics Weight Trends

Subsystems Weights

The Predator technology case subsystems weight trends are shown in Figure 12-38. The subsystems weights all decreased with time. The slowest to decrease was the communications system weight, because this weight was a function of the satellite communications dish diameter that followed a technology trend distinct from the other subsystems.

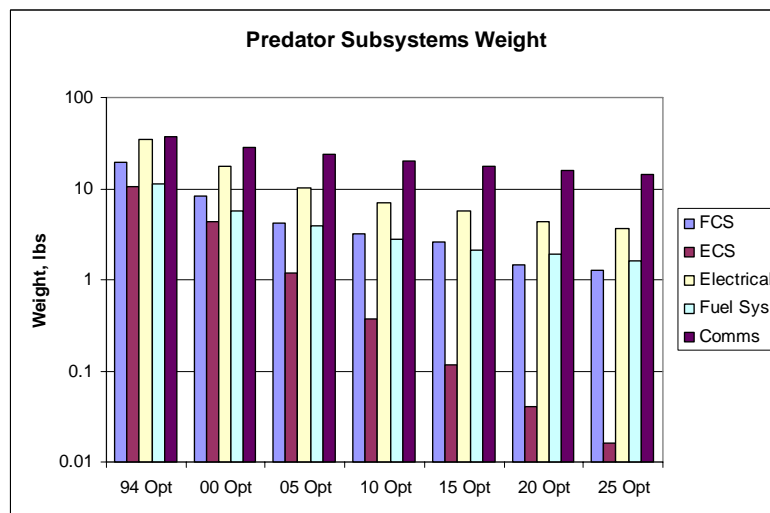


Figure 12-38 Predator Subsystems Weight Trends

Payload Weights

The Predator payload weight trends are presented in Figure 12-39. The payload weights exhibited similar behavior to those seen on Global Hawk. The relative weight reduction of the SAR payload from 1994 was identical to that on Global Hawk. The EO/IR saw

more weights improvement than on Global Hawk, because the more aggressive small EO/IR technology trend was applied.

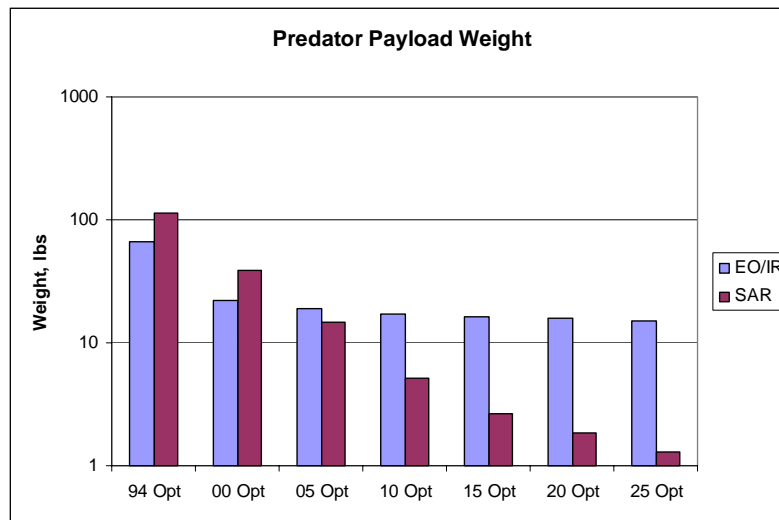


Figure 12-39 Predator Payload Weight Trends

Structural Weights

The Predator technology case structural weight trends are shown in Figure 12-40. The structural weights all decreased with time. The installation weight became increasingly dominant. This weight accounts for the structural mounting of avionics, subsystems, payload, and propulsion. The slowly decreasing payload weight was the primary contributor to the relatively intractable installation weight.

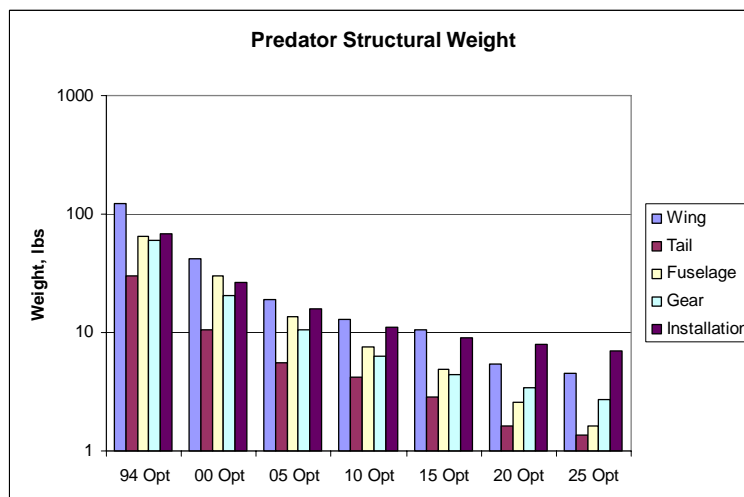


Figure 12-40 Predator Structures Weight Trends

12.3.5 Performance

The Predator technology case mission profiles and associated performance information are presented in Figure 12-41, Figure 12-42, Figure 12-43, and Figure 12-44. The Predator flight performance showed some variation.

The 1994 optimum reached the maximum altitude during loiter much more rapidly than later aircraft in the family. The higher flight velocity brought the 1994 Predator design to the loiter point rapidly. During loiter, the high lift to drag ratio permitted this aircraft to climb faster than its less aerodynamically efficient descendants. The 1994 Global Hawk also had a faster ingress than its descendants.

In general, the lift to drag ratio degraded with time. The culprit was that the size of the EO/IR ball relative to the wing made this very high drag sphere a larger contributor in the future cases. Improved specific fuel consumption in later years made aerodynamic performance less important to achieve the same performance results. Aerodynamic performance improvements can be attained by increasing the aspect ratio and wing span, but both of these options add structural weight that offsets the benefits of reduced fuel consumption.

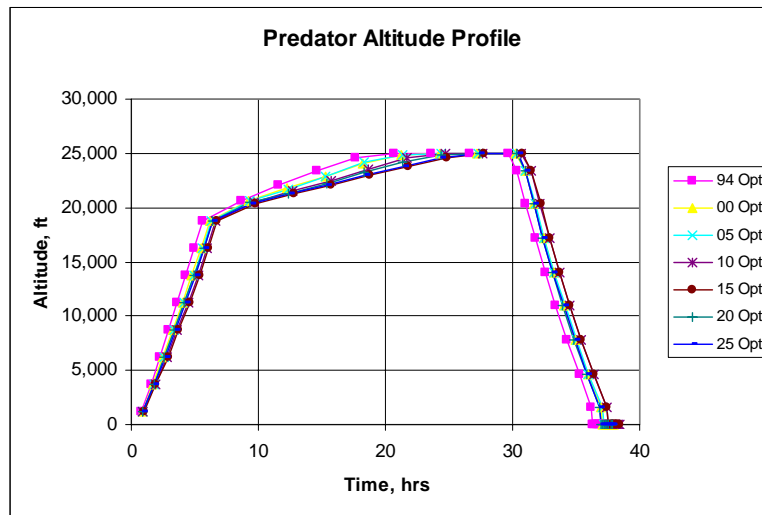


Figure 12-41 Predator Altitude Profile Trends

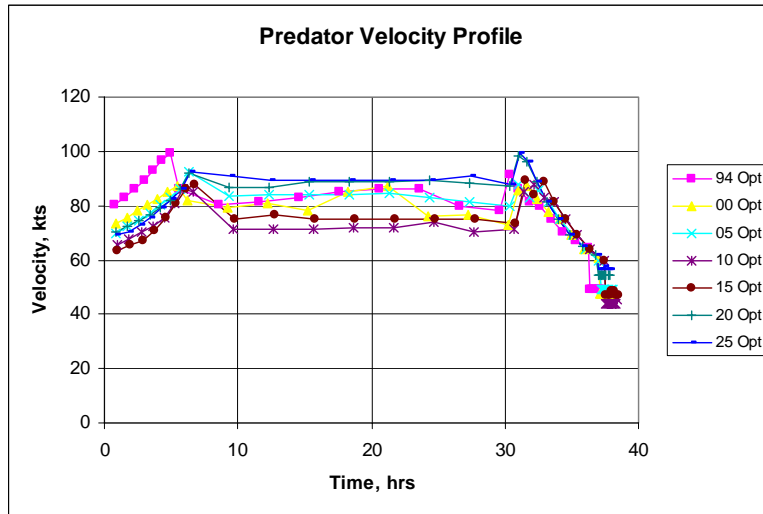


Figure 12-42 Predator Velocity Profile Trends

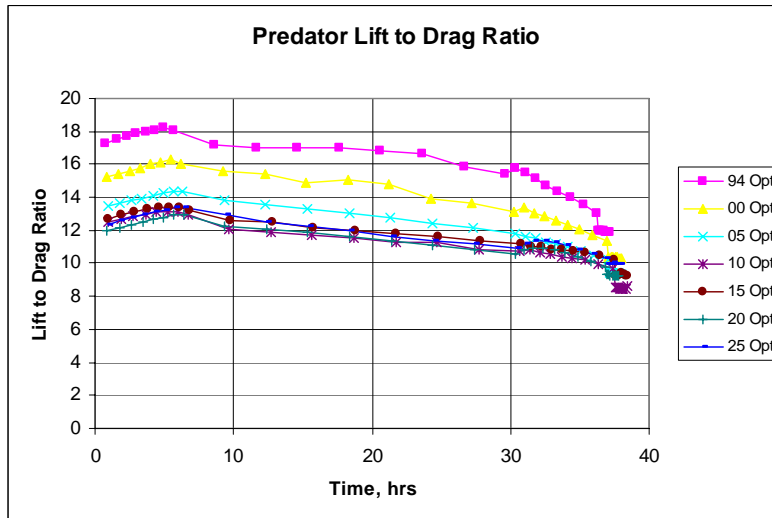


Figure 12-43 Predator Mission Lift to Drag Ratio Trends

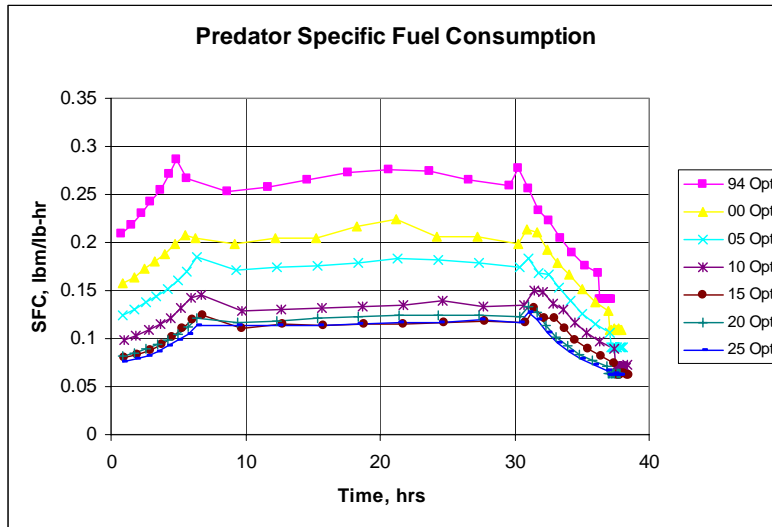


Figure 12-44 Predator Mission Fuel Consumption Trends

12.3.6 Technology Sensitivities

The Predator design gross weight sensitivities to various technologies are shown in Figure 12-45. The Predator showed 7.1% overall synergy, which is the highest of the three vehicle classes evaluated here. Predator is most sensitive to the payload technology category, followed by avionics/subsystems and propulsion technology categories.

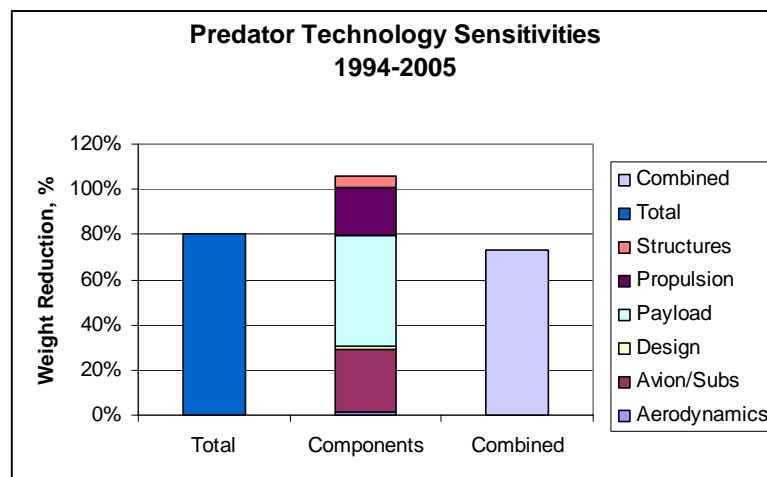


Figure 12-45 Predator Design Gross Weight Sensitivity to Technology

12.4 Shadow 200 Technology Impacts

12.4.1 Sizing Overview

The Shadow 200 family has shown the least improvement over time. This was caused by the relatively low fuel mass fraction lowering the weight escalation factor.

12.4.2 Geometry

The Shadow 200 technology case trends are shown graphically in Figure 12-46, Figure 12-47, and Figure 12-48. The wing geometry behavior is provided in Figure 12-49 and Figure 12-50. The fuselage length is shown presented in Figure 12-51. Two families of solutions, or niches, emerged through optimization. The first family sought to minimize physical size to reduce structural weight. The second family had a combination of high aspect ratio and low wing loading to improve aerodynamic performance and propulsion efficiency, which improved the fuel fraction. Figure 12-52 shows the wing loading and aspect ratio trends for all technology cases. The 2015 and 2025 cases fall into the latter family. No clear aspect ratio and taper ratio relationships are evident.

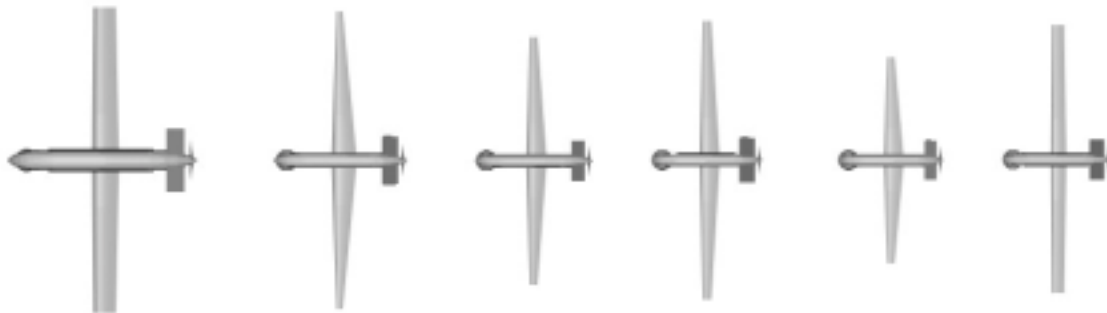


Figure 12-46 Shadow 200 Geometry Trends – Top View, Years (Left to Right): 2000, 2005, 2010, 2015, 2020, 2025



Figure 12-47 Shadow 200 Geometry Trends – Side View, Years (Left to Right): 2000, 2005, 2010, 2015, 2020, 2025



Figure 12-48 Shadow 200 Geometry Trends – Isometric View, Years (Left to Right): 2000, 2005, 2010, 2015, 2020, 2025

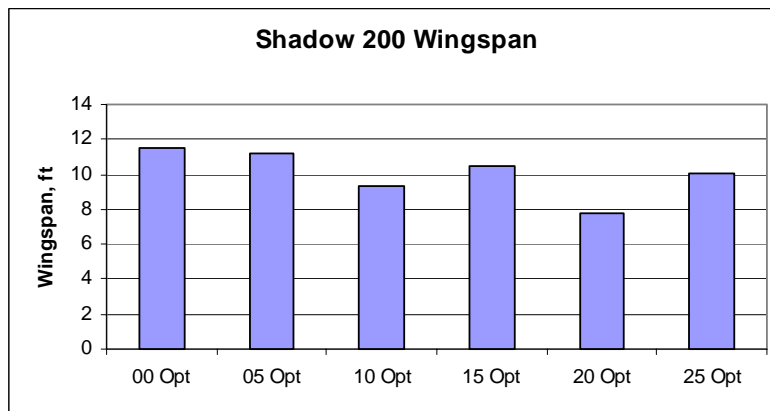


Figure 12-49 Shadow 200 Wing Span Trends

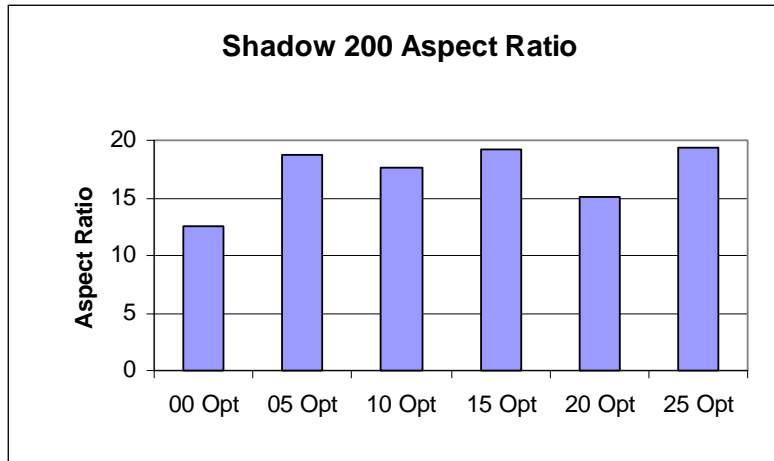


Figure 12-50 Shadow 200 Aspect Ratio Trends

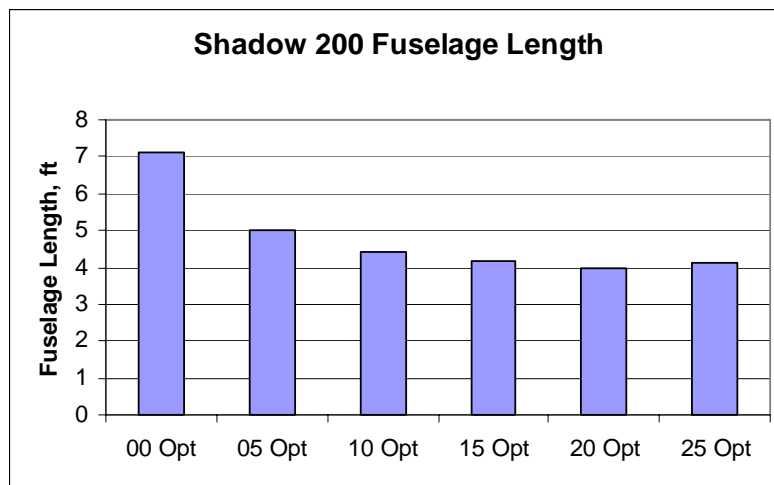


Figure 12-51 Shadow 200 Fuselage Length Trends

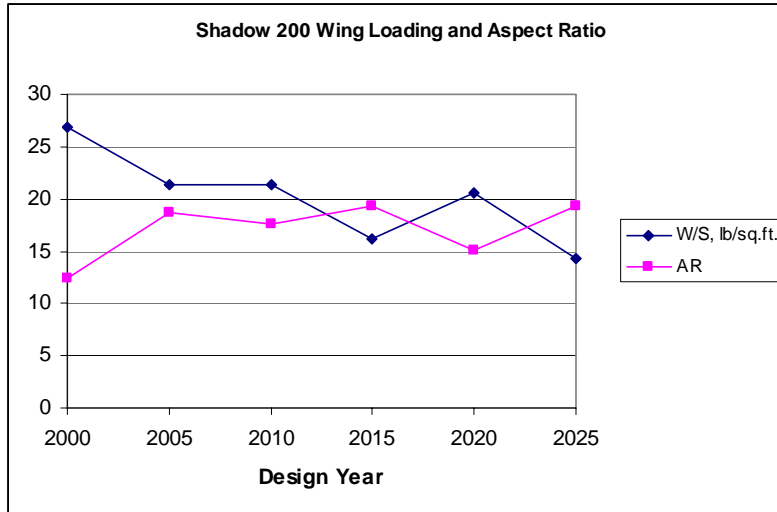


Figure 12-52 Shadow 200 Wing Loading – Aspect Ratio Relationships

12.4.3 Propulsion

The Shadow 200 technology case uninstalled power and uninstalled power to weight trends are shown in Figure 12-53 and Figure 12-54, respectively. The maximum power to weight difference among all optimized cases was 17%. This variation was more a function of the solution niche than the design year.

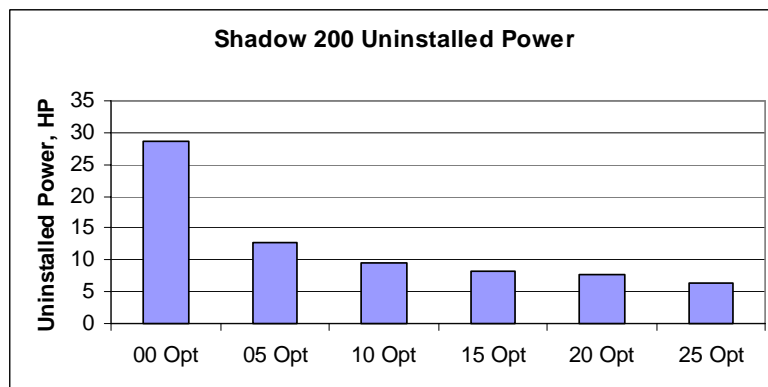


Figure 12-53 Shadow 200 Uninstalled Power Trends

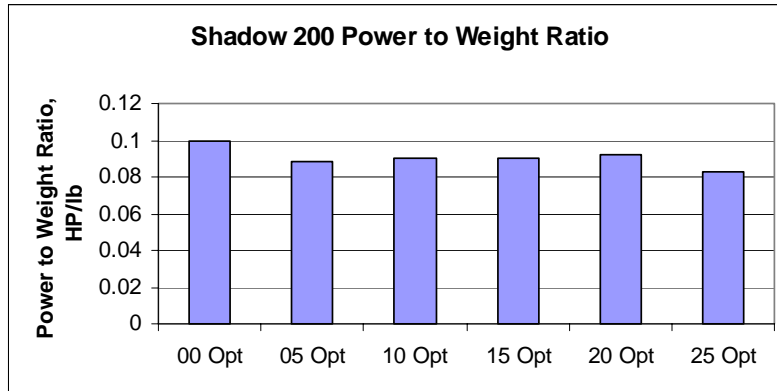


Figure 12-54 Shadow 200 Power to Weight Ratio Trends

12.4.4 Weights

Weight Summary

Figure 12-55 and Figure 12-56 show the Shadow 200 technology case weight and mass fraction trends, respectively. The Shadow 200 overall weights decreased with improving technology, as expected.

Figure 12-57 shows the weight improvement trends. The overall design gross weight improvement tracked the obligated weight improvement with an offset. The offset represented improvement in structures technology and technologies that affect the fuel fraction, including the aerodynamics and propulsion.

The decrease in the avionics and fuel mass fractions allowed an overall increase in payload mass fraction. The higher payload mass fraction translated to a higher utility.

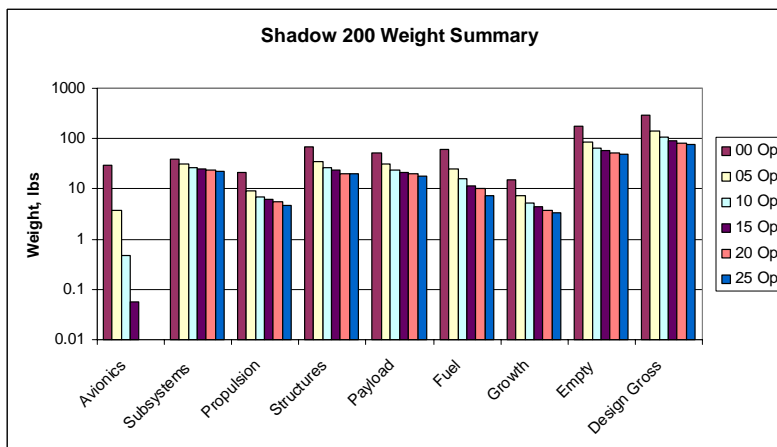


Figure 12-55 Shadow 200 Weight Trends

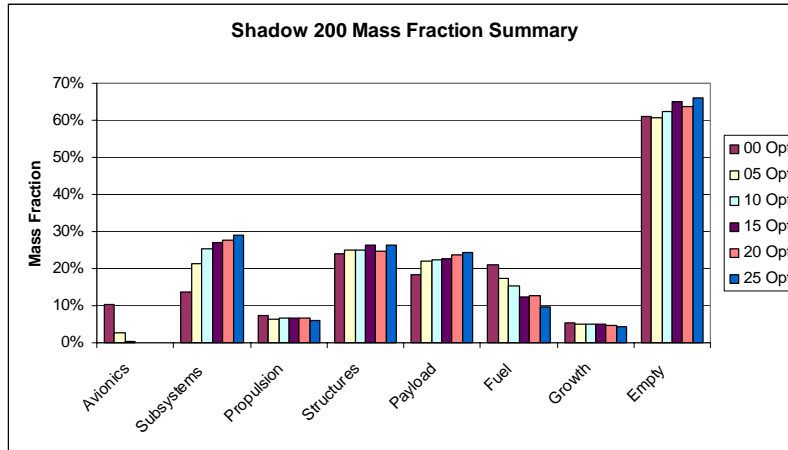


Figure 12-56 Shadow 200 Summary Mass Fraction Trends

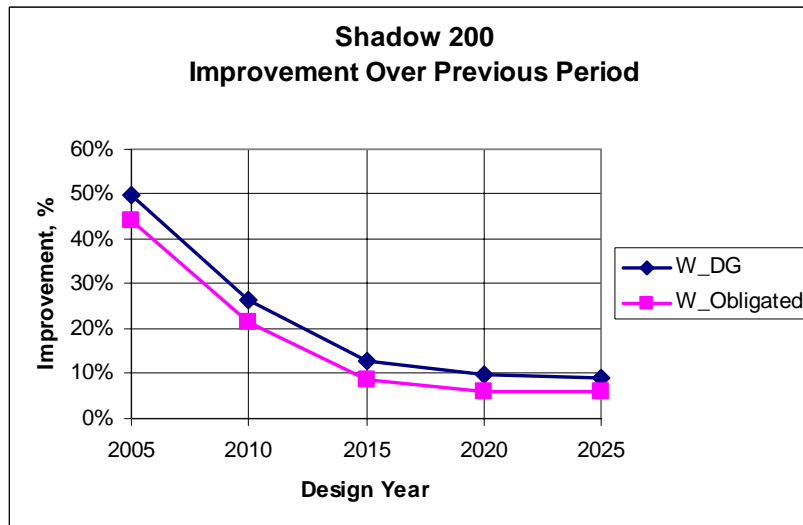


Figure 12-57 Shadow 200 Design Gross – Obligated Weights Trend

Avionics Weights

The Shadow 200 technology case avionics weights trends are shown in Figure 12-58. The avionics weights rapidly became negligible contributors by 2010 using the assumed avionics technology curves.

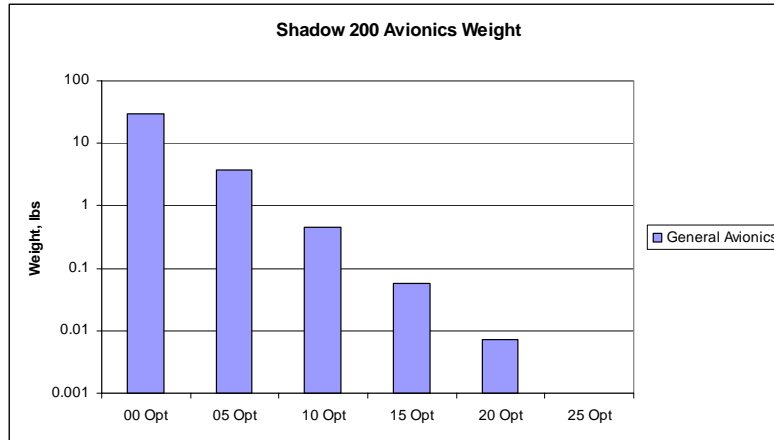


Figure 12-58 Shadow 200 Avionics Weight Trends

Subsystems Weights

Figure 12-59 shows the Shadow 200 subsystems weight trends. The subsystems weights all decreased with time. All subsystems except for the communications system were affected by vehicle sizing, so the communications subsystem weight did not decrease rapidly. The flight control system was a function of control surface size, so the large area of the 2015 and 2025 solutions resulted in a higher flight control weight than the adjacent cases.

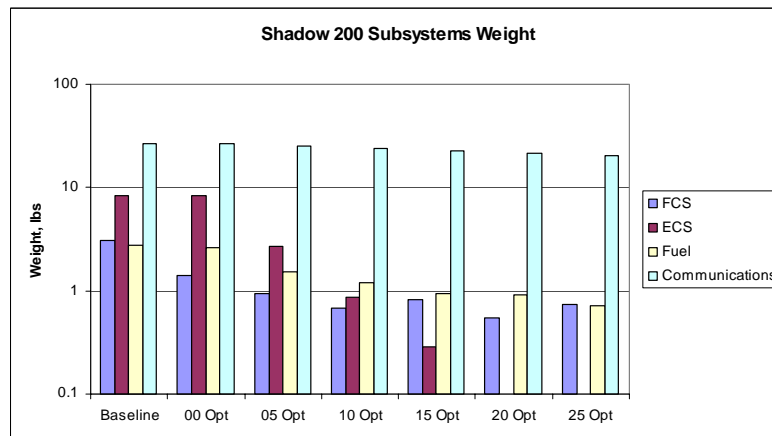


Figure 12-59 Shadow 200 Subsystems Weight Trends

Payload Weights

The Shadow 200 technology case payload weight trends are shown in Figure 12-60. Like the previous two cases, the SAR payload weight decreased much more rapidly than the EO/IR. Despite applying the small EO/IR technology curve, the EO/IR weight remained high relative to the SAR. The EO/IR became the primary air vehicle sizing driver in later years.

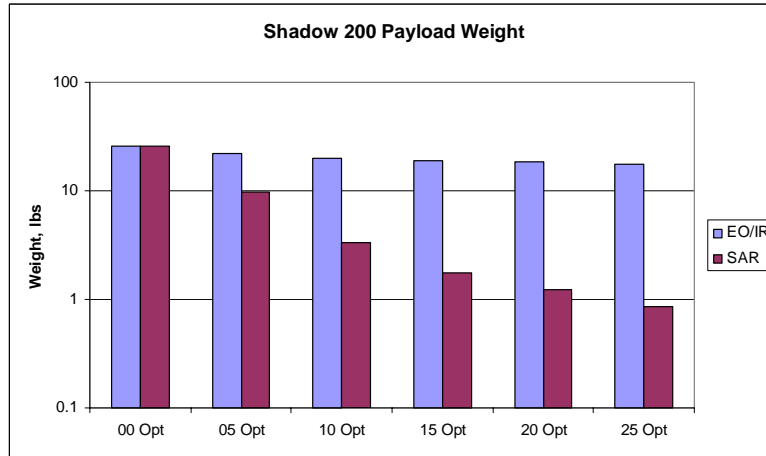


Figure 12-60 Shadow 200 Payload Weight Trends.

Structures Weights

The Shadow 200 structures weights technology trends are presented in Figure 12-61. The structures weights all decreased with time. The installation weight is the dominant contributor in all years because of the small vehicle size and high obligated weight fraction.

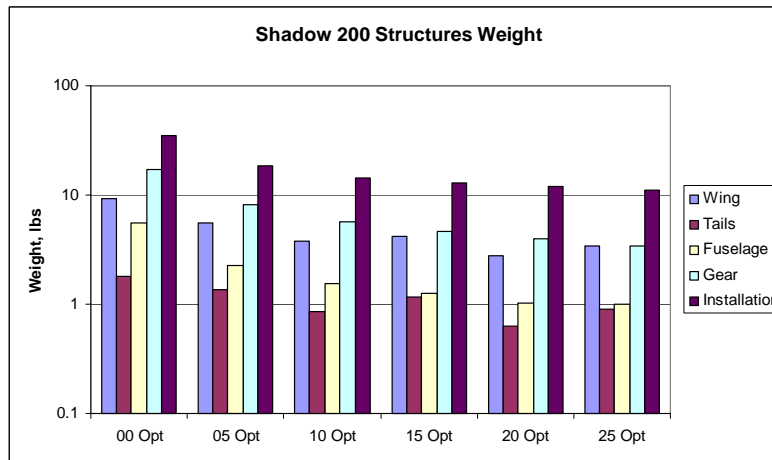


Figure 12-61 Shadow 200 Structures Weight Trends

12.4.5 Performance

Figure 12-62, Figure 12-63, Figure 12-64, and Figure 12-65 show the Shadow 200 flight profile and related performance trends. There were some variations in the optimized flight profiles.

As seen on Predator, the low technology cases tended to have a higher lift to drag ratio than the later cases. The relative contribution of the EO/IR ball drag was less on the

earlier optimal Shadow 200 cases because the ratio of ball area to wing area was smaller. The high lift to drag ratio of the early cases facilitated a more rapid climb.

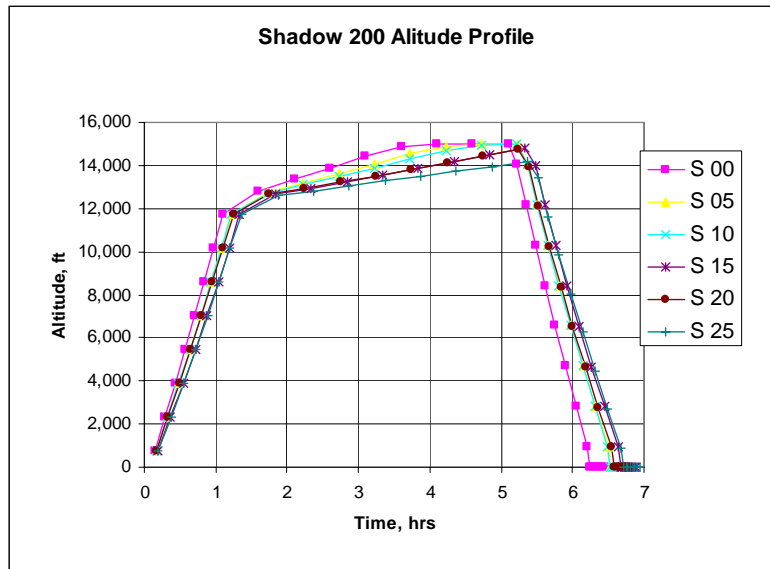


Figure 12-62 Shadow 200 Altitude Profile Trends

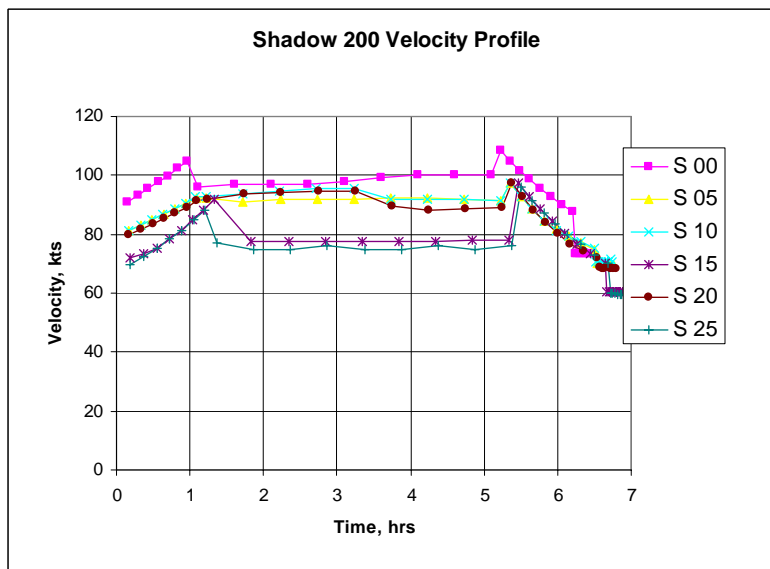


Figure 12-63 Shadow 200 Velocity Profile Trends

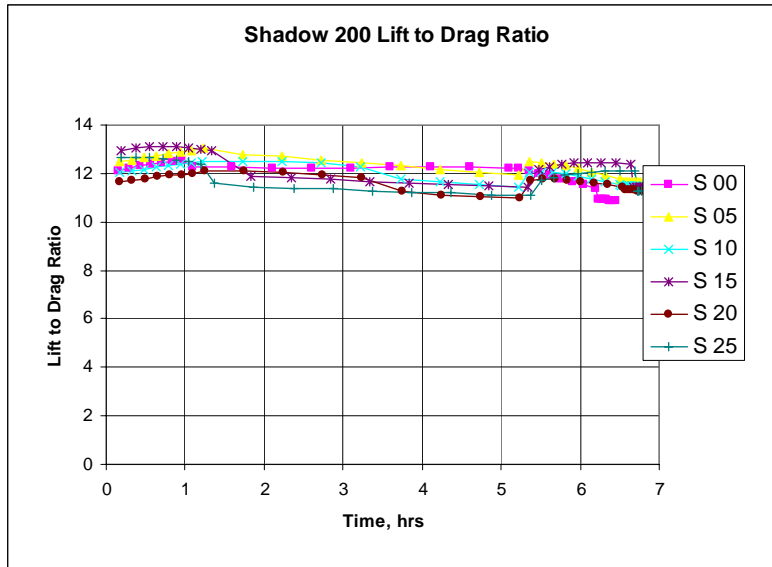


Figure 12-64 Shadow 200 Mission Lift to Drag Ratio Trends

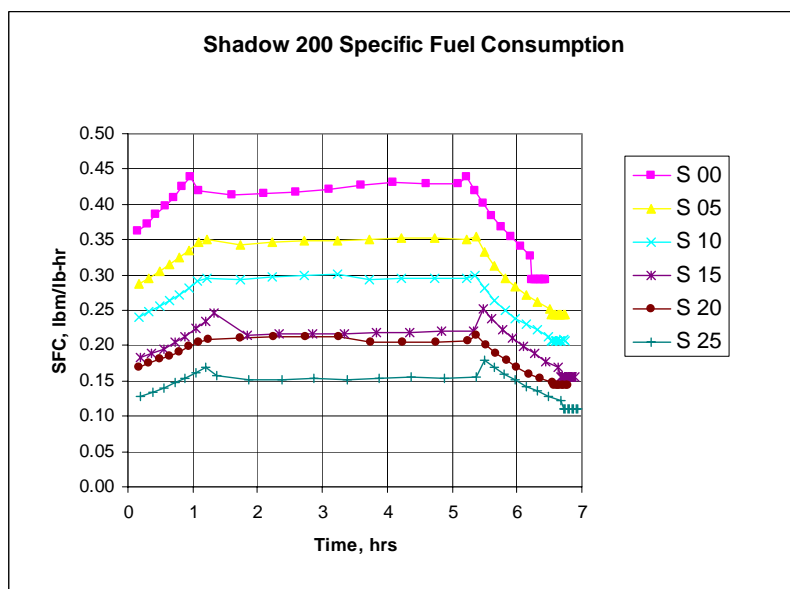


Figure 12-65 Shadow 200 Mission Fuel Consumption Trends

12.4.6 Technology Sensitivities

The Shadow 200 design gross weight sensitivities to various technologies are shown in Figure 12-66. The Shadow 200 had a 4.22% overall synergy, which is the lowest of all the cases evaluated here. Technology that affected the obligated weight directly had the greatest impact, given the small fuel fraction and associated low weight escalation factor. The strongest technology contributors were payloads and avionics/subsystems groups.

The higher fuel fraction of the previous cases created greater sensitivities to propulsion technology. The more modest Shadow 200 total improvement was only slightly higher than the combined payload and avionics/ subsystems groups.

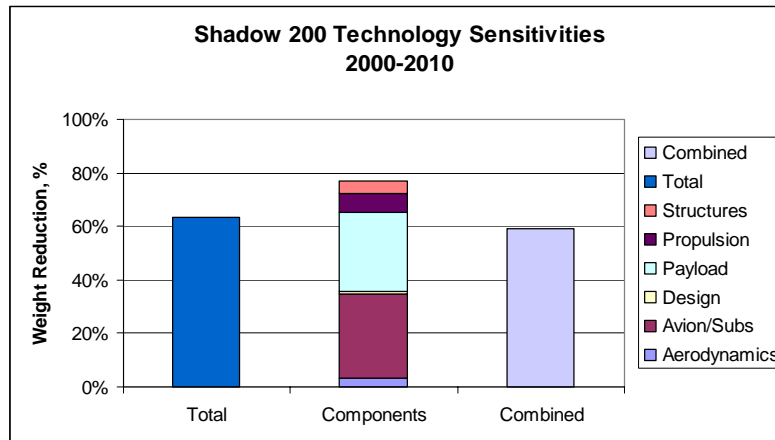


Figure 12-66 Shadow 200 Design Gross Weight Sensitivity to Technology

Chapter 13 Conclusions

13.1 AV Design Methodology Conclusions

The goal of achieving an effective and robust aircraft design methodology for unmanned aircraft has been realized. The methodology used here captures important phenomena affecting UAV design for the AV classes considered. Several analysis methods are available for many disciplines, and those ultimately selected for the final analysis adequately blend effectiveness and computational speed. Many models, such as airfoil profile performance, lift distribution prediction, propeller performance, and semi-analytic structures modeling provide high utility conceptual design capabilities beyond parametric equations. Integration of this MDO code onto a personal computer offers great convenience and severs reliance on more expensive computer resources. The methodology has been applied to three different classes of UAVs.

The applied genetic algorithm is well suited to the unmanned aircraft MDO problem. The noisy design space caused by the self-optimizing mission profiles and tabular drag polars necessitate a method as tolerant as a GA.

The aerodynamics methods are capable of modeling all cases considered. The parametric airfoil formulation adequately captures driving LRN phenomena. Other aerodynamic models employed proved effective for the problem set. The tabular drag polars are convenient for mission analysis look-up requirements and for post-design evaluations.

The propulsion models applied, while simple, adequately cover the propulsion phenomena of interest. The propulsion analysis methods are well-suited to the simple propulsion technology trends used here. The unused complex propeller performance model shows great promise despite the long relative computation time.

The AV size, weight and power model is flexible and covers the considerations of interest. The specialized avionics methods were unused with the exception of the air data system model, because every system has specific avionics suites. The subsystems models rely largely on manned aircraft parametric equations that generally operate outside the intended application. The piecewise linear beam model works well for all AV classes covered, though the lack of aerolastic analysis and stiffness-based design create limitations. The empirical fuselage weights equations should be improved in future research.

Integration of the self-optimizing mission profiles enables additional freedom in AV optimization. The alternative of simply specifying a fixed mission profile is more constraining on the design problem.

The parametric geometry formulation used in the optimization cases is robust. The vertical separation of the V-Tails and the wing ensure that no singularities occur in the lift distribution methods. The minimal tail length parametric functions effectively prevent the tail size to attain unrealistic proportions without adding additional constraints for the optimizer.

13.2 Calibration Cases Conclusions

The overall calibration achieved for the three UAV classes was successful. However, the calibration is based on often inconsistent and incomplete data. The calibration process provides the user with many means of achieving the desired results, so the target results are not difficult to obtain.

Unmanned aircraft, such as the Global Hawk and Shadow 200, experienced turbulent design histories that are difficult to replicate. Requirements and design goals evolve over time. The technologies change such that the reference technology year is difficult to identify. This calibration process, or perhaps any other, could not replicate the design history of the UAVs of interest.

Despite the inherent limitations of this process, all calibrations are within the bounds of the formulation, which lends credibility to the AV analysis methodology. The mission profiles, design gross weight, empty weight, and other known data was brought into close agreement with the available information on the UAVs of interest.

13.3 Technology Cases Conclusions

The technology impact study demonstrated the utility of the AV design methodology. The code optimized many AVs within a family over many technology years without a need for tailoring the design variables, constraint weighting, or analysis methods.

This research identified the formats for technology trends information that can be applied to AV trade studies. The process of tailoring existing technology trends to those applied resulted in substantial format modification. Existing trends frequently did not suit the needs of this research. Future AV technology modeling could benefit from following the model data requirements developed here.

The design gross weight improves with advancing technology within each vehicle family. The design gross weight is sensitive to weights that directly affect the obligated weights for all cases. Additionally, the propulsion technology strongly affects the high performance Global Hawk and Predator families, which have high fuel mass fractions relative to the Shadow 200. All three families show overall technology synergies.

The relatively steady EO/IR sensor payload weight limits the achievable size reductions. The EO/IR relative weight trends are assumed to match the EO/IR relative performance

trends here, which is probably conservative. The SAR performance per weight improved approximately 1-2 orders of magnitude more than the SAR performance during the timeframe under consideration. Unfortunately, there is no equivalent performance per weight prediction available for the EO/IR payload.

Only a limited set of potential payloads are considered. Electronics Intelligence (ELINT), Communications Intelligence (COMINT), Measurements and Signals Intelligence (MASINT), and other relevant payloads are not covered. Any one of these potential payloads could significantly impact the vehicle design.

Avionics technology impacts are significant for all families considered here. This is to be expected, because the avionics category includes a significant portion of the obligated weights. The avionics contribution to vehicle weight becomes negligible after approximately 2010 with the technology modeling used.

Not all avionics are likely to see the full potential gains modeled in this research. For example, the ATC equipment is largely driven by general aviation and commercial aviation, and is very slow to adapt to change. The unique ATC equipment trades are not considered in this research.

Miniaturization as a function of technology improvement has been practically demonstrated through the DARPA Micro Aerial Vehicle (MAV) program. One of the MAV program objectives is to demonstrate miniaturized technologies in vehicles with wingspans less than 6 inches. Many MAVs with sizes either achieving or approaching the goal were successfully developed. The MAV program achievements lend credibility to the weight reduction predictions.

Flight performance and payload performance requirements were held constant for this research. The resulting designs decreased in weight as technology advanced. This behavior is well represented by historical trends. For example, the requirement for close range battlefield surveillance has existed for decades. The vehicle sizes that support this role have greatly decreased over time. The technically attainable UAV sizes for this role have decreased from the 9-foot wingspan Pointer in the 1980's to the MAV class of today. Technology advancement for fixed requirements promotes miniaturization.

Technologies enable UAV requirements to improve, which often results in larger vehicles over time. Often, historical UAV designs within a manufacturer's line tend to increase in size as technology improves. This is due to new capabilities, previously not applicable to a vehicle class, become available to potential UAV systems that are slightly larger than the existing capability. Rather than wait for the technology to further improve, the UAV manufacturer will develop a new system to accommodate the new mission capability. The manufacturer, in this scenario, has an established capacity for UAV development and gains approval to develop a larger version of the existing family. This scenario has been demonstrated by Aerovironment with solar powered aircraft, General Atomics with the Gnat-Predator family, and Teledyne-Ryan (now Northrop Grumman) with the long lineage of reconnaissance UAVs that ultimately led to the Global Hawk. The General

Atomics Gnat-Predator family evolution is shown in Figure 1 - note that time progresses from right to left. The Teledyne Ryan UAV family evolution is shown in Figure 1-3 - again, time progresses from right to left. UAV design tools that capture technology insertion can facilitate requirements evolution.



Figure 13-1 General Atomics Gnat-Predator family evolution (Left to Right: Predator B, Predator A, Gnat)

13.4 Recommendations

Technology trends that are directly applicable to UAV design should be developed and refined. As an example, the EO/IR payload weight technology trend became a limitation to the ultimate size reductions of all cases considered here, despite its poor quality. The greatest resources should be placed on technologies that have the greatest impact on AV design, such as the EO/IR payload weight trend.

Detailed UAV subsystems definition and design methodology development should be conducted. UAV subsystems often operate beyond typical limitations of manned aircraft. Improved UAV subsystems weight methods are not possible without knowledge of the applicable design considerations.

Performance requirements for future UAV systems that leverage technology advancements should be further explored. These requirements could be applied to the AV design methodology to assess the potential solution space more realistically. Tomorrow's UAV systems will probably not be designed against today's requirements. Alternatively, this AV design methodology could be used to help define future requirements.

The performance models can be improved. The detailed propeller analysis method should be evaluated for gains in computational efficiency. The methodology should incorporate off-design propulsion models for reciprocating engines and turbofans. Electric and fuel cell propulsion system models should be added so that UAVs incorporating these options can be evaluated.

Future UAV design code enhancements should incorporate launch and recovery performance and system models. The constraints associated with this analysis will likely drive the configuration. Take-off and landing speeds, climb angles, field length, and other considerations may be drivers for UAVs equipped with conventional landing gear.

Pneumatic and rocket launch system integration will have structural impacts. Parachute recovery systems take up volume that scales as a function of the vehicle weight and descent requirements.

The wing structural model should be improved to capture more physical phenomena. Improvements should include higher quality secondary structure and control surface analysis. Key structural phenomena of interest include flutter analysis and stiffness-based design capabilities. The model should be more highly tailored to composites materials.

Future model should capture local post-stall behavior on the configuration. The current limitation that all surfaces operate in the approximately linear region prior to stall imposes limitations on the maximum permissible lift coefficient of the vehicle. In reality, local stall conditions on some portion of the vehicle typically occur prior to the vehicle achieving the maximum lift coefficient. The nonlinear behavior of the airfoils prior to and post stall creates limitations on the fidelity of the matrix methods for lift distribution calculations. The numerical lifting line theory presented in Anderson [1991] addresses these considerations for a wing, but not a lifting system. A similar numeric method could be applied to the vortex lattice method, incorporating the post-stall airfoil models developed in this research.

An entire graduate-level research effort could be dedicated exclusively to defining technology trends. Potential emphasis can be placed on generating physics and history-based technology trends. This research helps define useful formats for these technology predictions. As discussed previously, existing technology trends do not always lend themselves to integration into aircraft design and optimization codes.

As the vehicle size is reduced, the survivability will likely increase. Decreased visual, acoustic, and infrared signature levels, and potential decrease in radar cross section will reduce the probability of detection. Additionally, the overall vulnerability of the AV will decrease due to smaller presented area of flight critical components to threat systems. Future research efforts could focus on survivability benefits gained through integration of advanced technologies.

Appendix A Geometry Methods

Wing Geometry

This section provides the trapezoidal geometry formulation for the wing segments. The index for the number of wings is i , and the index for the number of segments for a given wing is j . For clarity, the index i is dropped from this discussion.

Some general geometry parameters of interest for the trapezoidal wing elements are shown in Figure A-1.

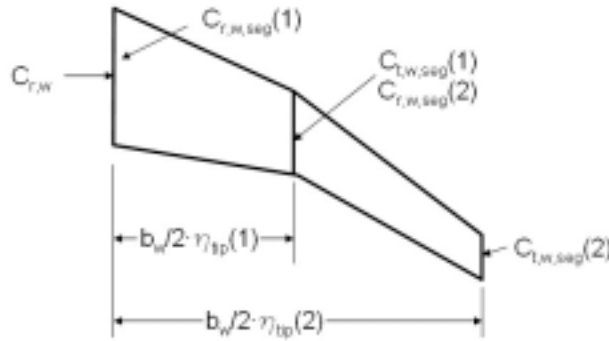


Figure A-1 Wing Geometry Parameters

First, a non-dimensional wing shape factor, SF , parameter must be defined. SF is analogous to a complex taper parameter. Note that if a single panel wing with a taper ratio of 1 is applied, then SF is equal to 2.

$$SF = \eta_{tip}(1) \cdot (1 + c_t c_{r,w}(1)) + \sum_{j=2}^{npan} [(\eta_{tip}(j) - \eta_{tip}(j-1)) \cdot (c_t c_{r,w}(j) - c_t c_{r,w}(j-1))]$$

The wing area equations are:

$$S_w = \frac{1}{2} \cdot b_w \cdot c_{r,w} \cdot SF$$

$$S_w = \frac{b_w^2}{AR_w}$$

$$S_w = \frac{1}{4} \cdot AR_w \cdot c_{r,w}^2 \cdot SF^2$$

The wing root chord equations are:

$$c_{r,w} = \frac{b_w}{\frac{1}{2} \cdot AR_w \cdot SF}$$

$$c_{r,w} = \frac{S_w}{\frac{1}{2} \cdot b_w \cdot SF}$$

$$c_{r,w} = \frac{2 \cdot \sqrt{\frac{S_w}{AR_w}}}{SF}$$

The wing span equations are:

$$b_w = \frac{2 \cdot S_w}{c_{r,w} \cdot SF}$$

$$b_w = \frac{1}{2} \cdot AR_w \cdot c_{r,w} \cdot SF$$

$$b_w = \sqrt{AR_w \cdot S_w}$$

The wing aspect ratio equations are:

$$AR_w = \frac{2 \cdot b_w}{c_{r,w} \cdot SF}$$

$$AR_w = \frac{b_w^2}{S_w}$$

$$AR_w = \frac{4 \cdot S_w}{c_{r,w}^2 \cdot SF^2}$$

To convert from the complex wing geometry to an equivalent single taper, the following equivalent taper ratio equation is used:

$$\lambda_{eq} = \frac{2 \cdot S_w}{b_w \cdot c_{r,w}} - 1$$

The segment paneling can now begin. It is necessary to know the leading edge Cartesian coordinates of the root and tip, leading edge sweep, quarter chord sweep, root and tip chords, and the root and tip incidence angles of all wing panels.

The segment dihedral-independent semispan, s_{seg} , for a wing or horizontal tail is found by:

$$s_{seg}(1) = \eta_{tip}(1) \cdot \frac{b_w}{2} \quad \text{if } j=1$$

$$s_{seg}(j) = \frac{b_w}{2} \cdot (\eta_{tip}(j) - \eta_{tip}(j-1)) \quad \text{if } j > 1$$

and for a vertical tail:

$$\begin{aligned} s_{seg}(1) &= \eta_{tip}(1) \cdot b_w \quad \text{if } j=1 \\ s_{seg}(j) &= b_w \cdot (\eta_{tip}(j) - \eta_{tip}(j-1)) \quad \text{if } j > 1 \end{aligned}$$

Similarly, the dihedral-independent segment tip location relative to the wing root for a wing or horizontal tail is:

$$s_{tip}(j) = \eta_{tip}(j) \cdot \frac{b_w}{2}$$

and for a vertical tail:

$$s_{tip}(j) = \eta_{tip}(j) \cdot b_w$$

The segment root and tip chords are found by:

$$c_{r,w,seg}(j) = c_r c_{r,w}(j) \cdot c_{r,w}(j)$$

$$c_{t,w,seg}(j) = c_t c_{r,w}(j) \cdot c_{r,w}(j)$$

The segment root incidence angle is found by:

$$\begin{aligned} inc_{r,w}(1) &= inc_w(1) \quad \text{if } j=1 \\ inc_{r,w}(j) &= inc_w - \varepsilon_w(j-1) \quad \text{if } j > 1 \end{aligned}$$

The segment tip incidence angle is found by:

$$inc_{t,w}(j) = inc_w - \varepsilon_w(j)$$

The segment quarter chord sweep for a wing or horizontal tail is:

$$\Lambda_{c/4,seg}(j) = \Lambda_{x,w}(j) + \tan^{-1} \left(\frac{(x/c_{\Lambda,w}(j) - 0.25)}{b_w/2} \cdot (c_{r,w,seg}(j) - c_{t,w,seg}(j)) \right)$$

and for a vertical tail:

$$\Lambda_{c/4,seg}(j) = \Lambda_{x,w}(j) + \tan^{-1} \left(\frac{(x/c_{\Lambda,w}(j) - 0.25)}{b_w} \cdot (c_{r,w,seg}(j) - c_{t,w,seg}(j)) \right)$$

The segment leading edge sweep for a wing or horizontal tail is:

$$\Lambda_{LE,seg}(j) = \tan^{-1} \left(\tan(\Lambda_{x,w}(j)) + \frac{x/c_{\Lambda,w}(j)}{b_w/2} \cdot (c_{r,w,seg}(j) - c_{t,w,seg}(j)) \right)$$

and for a vertical tail:

$$\Lambda_{LE,seg}(j) = \tan^{-1} \left(\tan(\Lambda_{x,w}(j)) + \frac{x/c_{\Lambda,w}(j)}{b_w} \cdot (c_{r,w,seg}(j) - c_{t,w,seg}(j)) \right)$$

Now the process of finding the coordinates for the segment root and tip leading edges can begin. Starting with the most inboard segment (j=1), the wing root coordinates are:

$$P_{r,w}(1) = P_w$$

otherwise (j>1),

$$P_{r,w}(j) = P_{t,w}(j-1)$$

Next, the difference in leading edge coordinates between the segment root and tip if dihedral is neglected is calculated:

$$\begin{aligned} \delta x = & s_{seg}(j) \cdot \tan(\Lambda_{LE,seg}(j)) \cdot \cos(inc_{r,w}(j)) + \\ & c_{t,w,seg}(j) \cdot x/c_{\varepsilon}(j) \cdot (1 - \cos(inc_{t,w}(j))) - \\ & c_{r,w,seg}(j) \cdot x/c_{\varepsilon}(j) \cdot (1 - \cos(inc_{r,w}(j))) \end{aligned}$$

$$\delta y = s_{seg}(j)$$

$$\begin{aligned} \delta z = & s_{seg}(j) \cdot \tan(\Lambda_{LE,seg}(j)) \cdot \sin(-inc_{r,w}(j)) + \\ & c_{t,w,seg}(j) \cdot x/c_{\varepsilon}(j) \cdot \sin(inc_{t,w}(j)) - \\ & c_{r,w,seg}(j) \cdot x/c_{\varepsilon}(j) \cdot \sin(inc_{r,w}(j)) \end{aligned}$$

Now the effects of dihedral can be taken into consideration:

$$\begin{aligned} \Delta x = & \delta x + \delta y \cdot \sin(\Gamma_w(j)) \cdot \sin(inc_{r,w}(j)) \cdot \cos(inc_{r,w}(j)) \\ \Delta y = & \delta y \cdot \cos(\Gamma_w(j)) \\ \Delta z = & \delta z + \delta y \cdot \sin(\Gamma_w(j)) \cdot \cos 2(inc_{r,w}(j)) \end{aligned}$$

The segment wing tip locations are then found by:

$$\begin{aligned} X_{t,w}(j) &= X_{r,w}(j) + \Delta x \\ Y_{t,w}(j) &= Y_{r,w}(j) + \Delta y \\ Z_{t,w}(j) &= Z_{r,w}(j) + \Delta z \end{aligned}$$

The overall projected planform reference area for a wing is:

$$S_{ref} = \sum_{j=1}^{n_{pan}} [(c_{r,w,seg}(j) - c_{t,w,seg}(j)) \cdot s_{seg}(j) \cdot \cos(\Gamma_w(j))]$$

The overall projected reference span for a wing and horizontal tail is:

$$b_{ref} = \sum_{j=1}^{n_{pan}} [2 \cdot s_{seg}(j) \cdot \cos(\Gamma_w(j))]$$

and for a vertical tail:

$$b_{ref} = \sum_{j=1}^{n_{pan}} [s_{seg}(j) \cdot \cos(\Gamma_w(j))]$$

Lift Distribution Paneling

There are two primary methods of paneling the wing. The first method panels each segment individually. The second method panels the entire wing by blending segments.

For the first method, each wing segment is broken into n_{pan} panels. For the index k values from 1 to n_{pan} , the following procedure is followed. The spanwise position of the segment root and tip before dihedral considerations is determined. Either even or sinusoidal spacing may be used. The sinusoidal spacing places more panels towards the tip to more fully capture the rapidly changing behavior at the wing tip. The even spacing root and tip panel spanwise locations, respectively, are:

$$\begin{aligned} ys1 &= s_{seg}(j) \cdot \frac{k-1}{n_{pan}} \quad \text{root} \\ ys2 &= s_{seg}(j) \cdot \frac{k}{n_{pan}} \quad \text{tip} \end{aligned}$$

The sinusoidal spacing equivalents are:

$$ys1 = s_{seg}(j) \cdot \sin\left(\frac{k-1}{n_{pan}} \cdot \frac{\pi}{2}\right) \quad \text{root}$$

$$ys2 = s_{seg}(j) \cdot \sin\left(\frac{k}{n_{pan}} \cdot \frac{\pi}{2}\right) \quad \text{tip}$$

Notice that no index is associated with $ys1$ or $ys2$. This is because each of these parameters is calculated for each panel, and the information does not need to be retained. The difference between $ys1$ and $ys2$, $\Delta ys(k)$, will be used for other calculations.

The non-dimensional panel spanwise station is:

$$\eta(k) = 2 \cdot \frac{s_{tip}(j) - s_{seg}(j) + \frac{ys1 + ys2}{2}}{b_w}$$

The root and tip chords of this panel are:

$$c1 = c_{r,w,seg}(j) + (c_{t,w,seg}(j) - c_{r,w,seg}(j)) \cdot \frac{ys1}{s_{seg}(j)} \quad \text{root chord}$$

$$c2 = c_{r,w,seg}(j) + (c_{t,w,seg}(j) - c_{r,w,seg}(j)) \cdot \frac{ys2}{s_{seg}(j)} \quad \text{tip chord}$$

The incidence angles of the root and tip of this panel are:

$$inc1(k) = inc_{r,w}(j) + (inc_{t,w}(j) - inc_{r,w}(j)) \cdot \frac{ys1}{s_{seg}(j)} \quad \text{root incidence}$$

$$inc2(k) = inc_{r,w}(j) + (inc_{t,w}(j) - inc_{r,w}(j)) \cdot \frac{ys2}{s_{seg}(j)} \quad \text{tip incidence}$$

The cartesian coordinates for the quarter chord of the panel root are:

$$X1(k) = X_{r,w}(j) + (X_{t,w}(j) - X_{r,w}(j)) \cdot \frac{ys1}{s_{seg}(j)} + \frac{1}{4} \cdot c1(k)$$

$$Y1(k) = Y_{r,w}(j) + (Y_{t,w}(j) - Y_{r,w}(j)) \cdot \frac{ys1}{s_{seg}(j)}$$

$$Z1(k) = Z_{r,w}(j) + (Z_{t,w}(j) - Z_{r,w}(j)) \cdot \frac{ys1}{s_{seg}(j)}$$

The cartesian coordinates for the quarter chord of the panel tip are:

$$\begin{aligned}
X2(k) &= X_{r,w}(j) + (X_{t,w}(j) - X_{r,w}(j)) \cdot \frac{ys2}{s_{seg}(j)} + \frac{1}{4} \cdot c2(k) \\
Y2(k) &= Y_{r,w}(j) + (Y_{t,w}(j) - Y_{r,w}(j)) \cdot \frac{ys2}{s_{seg}(j)} \\
Z2(k) &= Z_{r,w}(j) + (Z_{t,w}(j) - Z_{r,w}(j)) \cdot \frac{ys2}{s_{seg}(j)}
\end{aligned}$$

The second wing paneling method blends the wing segments such that the panels are distributed from wing root to wing tip rather than from segment root to tip. This method is primarily used for the lifting line theory, though the vortex lattice method and Trefftz plane analysis can use it as well.

The even spacing root and tip panel spanwise locations are:

$$\begin{aligned}
ys1 &= b_w \cdot \frac{k-1}{n_{pan}} \quad \text{root} \\
ys2 &= b_w \cdot \frac{k}{n_{pan}} \quad \text{tip}
\end{aligned}$$

The sinusoidal spacing equivalents are:

$$\begin{aligned}
ys1 &= b_w \cdot \sin\left(\frac{k-1}{n_{pan}} \cdot \frac{\pi}{2}\right) \quad \text{root} \\
ys2 &= b_w \cdot \sin\left(\frac{k}{n_{pan}} \cdot \frac{\pi}{2}\right) \quad \text{tip}
\end{aligned}$$

The non-dimensional panel spanwise station is:

$$\eta(k) = \frac{ys1 + ys2}{b_w}$$

The parameter $\theta(k)$ is used for the lifting line method. It can be thought of as an angular equivalent of the spanwise station. It is defined as:

$$\theta(k) = \cos^{-1}\left(\frac{ys1 + ys2}{b_w}\right)$$

Calculation of the other parameters uses the same equations as shown above. The one major difference is the selection of segment index j , which is now dependent upon the value of $ys1$ and $ys2$.

Regardless of which paneling method is used, other parameters can now be determined. The average panel chord is:

$$c_{ave}(k) = \frac{c1 + c2}{2}$$

The 3/4-chord panel control point used in the vortex lattice method and, except for the x-coordinate, in the Trefftz plane analysis is:

$$\begin{aligned} X_m(k) &= \frac{X1(k) + X2(k)}{2} + \frac{1}{2} \cdot c_{ave}(k) \\ Y_m(k) &= \frac{Y1(k) + Y2(k)}{2} \\ Z_m(k) &= \frac{Z1(k) + Z2(k)}{2} \end{aligned}$$

The point used to simulate the Trefftz plane (infinitely downstream) for induced drag calculations in the vortex lattice method is:

$$\begin{aligned} X_i(k) &= 100 \cdot b_w \\ Y_i(k) &= Y_m(k) \\ Z_i(k) &= Z_m(k) \end{aligned}$$

where b_w is the span of the main wing.

The equivalent panel dihedral angle, $\phi(k)$, is found by:

$$\phi(k) = \tan^{-1} \left(\frac{Z2(k) - Z1(k)}{Y3(k) - Y1(k)} \right)$$

The panel incidence angle is:

$$inc(k) = \frac{incl1(k) + incl2(k)}{2}$$

Appendix B Blade Element Propeller Methods

B.1 Overview

The propeller design and evaluation codes were developed from the work of Charles Adkins and Robert Liebeck described in their paper entitled, *Design of Optimum Propellers* [1994]. The methods used here differ from those of previous optimal propeller design codes in three ways. First, small angle approximations are not necessary. Second, there is no light disk loading requirement on the propeller. Third, viscous terms are included in the induced velocity calculations. (The airfoil drag affects the circulation distribution radially across the propeller blade). These methods bring optimal propeller design into agreement with analysis, which is an improvement on earlier blade element methods.

B.2 Blade Element Model Propeller Design

Design Results

A sample design and analysis case for a general aviation propeller was provided in Liebeck [1994]. In general, the results of this code correspond to the sample case with suitable repeatability.

There is little difference between the two airfoil interpolation methods. The differences between the code and the sample case can be partially explained by the use of different airfoil data methods. Adkins and Liebeck [1994] does not discuss the airfoil data look-up method in detail. Other differences may be explained by subtleties of two different codes. The chord distribution agreement is much better than that of the twist distribution.

The code was also evaluated for a three-bladed propeller under the same design conditions. The results in Figure B- (A-B) indicate that the local chord size is sensitive to the blade count, but the form of the chord distribution remains the same. The blade twist is very insensitive to blade count.

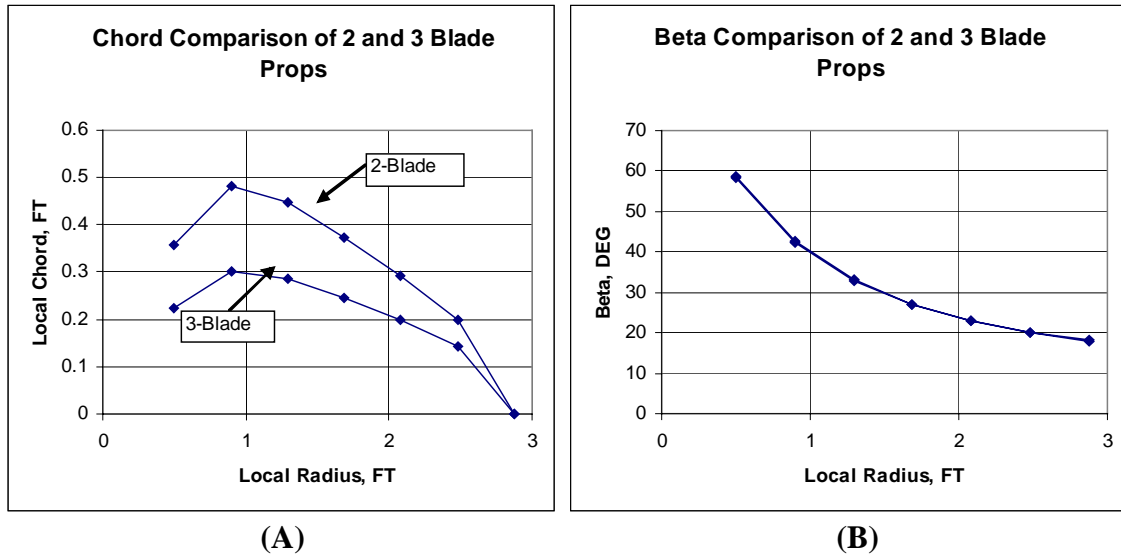


Figure B-1 Comparison Between Two and Three Bladed Propeller Designs

B.3 Blade Element Model Propeller Off-Design Analysis

The off-design analysis is necessary to determine how the propeller performs during the majority of operation. Propellers never act as point designs, rather propellers experience a range of operational conditions. The blade-element propeller off-design analysis is much more realistic at predicting off-design conditions than the disk actuator method. An added advantage of this method is the ability to predict static thrust.

The lift and drag coefficients are found as a function of angle of attack and Reynolds number through the airfoil interpolation subroutine. Note that the angle of attack and drag coefficients were determined in a similar way in the design code, except these parameters were functions of the lift coefficient and Reynolds number. By using the angle of attack as a look-up variable, it is possible to find feasible solutions of the lift and drag coefficients even beyond stall. A special model was created as part of the airfoil interpolation subroutines to calculate post-stall lift and drag values from 0 to 360 degrees angle of attack. These post-stall airfoil methods are described in the aerodynamics chapter.

The agreement with Liebeck [1994] is good in all cases. Both airfoil interpolation methods are presented here as well.

Appendix C Selected Avionics and Subsystem Weights Methods

C.1 Autopilot

Autopilots permit UAV systems to fly without pilots. Autopilots are defined here as electronic systems that control AV functions. There are four categories considered: radio control receivers, RPV autopilots, autonomous autopilots, and intelligent autopilots.

Radio Control (RC) Receivers

RC receivers have a broad range of sizes and capabilities. RC systems are generally driven by the model aircraft hobby industry.

The minimum weight of a RC receiver is assumed to be 0.1 ounces. The average RC receiver weight is 3 ounces. These numbers are based on typical commercially available RC systems. If a commercially available GPS system is included, the weight increases by approximately 4.4 ounces. If a low grade INS system is included, the weight increases by approximately 8 ounces.

RPV Autopilots

RPV autopilots contain, at minimum, an inner loop autopilot and a means of determining vehicle angular rates. The pilot typically controls the vehicle by issuing control commands in response to video and other data from the AV. RPV autopilots are becoming displaced by small autonomous autopilots.

The minimum weight of a RPV autopilot is assumed to be 2 ounces. The average RPV autopilot is assumed to weigh 1.5 pounds. If a GPS system is included, the weight increases by 8 ounces. If an INS system is included, the weight increases by 8 ounces. These weight increases are caused by the additional components plus the weight of the processors.

Autonomous Autopilots

Autonomous autopilots have the ability to perform most flight operations without pilot intervention. Pilots may or may not be in the flight control loop for launch and recovery operations. Most autonomous autopilots permit pilots to take control of the AV, and operate in a sophisticated RPV mode.

The minimum weight of an autonomous autopilot is assumed to be 4 ounces. The average autonomous autopilot weight is assumed to weigh 2 pounds. The addition of an INS system is assumed to add 1 pound. The addition of a GPS system is assumed to weigh 8 ounces.

Intelligent Autopilots

Intelligent autopilots provide additional functionality over autonomous autopilots. Intelligent autopilots can determine vehicle health, optimize collection, assist group UAV operations, and have adaptable characteristics.

The weights are assumed to be the same as for the autonomous autopilots, because little additional hardware is required. The difference between autonomous and intelligent autopilots primarily lies in the processing, which is driven by software.

General Autopilot Considerations

The autopilot weight is corrected for ruggedness, performance, and miniaturization. The corrections are valid for avionics boards and boxes. The factors are shown in Table C-1.

Driver	Minimum (0)	Mid (0.5)	Maximum (1)
Ruggedness	0.4	1.0	1.5
Performance	0.4	1.0	2.0
Miniaturization	0.4	1.0	1.5

Table C-1 Autopilot Factors

A limited database of autopilot systems was established to provide guidance on the range of autopilot solutions. This research influenced the above factors. While not exact, these correction factors provide an approximation where none previously existed.

After corrections, if the uninstalled autopilot weight is less than the minimum autopilot weight, then the uninstalled autopilot weight will be set to the minimum autopilot weight.

The volume for an autopilot is calculated. The reference density is assumed to be 45 pounds/cubic foot, which is based on Nicolai [1984]. The actual installed volume occupied by the autopilot is assumed to be 300% of the autopilot alone.

The autopilot power is assumed to be 4 Watts/pound.

C.2 Inertial Navigation System (INS)

Inertial Navigation Systems (INS) are used for almost all UAVs. Some unsophisticated systems that are little more than radio-controlled aircraft are the exception. All UAVs

under consideration in this study use an INS. The two categories of INS covered here are rate based and navigation grade INS systems.

Rate based INS systems provide angular rates and sometimes linear accelerations. Rate based INS systems are typically used by the inner loop of the flight control system. The minimum weight for a rate based INS system is assumed to be 2 ounces. A typical rate based INS system is assumed to weigh 2 pounds.

Navigation INS systems integrate the angular rates to find the angles and integrate the linear accelerations to find velocity. Often times the drift is contained by corrections enabled by GPS or air data sources. The minimum weight for a navigation INS system is assumed to be twice the weight of a C/A code GPS, because GPS is necessary if the INS sensors are crude. A typical navigation INS system is assumed to weight 5 pounds.

The INS weight is corrected for ruggedness, performance, and miniaturization. The factors are shown in Table C-2.

Driver	Minimum (0)	Mid (0.5)	Maximum (1)
Ruggedness	0.4	1.0	1.5
Performance	0.4	1.0	2.0
Miniaturization	0.1	1.0	1.5

Table C-2 INS Factors

A limited database of INS systems was established to provide guidance on the range of INS solutions. This research influenced the above factors. While not exact, these correction factors provide an approximation where none previously existed.

After corrections, if the uninstalled INS weight is less than the minimum INS weight, then the uninstalled INS weight will be set to the minimum INS weight.

The installed weight of the INS is assumed to be 150% of the uninstalled INS.

The volume for an INS is calculated. The reference density is assumed to be 70 pounds/cubic foot, which is based upon the popular LN-100G INS. The actual installed volume occupied by the INS is assumed to be 200% of the INS alone.

The INS power is assumed to be 1.73 Watts/pound, which is also based on the Litton LN100G.

C.3 Global Positioning System (GPS)

GPS is an essential element of modern UAV systems. Prior to the advent of GPS, it was necessary to fly unmanned aircraft as radio controlled models, as RPVs, or to accept

inaccurate navigation. GPS, when coupled to an autopilot or other navigation system, allows a UAV to navigate long distances accurately.

The basic GPS weight for a commercially available (C/A) code GPS is assumed to be 4.4 ounces based upon the TracPac GPS receiver. A precision (P) code GPS is assumed to be 50% heavier, because there are no commercial applications to drive the weight down.

The GPS power, cost, and volume are calculated based upon the weight using the functions for the INS. The weight and volume installation factors are calculated using the INS functions.

C.4 Processors

Processors are typically necessary to perform a variety of tasks. While autopilots typically take care of flight controls and managing flight critical systems, processors are often required. Some processor tasks may involve communications management, payload management, or pre-processing sensor data prior to sending to the autopilot.

A typical processor is assumed to weigh 3 pounds. This weight is corrected for ruggedness, performance, and miniaturization according to the boards and boxes functions described earlier. The power, volume, and installation factors are also found using boards and boxes functions.

C.5 Cameras

Cameras are often needed on UAVs. This can be to aid in take-off in landing operations or to provide general situational awareness. These cameras are considered distinct from cameras that are part of the payload.

Three types of cameras are considered: Electro-optical (EO), Infrared (IR), and low-light. The weight of a typical EO camera is assumed to be 0.5 pounds. The weight of a typical IR camera is assumed to be 2 pounds. The weight of a typical low-light camera is assumed to be 1 pound.

The camera weight is corrected for ruggedness, performance, and miniaturization. The factors are shown in Table C-3.

Driver	Minimum (0)	Mid (0.5)	Maximum (1)
Ruggedness	0.5	1.0	2.0
Performance	0.5	1.0	4.0
Miniaturization	0.5	1.0	2.0

Table C-3 Camera Factors

The power and volume are found using the boards and boxes functions. The weight and volume installation factors are also found using the boards and boxes functions.

C.6 Recorders

Recorders are sometimes necessary for recording payload data, flight data, and any other data of interest.

The recorder is assumed to weigh 0.5 pound per gigabyte.

The volume and power is found using the associated boards and boxes formulas. The weight and installation factors are from the boards and boxes formulas.

C.7 Air Traffic Control (ATC)

Several ATC options are covered in the code. ATC equipment makes it possible for UAVs to operate in the same airspace as manned aircraft. While the FAA and foreign ATC services have evolving UAV airspace operability requirements, the equipment covered here will be relevant.

ATC Radios

UAV systems may use ATC radios in one of three ways. First, the voice communications between the ATC personnel and the UAV ground personnel may be relayed through the AV. Second, the AV may generate a voice signal to ATC and interpret the ATC voice via voice recognition software. Third, the UAV system ground personnel may communicate directly with the local ATC with ground station ATC radios. Only the first two options affect the AV weight, so the third option is dropped from consideration.

The Filser ATR 720 A [Aircraft Spruce and Specialty 2002] ATC radio is used as a reference. The radio characteristics are shown below.

Weight: 1.56 pounds
Volume: 51 in³
Power: 4 Watts output (Assume 16 Watts input – 25% efficiency)
Cost: \$1095 (2002)

The ATC radio requires an antenna. A typical VHF ATC antenna has the following characteristics:

Weight: 0.5 pounds
Volume: 0. (Almost all external)
Power: 0.
Cost: \$97.50 (2002)

Mode 3A

Mode 3A transponders provide an identification code to ATC when interrogated. The ATC determines the aircraft position as the ATC radar makes the 360° sweeps. The reference transponder is the Garmin GTX327 [Aircraft Spruce and Specialty Co. 2002]. This is used for modes 3A, C, and S. The characteristics are shown below.

Weight: 2.1 pounds
Volume: 83.5 in³
Power: 15 Watts
Cost: \$1895 (2002)

The weight of the Mode 3A ATC also includes the ATC antenna weight.

Mode C

Mode C transponders have all of the features of the Mode 3A, but also add an altitude reporting capability. This requires an altitude encoder. The Ameri-King altitude encoder [Aircraft Spruce and Specialty Co 2002] is used as a reference. The characteristics are shown below.

Weight: 0.4 pounds
Volume: 33.25 in³
Power: 1 Watt (Guess)
Cost: \$500 (The cost is altitude dependent)

All other components and weights from the Mode 3A are included.

Mode S

Mode S transponders enable pilots to determine the position of other Mode S aircraft relative to their aircraft. This is a relatively new mode that is not widely adopted. Mode S is incorporated into TCAS, an aircraft collision avoidance system. Mode S uses all of the features of Mode C, and the weights are considered identical for the purposes of this code.

General ATC Considerations

No technology factors are applied to the ATC equipment for this formulation. Factors are applied when entered directly as avionics. ATC equipment is relatively mature. The hardware is largely driven by commercial and general aviation, which are slow to adopt new technologies. It is conceivable that a UAV program could modify the equipment, but this may introduce FAA acceptance issues.

Installation weight and installation volume factors are applied to the ATC equipment.
The functions for avionics boards and boxes are used.

Bibliography

- Abbot, Ira H., and Von Doenhoff, Albert E., *Theory of Wing Sections, Including a Summary of Airfoil Data*, Dover Publications, Inc., New York, 1959.
- Adkins, Charles N., Liebeck, Robert H., Design of Optimum Propellers, AIAA-83-0190, AIAA 21st Aerospace Sciences Meeting, January 1983.
- Adkins, Charles N., Liebeck, Robert H., *Design of Optimum Propellers*, AIAA Journal (NFI), Volume 10, Number 5, Sept-October 1994.
- Aircraft Spruce and Specialty Co., 2002-2003 Catalog*, Aircraft Spruce and Specialty Co., 2002.
- Air Force Scientific Advisory Board (SAB), *UAV Study*, Air University, 1996.
- Althaus, Dieter, *Profilpolaren fur den Modellflug, Band 2*, Neckar-Verlag GMBH, Germany, 1985.
- Altmann, Herman, *A Study of a Reconnaissance Surveillance Vehicle*, Course Materials Presented at the UCLA UAV Aircraft Design Short Course, August 2002.
- Anderson, John D., *Fundamentals of Aerodynamics, Second Edition*, McGraw-Hill, Inc., United States of America, 1991.
- Bertin, John J., and Smith, Michael L., *Aerodynamics for Engineers, Second Edition*, Prentice Hall, Inc., Englewood Cliffs, NJ, 1989.
- Boucher, Robert J., *Electric Motor Handbook*, Robert J. Boucher, Los Angeles, 1994.
- Brown, David R., *Unmanned Combat Aerial Vehicles: Evolution or Potential Revolution?*, Air University, April 1998.
- Brown, Robert B., *Compass Cope Airframe Design History*, AIAA Journal of Aircraft, Volume 17, Number 12, December 1980.
- Brown, Stuart F., "Batteries are Getting Charged Up," *Fortune*, October 27, 1997.
- Carmichael, Bruce W., DeVine, Troy E., et. al., *Strikestar 2025*, Research Paper Presented to Air Force 2025, August 1996.
- Carroll, David L., *GA170 Code Listing*, University of Illinois at Urbana Champaign, December 1998.

Davenport, William, *Virginia Tech AOE 5104 Graduate Incompressible Aerodynamics Course Notes*, 1998.

Defense Airborne Reconnaissance Office (DARO), *UAV Annual Report FY 1996*, 6 November 1996.

Defense Airborne Reconnaissance Office (DARO), *UAV Annual Report FY 1997*, 1997.

Defense and Aerospace, *Technology Foresight – Progress Through Partnerships*, Office of Science and Technology for HMSO, Vol 12, April 1995.

Drela, Mark, *XFOIL 6.9 User Guide*, MIT Aero and Astro, 2000.

Drezner, Jeffrey A., and Leonard, Robert S., *Innovative Development, Global Hawk and Darkstar, Executive Summary and Vol 1-3*, RAND Project Air Force, RAND, 2002.

Etkin, Bernard, and Reid, Lloyd D., *Dynamics of Flight, Stability and Control, Third Edition*, John Wiley and Sons, Inc, Canada, 1996.

Fahlstrom, Paul G., and Gleason, Thomas J., *Introduction to UAV Systems, Second Edition*, UAV Systems Inc., Columbia, Maryland, 1998.

Foch, Richard J., Ailinger, Kevin G., *Low Reynolds Number Long Endurance Aircraft Design*, AIAA 92-1263, AIAA, 1992.

Goldberg, David E., *Genetic Algorithms in Search, Optimization, and Machine Learning*, Addison Wesley Longman, Inc., USA, 1989.

Grasmeyer, Joel, *Truss-Braced Wing Code Description and User's Manual*, VPI-AOE-255, Virginia Tech, 1998.

1. Gundlach, John F., *Development of the Virginia Tech Forestry Unmanned Aerial Vehicle*, AIAA 99-0003, 1999.

2. Gundlach, John F., *Multidisciplinary Design Optimization and Industry Review of a 2010 Strut-Braced Wing Transonic Transport*, Masters Thesis, Virginia Tech, 1999.

Gundlach, John F., Tetrault, P.-A., Gern, F.H., Nagshineh-Pour, A.H., Ko, A.K., Schetz, J.A., Mason, W.H., Kapania, R.K., Grossman, B., Haftka, R.T., *Conceptual Design Studies of a Strut-Braced Wing Transonic Transport*, AIAA Journal of Aircraft, Volume 37, Number 6, December 2000.

Hall, David W., Fortenbach, Charles D., et. al., *A preliminary Study of Solar Powered Aircraft and Associated Power Trains*, NASA CR 3699, 1983.

Hall, David W., Hall, Stan A., *Structural Sizing of a Solar Powered Aircraft*, NASA Contractor Report 172313, 1984.

Hill, Philip G., Peterson, Carl R., *Mechanics and Thermodynamics of Propulsion, Second Edition*, Addison-Wesley Publishing Company, Inc., Reading, Massachusetts, 1992.

Hoerner, S.F., *Fluid-Dynamic Drag*, Hoerner Fluid Dynamics, Vancouver, WA, 1992.

Holder, Bill, *Unmanned Vehicles, An Illustrated History*, Schiffer Publishing Inc, China, 2001.

Irwin, Col. David W., Jr., *Reconnaissance is Black*, Turner Publishing Co., Paducah, Kentucky, 2000.

Johnstone, R., Arntz, N., *CONDOR – High Altitude Long Endurance (HALE) Automatically Piloted Vehicle (APV)*, AIAA 90-3279, AIAA, 1990.

McDaid, Hugh, and Oliver, David, *Smart Weapons, Top Secret History of Remote Controlled Airborne Weapons*, Barnes and Noble, Inc., Italy, 1997.

Munson, Kenneth, *Jane's Unmanned Aerial Vehicles and Targets, Issue Thirteen*, Jane's Information Group Limited, UK, 1999.

Munson, Kenneth, *World Unmanned Aircraft*, Jane's Publishing Company Limited, London, 1988.

L-3 Communications, *S/TAR Strategic/Tactical Airborne Recorder*, Brochure presented at AUVSI 2003, 2003.

Libeau, Michael, *Design Visualization Using the DXF.F Subroutine*, Unpublished documentation supporting the Virginia Polytechnic and State University Strut-Braced Wing (SBW) transonic transport research, May 1999.

Macci, S. H., *Semi-Analytical Method for Predicting Wing Structural Mass*, 54th Annual Conference of the Society of Allied Weights Engineers, Inc., Huntsville Alabama, 1995.

Mattingly, J. D., Et. Al., *Aircraft Engine Design*, AIAA Education Series, AIAA, New York, 1987.

McCormick, Barnes W., *Aerodynamics Aeronautics and Flight Mechanics, Second Edition*, John Wiley and Sons, Inc., New York, 1995.

Mises, Richard V., *Theory of Flight*, Dover Publications, Toronto, 1959.

Naghshineh-Pour, Amir H., *Preliminary Structural Analysis of a Strut-Braced Wing*, VPI-AOE-256, Department of Aerospace and Ocean Engineering, Virginia Polytechnic Institute and State University, 1998.

1. The National Academy of Sciences, *Review of ONR's Uninhabited Combat Air Vehicles Program*, National Academy Press, Washington DC, 2000.

2. The National Academy of Sciences, *Uninhabited Air Vehicles, Enabling Science for Military Systems*, National Academy Press, Washington DC, 2000.

Nelson, Robert C., *Flight Stability and Automatic Control*, McGraw Hill, Inc., Mexico, 1989.

Nichols, Mark J., and Martel, William C., *UCAVs and Commercial Satellites: "The Missing Link"*, Air War College, Air University, April 1998.

Nicolai, Leland M., *Fundamentals of Aircraft Design*, METS, inc., USA, 1984.

Noor, Ahmed K., *Future Aeronautical and Space Systems*, Volume 172, Progress in Astronautics and Aeronautics, AIAA, Reston, VA, 1997.

Noor, Ahmed K., *Structures Technology for Future Aerospace Systems*, Volume 188, Progress in Astronautics and Aeronautics, AIAA, Reston, VA, 2000.

Northrop Grumman, *RQ-4A Global Hawk, High Altitude Endurance Unmanned Aerial Vehicle*, Brochure presented at AUVERSI 2003, Northrop Grumman 452-AS-4209_06.03, 2003.

Oates, G. C., *The Aerothermodynamics of Gas Turbine and Rocket Propulsion*, AIAA Education Series, AIAA, New York, 1984.

Office of the Secretary of Defense (OSD), *Unmanned Aerial Vehicles Roadmap 2000-2025*, Washington DC, April 2001.

Office of the Secretary of Defense (OSD), *Unmanned Aerial Vehicles Roadmap, 2002-2027*, Draft Version 7, Washington DC, November 2002.

O'Reilly, Thomas G., and Beno, Andrew M., *Uninhabited Air Vehicles - Critical Leverage Systems for Our Nation's Defense in 2025*, Air Command and Staff College, Air University, April 1999.

Palumbo, Dominic J., *Design Evolution of the Shadow 200 Tactical Unmanned Aerial Vehicle*, Unmanned Systems 2000, Association of Unmanned Vehicle Systems International, 2000.

Power Computing Solutions, Inc. (PCS), *Electric Power System for High Altitude UAV Technology Survey*, NASA/CR-97-206337, 1997.

Raymer, Daniel P., *Aircraft Design: A Conceptual Approach*, 2nd Edition, AIAA Education Series, Washington, D.C., 1992.

Raymer, Daniel P., *UAV Aircraft Design*, UCLA Short Course Materials, August 2002.

Ritchie, D., *Aerodynamics Course Notes*, Academy of Aeronautics, Long Island, New York, 1968.

Roskam, Jan, *Airplane Design, Parts I-VIII*, Roskam Aviation and Engineering Corporation, Ottawa, Kansas, 1990.

SAWE (Society of Allied Weight Engineers), *Introduction to Aircraft Weight Engineering*, SAWE Inc, Los Angeles, 1996.

Selig, Michael S., Donovan, John F., and Fraser, David B., *Airfoils at Low Speed*, Soartech 8, H.A. Stokely, Virginia Beach, VA, 1989.

Selig, Michael S., Et. Al., *Summary of Low-Speed Airfoil Data, Volume 1*, SoarTech Publications, Virginia Beach, VA, 1995.

Sheldahl, R. E. and Klimas, P. C., *Aerodynamic Characteristics of Seven Airfoil Sections Through 180 Degrees Angle of Attack for Use in Aerodynamic Analysis of Vertical Axis Wind Turbines*, SAND80-2114, March 1981, Sandia National Laboratories, Albuquerque, New Mexico.

Sloan, Joel, *Design and Packaging of Electronics Equipment*, Van Nostrand Reinhold Company, NY, 1985.

Somers, Dan M., Maughmer, Mark D., *The SM701 Airfoil, An Airfoil for World Class Sailplanes*, The Pennsylvania State University, Circa 1992.

Stinton, Darrol, *The Design of the Aeroplane*, Blackwell Sciences Ltd., Oxford, 1995.

Sullivan, Lt. Col. James F., Brouillette, Maj. Gregory, Joles, Maj. Jeffery, *1998 Army After Next Unmanned Aerial Vehicle Studies*, Operations Research Center, July 1998.

Wagner, William, Sloan, William P., *Fireflies and other UAVs (Unmanned Aerial Vehicles)*, Aerofax Inc, Arlington, Texas, 1992.

Wagner, William, *Lightning Bugs and other Reconnaissance Drones, The can-do story of Ryan's unmanned 'spy planes'*, Armed Forces Journal International, Fallbrook, California, 1982.

Werrell, Kenneth P., The Evolution of the Cruise Missile, Air University Press, Maxwell AFB, Alabama, September 1985.

Whitford, R., *Fundamentals of Fighter Design*, Airlife Publishing Ltd., UK, 2000.

List of Acronyms

AAI	Company name
AC	Aerodynamic Center
ACTD	Advanced Concept Technology Demonstrator
AIAA	American Institute of Aeronautics and Astronautics
ATC	Air Traffic Control
AUVS	Association of Unmanned Vehicle Systems
AUVSI	Association of Unmanned Vehicle Systems International
AV	Air Vehicle
BLOS	Beyond Line of Sight
CFD	Computational Fluid Dynamics
COMINT	Communications Intelligence
DGPS	Differential Global Positioning System
ECS	Environmental Control System
ELINT	Electronics Intelligence
EO	Electro-Optical
EO/IR	Electro-Optical/Infrared
FCS	Flight Control System
FOM	Figure of Merit
FOS	Factor of Safety
GN&C	Guidance, Navigation and Control
GPS	Global Positioning System
HALE	High Altitude Long Endurance
HAPP	High Altitude Powered Platform
IFF	Identify Friend of Foe
INS	Inertial Navigation System
IR	Infrared
LHS	Left-Hand-Side
LLT	Lifting Line Theory
LOS	Line of Sight
LRN	Low Reynolds Number
MAE	Medium Altitude Endurance
MASINT	Measurements and Signals Intelligence
MAV	Micro Aerial Vehicle
MDO	Multi-Disciplinary Design Optimization
RHS	Right-Hand-Side
ROA	Remotely Operated Aircraft
RPV	Remotely Piloted Vehicle
SATCOM	Satellite Communications
SAWE	Society of Allied Weights Engineers
SBW	Strut-Braced Wing
SLS	Sea Level Static Conditions
SWaP	Size, Weight and Power
UAV	Unmanned Aerial Vehicle

UCAS	Uninhabited Combat Aircraft System
UCAV	Uninhabited Combat Aerial Vehicle
UFP	Unit Flyaway Price
UIUC	University of Illinois at Urbana Champaign
VLM	Vortex Lattice Method

Formatting Notes

The code architecture descriptions use capitalized and italicized letters to name subroutines. The names presented may differ from the source code names when clarity is gained from doing so. The functional architecture is accurate. When practical, minor subroutines are not listed when there are significant differences in level.

The consolidated nomenclature definition list is defined initially within the document. When a single variable name represents two or more variables, then the variable name is used once and is followed by all definitions. Some variables with limited usage are defined within the text of the document and not captured within the consolidated nomenclature definition list. The units of variables are covered in the nomenclature list to streamline the rest of the document.

Vita

John F. Gundlach IV has worked on several manned and unmanned aircraft research and development projects. John has built over 50 radio controlled model aircraft starting at the age of 13, with many original designs. At age 15, John helped build a wind tunnel and static display model of a 50-60 passenger turboprop design for a fledgling aircraft company. At 17, John joined Aurora Flight Sciences, where he helped build the full-scale mock-up of the Theseus high-altitude UAV. He also developed radio-controlled flying engineering models and conducted Multidisciplinary Design Optimization (MDO) work for Aurora Flight Sciences on Jason, a Mars atmospheric flight vehicle. He graduated Suma Cum Laude in undergraduate Aerospace Engineering at Virginia Tech in 1998. While an undergraduate, John received the 1998 Sigma Gamma Tau National Aerospace Honor Society Ammon S. Andes National Award, won first prize in the AIAA 1998 Mid-Atlantic Regional Student Conference, was chairman of the Virginia Tech AIAA, was the team leader of the 2nd place winner of the 1997 AIAA Design/Build/Fly UAV Competition, published three AIAA papers, led the NASA Forestry UAV project, and received several other honors and awards. During the undergraduate years, he worked at Naval Research Laboratory on over a dozen UAV programs. John went on to complete his Masters degree in Aerospace Engineering from Virginia Tech in 1999, working on the Strut-Braced Wing (SBW) MDO project. His SBW research resulted in four published papers, including a Journal of Aircraft article. John works for the United States Government today.